Universitat de València

Facultat de Física

Departament de Física de la Terra i Termodinàmica

Characterization of the surface emissivity and temperature at heterogeneous sites for different zenith viewing angles using remote sensing

Doctorado en Teledetección

Lluís Pérez Planells

Noviembre, 2020

Directores: Dr. Enric Valor i Micó

Dra. Raquel Niclòs Corts

D. ENRIC VALOR I MICÓ, Catedrático de Física de la Tierra en el Departamento de Física de la Tierra y Termodinámica de la Facultad de Física, Universitat de València, Y

Dña. RAQUEL NICLÒS CORTS, Profesora titular de Física de la Tierra, en el Departamento de Física de la Tierra y Termodinámica de la Facultad de Física, Universitat de València,

CERTIFICAN: Que la presente memoria "*Characterization of the surface emissivity and temperature at heterogeneous sites for different zenith viewing angles using remote sensing*", presentada por Lluís Pérez Planells ha sido realizada bajo su dirección constituyendo su tesis doctoral para optar al grado de doctor por la Universitat de València dentro del Doctorado en teledetección.

Y para que así conste, en cumplimiento de la legislación vigente, firman el presente certificado en Burjassot, a 23 de noviembre de 2020

Fdo.: Enric Valor i Micó

Fdo.: Raquel Niclòs Corts

Este trabajo ha sido posible gracias a la financiación recibida por parte de los siguientes proyectos:

- Impacto térmico en fenómenos meteorológicos de ecosistemas mediterráneos: desarrollo de técnicas de teledetección y una red automática de radiometría angular de campo (CGL2011-30433-C02-02), Ministerio de Ciencia e Innovación (MICINN).

- Estimación y seguimiento de la temperatura y la emisividad de la superficie terrestre mediante los últimos avances en teledetección (CGL2013-46862-C2-1-P), Ministerio de Economía y Competitividad (MINECO).

- Impacto del cambio climático sobre ecosistemas: patrones a fina escala, índices y vigilancia de temperaturas extremas mediante nuevas técnicas de teledetección (CGL2015-64268-R), Ministerio de Economía y Competitividad y los fondos europeos de desarrollo regional (MINECO/FEDER, UE).

- El uso de la teledetección para una mejor comprensión del cambio Climático (PROMETEOII/2014/086), Generalitat Valenciana, Conselleria d'Educació i Ciència, en el marco del Programa Prometeo (I+D) para grupos de investigación de excelencia.

Y gracias a la contratación como Técnico de investigació dentro de los proyectos: CGL2011-30433-C02-02 mediante la ayuda Gerónimo Forteza FPA/2015/081, CGL2013-46862-C2-1-P, PROMETEOII/2014/086.

Y al contrato establecido de Técnico Superior de Investigación financiado por la Generalitat Valenciana, Conselleria de Educación, Investigación, Cultura y Deporte, mediante las subvenciones para la mejora de la formación y empleabilidad de personal técnico y de gestión de la I+D+i, en el marco del Sistema Nacional de Garantía Juvenil y cofinanciadas por el Fondo Social Europeo y la Iniciativa de Empleo Juvenil (GJIDI-2018-A-142).

Asimismo, agradecer las ayudas recibidas para la realización de estancias los centros de investigación:

- Instituto de Hidrología de Llanuras (IHLLA) – Universidad del Centro de la Provincia de Buenos Aires (UNICEN) por parte de la Universitat de València mediante las Becas de Movilidad Internacional de Doctorado 2019.

- Karlsruhe Institute Technology (KIT) por parte del Servicio Alemán de Intercambio Académico (DAAD) mediante el programa de Becas de investigación de estancias cortas 2020 (Nº de subvención: 57507441).

És per tots sabut que la ciència està lligada incondicionalment amb l'avanç de l'ésser humà. Forma part del nostre passat, present i futur. D'aquesta manera i, a tall d'analogia amb la ciència, existeixen determinades persones que han demostrat estar incondicionalment amb mi, ajudant-me en el passat, present i, espere, en un futur.

Mentiria si no diguera que aquesta part de la meua tesi ha sigut una de les més difícils de redactar. La realitat és que he dedicat els darrers cinc anys de la meua vida a escriure en termes científics i, ara, em resulta més complex expressar amb paraules eloqüents la meua gratitud a aquells que m'heu acompanyat en aquest camí. Espere haver aconseguit finalment el meu objectiu principal: agrair-vos tots els vostres ensenyaments, els quals han contribuït enormement en el meu avanç personal, i, dir-vos, que estareu presents en mi de la mateixa manera que la ciència, incondicionalment.

En primer lloc, vull agrair als directors d'aquesta Tesi Doctoral, el Dr. Enric Valor i la Dra. Raquel Niclòs, per la seua disposició, pel seu afecte sincer i per guiar-me en tot aquest recorregut. Sense vosaltres, aquest treball no haguera estat possible.

Al Dr. Vicente Caselles i al Dr. Vicente García Santos, agrair la seua confiança depositada en mi quan em van donar l'oportunitat de fer els primers passos en la ciència. L'experiència recollida amb els primers treballs i els vostres consells han sigut clau per emprendre aquest camí.

Al Dr. César Coll, agrair el seu continu interés en el meu treball i les valuoses aportacions realitzades en el desenvolupament de cada investigació.

Al Departament de Física de la Terra i Termodinàmica, agrair especialment a l'equip administratiu: Quique, Mónica i Mª Ángeles per tota l'ajuda administrativa rebuda en aquest temps; a Vicente Marín, per la seua disposició en les diferents necessitats tècniques; i a la Dra. Pilar Utrillas, Directora del Departament, per la seua atenció en resoldre tots els dubtes que han sorgit en aquest període.

Als companys del Laboratori de Teledetecció Tèrmica, agrair a tots el seu suport diari: al Dr. Joan Miquel Galve, per tota l'ajuda aportada en els infinits consells de roca, a la Dra. Carolina Doña i la Dra. Maria Jesús Barberà, per la motivació i l'alegria que han

aportat al laboratori amb els seus ànims inacabables, i a Jesús Puchades, gran company de batalla i de sentiment blanc-i-negre. I a tots aquells que han passat pel laboratori en períodes més reduïts, especialment a Diego, amb qui vaig iniciar aquesta etapa.

Al Dr. Raúl Rivas y a todos los miembros del Instituto de Hidrología de Llanuras, agradecer el recibimiento con los brazos abiertos en su unidad. Siempre llevaré una parte de vosotros allá donde esté (y de la receta de Mati también). En este momento, quisiera agradecer especialmente el cariño recibido por Flor y Zufi, quienes me hicieron sentir como en casa a pesar de estar tan lejos de ella. Espero poder devolver, más pronto que tarde, todo lo que me aportasteis.

To Dr. Jan Cermak and Dr. Frank Göttsche, thanks for your reception and attention during my short-stay at Karlsruhe Institute of Technology. And thanks also for the different advises and contributions in this last period. I want to thanks to all the IMK-ASF colleagues, for transmitting that good mood every morning in the virtual coffee, despite of the atypical situation, and sharing time not only for science but also for joy.

Als meus amics, a tots i cada un d'ells, gràcies per cada moment compartit al vostre costat. No haguera sigut el mateix sense cada aventura viscuda. Aquestes han donat més força de la que ens podem imaginar.

A Gloria, a tu és molt més que unes paraules d'agraïment. La teua confiança i estima són essencials per a mi. Al nostre llibre hi haurà molt més que 124 fulles.

Als meus pares, que són part fonamental en la meua vida. El seu suport en cada pas ha sigut imprescindible per arribar fins ací. Agrair a la meua germana Victoria i a Javi, pel seu consell i ajuda en tot moment, i als xicotets de la casa, que ens omplin d'energia cada dia. Així, no puc deixar d'agrair a la resta de la meua família, especialment a les ties Tere i Maru i al tio Pepe, que a més del suport i interés mostrat, han aportat al desenvolupament d'aquesta tesi amb els seus diferents coneixements.

Contenido

Resumen

Para estimar con precisión la temperatura de la superficie terrestre (TST) es necesario conocer con exactitud la emisividad de dicha superficie. Sobre zonas vegetadas, la estimación de la emisividad es más compleja debido a las reflexiones múltiples de la radiación (emitida y reflejada) entre los distintos elementos que forman la vegetación (suelo y elementos de la planta). En la literatura pueden encontrarse diversos métodos que modelan la emisividad de la vegetación. En este trabajo, se ha profundizado en el análisis y evaluación de los modelos de transferencia radiativa (MTR) para la obtención de la emisividad direccional de la vegetación. Los modelos utilizados para este estudio han sido: FR97 (François et al., 1997), Mod3 (François, 2002), Rmod3 (Shi, 2011), REN15 (Ren et al., 2015), CE-P (Cao et al., 2018) y 4SAIL (Verhoef et al., 2007). Estos modelos han sido validados con medidas *in-situ*, aplicados a datos de satélite y evaluados cuando las emisividades resultantes se usan como entrada de un algoritmo split-window (SW) para la obtención de la TST.

Validación de los MTR

Los MTR fueron evaluados realizando medidas *in-situ* de emisividad sobre una muestra de rosales y dos suelos con características distintas: un suelo orgánico con alta emisividad y un suelo inorgánico (arena) con baja emisividad. Para la realización de medidas *in-situ* se utilizaron dos radiómetros CE312 con cinco canales estrechos entre 8 y 13 µm, los cuales permitieron aplicar un método de separación temperatura-emisividad (TES). En un primer estudio, donde se utilizó un suelo orgánico, se realizaron 15 medidas de radiancia para 7 ángulos de observación y 6 valores de LAI en cada caso. En un segundo estudio, el suelo orgánico se cambió por arena y se tomaron 15 medidas de radiancia para 2 ángulos de observación distintos y 6 valores de LAI. Además, para la aplicación de los modelos se midieron las muestras de hoja de rosal y de los dos suelos. De estas medidas se obtuvo una emisividad constante en el caso de las hojas, cercana a 0,98. Para el suelo orgánico, la emisividad obtenida varió entre 0,949 y 0,967 según el canal espectral, mientras que para el suelo inorgánico la emisividad mostró tener un mayor contraste espectral, con una emisividad entre 0,732 y 0,962.

La emisividad derivada de los MTR se comparó primero con la emisividad medida en observación a nadir. Para el suelo orgánico, los resultados mostraron que las medidas de emisividad TES no diferían con la variación del LAI. Sin embargo, sobre el suelo inorgánico se observó en la emisividad TES el incremento en emisividad predicho por los MTR, principalmente debido a la mayor diferencia entre la emisividad del suelo inorgánico y de las hojas. Esta variación de la emisividad con el LAI, observada con las medidas *in-situ*, fue ajustada mediante regresión, obteniendo coeficientes de correlación entre 0,986 y 0,999 según el canal espectral. El MTR Mod3 obtuvo valores más cercanos a las medidas TES que el resto de modelos, teniendo en cuenta el análisis estadístico tanto del suelo orgánico como inorgánico. Estos mejores resultados del MTR Mod3 destacaron especialmente en aquellos canales donde la diferencia entre la emisividad de suelo y hoja era mayor.

La evaluación de la emisividad obtenida en función del ángulo de observación mostró poca variación, tanto en el caso de los MTR como en el de las medidas TES, sobre cualquiera de las muestras con los distintos suelos utilizados. Por lo tanto, para condiciones similares a las analizadas en este estudio no se espera ninguna variación de la emisividad de la vegetación con el ángulo. En cuanto a la comparación entre los MTR y el método TES, para el suelo orgánico, donde la diferencia en emisividad entre suelo y hoja es mínima, el modelo Mod3 en global obtuvo los valores más cercanos a la emisividad TES en términos de RMSE. Sin embargo, estos valores fueron muy próximos a los obtenidos por los modelos FR97, REN15, CE-P y 4SAIL, con diferencias inferiores a la incertidumbre de las medidas. Si analizamos los resultados en función del intervalo de variación del LAI, el MTR que mejor se ajustó a los valores TES obtenidos de las medidas realizadas cuando LAI > 1,5 m^2/m^2 fue el MTR Mod3, pero para LAI < 1,5 m^2/m^2 el modelo con resultados más próximos a la emisividad TES fue el FR97. Cuando la diferencia entre la emisividad de suelo y hoja aumentó, como fue el caso de las medidas en el intervalo espectral 8,0 – 9,5 µm sobre la muestra con suelo inorgánico, el MTR Mod3 obtuvo los mejores resultados comparando con las medidas de emisividad TES para todos los valores de LAI. En este caso, los modelos FR97, REN15, CE-P y 4SAIL

sobreestimaron considerablemente las medidas TES y el MTR Rmod3 la subestimó, especialmente para valores de LAI < 2 m^2/m^2.

Aplicación a satélite

Los MTR se utilizaron para generar mapas de emisividad direccional de la vegetación para imágenes del sensor MODIS a bordo del satélite EOS – Aqua sobre la Península Ibérica. El MTR Rmod3 fue excluido de este estudio debido a las grandes diferencias observadas en las medidas *in-situ* y su mayor coste computacional en la generación de los mapas. Estos mapas fueron generados para una rejilla de coordenadas constante con proyección WGS84 a una resolución espacial de 500 m, como máxima resolución, y a una resolución de 1 km para la comparación directa con los productos de emisividad MYD11 y MYD21 del sensor MODIS.

Para generar los mapas de emisividad direccional de la vegetación se utilizaron distintos productos MODIS: el producto de LAI MCD15A2H, el producto de tipo de cobertura de superficie MCD12Q1 y el producto de temperatura y emisividad MYD21A1 (obtenido con el uso de un método TES), el cual fue utilizado tanto para obtener el ángulo de observación de cada pixel, así como para una posterior comparación con los datos obtenidos. Además, para la asignación de la emisividad de suelo, se utilizó un mapa mundial de clasificación de taxonomía de suelo. Las emisividades seleccionadas tanto para cada suelo como tipo de hoja fueron obtenidas a partir de los distintos espectros de la librería espectral ECOSTRESS (Meerdink et al., 2019). La emisividad obtenida al aplicar los MTR con datos de satélite fue comparada con datos de referencia tomados en una zona experimental de validación en Cortes de Pallás. Esta zona es una planicie de ~200 km^2 de matorrales. Al tratarse de una zona con poca variación de la cantidad de vegetación a lo largo del año, no se observó ninguna variación temporal. En cuanto a los MTR, estos mostraron una diferencia entre ellos inferior a 0,015, siendo la mayor diferencia la observada entre los modelos CE-P (emisividad ~0,985) y Mod3 (emisividad ~0,970). Esta emisividad fue comparada con la obtenida por los productos MODIS MYD11A1, MYD11B1 y MYD21A1 y el producto de emisividad IREMIS de la Universidad de Wisconsin. Los valores de emisividad extraídos de los productos MODIS eran

concordantes con los valores obtenidos con los MTR sobre la zona de estudio. El producto MYD21A1 mostró una mayor dispersión de datos, especialmente con valores de emisividad inferiores a los esperados. Esta dispersión pudo ser debida a la mayor sensibilidad en la corrección atmosférica del método TES utilizado para su generación. Tal como ocurrió en las medidas experimentales, para el suelo orgánico y valores de LAI cercanos a 1 m^2/m^2, el MTR FR97 se ajustó mejor a los valores obtenidos con los productos MODIS. Por otra parte, el producto IREMIS mostró valores de emisividad poco realistas, con valores propios de suelo sin vegetación, los cuales no coinciden con la descripción de la zona de estudio.

La emisividad direccional de los MTR fue comparada frente al producto MYD21A1 sobre las distintas clases de coberturas de superficie de la Península Ibérica. El Mod3 mostró, en términos globales, un resultado más cercano a la emisividad obtenida con el producto MYD21A1 en los canales centrados en 11 y 12 µm. En cambio, en el canal centrado en 8,55 µm se observaron resultados similares en todos los modelos. Todos ellos obtuvieron mejores resultados en los canales de 11 y 12 µm, donde las diferencias entre la emisividad de las componentes de la superficie son, generalmente, más pequeñas. En el canal de 8,55 µm tanto la emisividad de suelo como de las hojas cubren un mayor intervalo, esto provocó una mayor dispersión en los datos observados, así como un mayor error sistemático en las distintas clases de superficie.

Evaluación del efecto de la emisividad de los MTR sobre la TST

La validación de los productos de TST es una tarea necesaria para el control del funcionamiento de los sensores térmicos a bordo de satélites, así como la mejora de la precisión de los algoritmos utilizados para la obtención de la TST. Con el fin de evaluar el efecto de la emisividad estimada a partir de cada MTR sobre la TST, la emisividad de los canales de 11 y 12 µm se utilizó en el algoritmo SW usado como operativo para MODIS (Wan, 2014), con los coeficientes propuestos por Wang et al. (2019). La TST obtenida con la emisividad de cada modelo, así como con la emisividad de los distintos productos MODIS, fue comparada con datos tomados *in-situ* en la zona de validación de

Cortes de Pallás, tanto con los datos obtenidos con un sistema de barrido angular como con los radiómetros instalados con ángulo de observación fijo.

Los resultados obtenidos de la comparación con ambos sistemas fueron similares. En los dos casos, se observó un error sistemático entre +0,0 y +0,6 K y un error aleatorio cercano a ±1 K para todos los MTR y productos MODIS, excepto para el producto de emisividad IREMIS, que obtuvo un error sistemático superior a +1 K. Dentro de estos resultados, la TST obtenida con la emisividad de los MTR CE-P, REN15, 4SAIL y FR97 obtuvo el menor error sistemático (< 0,2 K). En cuanto a la TST obtenida con la emisividad de los productos de MODIS MYD11A1, MYD11B1 y MYD21A1, mostraron resultados muy próximos a los obtenidos con los MTR, ya que la emisividad de estos productos es similar a la obtenida por los MTR en esta zona. La validación de la TST realizada para estos mismos productos sobre la zona obtuvo buenos resultados en términos de exactitud, con un error sistemático de +0,3 K y +0,4 K para los productos MYD11A1 y MYD21A1, respectivamente.

Finalmente, se realizó complementariamente una validación *R-based* sobre dos zonas en la Península Ibérica: una de olivos y una de viña. En esta validación se observó un error aleatorio inferior a ±1 K en ambas zonas para la temperatura obtenida con la emisividad proporcionada por los MTR. En cuanto al error sistemático obtenido por los MTR fue distinto para cada una de las zonas, siendo entre -0,6 y -0,1 K en la zona de olivos y entre -0,1 y +0,2 K en la viña. Para la temperatura determinada con la emisividad del producto MYD11A1 se obtuvo un error sistemático y aleatorio igual que los MTR 4SAIL y REN15 sobre la zona de olivos y un error sistemático ligeramente superior en la zona de viña. Por lo tanto, se observaron mejores resultados con el MTR Mod3 que con la emisividad de los otros MTR y de los productos MODIS sobre la zona de olivos. En cambio, estos resultados fueron similares tanto en la zona de validación de Cortes de Pallás, con datos de validación *in-situ*, como sobre la zona de viña, con datos de validación *R-based*. En este último caso, a pesar del valor reducido de fracción de cobertura vegetal (< 0,27) y de LAI (< 0,7 m^2/m^2), la emisividad obtenida por el producto MYD11A1 era muy elevada, propia de una superficie vegetada (> 0,984). Sin embargo,

la emisividad obtenida por los MTR (entre 0,97 y 0,98) resultaba más realista, teniendo en cuenta el tipo de superficie de la zona de estudio. Con todo ello, los MTR demuestran proporcionar buenos resultados en la estimación de la emisividad requerida para la determinación de la TST desde satélites con sensores térmicos como el MODIS, ya que los resultados son similares o, en algunos casos, incluso mejores a los obtenidos mediante los procedimientos actualmente operativos. Estos resultados hacen interesante la extensión de los MTR a otros sensores satelitales, para los que permitiría obtener la emisividad de la superficie considerando las posibles variaciones en la cubierta vegetal en términos de LAI.

Summary

Introduction and objectives

Land surface temperature (LST) was recognized as an essential climate variable by the World Meteorological Organization, as it is directly related with the energy balance between the Earth surface and the atmosphere. Atmospheric absorption and surface emissivity corrections are the main factors that affect an accurate retrieval of LST for data acquired from satellite sensors in the thermal infrared (TIR) spectrum. Therefore, an accurate characterization of the surface emissivity on the TIR spectrum is required for an accurate retrieval of LST. Surface emissivity was well-characterized in the last decades for homogeneous and flat surfaces, e.g. water or arid bare soil sites. However, for heterogeneous surfaces the emissivity modeling is a more challenging issue because of its structural complexity. The difficulties on the estimation of the canopy emissivity are higher due to the multiple reflections of the radiance (emitted and reflected) among the canopy components (soil and plant elements). For that, it is necessary to consider the multiple reflections that take place inside the canopy when the emissivity is being modeled. Different canopy emissivity models are found in the literature. These models can be classified as: geometrical models, bidirectional reflectance distribution function (BRDF) models and radiative transfer models (RTMs).

In this work, several RTMs to obtain the directional canopy emissivity were analyzed and evaluated. These RTMs were: FR97 (François et al., 1997), Mod3 (François, 2002), Rmod3 (Shi, 2011), REN15 (Ren et al., 2015), CE-P (Cao et al., 2018) and 4SAIL (Verhoef et al., 2007). These models have common input parameters, which are soil and leaf emissivity, observation zenith angle and leaf area index (LAI). The RTMs were validated against in-situ measurements and applied to satellite data. Moreover, they were used to obtain the LST applying a split-window (SW) algorithm, and the retrieved LST was evaluated with in-situ data.

The main objectives of this thesis are:

- To evaluate the RTMs performance over canopy with in-situ measurements.

- To evaluate the angular variation of the canopy emissivity from the RTMs and in-situ measured data.
- To generate directional emissivity maps using the RTMs for moderate resolution data (e.g., 500 m and 1 km).
- To compare the directional emissivity maps with the MODIS MYD21 emissivity product, which is obtained with the TES method.
- And to evaluate the RTMs emissivity effect when applying them to retrieve the LST from satellite data.

Methodology

The FR97 and Mod3 models are based on the RTM proposed by Prevot (1985) which takes into account the soil and leaves contributions to the canopy emissivity. The main difference between these models lies in the fact that the Mod3 model does not take into account the multiple reflections that take place among the vegetated components (i.e. the different leaves inside the canopy), considering just the interaction between the soil and the leaves. For that, the cavity effect coefficient is not used in the Mod3 model, while it is part of the leaves contribution in the FR97 model. The Rmod3 model was presented as a modified version of the Mod3 model for satellite mixed pixels. This model introduced the vegetation fraction (P_v) as an input parameter modifying the Mod3 model, and added an additional term relating the bare soil emissivity with the bare soil fraction ($1 - P_v$). The 4SAIL model is an extension to the TIR of the four components Scattering by Arbitrarily Inclined Leaves (SAIL) model. The model is expressed in four differential equations which describe the interaction among four fluxes (two direct and two diffuse fluxes). A free distributed program code to solve these equations analytically was used in this study. The REN15 model follows the theory of the FR97 model, but it uses the 4SAIL model to estimate the cavity effect coefficient instead of the given coefficients for the FR97 model. Due to this modification, REN15 obtains closer values to the 4SAIL model than the FR97. The CE-P model is based on the recollision probability parameter instead of the cavity effect coefficient to consider the multiple reflections inside the canopy. This parameter is defined as the probability of a

photon to interact with a canopy component after an interaction with another component. The recollision parameter was originally used in the visible and near infrared spectral range, and it is extended in this model to the TIR spectrum.

A sensitivity analysis of the RTMs was done to estimate each model uncertainty and the contribution of each parameter to the uncertainty. For that, typical soil and leaves emissivities were used, i.e. 0.94 and 0.98, respectively. It was estimated for observation zenith angles ranging from 0º to 60º in steps of 10º, and for LAI values ranging from 0.5 to 3.0 m^2/m^2 in steps of 0.5 m^2/m^2. Uncertainties of ±0.01 were assigned to each input emissivity, ±0.5º to the input observation zenith angle and ±23 % to the LAI uncertainty. An emissivity uncertainty between ±0.003 and ±0.010 was observed for most models, depending on the LAI and observation zenith angle. The highest contribution to the models uncertainty was the input emissivities, showing the soil emissivity the highest contribution when LAI < 1 m^2/m^2 and the leaves emissivity when LAI > 1 m^2/m^2. The contribution of the LAI uncertainty to the model uncertainty was also relevant for LAIs < 2 m^2/m^2. The contribution of the observation zenith angle to the models uncertainties was negligible.

The RTMs were validated with in-situ emissivity measurements over a set of rose plants and two soils with different features: an organic soil (OS) with high emissivity and an inorganic soil (IS, sand) with low emissivity. The rose plants were selected because they form a continuous canopy, which allowed to control the structure when cutting off the leaves, and the steam was strong but fine enough to have a negligible contribution on the canopy emissivity. Moreover, this continuous canopy is in agreement with the type of canopy for which the RTMs are defined. Two CIMEL Electronique CE312 radiometers were used to take in-situ radiance measurements for five narrow channels in the 8 – 14 µm spectral range. In-situ directional emissivity measurements were obtained using the Temperature and Emissivity Separation (TES) method. These radiometers were calibrated in 2016 with a reference blackbody source during an international experiment in the framework of the Fiducial Reference Measurements for validation of Surface Temperature from Satellites (FRM4STS) project. They are regularly calibrated in

our laboratory with a temperature variable Landcal P80P blackbody source, which was also calibrated in the 2016 FRM4STS experiment showing a root mean square error (RMSE) of ±0.05 K. Both radiometers (CE1 and CE2) were calibrated following the guidelines proposed by the Joint Committee for Guides in Metrology (JCGM, 2008), taking into account the random and systematic uncertainties. It was obtained a total uncertainty of ±0.15 K and ±0.12 K for CE1 and CE2 radiometers, respectively.

The experiment took place at the Physics Faculty of University of Valencia, Spain. All measurements were taken at nighttime on cloudless days, in order to avoid shadow effects and to reduce the atmospheric absorption contribution in the methodology applied for the in-situ emissivities retrieval. In a first study, in which the organic soil was used, 15 radiance measurements were taken for 7 observation zenith angles (from 0^o to 60^o in steps of 10) and 6 different LAI values (ranging from 0 to 2.8 m^2/m^2). In a second study, the organic soil was replaced by sand, and 15 radiance measurements were taken for 2 observation zenith angles (0^o and 55^o) and 6 LAI values (ranging from 0 to 3.3 m^2/m^2). The two soil samples and rose leaves were also measured at nadir observation in order to apply the RTMs. For each sample measurement, a simultaneous radiance measurement was taken over a high reflectance gold panel in order to estimate the sky radiance. To obtain the in-situ emissivity, the TES method was applied with the measured radiances previously corrected from the atmospheric contribution by subtracting the measured sky radiance. An emissivity close to 0.98 was obtained for the leaves for all CE312 channel. For the OS, the measured emissivity was between 0.949 and 0.967 depending on the spectral channel, while for the IS a higher spectral contrast was observed, with emissivity values between 0.732 and 0.962. In addition, the angular emissivity variation between nadir and 60^o was measured, obtaining an emissivity decrease of 0.01 for the 10 - 12 µm spectral range and of 0.02 for the 8.0 – 9.5 µm spectral range for the OS. However, for the IS, it was observed a decrease of 0.03 for the 10 - 12 µm and of 0.06 for the 8.0 – 9.5 µm. The measured at-nadir emissivities were used as input for the RTMs. The LAI was measured with Pocket-LAI Android app after cutting out the quantity of leaves (to reduce the LAI value) and previously to each set of radiance measurements. For each LAI value, 36 Pocket-LAI measurements were taken,

considering their average as the corresponding LAI value for using as input parameter. This application has an associated uncertainty for broadleaf samples of ±23 %.

After the validation of the RTMs with in-situ data, the RTMs were used to generate directional emissivity maps over the Iberian Peninsula for scenes of the MODIS sensor onboard the EOS – Aqua satellite. The Rmod3 RTM was excluded of this study due to the large differences observed with the in-situ measurements and its higher computational cost in the generation of the maps. These maps were generated for a constant grid in WGS84 at a spatial resolution of 500 m, as maximum resolution, but also at spatial resolution of 1 km for comparison with MYD11 and MYD21 emissivity products of MODIS sensor.

In order to generate the directional emissivity maps, different MODIS products were used: LAI product MCD15A2H, land cover type product MCD12Q1, and temperature and emissivity product MYD21A1 (obtained using the TES method), which was used to obtain the observation zenith angle at each pixel, but also for comparison with the emissivity data obtained from the RTMs. These products were downloaded from the AppEEARS web tool, which allows to download level 3 MODIS data for a polygon of coordinates chosen by the user. Moreover, this web tool allows to change the scene projection from the sinusoidal MODIS projection original of the MODIS level 3 data to the wanted WGS84 projection (among others). Additionally, a world soil taxonomy classification based on the USDA taxonomy was used to assign the soil emissivity. This soil classification map is produced with data from the World Soil Information Service (WoSIS) and distributed by the International Soil Reference and Information Center (ISRIC). The selected emissivities for each soil and leaves were obtained from different spectra of the ECOSTRESS spectral library. Then, these spectra were convolved with the response functions of the MODIS TIR channels centered at 8.55 µm (channel 29), 11.03 µm (channel 31) and 12.02 µm (channel 32).

The canopy emissivity derived from the RTMs with satellite data was compared with reference data taken on an experimental site for LST validation at Cortes de Pallás (Valencia). This site is an ~200 km^2 shrubland plain, with a constant P_v throughout the

year close to 0.5. Different emissivity MODIS products (i.e., MYD11A1, MYD11B1 and MYD21A1 MODIS products) and the IREMIS product of the University of Wisconsin were also compared with the RTMs emissivity at this site for the period from March to September, 2015. The emissivity for the three MODIS products are generated by means of different methods: MYD11A1 product is based on tabulated emissivities for each land cover obtained from BRDF methods; MYD11B1 is based on the day/night algorithm, which makes use of the daytime and nighttime satellite overpass to break the LST and emissivity indeterminacy; and the MYD21A1 is based on the TES method applied with the MODIS TIR channels 29, 31 and 32. The IREMIS product is based on the version 4 of the MYD11B2 product, which is a monthly average of the MYD11B1 product.

Additionally, a comparison with the emissivities of the MYD21A1 product was carried out over the Iberian Peninsula. This comparison was taken for the different vegetation land covers of the International Geosphere Biosphere Program (IGBP) land cover classification. All pixels of the year 2015 over the Iberian Peninsula which were identified as cloudless by the MODIS cloud mask product were used. The IGBP classes related with forest (IGBP classes from 1 to 5) were grouped into a unique 'Forest' class, as well as shrubland classes (IGBP classes 6 and 7) and savanna classes (IGBP classes 8 and 9) were grouped into 'Shrubland' and 'Savanna' classes, respectively. Also, bare soil class was added to this analysis, as it could contain vegetation in some periods throughout the year.

The validation of the LST satellite products is a task required to control the performance of thermal sensors, as well as to improve the accuracy and precision of the algorithms applied for the LST retrieval. With the aim of evaluating the effect of the RTMs emissivity on the LST retrieval, the emissivity obtained for channels centered at 11 and 12 μm was used to apply the current MODIS operational SW algorithm (Wan, 2014) with the coefficients proposed by Wang et al. (2019). The brightness temperatures given by the MODIS MYD021KM product were used to apply the SW algorithm. The LSTs estimated with the emissivity of each RTM and the emissivity of the different MODIS emissivity products were compared with in-situ data at the Cortes de Pallás validation site for the

period from March to September, 2015. Data acquired with Apogee-121 wide band (8 – 14 µm) radiometers installed on a system with sweeping measurements at defined angles were used as reference for the validation, but also measurements with radiometers installed at the same station with a fixed viewing angle. These radiometers were calibrated at our laboratory with a Landcal P80P blackbody source and with a reference blackbody source of the National Institute of Standards and Technology during an international campaign organized by the Committee on Earth Observation Satellites in 2009. In both calibrations, in the international campaign but also in our laboratory, these radiometers showed uncertainties equal or better than ±0.2 K, which were in accordance with the uncertainty given by the manufacturer. A total of 55 match-ups were available for the validation with the radiometer installed on the angular system and 107 match-ups were available for the fixed view radiometers.

The LSTs retrieved using the RTMs emissivity and the emissivity MODIS products were also validated over an olive orchard and a vineyard. Since no in-situ ground data were available at these sites, a radiance-based (R-based) validation was carried out. The R-based technique uses the temperature of the channel centered at 11 µm as reference (T_{11}) corrected from the atmospheric absorption and emissivity. Furthermore, a procedure to detect the most precise atmospheric profiles (ΔT Test) was required for this method. In the ΔT Test, the temperatures T_{11} are assumed as valid reference data when the difference between the T_{11} and the corrected temperature of the channel centered at 12 µm is lower than the uncertainty obtained for these differences. After selecting the valid data, a total dataset of 130 match-ups were available at the olive orchard and 139 match-ups were available at the vineyard.

Results

The RTMs were firstly validated against in-situ TES emissivities taken from the experimental measurements over the rose plants with OS and IS at the background. Emissivities derived from the RTMs were first compared with the TES emissivities measured at nadir observations. TES emissivities ranged from 0.975 from 0.985 for the OS sample, depending on the LAI and CE312 radiometer spectral channel, while for the

IS sample, the emissivities ranged from 0.887 to 0.984. For the IS sample, the emissivities of the 10 – 12 µm channels were similar to the OS sample emissivities, because the sand emissivity on that spectral range is similar to that of the OS. However, higher differences were observed on the 8.0 – 9.5 µm spectral range. TES emissivities from the IS sample were adjusted by regression with LAI to a non-linear function, obtaining regression coefficients of 0.986 and 0.999 depending on the spectral range. Similar emissivity values were found for FR97, 4SAIL, REN15 and CE-P, especially with the OS sample. For lower LAI values, Mod3 model showed similar values to FR97 model, but they differ with LAI, yielding to differences up to 0.013 for both soils. In comparison with the TES emissivities at nadir observation, if the overall results are analyzed, the Mod3 model showed the best agreement, with a RMSE of ±0.004 (±0.005) over the OS (IS) sample. However, over the OS sample, similar results were obtained with the other models, with RMSE values ranging from ±0.007 to ±0.009. Furthermore, for LAIs ≤ 1 m^2/m^2 the FR97, 4SAIL, REN15 and CE-P models showed better results than the Mod3. These models disagree in higher manner with the TES emissivities over the IS sample, where the RMSE values range from ±0.010 to ±0.013. In this case, the Rmod3 model obtained an overall RMSE of ±0.036, being up to ±0.06 for LAI = 0.5 m^2/m^2.

The angular in-situ measurements were used to evaluate the angular performance of the RTMs, but no variation was found on the TES emissivities over the OS sample for the observation zenith angles measured in this study. Over the IS sample, very little variation was observed for LAIs ≤ 1 m^2/m^2, but it was within the emissivity uncertainty. In the comparison of the RTMs values with the TES emissivities, over the OS sample, the FR97, 4SAIL, REN15 and CE-P differences increased with LAI, with RMSE values ranging from ±0.002 to ±0.012. However, for the Mod3 and Rmod3 models, these differences decreased with LAI. In this case, the RMSE for the Mod3 models ranged from ±0.002 to ±0.007. If these results are analyzed according to the LAI range, for LAI > 1.5 m^2/m^2 the Mod3 model showed a better agreement with the TES emissivity, but for LAI < 1.5 m^2/m^2, the FR97 model showed closer emissivities to the ones obtained with the in-situ measurements. Over the IS sample, all models, except Rmod3, overestimated the TES emissivities. In this case, the Mod3 model showed the best agreement with the TES

emissivities for all LAIs, with RMSE values ranging from ±0.002 to ±0.014, where the higher RMSE were found for the lower LAIs. The other RTMs showed RMSE values from ±0.009 to ±0.0018. Therefore, the Mod3 model was observed to obtain overall better results from the comparison with the in-situ TES emissivities over the rose plants samples.

The FR97, Mod3, 4SAIL, REN15 and CE-P RTMs were used to generate directional emissivity maps over the Iberian Peninsula. These RTMs were compared with the MODIS emissivity products MYD11A1, MYD11B1 and MYD21A1 and the IREMIS product of the University of Wisconsin over the Cortes de Pallás LST validation site. As there is little variation on the quantity of vegetation over this site throughout the year, no significant temporal variation was observed. The differences observed among the RTMs were lower than 0.015, with the maximum emissivity difference between the CE-P model (~0.985) and the Mod3 model (~0.970). Just a little effect with the observation zenith angle was showed by the FR97 and Mod3 model, which was a periodically variation related with the revisit period of the MODIS – Aqua sensor. This emissivities were compared with the emissivity obtained by the MYD11A1, MYD11B1 and MYD21A1 MODIS products and the IREMIS emissivity product of the University of Wisconsin. The values extracted from the MODIS products were in agreement with the RTMs emissivity values at the study site, with values close to 0.980 in most cases. It was observed a higher variability for the MYD21A1 data, especially for the spectral channel centered at 8.55 µm, underestimating the expected values in many cases. This variability could be caused by the higher sensibility on the atmospheric correction of the TES method when it is applied to generate the product. As happened with the in-situ measurements for the case of OS and LAI values close to 1 m^2/m^2, the FR97 RTM obtained emissivity values closer to the emissivity obtained from the MODIS products. Contrarily, the IREMIS product showed unrealistic values, with emissivity values typical for bare soils (from 0.94 to 0.97), which are not consistent with the description of the surface at the study site.

The directional emissivity maps were compared with the MYD21A1 emissivity product over the different surface types found at the Iberian Peninsula. In this case, due to the huge quantity of available data (more than 10^4 pixels for each class), robust statistics were used, i.e. median (systematic uncertainty), robust standard deviation (RSD, random uncertainty) and robust root mean square error (R-RMSE). From this comparison, FR97, 4SAIL, REN15 and CE-P overestimated the MYD21A1 emissivity for most classes and the three MODIS TIR channels, except for the shrubland class for channel centered at 8.55 µm and, in the case of the FR97 and REN15 models, for the savanna class for the same channel. The Mod3 model overestimated the MYD21A1 emissivity for the classes forest, savanna, shrubland and vegetation mosaics. The differences observed on the 8.55 µm channel were higher than at 11 and 12 µm channels, mainly due to the higher variability of the surface emissivity at the 8.55 µm channel. For channel centered at 11 µm, the random uncertainty for all models ranged from ±0.004 and ±0.005 and for the 12 µm channel ranged from ±0.006 to 0.007, being similar for all models. However, the median of the Mod3 was lower than for the other models, with an overall median value of +0.001 at both channels. For the FR97, 4SAIL, REN15 and CE-P models, these values ranged from +0.004 to +0.009 at 11 and 12 µm channels. The bare soil class showed larger systematic and random uncertainties for the 8.55 µm channel, with systematic (random) uncertainty values of +0.03 (±0.03) for all models. These large differences could be attributed to an incorrect estimation of the LAI which causes a high emissivity estimated by the models, an overestimation of the soil emissivity used as input parameter or a decrease of the soil emissivity with the observation angle which is not taken into account by the RTMs, since they are defined for canopy.

The effect on the LST when the RTMs emissivities are applied to its estimation was evaluated applying the MODIS operational SW algorithm and using in-situ data acquired at the Cortes de Pallás validation site. Similar results were obtained from the comparison with the data acquired with the radiometers installed on the angular observation system and the radiometers installed with fixed viewing. In both cases, it was observed a systematic uncertainty between +0.0 and +0.6 K and a random

uncertainty close to ±1 K for all RTMs and MODIS emissivity products, except for the IREMIS emissivity product, which showed a systematic uncertainty larger than +1 K. The FR97, REN15, CE-P and 4SAIL RTMs obtained the lowest systematic uncertainty (≤ 0.2 K). The LSTs retrieved with the emissivity of the MYD11A1, MYD11B1 and MYD21A1 products showed values in agreement with those obtained using the RTMs emissivity. This occurred because the observed MODIS and RTMs emissivities were similar at the site. The validation results of the LST at the site given by the MYD11A1 and MYD21A1 products showed a good performance, with a systematic uncertainty of +0.3 K and +0.4 K for the MYD11A1 and MYD21A1 products, respectively.

Finally, a complementary R-based validation was applied over two sites in the Iberian Peninsula: an olive orchard and a vineyard. The estimated ΔT threshold to choose the most accurate atmospheric profiles was of ±0.7 K at the olive orchard and of ±0.5 K at the vineyard and the uncertainty of the reference T_{11} was of ±1.2 K at the olive orchard and of ±0.7 K at the vineyard. The validation results showed a random uncertainty lower than ±1 K at both sites for the LSTs retrieved with the RTMs emissivities. However, the systematic uncertainty was different in each site: it was between -0.6 and -0.1 K at the olive orchard and between -0.1 and +0.2 K at the vineyard. The Mod3 model showed a R-RMSE of ±0.8 K, while the other RTMs obtained a R-RMSE of ±1.1 K. At the vineyard, the FR97 model obtained a R-RMSE of ±0.8 K, and it was of ±0.9 K for the other RTMs. The LST obtained using the MYD11A1 emissivity showed the same systematic and random uncertainty than the 4SAIL and REN15 RTMs at the olive orchard site, but the systematic uncertainty at the vineyard was slightly higher. The LST obtained with the MYD11B1 emissivity obtained a slightly higher random uncertainty than the RTMs at the olive orchard site, but the same results than the FR97 at the vineyard. The LSTs estimated with MYD21A1 emissivity showed a slightly higher random uncertainty at both sites. And the IREMIS product obtained a higher overestimation of the reference data, with a large systematic uncertainty. The LST given by the MYD11A1 and MYD21A1 products were also validated, showing a systematic and random uncertainty lower than 1 K at both sites.

Conclusions

The RTMs were validated with TES in-situ emissivity measurements over a set of rose plants with OS at the background in a first period and with IS at the background in a second period. The in-situ TES emissivities over the rose plants with OS showed no significant variation with LAI. Nevertheless, an increase of the emissivity with LAI was observed over the sample with IS, as it was predicted by the RTMs. This increase was mainly due to the significant difference between the IS and leaves emissivities. The observed variation of the emissivity with LAI was adjusted by regression, obtaining high correlation coefficients. For the overall results, the Mod3 RTM showed the best agreement with the TES emissivities. These results were especially better in the cases with higher differences between soil and leaves emissivities.

From the evaluation with the viewing angle over the rose plants samples, little variation was observed for the emissivity derived from the RTMs but also for the measured emissivity. Then, for similar conditions to the ones analyzed in this study, no significant variation of the canopy emissivity with the viewing angle is expected. The Mod3 RTM obtained a slightly better agreement with TES emissivities over the sample with OS. But similar results were obtained by the FR97, REN15, CE-P and 4SAIL models. However, the Mod3 RTM showed the best agreement with the measured TES emissivities for all LAI values over the IS, especially for channels in 8.0 – 9.5 µm spectral range. In this case, the FR97, REN15, CE-P and 4SAIL models overestimated and the Rmod3 model underestimated the TES emissivity values, especially for LAI < 2 m^2/m^2.

The RTMs were used to generate directional canopy emissivity maps. They were compared with MODIS emissivity products, i.e. MYD11A1, MYD11B1, MYD21A1 and IREMIS, at the Cortes de Pallás validation site. No variation throughout the year was observed in the RTMs emissivity because of the constant quantity of vegetation at the site. Just FR97 and Mod3 models showed a little variation of the emissivity with the observation zenith angle. The emissivity of the MYD11A1, MYD11B1 and MYD21A1 products were in agreement with the RTMs canopy emissivity. But the IREMIS product

showed emissivity values lower than the expected, underestimating the emissivities obtained with the MODIS products and the RTMs.

The directional emissivity maps produced with the RTMs were compared with the MYD21A1 emissivity product over the different surface types found at the Iberian Peninsula. In global terms, the Mod3 obtained the best agreement with the MYD21A1 emissivity for channels centered at 11 and 12 µm. However, similar results were obtained with all the RTMs for the channel centered at 8.55 µm. All the models obtained lower differences with the MYD21 emissivity for channels centered at 11 and 12 µm, where the differences between the emissivity of the canopy components are, typically, lower.

The LSTs retrieved applying the MODIS operational SW algorithm with the emissivities from the directional emissivity maps were evaluated with in-situ data at the Cortes de Pallás validation site and with R-based data at an olive orchard and a vineyard. The results given by the Mod3 RTM showed the best agreement with the reference data at the olive orchard site. However, similar results were observed for all RTMs and MODIS emissivity products at the Cortes de Pallás validation site, using in-situ data as reference, as well as at the vineyard, using R-based validation data. For the latter, despite the low fraction vegetation cover (< 0.27) and LAI (< 0.7 m^2/m^2), the MYD11A1 emissivity was higher than expected, with typical values of full canopy surface (> 0.984). However, the RTMs emissivity values (between 0.97 and 0.98) were found more realistic according to the surface cover.

These results showed that the RTMs provided good results in the estimation of the emissivity required for the LST retrieval from satellite thermal sensors, e. g. MODIS, since the results were similar or even better to those given by the currently operational procedures. The extension of the RTMs to other satellite sensors are shown to be interesting, as it would allow to estimate the canopy emissivity considering possible variations in the canopy in terms of LAI.

Capítulo 1

Introducción

En este capítulo se introduce la temática principal de esta tesis. Para ello, se introduce el término de emisividad y su importancia para la estimación de la temperatura de la superficie terrestre, en concreto sobre superficies vegetadas.

Además, se definen los objetivos principales que motivan la realización de esta tesis, así como la estructura seguida para su desarrollo.

1.1. Variable climática esencial: temperatura de la superficie terrestre. Importancia de la emisividad

La temperatura de la superficie terrestre (TST) ha sido reconocida por la Organización Meteorológica Mundial como una de las variables climáticas esenciales (ECV) en la monitorización y la predicción del cambio climático (GCOS, 2016). Además, se trata de una variable fundamental en estudios climáticos, ya que se relaciona directamente con el balance de energía entre la superficie terrestre y la atmosfera (Li et al., 2013a; Sánchez et al., 2015; Bian et al., 2020). La Agencia Espacial Europea (ESA) ha lanzado el programa Iniciativa Cambio Climático (CCI) para el seguimiento de veintiséis ECVs, entre ellas la TST, haciendo uso de datos de satélites de observación de la Tierra (Hollmann et al., 2013).

La teledetección en el infrarrojo térmico (IRT) nos permite obtener la TST a partir de medidas de radiancia haciendo uso de sensores con canales espectrales en dicho intervalo espectral, de 8 a 14 μm, en el cual la emisión atmosférica es más débil. Para obtener la TST con precisión, es necesario corregir la radiancia medida por el sensor de la contribución debida a la absorción atmosférica y de la emisividad de la superficie (Garcia-Santos et al., 2013; Li et al., 2013a; Cao et al., 2019).

La emisividad es una propiedad intrínseca de cada material, que se define, para una longitud de onda λ y una temperatura T, como el cociente entre la radiancia emitida por un cuerpo a una temperatura dada y la radiancia emitida por un cuerpo negro a esa misma temperatura (Norman y Becker, 1995). La emisividad es un parámetro clave tanto para la obtención de la TST como para distintas aplicaciones, p. ej., el reconocimiento de materiales (minerales, especies de plantas, materiales de construcción) o desarrollo de mapas geológicos y de uso de suelos (Gillespie, 1986; Salisbury y D'Aria, 1994; Baldridge et al., 2009; Caselles et al., 2012; Ullah et al., 2014).

Sobre superficies terrestres homogéneas, como zonas áridas de suelo sin vegetación o extensiones de agua, la emisividad ha sido analizada y bien caracterizada en las últimas décadas. Distintos estudios se han centrado en la anisotropía de la emisividad sobre

superficies homogéneas mediante la realización de medidas *in-situ* de emisividad. Por ejemplo, Niclòs et al. (2009) analizaron la variación angular de la emisividad del agua del mar y calcularon su valor en función del ángulo de observación del satélite y el canal espectral. Por otro lado, García-Santos et al., (2012) analizaron la variación angular de la emisividad sobre distintos suelos inorgánicos, observando una disminución de la emisividad entre el 3% y el 6% para un conjunto de muestras de suelos inorgánicos representativos de zonas áridas del planeta.

Sin embargo, cuando se observa la superficie terrestre desde satélite, esta es en muchos casos heterogénea. Este es el caso de las superficies vegetadas, donde la definición de la emisividad es más compleja ya que, además de la contribución de cada uno de los elementos (por ejemplo, suelo y hojas) hay que tener en cuenta las reflexiones múltiples de la radiación entre los distintos elementos (Norman y Becker, 1995; Li et al., 2013b; Cao et al., 2019). Debido a esta dificultad en la obtención de la emisividad de superficies vegetadas, distintos autores han tratado de modelar la emisividad de superficies vegetadas, generando modelos que tuviesen en cuenta tanto las propiedades de la vegetación como la geometría de observación.

1.2. Estimación de la emisividad

La emisividad se relaciona con la TST mediante la ecuación de transferencia radiativa (ETR), la cual define la radiancia medida por un sensor aerotransportado en cierto canal espectral i como:

$$B(T_i) = \left[\varepsilon_i B_i(T) + (1-\varepsilon_i)L_i^{\downarrow}\right]\tau_i + L_i^{\uparrow} \quad (1)$$

donde $B(T_i)$ es la radiancia medida por el sensor, ε_i es la emisividad del canal i, $B_i(T)$ es la radiancia de cuerpo negro a la TST T, y $L_i^{\downarrow}$, τ_i y $L_i^{\uparrow}$ son parámetros atmosféricos correspondientes a la radiancia descendente, la transmisividad y la radiancia ascendente, respectivamente. Por lo tanto, se establece que la medida realizada por el sensor tiene tres contribuciones: la radiancia emitida por la superficie, la radiancia atmosférica descendente que es reflejada en la superficie y, en el caso de un sensor

aerotransportado, estos dos términos se multiplican por la transmisividad y se añade la radiancia atmosférica ascendente emitida por la atmósfera en la dirección del sensor. En el caso de las medidas *in-situ*, la radiancia medida por un sensor vendría dada por los dos primeros términos entre corchetes, excluyendo el factor de la transmisividad y la emisión propia atmosférica.

Debido a la dependencia de la radiancia con la temperatura y la emisividad simultáneamente en la ETR, e incluso considerando las medidas realizadas para N canales espectrales, no podemos obtener la emisividad para ellos sin conocer previamente la TST, y viceversa, ya que tenemos N+1 incógnitas. Por ello, para obtener la emisividad debemos hacer uso de distintas técnicas, como medidas *in-situ*, modelos de emisividad o algoritmos de separación de temperatura y emisividad.

1.2.1. Medidas *in-situ*

Para la obtención de la emisividad mediante medidas *in-situ* es necesaria la realización de medidas radiométricas en el IRT. La técnica más adecuada para la obtención de la emisividad depende de distintos factores: las características espectrales de la muestra y su tamaño, los canales espectrales en el IRT del radiómetro con el que se realizan las medidas y las condiciones externas, como el lugar (laboratorio o exterior) o la presencia de nubes si las medidas se realizan en el exterior. Entre los distintos métodos de obtención de la emisividad destacamos: método de la caja (Rubio et al., 1997), medidas relativas a nadir (García-Santos et al., 2012), método de separación de temperatura-emisividad (TES, Gillespie et al., 1998; Mira et al., 2009) y medidas con espectrómetro de campo (Korb et al., 1996).

Método de la caja

El método de la caja consiste en la realización de medidas radiométricas sobre una muestra aislada del exterior mediante una caja con cuatro paredes de aluminio, que reflejan la emisión de la muestra (Rubio et al., 1997). Además, esta caja tiene 3 tapas: dos tapas de aluminio, una para la parte superior, con una apertura del tamaño del sensor, y otra para la parte inferior, la cual se utilizará para medir la contribución de la

caja en las medidas sobre la muestra; la tercera, utilizada como tapa superior, consiste en un material emisor con una temperatura sobre 60 ^{o}C. Además, tanto las paredes como las tapas, están cubiertas externamente con material aislante térmico. Para obtener la emisividad, deben realizarse cuatro medidas combinando las tapas disponibles y la muestra (Rubio et al., 2003): 1) tapa superior de aluminio – muestra, 2) tapa superior caliente – muestra, 3) tapa superior caliente – tapa inferior de aluminio, 4) tapa superior de aluminio – tapa inferior de aluminio. El montaje experimental para la realización de medidas con el método de la caja se muestra en la Figura 1. Este método tiene la ventaja de que nos permite calcular la emisividad de la muestra para cada uno de los canales de los instrumentos en el laboratorio, por lo que no tiene dependencia de factores externos como la climatología. La emisividad obtenida con este método es hemisférica, es decir, obtenemos un valor integrado de la emisividad emitida en todas las direcciones. Esto implica que, si tenemos una muestra anisótropa, la emisividad obtenida va a ser diferente a la emisividad direccional.

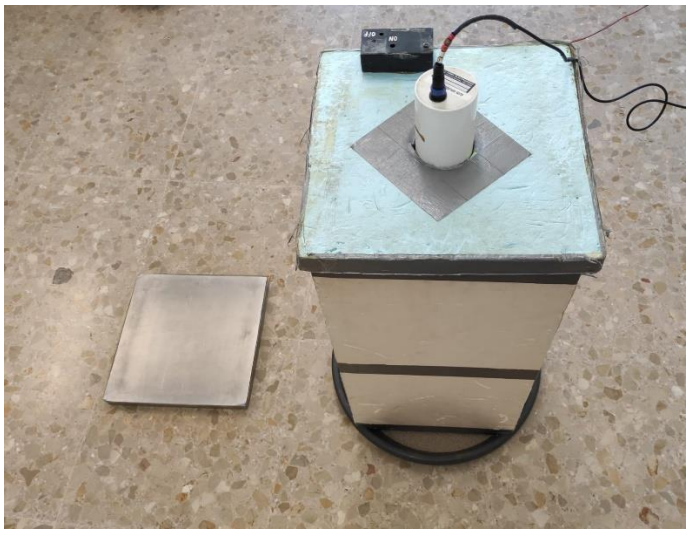

Figura 1. Montaje experimental para la realización de medidas con el método de la caja.

Medidas relativas a nadir

Las medidas relativas a nadir nos permiten obtener la emisividad direccional relativa de una muestra, a un ángulo distinto de nadir, mediante la realización de dos medidas radiométricas simultáneas: una en dirección de observación nadir y la otra en la

dirección de observación a la cual se quiere conocer la emisividad de la muestra (García-Santos et al., 2012). Para conocer la emisividad direccional en cada dirección medida con este método, es necesario conocer la emisividad a nadir de la muestra, ya que sin este valor tan solo podemos conocer los valores relativos. La Figura 2 muestra la emisividad relativa respecto a nadir de una muestra de arena para canales espectrales centrados en 8,5 µm y 10,6 µm con anchura a media altura (FWHM) de 0,3 µm y 0,2 µm, respectivamente.

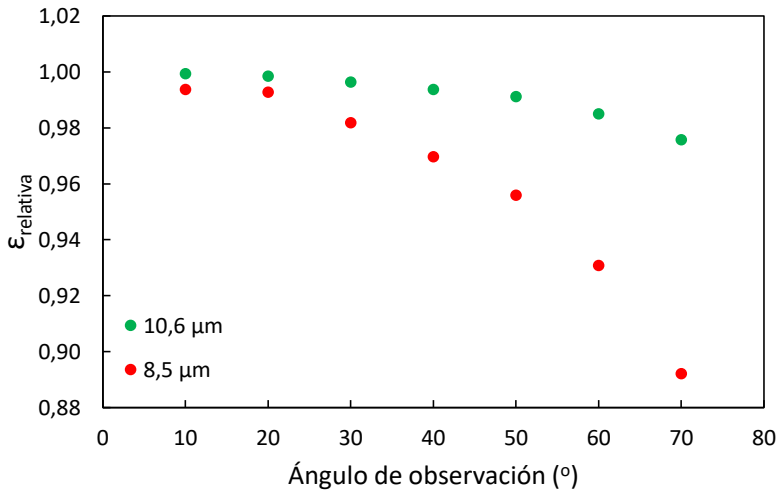

Figura 2. Emisividad relativa en función del ángulo de observación de una muestra de arena para canales espectrales centrados en 8,5 µm y 10,6 µm con FWHM de 0,3 µm y 0,2 µm, respectivamente (García-Santos et al., 2012).

Método TES

El método TES forma parte de los conocidos como métodos de separación de temperatura y emisividad. Este método consigue deshacer la indeterminación entre la temperatura y la emisividad a partir del método de normalización de la emisividad (NEM, Gillespie, 1986) y una relación empírica obtenida a partir de espectros de distintas muestras obtenidos en laboratorio. Este método fue generado por primera vez para el sensor *Advanced Spaceborne Thermal Emission and Reflection Radiometer* (ASTER), el cual tiene cinco canales espectrales en el IRT (Gillespie et al., 1998). Este método requiere de, al menos, tres canales espectrales en el IRT para su aplicación (Hulley y Hook, 2009), como ocurre con el sensor *Moderate-Resolution Imaging*

Spectroradiometer (MODIS) y el *Visible Infrared Imaging Radiometer Suite* (VIIRS). Este método es utilizado tanto para medidas *in-situ* (Mira et al., 2009), como para generar los productos satelitales de temperatura y emisividad de MODIS (MOD21/MYD21) y VIIRS (VNP21) (Hulley et al., 2016a, 2016b). Para obtener una buena precisión al aplicar este método, es necesario realizar las medidas bajo cielo libre de nubes para obtener una correcta corrección atmosférica. La metodología TES será vista en más detalle en la sección 3.3.

1.2.2. Modelización

La modelización de la emisividad nos permite conocer su valor direccional a partir de distintos parámetros de entrada. Existen modelos de emisividad tanto para suelos sin vegetación como para superficies vegetadas con diferentes grados de cobertura. Entre los modelos para obtener la emisividad de suelos sin vegetación, destacan los modelos basados en la teoría de Mie (Warren y Wiscombe, 1980; Hapke, 2011), los cuales predicen la emisividad de estas superficies considerando distintas propiedades, como el índice de refracción y la distribución del tamaño de la partícula (García-Santos et al., 2016).

En cuanto a superficies heterogéneas, y especialmente en el caso de los modelos de emisividad para superficies vegetadas, estos tienen una mayor complejidad debido a la interacción entre la radiancia emitida por la superficie y los distintos elementos que forman la estructura de la vegetación, y entre las distintas capas que forman la planta (Cao et al., 2019). Por ello, es necesario considerar las reflexiones múltiples que tienen lugar entre los elementos de la vegetación cuando la emisividad está siendo modelada. En las últimas décadas, se han propuesto distintos modelos para obtener la emisividad direccional de superficies vegetadas. Estos modelos pueden clasificarse principalmente en tres tipos: modelos de función de distribución de reflectancia bidireccional, BRDF (Snyder y Wan, 1998), modelos geométricos, MG (Valor y Caselles, 2005) y modelos de transferencia radiativa, MTR (François et al., 1997; François, 2002; Verhoef et al., 2007). Los modelos BRDF hacen uso de una combinación lineal de *kernels* definidos para obtener la reflectancia hemisférica-direccional, para después obtener la emisividad

direccional aplicando la ley de Kirchhoff. Los MGs se basan en la estimación de las proporciones de cada uno de los elementos de la vegetación vistas por el sensor. Para aplicar los MGs es necesario el conocimiento previo de las dimensiones de los distintos elementos de la superficie vegetada vistos por el instrumento. Con ello, la emisividad es calculada teniendo en cuenta la contribución de cada uno de los elementos a la radiancia total medida. Por último, los MTR calculan la emisividad direccional a partir de la simulación de las interacciones radiativas con los distintos componentes de la vegetación en sus distintos niveles. Para obtener la emisividad, estos modelos se basan en la función de densidad de hoja, con la que simulan la radiancia en la parte superior de la cobertura vegetal (Pérez-Planells et al., 2019b). Estos modelos difieren de los MGs, principalmente, en el hecho de que la vegetación no es considerada como un medio opaco, sino que se considera la interacción entre los distintos niveles de la estructura de la vegetación.

1.2.3. Obtención de la emisividad desde satélite

Los sensores multiespectrales a bordo de satélite con tres o más canales en el IRT (p. ej., ASTER, MODIS y VIIRS) hacen posible la aplicación de métodos de separación de temperatura y emisividad, como el método TES (Gillespie et al., 1998) o el método ajustado de emisividad normalizada (ANEM, Coll et al., 2003; Pérez-Planells et al., 2017), entre otros. Estos métodos permiten obtener la emisividad de un píxel a partir de las medidas realizadas por el propio sensor en diversos canales espectrales, haciendo uso de las radiancias corregidas del efecto atmosférico, es decir, utilizando las radiancias a nivel de superficie.

Otras técnicas para la generación de mapas de emisividad, generalmente empleados para la estimación de la TST desde satélite, se centran en la asignación de valores de emisividad a cada una de las clases utilizadas en mapas de clasificación de superficies terrestres. Estos mapas de clasificación son generalmente estáticos por lo que no suelen considerar las variaciones temporales de una región, como pueden ser crecimiento y cosecha de cultivos, vegetación caduca, inundaciones, incendios, construcciones, etc. Para tener en cuenta estos cambios en la superficie, especialmente los relacionados con

los cambios en la vegetación, estos mapas deben de ser generados periódicamente (Niclòs et al., 2011) y, además, hacer uso de métodos que permitan la obtención de la emisividad en función de la cantidad de vegetación, como el MG de cobertura vegetal (Caselles et al., 2012; Valor y Caselles, 2005). Otros productos de TST, como el producto MOD11_L2, hacen uso de modelos de emisividad BRDF para generar valores tabulados para cada clase del mapa de superficies terrestres en función del ángulo de observación (Snyder et al., 1998). De esta manera, se tiene en cuenta la variación angular debida al ángulo de observación, pero no tienen en cuenta los cambios temporales que puedan darse en la superficie.

1.3. Objetivos principales

En este trabajo se pretende abordar la validación de los MTR para la obtención de la emisividad direccional de las superficies vegetadas. Por ello, los objetivos principales de este trabajo son los siguientes:

- Evaluar distintos MTR de emisividad sobre superficies vegetadas, a partir de medidas experimentales realizadas *in-situ*.
- Evaluar la obtención de la variación angular en la emisividad sobre superficies vegetadas a partir de los MTR y las medidas experimentales.
- Generar un algoritmo para la creación de mapas de emisividad direccional de resolución moderada haciendo uso de MTR.
- Comparar los mapas de emisividad generados con el producto MYD21 de emisividad obtenido con el método TES del sensor MODIS a bordo del satélite Aqua (MODIS – Aqua).
- Evaluar el efecto en la obtención de la TST al aplicar los modelos de emisividad haciendo uso de datos de satélite. Para ello, se aplicarán las emisividades calculadas en el algoritmo de corrección atmosférica *split-window* utilizado en el producto operacional de MODIS (MOD11/MYD11) y se realizará una validación de las TST obtenidas.

1.4. Estructura de la tesis

El siguiente trabajo se desarrolla según se expone a continuación. En la sección 2 se definen los MTR para la obtención de la emisividad direccional de la vegetación, en los cuales se centran los principales objetivos de este trabajo. Estos MTR son evaluados con medidas experimentales de emisividad tomadas *in-situ*. El diseño del montaje experimental para la realización de estas medidas, así como el material e instrumental utilizado y la metodología empleada se definen en la sección 3. En esta sección, además, se expone de forma detallada el proceso de calibración en el laboratorio de los radiómetros utilizados para las medidas experimentales. En la sección 4 se muestran los resultados obtenidos de la evaluación de los MTR a partir de las medidas experimentales. Esta evaluación se realiza, por un lado, teniendo en cuenta la variación de la emisividad en función del índice de área foliar (LAI) observado para las superficies vegetadas a nadir y, por otro lado, teniendo en cuenta la variación angular de la emisividad para los distintos valores de LAI.

Una vez evaluados los MTR con las medidas experimentales, estos son aplicados a datos de satélite para la generación de mapas de emisividad de resolución moderada. La metodología seguida para la generación de estos mapas de emisividad, así como como la descripción de los productos utilizados, se muestra en la sección 5. Además, en esta sección se definen los distintos productos de emisividad de MODIS, los cuales son comparados con los mapas obtenidos, tanto a nivel de imagen de satélite como sobre una zona de validación de TST. Haciendo uso de los mapas de emisividad generados con los distintos MTR, se aplica el algoritmo *split-window* operativo de MODIS para la obtención de la TST. En la sección 6 la TST obtenida haciendo uso de los distintos mapas de emisividad es validada frente a datos *in-situ* obtenidos en la zona de validación de TST. Finalmente, en la sección 7 se presentan las conclusiones extraídas a lo largo de todo el trabajo realizado.

Capítulo 2

Modelización de la emisividad sobre superficies vegetadas

En este capítulo se presentan los modelos de transferencia radiativa para la obtención de la emisividad direccional sobre superficies vegetadas que son analizados a lo largo de este estudio. Estos modelos se describen en Pérez-Planells et al. (2019b) (Anexo I). Además, se realiza un análisis de incertidumbre de los modelos para valores típicos de los parámetros de entrada.

Los MTR permiten obtener la emisividad de la cubierta vegetal a partir de distintos parámetros de entrada: emisividad de la hoja, emisividad del suelo, LAI y ángulo cenital de observación (Pérez-Planells et al., 2019b) (ver Anexo I).

2.1. Modelo FR97

François et al. (1997) propusieron un modelo físico para obtener la emisividad direccional de la superficie vegetada, el cual está basado en el MTR propuesto por Prévot (1985). El MTR FR97 tiene como objetivo obtener la temperatura de los componentes de la superficie vegetada. Para ello, modeliza la emisividad direccional proporcionando su valor a partir de una ecuación paramétrica. François et al. (1997) afirman que la emisividad debe reaccionar a los cambios en la cantidad de vegetación, por ello, la ecuación paramétrica está definida en función del LAI, de la función de distribución de la inclinación de la hoja (LIDF, por sus siglas en inglés), de la emisividad del suelo, de la emisividad de las hojas y del ángulo de observación cenital. Teniendo en cuenta estos parámetros, el modelo FR97 define la emisividad direccional como:

$$\varepsilon_c(\theta) = 1 - k_s(\theta)(1 - \varepsilon_s) - k_l(\theta)(1 - \varepsilon_l) \quad (2)$$

donde k_s y k_l son los coeficientes de suelo y hoja, ε_s y ε_l son las emisividades de suelo y hoja, respectivamente, y θ es el ángulo de observación cenital. Los coeficientes k_s y k_l son dependientes del LAI, de la frecuencia de espacio direccional $\big(b(\theta)\big)$ y la frecuencia de espacio hemisférica (M). Estos coeficientes se definen como $k_s(\theta) = b(\theta)M$ y $k_l(\theta) = \alpha(1 - b(\theta)M)$, donde α es el coeficiente de efecto de cavidad. François et al. (1997) definen el coeficiente α como un parámetro dependiente de ε_l y de la emisividad límite (ε_{lim}), definida como el valor al cual tiende la emisividad de la cubierta vegetal para valores elevados de LAI. Además, François et al. (1997) determinan que α no es dependiente del LAI, pero sí del ángulo de observación y del LIDF, ya que la ε_{lim} depende de estos dos parámetros. El coeficiente α se define como:

$$\alpha = \frac{1-\varepsilon_{lim}}{1-\varepsilon_l} \quad (3)$$

François (2002) analiza el coeficiente α y proporciona su valor tabulado a distintos ángulos de observación asumiendo una LIDF esférica. Para una LIDF esférica y considerando una dispersión aleatoria de la energía, $b(\theta)$ viene definida como $b(\theta) = e^{-0,5LAI/\cos(\theta)}$, mientras que M se puede aproximar como $M = e^{-0,825LAI}$.

Teniendo en cuenta todas estas expresiones y la ecuación (2), la emisividad direccional de la vegetación definida por el modelo FR97 viene dada como:

$$\varepsilon_c(\theta) = 1 - b(\theta)M(1 - \varepsilon_s) - \alpha(1 - b(\theta)M)(1 - \varepsilon_l) \quad (4)$$

2.2. Modelo Mod3

El modelo Mod3 fue propuesto por François (2002). Igual que el modelo FR97, este modelo define la emisividad direccional de la superficie vegetada con una ecuación paramétrica basada en el modelo de Prévot (1985). Este modelo consiste en una variación del modelo Mod2, descrito por Chehbouni et al. (2001). François (2002) justifica esta variación argumentando que el modelo Mod2 considera incorrectamente las interacciones radiativas entre las hojas y el suelo, hecho que afecta a la expresión que define la emisividad direccional de la vegetación. Por ello, el Mod3 añade el factor M, el cual no se encuentra en el modelo Mod2. Teniendo esto en cuenta, François (2002) presenta la emisividad de la cubierta vegetal dada por el MTR Mod3 según la ecuación (5):

$$\varepsilon_c(\theta) = 1 - [1 - b(\theta)](1 - \varepsilon_l) - \frac{b(\theta)M(1-\varepsilon_s)}{1-(1-\varepsilon_s)M(1-\varepsilon_l)} \quad (5)$$

Este modelo no incluye las reflexiones múltiples dentro de la estructura vegetal, tan solo tiene en cuenta las reflexiones entre las componentes de la vegetación y el suelo. Por ello, la principal diferencia entre el modelo FR97 y el Mod3 es la ausencia del coeficiente de efecto de cavidad en este último.

2.3. Modelo Rmod3

Cuando observamos la superficie terrestre desde satélite, sobre zonas semiáridas es frecuente encontrar píxeles mezcla, es decir, zonas de vegetación y suelo sin vegetación

en un mismo píxel. Para abordar estos píxeles mezcla, Shi (2011) propone el modelo Rmod3, que consiste en una variación del modelo Mod3 mediante la introducción de la proporción de vegetación (P_v) como parámetro de entrada adicional.

La reflectancia direccional de la superficie vegetada obtenida en el modelo Mod3 es ponderada por P_v en este modelo. Además, añade un término adicional relacionando la emisividad del suelo y la fracción de suelo sin vegetación vista por el sensor. La expresión paramétrica correspondiente al modelo Rmod3 se define como:

$$\varepsilon_c(\theta) = 1 - P_v\left\{[1 - b(\theta)](1 - \varepsilon_l) - \frac{b(\theta)M(1-\varepsilon_s)}{1-(1-\varepsilon_s)M(1-\varepsilon_l)}\right\} - (1 - P_v)(1 - \varepsilon_s) \qquad (6)$$

2.4. Modelo 4SAIL

El modelo SAIL es un MTR de cuatro componentes propuesto por Verhoef (1984). Este modelo calcula los coeficientes de dispersión y extinción de la estructura vegetal en la región espectral del visible e infrarrojo cercano, mediante la LIDF, propiedades ópticas de la hoja y la geometría de la observación. El modelo distingue entre dos flujos de energía directa (el incidente solar y la radiancia en la dirección de visión) y dos flujos de energía difusa (correspondientes a los flujos hemisféricos ascendente y descendente). La base de este modelo está definida por cuatro ecuaciones diferenciales que describen la interacción entre los cuatro flujos. Estas cuatro ecuaciones pueden ser resueltas analíticamente.

El MTR 4SAIL es una versión extendida del MTR SAIL al IRT descrita por Verhoef et al. (2007). Esta versión está programada y es ofrecida libremente en lenguaje de programación FORTRAN (Disponible en http://teledetection.ipgp.jussieu.fr/prosail/). En la versión utilizada, la emisividad de la vegetación puede ser obtenida utilizando los siguientes parámetros de entrada: la emisividad de suelo y hoja, el LAI y el ángulo de observación cenital. La reflectividad direccional de la superficie vegetada es obtenida como parámetro de salida, a partir de la cual podemos obtener la emisividad direccional de la superficie vegetada mediante la ley de Kirchhoff.

2.5. Modelo REN15

Ren et al. (2015) observaron que el coeficiente α tabulado por François (2002) para el MTR FR97 estaba sobreestimado, llevando a diferencias entre los MTR FR97 y 4SAIL, especialmente para ángulos de observación grandes. El MTR REN15 actualiza el modelo FR97 recalculando el término del coeficiente de cavidad. Para ello, calcula la emisividad límite haciendo uso del modelo 4SAIL para después obtener el coeficiente α mediante la ecuación (3). Finalmente, la emisividad de la superficie vegetada se calcula usando la descripción del modelo FR97, mediante la ecuación (2) y el nuevo coeficiente α.

2.6. Modelo CE-P

El modelo CE-P es un modelo de emisividad direccional de la superficie vegetada basado en invariantes espectrales propuesto por Cao et al. (2018). Este modelo hace uso del parámetro de probabilidad de recolisión (p) en vez del coeficiente α utilizado en los modelos FR97 y REN15 para explicar el efecto de las reflexiones múltiples entre la vegetación. El parámetro p indica la probabilidad de que un fotón interaccione con un elemento de la estructura vegetal después de haber interaccionado con otro elemento. El parámetro p suele utilizarse en el espectro del visible y del infrarrojo cercano, y en el modelo CE-P se extiende su aplicación al intervalo espectral del IRT. Este parámetro viene definido como $1 - e_u - e_d$, donde e_u es la probabilidad de escape ascendente y e_d es la probabilidad de escape descendente (Cao et al., 2018). Como en los modelos anteriores, el modelo CE-P está definido considerando una superficie vegetal homogénea y una LIDF esférica. Esta expresión viene dada en la siguiente ecuación:

$$\varepsilon(\theta) = \frac{i_0\varepsilon_l}{1-p(1-\varepsilon_l)} + \frac{\left(1-i_0(\theta)\right)(1-\varepsilon_s)i'_0\frac{\varepsilon_l}{1-p(1-\varepsilon_l)}}{1-r^*_{c2}(1-\varepsilon_s)i'_0} + \frac{i_0(\theta)r^*_{c1}(1-\varepsilon_s)i'_0\frac{\varepsilon_l}{1-p(1-\varepsilon_l)}}{1-r^*_{c2}(1-\varepsilon_s)i'_0} + \frac{(1-i_0(\theta))\varepsilon_s}{1-r^*_{c2}(1-\varepsilon_s)i\prime_0} + \frac{i_0(\theta)r^*_{c1}\varepsilon_s}{1-r^*_{c2}(1-\varepsilon_s)i\prime_0} \quad (7)$$

donde i_0 es la probabilidad de intercepción direccional $\left(i_0(\theta) = 1 - b(\theta)\right)$, i'_0 es la probabilidad de intercepción hemisférica $(i'_0 = 1 - M)$, r^*_{c1} y r^*_{c2} son la reflectancia

difusa de la vegetación en dirección ascendente y descendente, que vienen dados por $r_{c1}^{*} = (1-\varepsilon_l)e_u/(1-(1-\varepsilon_l)p)$ y $r_{c2}^{*} = (1-\varepsilon_l)e_d/(1-(1-\varepsilon_l)p)$.

Cao et al. (2018) y Guo et al. (2019) proponen distintas simplificaciones para este modelo. Sin embargo, estas simplificaciones no son recomendadas por los autores para emisividades de hoja inferiores a 0,98 ni para emisividades de suelo inferiores a 0,94.

2.7. Análisis de sensibilidad

Para la realización del análisis de sensibilidad de los MTR, se ha calculado la contribución de cada parámetro a la incertidumbre del modelo mediante la propagación de incertidumbres:

$$\delta(\varepsilon) = \sqrt{\sum_i \left[\frac{\partial \varepsilon}{\partial x_i}\delta(x_i)\right]^2} \quad (8)$$

donde x_i hace referencia a los distintos parámetros de los MTR y $\delta(x_i)$ es la incertidumbre asociada a dichos parámetros.

Para el cálculo de la incertidumbre de cada uno de los modelos, se han utilizado valores de emisividad de suelo y hoja de 0,94 y 0,98, respectivamente (Sobrino et al., 2005; Verhoef et al., 2007; Cao et al., 2018). A estos valores, se les ha asignado una incertidumbre de emisividad de ±0,01, siendo del mismo orden que el error experimental del método TES utilizado en este estudio (Coll et al., 2019). Estos valores han sido utilizados para calcular la emisividad con distintos valores de LAI y ángulo de observación. El LAI varió de 0,5 a 3,0 m^2/m^2, en pasos de 0,5 m^2/m^2. En cuanto a la incertidumbre, Orlando et al. (2015) observaron una incertidumbre del LAI obtenido con la aplicación Pocket-LAI utilizada en este estudio de ±23 % sobre distintas muestras de vegetación (árboles y matorrales) de hoja ancha. Esta incertidumbre para el LAI es ligeramente superior a la incertidumbre de ±15 % requerida por GCOS (2016). La incertidumbre de ±23 % obtenida por Orlando et al. (2015) ha sido utilizada para calcular la contribución del LAI a la incertidumbre de la emisividad de los modelos. El ángulo de observación, por su parte, varió de 0º a 60º en pasos de 10º. Al ángulo de observación se le atribuyó una incertidumbre de ±0,5º, para tener en cuenta tanto la incertidumbre

del inclinómetro, la cual es de ±0,01º, como posibles movimientos en el sistema de sujeción (Niclòs et al., 2005). Además, en el caso del modelo Rmod3, se han interpolado los valores de P_v medidos en función del LAI, y se les ha asignado una incertidumbre de ±15%, obteniendo valores de incertidumbre ligeramente superiores a la desviación estándar de las medidas realizadas.

La Figura 3 muestra la contribución de cada parámetro a la incertidumbre de los modelos FR97 y Mod3 para los ángulos de observación de 0º y 60º y para cada LAI, así como la incertidumbre del modelo. Las gráficas obtenidas para todos los modelos se muestran en el Anexo A. La variación observada en la Figura 3 a) y b) muestra la tendencia generalizada para los modelos FR97, REN15, CE-P y 4 SAIL, donde la incertidumbre de la emisividad del modelo decrece con el LAI. La variación observada en la Figura 3 c) y d) para los modelos Mod3 y Rmod3, la tendencia encontrada muestra que la incertidumbre aumenta con el LAI. La incertidumbre de los MTR toma valores entre ±0,003 y ±0,011 según el LAI y ángulo de observación.

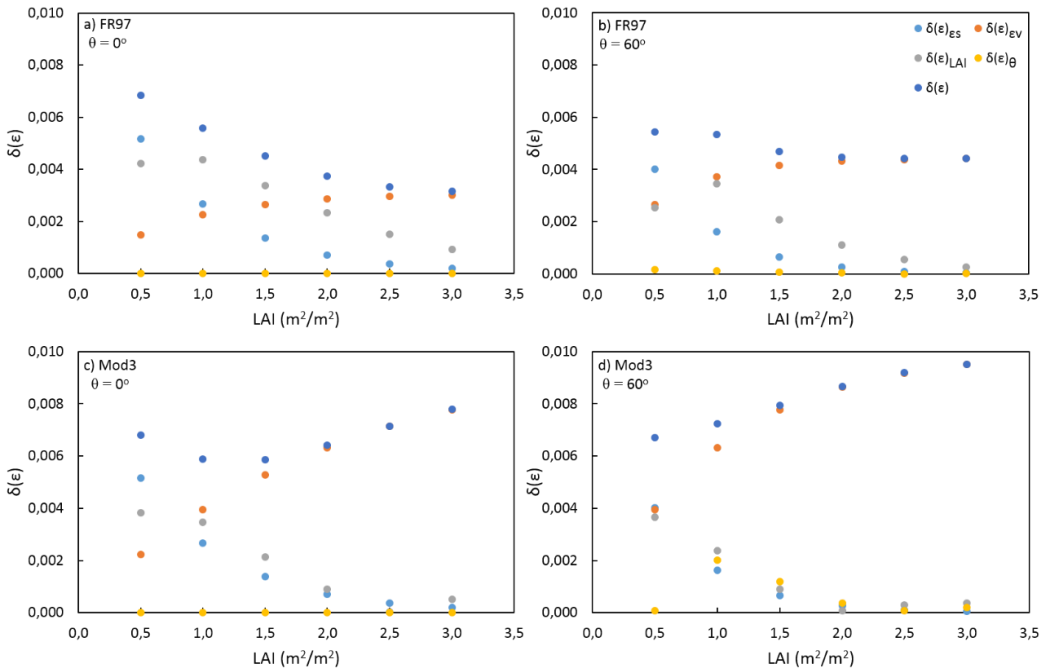

Figura 3. Contribución de la incertidumbre de emisividad de suelo ($\delta(\varepsilon)_{\varepsilon s}$), de emisividad de hoja ($\delta(\varepsilon)_{\varepsilon v}$), del LAI ($\delta(\varepsilon)_{LAI}$) y del ángulo de observación ($\delta(\varepsilon)_{\theta}$) a la incertidumbre asociada a la emisividad de los MTR ($\delta(\varepsilon)$) FR97 (a, b) y Mod3 (c, d) para los ángulos de observación de 0º (a, c) y 60º (b, d) y distintos valores de LAI.

En la Figura 3 se observa como la principal fuente de incertidumbre para cada MTR es la emisividad de entrada. Para valores de LAI superiores a 1 m^2/m^2, la ε_v muestra la mayor contribución a la incertidumbre del MTR. Para valores elevados de LAI, tan solo la incertidumbre introducida por la P_v en el MTR Rmod3 muestra una relevancia significativa (ver Anexo A). Para valores de LAI = 3 m^2/m^2 los MTR FR97, REN15, CE-P y 4SAIL obtienen la menor incertidumbre, con valores entre ±0,002 y ±0,004 según el MTR y el ángulo de observación. En el caso de los MTR Mod3 y Rmod3, muestran la mayor incertidumbre, con valores entre ±0,008 y ±0,011 según el MTR y el ángulo de observación. En cambio, para un valor de LAI = 0,5 m^2/m^2, la mayor contribución a la incertidumbre de los MTR viene dada por la ε_s, aunque también tiene un efecto considerable la incertidumbre introducida por el LAI y, en menor medida, la ε_v. En este caso, los MTR FR97, REN15, CE-P y 4SAIL obtienen una incertidumbre mayor que para valores de LAI superiores, con valores alrededor de ±0,006. Mientras que los MTR Mod3 y Rmod3 obtienen una incertidumbre de ±0,006 y ±0,010, respectivamente.

En cuanto a la incertidumbre introducida por el ángulo de observación, esta se observa despreciable en la mayoría de casos. Tan solo se observa una incertidumbre debida al ángulo de observación mayor a ±0,001 para ángulos de 60º y LAI < 1,5 m^2/m^2 para los MTR Mod3, Rmod3 y 4SAIL.

Capítulo 3

Medidas experimentales

En este capítulo se expone el proceso experimental seguido para la evaluación de los distintos modelos de transferencia radiativa para la obtención de la emisividad direccional mediante medidas de emisividad tomadas in-situ.

Previamente, se introduce el instrumental utilizado, en concreto las características principales de los radiómetros multicanal CIMEL-ELECTRONIQUE CE312 y su calibración en laboratorio (Coll et al., 2019) (Anexo H). Además, se define el método TES para la obtención de la emisividad direccional (Pérez-Planells et al., 2017) (Anexo F). Finalmente se detalla el proceso seguido para la realización de las medidas realizadas, así como la caracterización de las muestras utilizadas (Pérez-Planells et al., 2019b) (Anexo I).

3.1. Radiómetro multicanal CIMEL-ELECTRONIQUE CE312

En la realización de este trabajo, se han utilizado dos radiómetros multicanal CIMEL-Electronique CE312. Estos radiómetros disponen de 6 canales espectrales en el IRT en el intervalo espectral entre 8 y 13 µm: un canal ancho C1 abarcando el intervalo espectral completo (8 – 13,3 µm) y cinco canales estrechos C2 (10,9 – 11,7 µm), C3 (10,2 – 11,0 µm), C4 (9,0 – 9,3 µm), C5 (8,5 – 8,9 µm) y C6 (8,3 – 8,6 µm). Estos canales estrechos se encuentran dentro del intervalo que cubre el canal C1 y son similares a los canales del sensor térmico ASTER a bordo del satélite EOS-Terra. El campo de visión del sensor es de 10º (Legrand et al., 2000).

Según el fabricante, la incertidumbre asociada a las medidas de este instrumento es de ±0,2 K. Sin embargo, debido a la degradación del sensor, todos los radiómetros son recalibrados periódicamente. En el marco del proyecto *FIducial Reference Measurements for validation of Surface Temperature from Satellites* (FRM4STS) financiado por la Agencia Espacial Europea (ESA, por sus siglas en inglés), en el año 2016 se llevó a cabo la calibración de estos radiómetros frente a cuerpos negros de referencia participando en un experimento internacional (Theocharous et al., 2017; Coll et al., 2019). Para la calibración de los radiómetros en nuestro laboratorio se utiliza una fuente de cuerpo negro Landcal P80P (www.landinst.nl/wordpress/calibration/p80p) también calibrada en dicho experimento. Esta fuente de calibración de temperatura variable puede situarse entre -10 ºC y 80 ºC. La cavidad del cuerpo negro consiste en un cono de 120º con unas medidas de 50 mm de diámetro y 155 mm de longitud, con una emisividad >0,995 según el fabricante. El cuerpo negro fue comparado en el experimento FRM4STS 2016 frente al radiómetro AMBER del *National Physics Laboratory* (NPL), el cual tiene una incertidumbre asociada de ±53 mK (Theocharous et al., 2017). De esta comparación, se obtuvo que el cuerpo negro tiene un sesgo y una raíz del error cuadrático medio (RMSE, por sus siglas en inglés) de +0,02 K y ±0,05 K, respectivamente, cuando se realiza la corrección de emisividad al cuerpo negro.

Para la calibración de los dos radiómetros CE312 en nuestro laboratorio, estos se colocaron a 20 mm de la fuente, de manera que se aseguró que tan solo la cavidad del

cuerpo negro se encontraba dentro del campo de visión del instrumento. Los radiómetros fueron calibrados a 6 temperaturas distintas entre 0 y 50 ^{o}C, realizando las medidas en dos vueltas, es decir, cada temperatura fue medida dos veces, y realineando el radiómetro en la segunda vuelta. Las medidas a temperaturas negativas no fueron realizadas ya que, a pesar de que el cuerpo negro puede llegar a -10 ^{o}C según el fabricante, a temperaturas negativas se forman gotas de condensación en la cavidad que influyen en las medidas, llevando a resultados erróneos. Para cada una de las temperaturas se realizaron 15 medidas para cada canal del radiómetro CE312. De estas medidas, se calculó la reproducibilidad y repetitividad del instrumento. La reproducibilidad fue obtenida mediante la diferencia entre el promedio de los valores medidos para una misma temperatura en las dos vueltas (teniendo en cuenta el realineamiento) y la temperatura fija de la medida. Mientras que la repetitividad fue calculada a partir de la desviación estándar de las 15 medidas a una temperatura fijada, sin juntar las medidas de las dos vueltas (Coll et al., 2019).

Los resultados obtenidos fueron ajustados linealmente teniendo en cuenta la temperatura del detector, representando para cada canal la diferencia entre la temperatura del cuerpo negro y la temperatura de brillo frente a la diferencia entre la temperatura de brillo y la temperatura del detector (Coll et al., 2019). Los coeficientes de correlación obtenidos para cada canal de los dos radiómetros oscilan entre 0,90 y 0,99, obteniendo los mejores ajustes para los canales C1 y C5 en ambos radiómetros. En cuanto a las incertidumbres obtenidas de la regresión estándar, estas oscilan entre ±0,03 y ±0,06 K.

A partir de estas medidas, se realizó un análisis de sensibilidad de los dos radiómetros CE312 (CE1 y CE2) siguiendo las líneas establecidas por el *Joint Committee for Guides in Metrology* (JCGM, 2008). Según el JCGM, se definen dos tipos de contribución a la incertidumbre: Tipo A, que hace referencia a la evaluación de la incertidumbre de un componente a partir de la estadística de las medidas realizadas bajo unas determinadas condiciones, y Tipo B, que corresponde a la incertidumbre en las medidas de un componente debido a cálculos no estadísticos, como incertidumbres asociadas a

certificados de calibración o de caracterización previa del funcionamiento de los instrumentos. La incertidumbre de Tipo A corresponde a incertidumbres obtenidas de un análisis aleatorio de medidas bajo condiciones controladas, mediante el análisis de reproducibilidad y repetitividad de las medidas, mientras que el Tipo B corresponde a incertidumbres sistemáticas, determinadas por valores no estadísticos, como: la calibración primaria, para la cual se toma la incertidumbre total del cuerpo negro P80P (Theocharous et al., 2017); la linealidad del radiómetro, para la cual se toma el valor de incertidumbre típica para el intervalo de temperaturas de calibración (Legrand et al., 2000); corrección en la tendencia de calibración, que tiene en cuenta la incertidumbre de la regresión lineal y la propagación en la ecuación lineal de recalibrado de la incertidumbre en las temperaturas medidas; y las fluctuaciones en la temperatura ambiente durante las medidas, para la cual se asigna la incertidumbre asociada al termómetro interno de resistencia de platino del instrumento, ya que esta variación se compensa con la medida de la temperatura interna del instrumento. Todas las incertidumbres obtenidas en esta calibración se muestran en la Tabla 1 para los radiómetros CE1 y CE2, obteniendo para la raíz cuadrada de la suma cuadrática (RSC) de las incertidumbres de Tipo A y Tipo B un valor de de ±0,15 K para el radiómetro CE1 y de ±0,12 K para el radiómetro CE2.

Tabla 1. Análisis de incertidumbre de los radiómetros CE312 realizado a partir de las medidas de calibración y las distintas fuentes de incertidumbre. RSC es la raíz cuadrada de la suma cuadrática de los distintos términos. RSC total es la RSC de las incertidumbres A y B y representa la incertidumbre estándar del radiómetro.

Incertidumbre	**Radiómetro CE1**		**Radiómetro CE2**	
	Tipo A (K)	Tipo B (K)	Tipo A (K)	Tipo B (K)
Reproducibilidad	0,08		0,03	
Repetitividad	0,05		0,06	
Calibración primaria		0,05		0,05
Linealidad del radiómetro		0,06		0,06
Corrección de la tendencia de calibración		0,07		0,05
Fluctuación de la temperatura ambiente		0,04		0,04
RSC	0,09	0,11	0,07	0,10
RSC total	**0,15**		**0,12**	

Los coeficientes obtenidos en la calibración fueron probados frente al cuerpo negro de referencia del NPL, caracterizado con una incertidumbre de ±0,04 K, durante la campaña de calibración de sensores en el NPL en junio de 2016, dentro del marco del proyecto

FRM4STS (Theocharous et al., 2017). El intervalo de temperaturas para la comparación de los radiómetros recalibrados fue entre 0 y 45 ºC. De esta comparación se obtuvo un sesgo entre -0,05 y -0,02 K para el CE1 y -0,02 y +0,01 K para el CE2, mientras que se obtuvo un intervalo de RMSE, calculado como la RSC del error sistemático y aleatorio, entre ±0,06 y ±0,10 K para los canales C1 – C3, y entre ±0,13 y ±0,26 K para los canales C4 – C6 para ambos radiómetros CE312. Estos resultados demuestran el buen funcionamiento de los dos radiómetros CE312, justificando su validez tanto para tareas de validación de la TST medida desde satélite, así como para distintas tareas de investigación en el IRT, como la medida de la emisividad.

3.2. Metodología: Método TES

El método TES fue propuesto por Gillespie et al. (1998) para obtener la TST y la emisividad de la superficie terrestre simultáneamente a partir de los cinco canales espectrales en el IRT del sensor ASTER. Debido a la similitud entre los canales del sensor ASTER y los radiómetros CE312, la misma metodología TES se puede aplicar a ambos sensores (Mira et al., 2009). Además, Hulley y Hook (2009) aplicaron el método TES al sensor MODIS utilizando los canales 29 (8,3 µm), 31 (11,03 µm) y 32 (12,02 µm). El método TES se aplica utilizando la radiancia a nivel de superficie de cada canal i ($L_{surf,i}$), que siguiendo la notación de la ecuación (1), viene definida como:

$$L_{surf,i} = \varepsilon_i B_i(T) + (1 - \varepsilon_i) L_i^{\downarrow} \quad (9)$$

donde $L_{surf,i}$ es la radiancia medida por el sensor a nivel de superficie para el canal i. El método TES se inicia aplicando el módulo correspondiente al método NEM (Gillespie, 1986). En el módulo NEM, se hace uso de $L_{surf,i}$ y una emisividad inicialmente asignada, cercana al valor máximo esperado (Gillespie et al., 1998), para obtener la radiancia de cuerpo negro mediante la función de Planck $B_i(T)$ para cada canal del sensor:

$$B_i(T) = \frac{L_{surf,i} - (1-\varepsilon_i) L_i^{\downarrow}}{\varepsilon_i} \quad (10)$$

Las radiancias obtenidas de la ecuación (10) para cada canal son invertidas obteniendo cinco valores de temperatura. La temperatura máxima de las cinco obtenidas es seleccionada como la primera aproximación a la TST. Esta temperatura recibe el nombre de T_{NEM}. Utilizando T_{NEM} nuevamente en la ecuación (9), obtenemos los valores de emisividad (ε_{NEM}) correspondientes a cada canal para la temperatura T_{NEM} según:

$$\varepsilon_{NEM,i} = \frac{L_{surf,i} - L_i^{\downarrow}}{B_i(T_{NEM}) - L_i^{\downarrow}} \tag{11}$$

Los valores $\varepsilon_{NEM,i}$ son utilizados para calcular el índice independiente de temperatura (β_i, conocido como espectro β).

$$\beta_i = \frac{\varepsilon_{NEM,i}}{\bar{\varepsilon}} \tag{12}$$

donde $\bar{\varepsilon}$ es el promedio de las emisividades NEM de los cinco canales del IRT. Una vez calculado el espectro β, se calcula la diferencia entre su valor máximo y mínimo (MMD). La MMD se relaciona con el valor mínimo del espectro de emisividad (ε_{min}) mediante una ecuación empírica, conocida como curva de calibración, la cual se obtuvo a partir de una base de espectros de emisividad de rocas, suelos, vegetación, agua y nieve pertenecientes a la librería espectral ASTER (Gillespie et al., 1998; Baldridge et al., 2009), actualmente conocida como ECOSTRESS (Meerdink et al., 2019).

$$\varepsilon_{min} = A - B \times MMD^C \tag{13}$$

La Tabla 2 reúne los coeficientes de los ajustes de la curva de calibración realizados por distintos autores para los sensores ASTER, MODIS, VIIRS y *Spinning Enhanced Visible and Infrared Imager* (SEVIRI).

Tabla 2. Coeficientes de la curva de calibración del método TES obtenidos para distintos sensores.

Sensor	Autor	Coeficientes		
		A	B	C
ASTER	Gillespie et al. (1998)	0,994	0,687	0,737
ASTER	Hulley y Hook (2009)	0,9951	0,7264	0,7873
ASTER	Jacob et al. (2017)	0,989	0,737	0,834
MODIS	Hulley et al. (2016b) (cuerpo gris)	0,997	0,7050	0,7430
MODIS	Hulley et al. (2016b)	0,985	0,7503	0,8321
MODIS	Jacob et al. (2017)	0,989	0,737	0,834
VIIRS	Islam et al. (2017)	0,9830	0,7591	0,8301
SEVIRI	Jimenez-Munoz et al. (2014)	0,998	0,684	0,747

Para el sensor ASTER, Hulley y Hook (2009) obtuvieron los coeficientes de la expresión MMD aportando una mayor cantidad de muestras de vegetación, pesando las muestras de vegetación existentes en la librería ASTER con distintas proporciones de vegetación junto con los mismas muestras de suelos utilizados por Gillespie et al. (1998). Por otra parte, Jacob et al. (2017) generó una nueva base de datos de vegetación utilizando las emisividades obtenidas al aplicar el MTR 4SAIL con las emisividades de vegetación y suelo de distintas librerías espectrales.

Finalmente, el espectro de emisividad se calcula utilizando la ε_{min} junto con el espectro β como:

$$\varepsilon_i = \varepsilon_{min} \frac{\beta_i}{\min(\beta_i)} \tag{14}$$

El espectro emisividad obtenido a partir de la ecuación (14) es utilizado en la ecuación (10), obteniendo cinco nuevas temperaturas. Las nuevas temperaturas deberían de ser iguales, pero suelen presentar pequeñas diferencias. Si esta diferencia es menor que la diferencia de temperatura equivalente de ruido del sensor (NEΔT), la mayor temperatura obtenida es aceptada como la TST. En caso de obtener una diferencia de temperaturas mayor que NEΔT, el proceso debe repetirse tantas iteraciones como sean necesarias hasta obtener una diferencia entre las temperaturas finales menor que la NEΔT del sensor (Gillespie et al., 1998; Hulley et al., 2016b).

Basándose en el módulo NEM, Coll et al. (2003) propusieron el método ANEM. Este método permite obtener la emisividad de cada canal del sensor ajustando la emisividad inicial del módulo NEM, seleccionando la emisividad máxima en función del tipo de cobertura. Coll et al. (2003) aplicaron el método ANEM con datos del sensor aerotransportado *Digital Airborne Imaging Spectrometer* (DAIS), ajustando la emisividad inicial a partir del método de cobertura vegetal (Valor y Caselles, 1996). En Pérez-Planells et al. (2017) (ver Anexo F) aplicamos el método ANEM a imágenes ASTER, y realizamos la comparación de los resultados obtenidos con los productos operativos ASTER de TST (AST08) y emisividad (AST05) y los valores de TST y emisividad obtenidos haciendo uso de la ecuación empírica de la curva de calibración propuesta por Hulley y

Hook (2009). Como medidas de referencia se utilizaron, por un lado, medidas tomadas con radiómetros CE312 simultáneas al paso del sensor ASTER sobre la zona de arrozales de Valencia (39º15'54" N, 0º18'29" W) con superficie de vegetación completa y, por otro lado, datos de temperatura del mar del producto MOD28 de MODIS sobre el Mar Mediterráneo. Esta comparación demostró que, en las zonas de estudio y aplicando una corrección atmosférica local mediante radiosondeos lanzados *in-situ*, los dos algoritmos funcionan correctamente, dentro de las incertidumbres establecidas por el método TES (±1,5 K para TST y ±0,015 para la emisividad, según Gillespie et al., 1998). Se observó que el método ANEM obtiene ligeramente mejores resultados que el método TES sobre superficies de bajo contraste espectral (p. ej., agua y vegetación), posiblemente debido a mayor sensibilidad del método TES a errores residuales en la corrección atmosférica. Sin embargo, los productos AST05 y AST08 obtuvieron mejores resultados que los métodos TES y ANEM sobre superficies con alto contraste espectral (p. ej., zonas de arena en la costa).

3.3. Montaje experimental

El montaje para las medidas experimentales de emisividad requeridas para la evaluación de los MTR para la obtención de la emisividad sobre superficies vegetadas tuvo lugar en la Facultad de Física de la Universidad de Valencia, España (39º30'25'' N, 0º25'13'' W). Las medidas fueron realizadas en dos periodos distintos: el primero entre los meses de octubre y noviembre de 2017, y el segundo en cuatro días consecutivos entre el 29 de mayo y el 1 de junio de 2019. En los dos periodos las medidas fueron realizadas de noche y con cielo despejado para evitar posibles efectos de sombra (que generen heterogeneidades térmicas) y reducir la contribución de la absorción atmosférica en la metodología utilizada para la obtención de la emisividad *in-situ*. En ambos casos se usó la misma especie de planta (un conjunto de rosales, *Rosa*) como muestra en las medidas, pero en cada uno de ellos se utilizó un tipo de suelo diferente: en el primer periodo se usó un suelo orgánico (SO), mientras que en el segundo periodo se utilizó un suelo inorgánico (SI), concretamente arena de la playa de Valencia, con un elevado contenido en cuarzo; ambos suelos presentaban espectros de emisividad bien

diferentes, representando casos extremos de elevada y baja emisividad. La muestra de rosales fue seleccionada por varias razones. Primero, cuando todas las plantas se colocan juntas, al ser una planta de hoja ancha, forman una vegetación continua, que coincide con la descripción de la vegetación para la cual son definidos los MTR. La distribución aleatoria de las hojas de los rosales permite cortar las hojas controlando la estructura de la planta a conveniencia para mantener una distribución uniforme durante las medidas. Además, el tallo del rosal es fuerte pero suficientemente fino como para tener una influencia mínima en la emisividad del conjunto de la muestra (Pérez-Planells et al., 2019b).

Para la realización de las medidas, se dispuso un radiómetro CE312 (CE1) junto con un goniómetro para realizar las medidas sobre la muestra. En el primer periodo, se consideraron las medidas a siete ángulos de observación distintos, variando de 0º a 60º en intervalos de 10º (Pérez-Planells et al., 2019b). Para reducir los valores de LAI de la muestra, la cantidad de hojas de los rosales fue reducida de forma uniforme en la muestra después de cada conjunto de medidas angulares. Las medidas se repitieron para seis valores de LAI en el intervalo de 0,5 m^2/m^2 a 2,8 m^2/m^2. Los valores de LAI fueron medidos con la aplicación Android Pocket-LAI (Confalonieri et al., 2013; Campos-Taberner et al., 2016), realizando 36 medidas para cada valor de LAI. La desviación estándar de estas medidas fue asignada como la incertidumbre asociada a las medidas. En el segundo periodo, se llevó a cabo un procedimiento similar: se consideraron 2 ángulos de observación, uno a nadir y otro a 55º, y las medidas de LAI se realizaron en el intervalo de 0,6 m^2/m^2 a 3,3 m^2/m^2. Además, el número de ángulos se redujo por dos motivos: primero, García-Santos et al. (2012) observaron que la variación en emisividad de los suelos inorgánicos se produce para ángulos de observación mayores a 40º y, además, en el primer periodo no se observó en las medidas de emisividad ningún efecto de variación angular. Así, las medidas se realizaron tan solo para dos ángulos de observación porque no se esperaban diferencias significativas en ángulos menores y, además, esto permitió realizarlas en un periodo de cuatro días consecutivos al reducir considerablemente el tiempo de medidas (Pérez-Planells et al., 2019b).

Con el fin de tener suficientes medidas para un análisis estadístico adecuado, se realizaron 15 medidas de radiancia para cada canal, ángulo de observación y valor de LAI. Por lo tanto, para este estudio se realizaron 630 medidas para cada canal sobre la muestra en el primer periodo y 180 medidas para cada canal en el segundo. La altura a la cual se encontraba el radiómetro se fue variando con el ángulo de observación para mantener un campo de visión constante de 0,048 m^2 sobre la muestra. Además, se utilizó un segundo radiómetro CE312 (CE2) para medir la radiancia hemisférica descendente, simultáneamente a cada medida del CE1, sobre un panel de oro de alta reflectividad difusa en el IRT (IRT-94-100) de la casa Labsphere (Garcia-Santos et al., 2013; Guillevic et al., 2018). La reflectividad de este panel es cercana a 0,92 para los seis canales del radiómetro CE312. El montaje experimental puede observarse en la Figura 4.

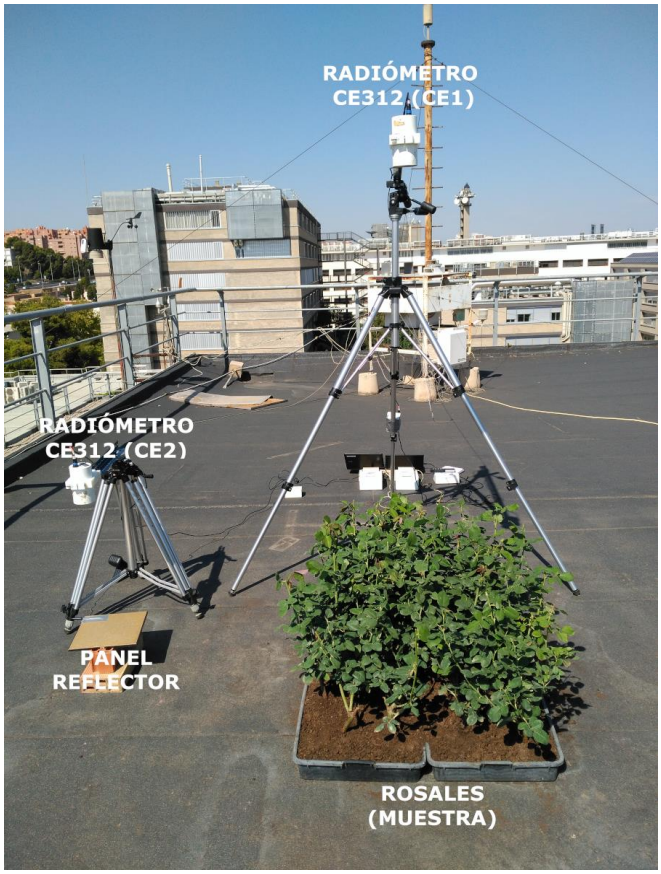

Figura 4. Montaje experimental establecido para las medidas radiométricas.

Para el estudio se utilizaron dos conjuntos de veintisiete rosales plantados en suelo orgánico. Durante el primer periodo, las medidas se realizaron sobre este suelo, mientras que en el segundo periodo el suelo fue cubierto con arena, utilizando una tela para separar la arena del suelo orgánico y evitar mezclar las muestras. El recipiente utilizado para los rosales tenía unas dimensiones de 113 cm × 84 cm × 9 cm. Durante el primer periodo, las plantas fueron regadas dos veces a la semana. Para asegurar un valor constante en la emisividad del suelo durante el estudio, el suelo de la muestra se cubrió con SO seco antes de iniciar cada conjunto de medidas. Durante el segundo periodo, las plantas fueron regadas antes de cubrir el suelo orgánico con la arena y, debido al corto plazo en el que se realizaron las medidas, no fue necesario volver a regar hasta la finalización de las medidas.

La variación espectral y angular de la emisividad de la muestra de SO fue analizada. Se midió la variación angular de la emisividad entre nadir y 60º, obteniendo como resultado un decrecimiento de la emisividad de 0,01 para el intervalo espectral entre 10 y 12 μm y de 0,02 entre 8,0 y 9,5 μm. En cambio, la arena tiene un alto contraste espectral y angular de la emisividad, especialmente entre 8,0 – 9,5 μm. García-Santos et al. (2012) midieron la emisividad de la arena utilizada en este trabajo, observando una caída de la emisividad con el ángulo de 0,03 para el intervalo 10 – 12 μm y de 0,06 para el intervalo 8,0 – 9,5 μm.

La emisividad a nadir de las hojas de la planta, del SO y del SI es un parámetro de entrada necesario en los MTR para obtener la emisividad direccional de la vegetación. Por ello, se usó un conjunto de hojas de rosal cortadas y una muestra de SO y SI para caracterizar la emisividad de las muestras mediante medidas radiométricas a nadir con los radiómetros CE312. Para obtener la emisividad de estas muestras, se realizaron veinte medidas de radiancia sobre cada muestra y se aplicó el método TES con dichas radiancias, siguiendo la metodología de la Sección 3.2. Coll et al. (2019) analizaron la incertidumbre del método TES aplicado con los radiómetros CE312, obteniendo una incertidumbre de medida de 0,01 en emisividad. La incertidumbre de medida se obtiene como la RSC de la desviación estándar de las veinte medidas y la incertidumbre asociada

al método TES. La Figura 5 muestra el espectro obtenido para cada elemento medido, siendo las barras de error de cada valor la desviación estándar de las medidas realizadas (Pérez-Planells et al., 2019b).

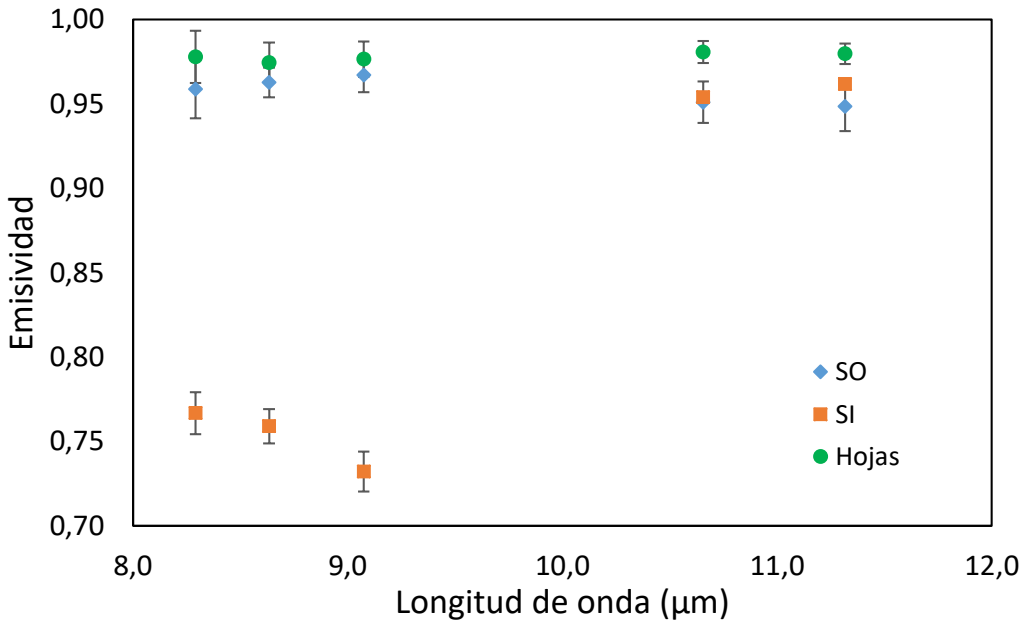

Figura 5. Emisividad de las muestras de hojas de rosal, suelo orgánico y suelo inorgánico para los cinco canales estrechos del radiómetro CE312. Emisividades obtenidas mediante medidas *in-situ* con el método TES.

En la Figura 5 se observa como el espectro de emisividad de las hojas de rosal es prácticamente plano, con un valor promedio de 0,978 y una diferencia entre el valor máximo y mínimo de 0,006. Por el contrario, se observan valores de emisividad más bajos para las muestras de suelo. Para el SO, se obtuvo una diferencia de 0,018 entre el valor máximo y mínimo, con un valor máximo de 0,967. En el caso del SI, se obtiene un valor máximo de emisividad de 0,962, mientras que la diferencia entre la emisividad de los distintos canales alcanza valores de 0,23. En el intervalo espectral 8,0 – 9,5 µm podemos observar la diferencia de emisividad esperada entre el SO y el SI, con diferencias en emisividad entre 0,19 y 0,24 dependiendo del canal observado. La desviación estándar promedio observada de las medidas es de ±0,010 para las hojas y el SO, mientras que para el SI es de ±0,008.

Capítulo 4

Evaluación de los modelos de emisividad

En este capítulo se evalúa la emisividad direccional obtenida con los modelos de transferencia radiativa para las muestras de rosales utilizando las emisividades TES como referencia. Además, se analiza la variación de la emisividad con el LAI en observación a nadir y la variación de la emisividad con el ángulo de observación para distintos valores de LAI. Estos resultados fueron publicados en Pérez-Planells et al. (2019b).

4.1. Variación de la emisividad con el LAI en observación a nadir

Para la aplicación de los MTR es necesario calcular el LAI y, en el caso del MTR Rmod3, la P_v. En el caso del LAI, este fue calculado utilizando la aplicación Android Pocket-LAI (Confalonieri et al., 2013). Para ello se realizaron 36 medidas para cada LAI. El promedio de estas medidas para cada LAI se muestra en la Tabla 3, junto con la desviación estándar de las medidas. Para la estimación de la P_v, se tomaron seis fotografías de las plantas cubriendo toda la muestra de forma uniforme después de reducir la cantidad de hojas. A partir de las fotografías tomadas sobre la vegetación, se utilizó el software libre de edición de imagen Gimp2.10 para discriminar entre los píxeles de vegetación y de cielo haciendo uso de la herramienta de selección de color (Figura 6). La selección fue convertida a una imagen de blanco y negro para contabilizar los píxeles de color negro, correspondientes a la vegetación, y los píxeles blancos, correspondientes al cielo. La P_v fue obtenida como la fracción entre los píxeles de vegetación y el total de píxeles de la imagen. El proceso se repitió para las 6 imágenes tomadas en cada LAI, determinando el valor de P_v como el promedio de las 6 imágenes. La incertidumbre asociada a cada valor P_v se calculó como la desviación estándar de los 6 valores de P_v. Los valores de P_v y su incertidumbre asociada se muestran en la Tabla 3.

Figura 6. Imagen tomada sobre el conjunto de rosales para la estimación de la P_v (izquierda) para el LAI = 2,8 m^2/m^2. Imagen para la estimación de la P_v convertida a blanco y negro después de la selección de píxeles de vegetación (derecha).

Tabla 3. Valores medidos de índice de área foliar (LAI) y proporción de vegetación (P_v) necesarios para aplicar los distintos modelos de emisividad direccional de vegetación sobre la muestra con suelo orgánico (SO) y suelo inorgánico (SI).

LAI (m^2/m^2) – SO	P_v – SO	LAI (m^2/m^2) – SI	P_v – SI
2,8 ± 0,4	0,95 ± 0,03	3,3 ± 0,5	0,98 ± 0,03
2,4 ± 0,4	0,90 ± 0,03	2,8 ± 0,3	0,96 ± 0,04
2,0 ± 0,3	0,83 ± 0,06	2,4 ± 0,3	0,91 ± 0,05
1,5 ± 0,2	0,77 ± 0,05	1,8 ± 0,3	0,81 ± 0,05
0,9 ± 0,2	0,57 ± 0,06	1,1 ± 0,2	0,62 ± 0,03
0,52 ± 0,12	0,41 ± 0,04	0,64 ± 0,07	0,44 ± 0,03

En la Figura 7 se comparan las emisividades medidas *in-situ* a nadir con el método TES sobre las muestras de rosales con las emisividades obtenidas al aplicar los MTR a nadir con los distintos valores de LAI y la emisividad de hoja y SO como datos de entrada. La Figura 7 se compone de cinco gráficas, cada una correspondiente a un canal espectral estrecho del radiómetro CE312.

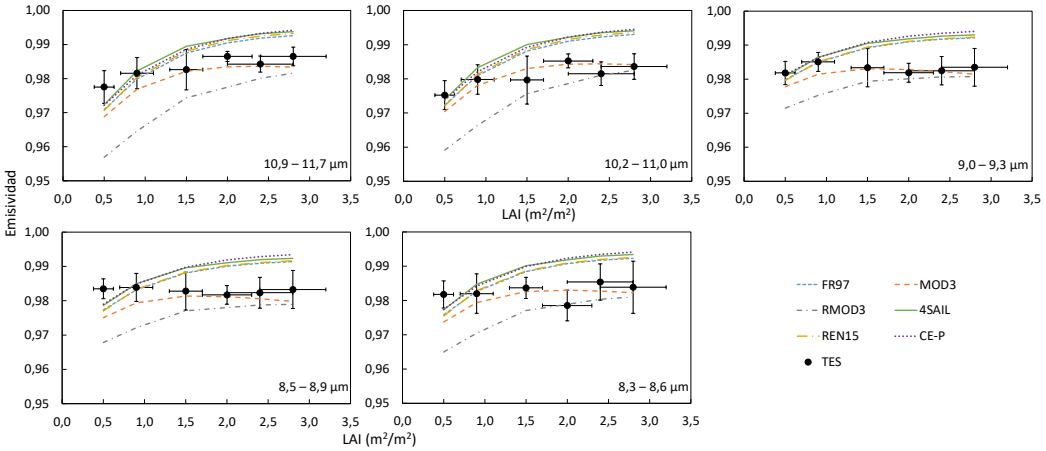

Figura 7. Emisividad TES medida *in-situ* a nadir y valores de emisividad obtenidos con los modelos FR97, Mod3, Rmod3, REN15, CE-P y 4SAIL considerando observaciones a nadir sobre suelo orgánico para distintos valores de LAI.

En la Figura 7 observamos valores de emisividad TES entre 0,975 y 0,987 para los distintos canales del radiómetro CE312. Los valores de emisividad más bajos se observan para los valores de LAI de 0,5 m^2/m^2 en el intervalo espectral 10,2 – 11,0 µm, mientras que las emisividades más elevadas se obtienen para el mayor valor de LAI en el intervalo espectral 10,9 – 11,7 µm. Las desviaciónes estándar mostradas como barra de error para las emisividades TES oscilan entre ±0,002 y ±0,008. La incertidumbre asociada a estas medidas se obtiene con la suma cuadrática de estas desviaciones

estándar y el error asociado al método TES para el radiómetro utilizado (±0,01). Así, la incertidumbre asociada oscila entre ±0,010 y ±0,013. Las desviaciones estándar de los valores de LAI, mostradas como barra de error en la Figura 7, son aquellas mostradas en la Tabla 3.

La Figura 8 muestra la emisividad a nadir obtenida de las medidas TES y la emisividad calculada con los MTR sobre la muestra con SI.

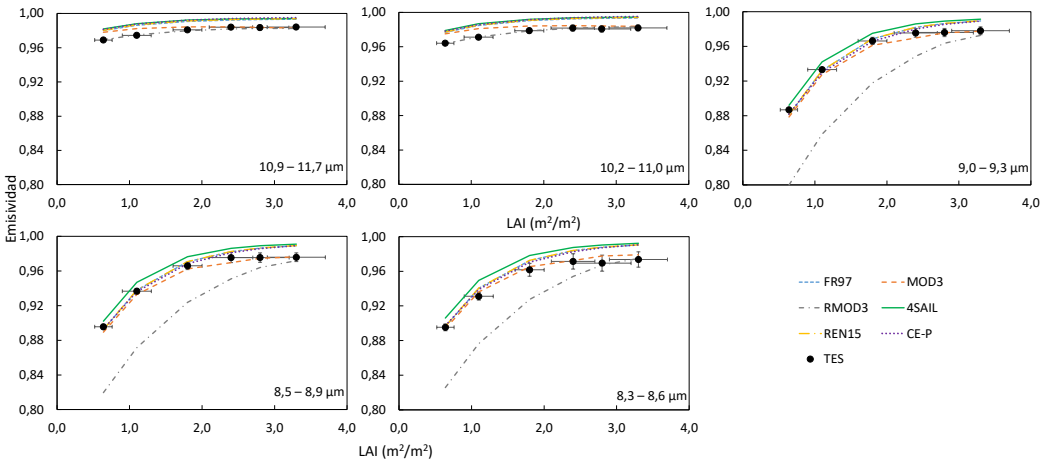

Figura 8. Emisividad TES medida *in-situ* a nadir y valores de emisividad obtenidos con los modelos FR97, Mod3, Rmod3, REN15, CE-P y 4SAIL considerando observaciones a nadir sobre suelo inorgánico para distintos valores de LAI.

En la Figura 8, el intervalo de las emisividades TES es de 0,887 a 0,984, obtenido para el intervalo espectral 9,0 – 9,3 µm y 10,9 – 11,7 µm, respectivamente. La desviación estándar obtenida para cada emisividad oscila entre ±0,002 y ±0,009. En el caso del SI, para el intervalo espectral 10 – 12 µm se observa una menor variación espectral con el LAI (sobre 0,02) debido a que la emisividad del SI en esta región espectral es más cercana a la emisividad de las hojas. Sin embargo, la baja emisividad del SI en el intervalo espectral de 8,0 – 9,5 µm causa una mayor variación de la emisividad con el LAI. Esta variación tiene una fuerte pendiente para LAI < 2 m^2/m^2, intervalo en el cual la variación del LAI tiene un gran impacto en la emisividad. Para valores de LAI > 2 m^2/m^2, tiende hacia un valor constante, tomando valores cercanos a la ε_{lim}.

En la comparación entre los MTR, las diferencias más significativas entre los modelos se observan en los canales espectrales donde existe una mayor diferencia entre la emisividad de suelo orgánico e inorgánico, es decir, en los canales entre 8,0 y 9,5 µm. Para estos canales se obtienen valores similares entre los modelos FR97, REN15, 4SAIL y CE-P, observando diferencias inferiores a 0,01. En el caso del modelo Mod3, los valores de emisividad son muy cercanos a los de FR97 para un LAI reducido (< 1,5 m^2/m^2), obteniendo mayores diferencias con el LAI, llegando a ser de 0,013 para LAI = 3,3 m^2/m^2. Estas diferencias se observan de forma similar en las muestras de los dos suelos utilizados. Por el contrario, el modelo Rmod3 difiere del Mod3 para los valores bajos de LAI, con diferencias significativas de emisividad de hasta 0,078, reduciendo considerablemente esta diferencia para los valores elevados de LAI. Esta aproximación para los valores altos de LAI es predecible ya que la expresión del modelo Rmod3 tiende a la de Mod3 cuando la P_v tiende a la unidad, hecho que se cumple con el aumento del LAI.

Las emisividades obtenidas con los MTR fueron comparados con las emisividades TES a nadir. Los resultados estadísticos se resumen para los distintos valores de LAI en las Tablas 4 y 5 para las medidas sobre la muestra con SO y SI, respectivamente. En el caso de la muestra con SO (Tabla 4), las diferencias observadas entre las emisividades TES y las emisividades de los MTR son pequeñas. Mientras que para LAIs < 1,5 m^2/m^2, los modelos FR97, 4SAIL, REN15 y CE-P son los que obtienen valores más cercanos a las emisividades TES y menor RMSE, para LAIs ≥ 1,5 m^2/m^2 el MTR Mod3 obtiene los valores más cercanos a las emisividades TES y menor RMSE. Teniendo en cuenta todas las medidas realizadas en todos los canales y para todos los LAIs, el modelo que obtiene menor sesgo y RMSE es el Mod3, aunque el resto de MTR, excepto el Rmod3, obtienen valores similares. En cambio, en el caso de la muestra con SI (Tabla 5), estas diferencias cambian, siendo el MTR Mod3 el que obtiene mejores resultados para todos los valores de LAI. Tan solo para el valor más bajo de LAI (LAI = 0,64 m^2/m^2), el valor de RMSE es el mismo que en los modelos FR97 y REN15, pero las diferencias aumentan con el LAI. El modelo Rmod3 obtiene en este caso los valores más cercanos a las emisividades TES en el intervalo espectral 10 – 12 µm, pero las diferencias en los canales entre 8,0 – 9,5 µm

llevan a valores muy distantes con las emisividades de referencia, debido a un exceso en el decrecimiento de las emisividades de Rmod3. Si se observan los valores de sesgo y RMSE de todo el conjunto de medidas, el modelo Mod3 obtiene un sesgo y RMSE bajos en las diferencias con las medidas TES (+0,001 y ±0,005, respectivamente), mientras que el resto de modelos obtienen diferencias mayores, con valores de RMSE entre ±0,010 y ±0,013 en el caso de los MTR FR97, 4SAIL, REN15 y CE-P, y de ±0,036, y por tanto, una diferencia mucho más significativa, en el caso del MTR Rmod3.

Tabla 4. Valores estadísticos de la comparación a nadir de la emisividad de la vegetación obtenida con los MTR y las medidas TES sobre la muestra con suelo orgánico (SO). Los estadísticos se han calculado para cada uno de los valores de LAI, juntando los valores obtenidos para los distintos canales del radiómetro CE312.

LAI	FR97		MOD3		RMOD3		4SAIL		REN15		CE-P	
(m^2/m^2)	Sesgo	RMSE	Sesgo	RMSE	Sesgo	RMSE	Sesgo	RMSE	Sesgo	RMSE	Sesgo	RMSE
0,5	-0,005	0,005	-0,007	0,007	-0,016	0,016	-0,003	0,004	-0,005	0,005	-0,003	0,004
0,9	-0,0001	0,0012	-0,003	0,004	-0,013	0,013	0,0019	0,002	0,0001	0,0011	0,0013	0,0017
1,5	0,006	0,006	0,000	0,002	-0,006	0,006	0,008	0,008	0,006	0,006	0,007	0,007
2,0	0,008	0,008	0,000	0,003	-0,004	0,006	0,009	0,009	0,008	0,009	0,009	0,010
2,4	0,008	0,009	-0,001	0,002	-0,003	0,004	0,010	0,010	0,009	0,009	0,010	0,010
2,8	0,008	0,008	-0,0019	0,003	-0,003	0,004	0,009	0,009	0,009	0,009	0,010	0,010
Total	**0,004**	**0,007**	**-0,002**	**0,004**	**-0,007**	**0,009**	**0,006**	**0,008**	**0,004**	**0,007**	**0,006**	**0,008**

Tabla 5. Valores estadísticos de la comparación a nadir de la emisividad de la vegetación obtenida con los MTR y las medidas TES sobre la muestra con suelo inorgánico (SI). Los estadísticos se han calculado para cada uno de los valores de LAI, juntando los valores obtenidos para los distintos canales del radiómetro CE312.

LAI	FR97		MOD3		RMOD3		4SAIL		REN15		CE-P	
(m^2/m^2)	Sesgo	RMSE	Sesgo	RMSE	Sesgo	RMSE	Sesgo	RMSE	Sesgo	RMSE	Sesgo	RMSE
0,64	0,003	0,009	0,001	0,009	-0,047	0,063	0,010	0,011	0,003	0,009	0,004	0,010
1,1	0,007	0,010	0,003	0,008	-0,039	0,053	0,013	0,014	0,007	0,010	0,006	0,010
1,8	0,008	0,009	0,001	0,005	-0,025	0,034	0,012	0,012	0,008	0,009	0,007	0,009
2,4	0,009	0,009	-0,001	0,004	-0,014	0,019	0,012	0,012	0,009	0,010	0,009	0,009
2,8	0,012	0,013	0,002	0,004	-0,005	0,008	0,014	0,015	0,013	0,013	0,012	0,013
3,3	0,012	0,013	0,001	0,003	-0,002	0,003	0,014	0,014	0,013	0,013	0,013	0,013
Total	**0,009**	**0,010**	**0,001**	**0,005**	**-0,022**	**0,036**	**0,013**	**0,013**	**0,010**	**0,011**	**0,009**	**0,011**

Por lo tanto, de las medidas realizadas a nadir, el MTR Mod3 es el que mejor se ajusta a las medidas TES, utilizadas como referencia, especialmente en el caso donde existe una mayor diferencia entre la emisividad de suelo y de hoja. Cuando las diferencias entre suelo y hoja se reducen, esto es, en las medidas sobre la muestra con SO y los canales entre 10 – 12 µm sobre la muestra de SI, el modelo Mod3 tiende a obtener mejores resultados considerando las medidas TES como referencia. En este caso, los resultados no pueden ser determinantes ya que depende del valor LAI y canal espectral

analizados; además, las diferencias se encuentran dentro de la incertidumbre asociada a las medidas TES.

Así mismo, de estas medidas se observa que, generalmente, los MTR FR97, 4SAIL, REN15, y CE-P sobreestiman los valores de emisividad TES. La principal diferencia de estos modelos con el Mod3 es que los primeros tienen en cuenta las reflexiones múltiples de la radiancia entre los distintos niveles de la vegetación, mientras que el modelo Mod3 tan solo considera las reflexiones entre la vegetación y el suelo. Esto explica que los valores de emisividad dados por los primeros modelos sean superiores a los del Mod3 y, además, que esta diferencia aumente cuando la cantidad de vegetación es mayor.

La variación de la emisividad observada con el LAI en el caso del SI fue ajustada a una función exponencial (ecuación 15) para cada canal espectral del radiómetro CE312.

$$\varepsilon_i(LAI) = a_i e^{-b_i LAI} + c_i \quad (15)$$

donde a_i, b_i y c_i son los coeficientes para cada canal espectral i del radiómetro CE312 obtenidos del ajuste de regresión a partir de los datos TES de las medidas realizadas a nadir sobre la muestra con SI (Figura 8). Los coeficientes a_i, b_i y c_i obtenidos para cada canal i del radiómetro CE312 se muestran la Tabla 6, así como el coeficiente de correlación (r^2) y el RMSE obtenido del ajuste. La emisividad de la muestra de SI fue añadida al conjunto de datos para un valor de LAI = 0,0 m^2/m^2 para realizar la regresión.

Tabla 6. Coeficientes obtenidos del ajuste de regresión para la ecuación 15 obtenidos a partir de los datos experimentales de emisividad de vegetación sobre SI.

Canal CE312 (µm)	a	b	c	r^2	RMSE
10,9 - 11,7	-0,026 ± 0,004	0,8 ± 0,3	0,987 ± 0,004	0,983	0,0013
10,2 - 11,0	-0,031 ± 0,005	0,9 ± 0,3	0,984 ± 0,004	0,985	0,0015
9,0 - 9,3	-0,248 ± 0,004	1,66 ± 0,06	0,980 ± 0,002	0,999	0,0014
8,5 - 8,9	-0,220 ± 0,005	1,65 ± 0,09	0,978 ± 0,002	0,999	0,0017
8,3 - 8,6	-0,208 ± 0,006	1,59 ± 0,10	0,974 ± 0,003	0,999	0,0019

4.2. Variación angular de la emisividad para distintos valores de LAI

Los seis MTR fueron analizados frente a medidas TES para estudiar la variación angular de la emisividad en la vegetación.

4.2.1. Suelo orgánico

Las medidas TES para obtener la emisividad direccional de la vegetación se realizaron sobre el SO para siete ángulos de observación distintos, entre 0º y 60º, y para seis valores de LAI. En las Figuras 9 – 13, se muestra la comparación entre las emisividades TES obtenidas con el radiómetro CE312 y las emisividades obtenidas utilizando los MTR. Cada figura corresponde a un canal espectral estrecho del radiómetro CE312.

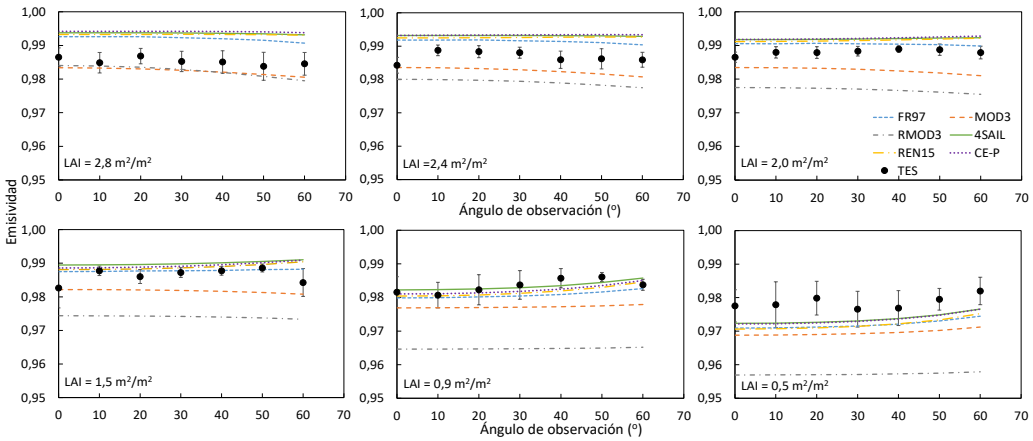

Figura 9. Emisividad obtenida de las medidas TES sobre la muestra con SO y de los MTR FR97, Mod3, Rmod3, 4SAIL, REN15 y CE-P para los siete ángulos de observación cenital y los seis valores LAI para el canal espectral de 10,9 – 11,7 µm del radiómetro CE312.

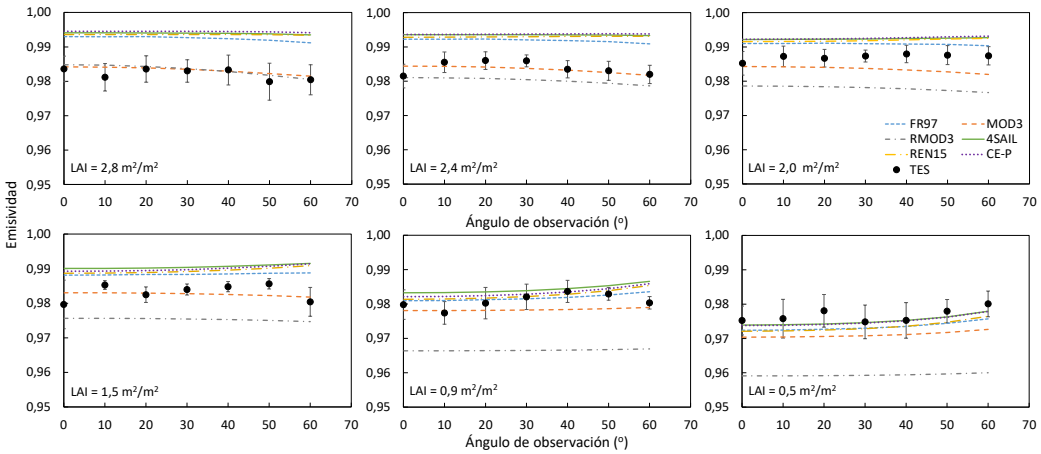

Figura 10. Emisividad obtenida de las medidas TES sobre la muestra con SO y de los MTR FR97, Mod3, Rmod3, 4SAIL, REN15 y CE-P para los siete ángulos de observación cenital y los seis valores LAI para el canal espectral de 10,2 – 11,0 µm del radiómetro CE312.

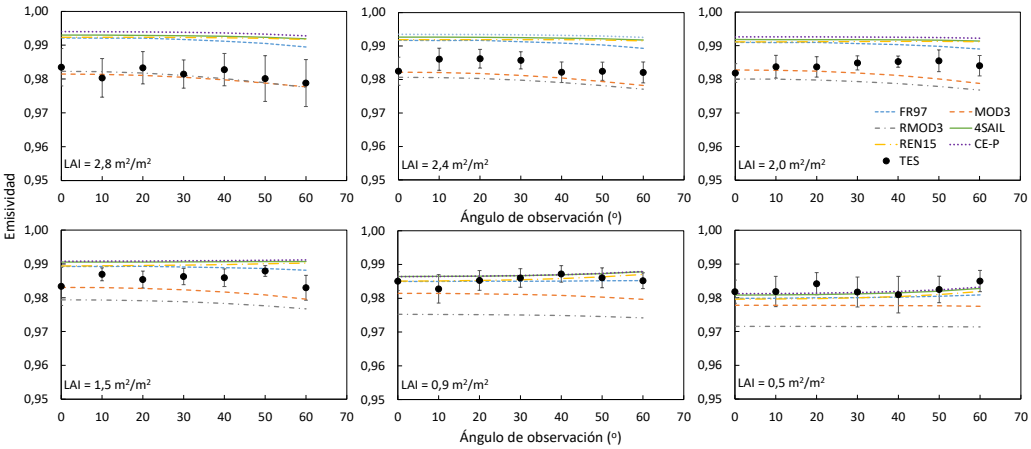

Figura 11. Emisividad obtenida de las medidas TES sobre la muestra con SO y de los MTR FR97, Mod3, Rmod3, 4SAIL, REN15 y CE-P para los siete ángulos de observación cenital y los seis valores LAI para el canal espectral de 9,0 – 9,3 µm del radiómetro CE312.

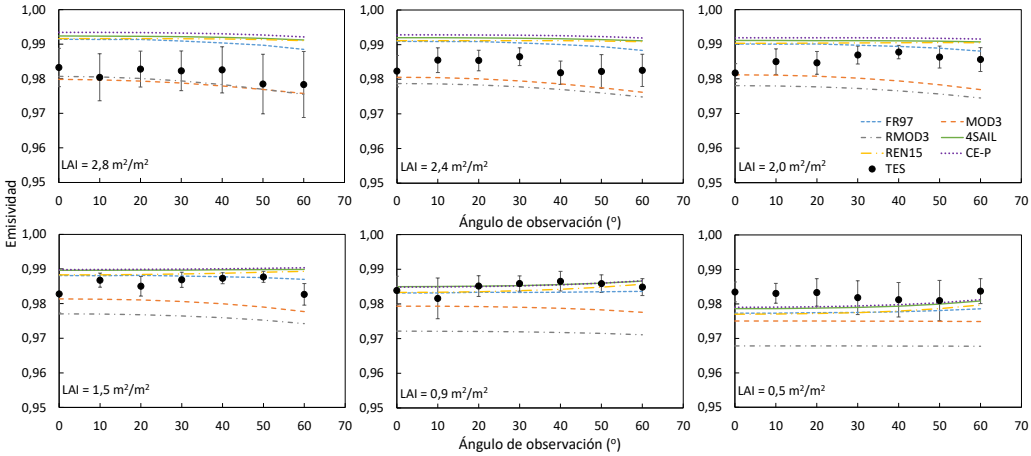

Figura 12. Emisividad obtenida de las medidas TES sobre la muestra con SO y de los MTR FR97, Mod3, Rmod3, 4SAIL, REN15 y CE-P para los siete ángulos de observación cenital y los seis valores LAI para el canal espectral de 8,5 – 8,9 µm del radiómetro CE312.

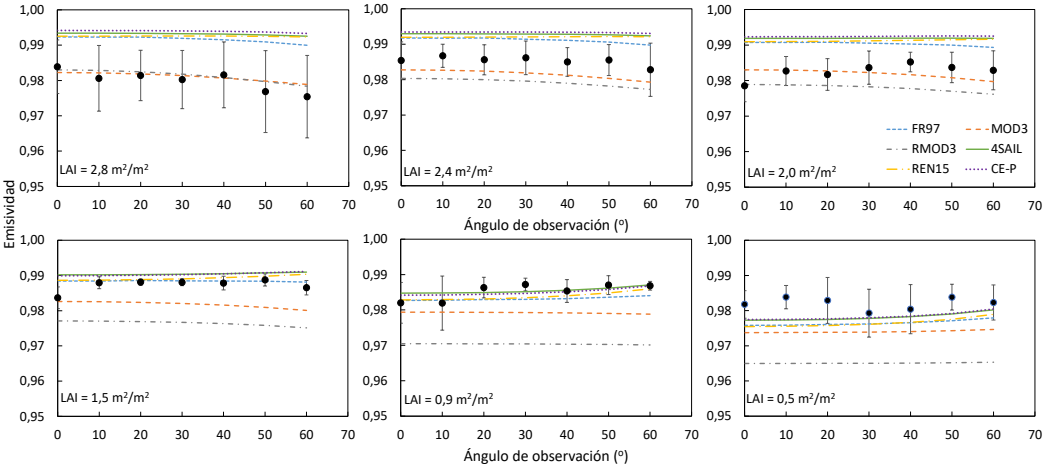

Figura 13. Emisividad obtenida de las medidas TES sobre la muestra con SO y de los MTR FR97, Mod3, Rmod3, 4SAIL, REN15 y CE-P para los siete ángulos de observación cenital y los seis valores LAI para el canal espectral de 8,3 – 8,6 µm del radiómetro CE312.

En las figuras 9 – 13 se observa una variación de emisividades TES entre 0,975 y 0,989 dependiendo del LAI, ángulo de observación cenital y canal espectral. Las desviaciones estándar de las medidas, mostradas como barras de error, se encuentran entre ±0,002 (Figuras 9 y 10) y ±0,012 (Figura 13). En estas figuras, se observa una ligera fluctuación en las emisividades TES, pero todas ellas dentro de la incertidumbre de las medidas.

La comparación entre los MTR muestra que los modelos FR97, 4SAIL, REN15 y CE-P, como se ha visto también en los resultados de observación a nadir, obtienen resultados muy similares, con diferencias cercanas a 0,002 para todo LAI, ángulo de observación y canal espectral. Así mismo, se reproduce nuevamente la variación del modelo Mod3 respecto a los otros MTR, siendo más cercana al modelo Rmod3 para valores de LAI > 1,5 m^2/m^2, pero acercándose a los otros modelos cuando el LAI se reduce.

La relación de los MTR con las emisividades TES varía ligeramente con el LAI. Los modelos FR97, 4SAIL, REN15 y CE-P sobreestiman las emisividades TES para LAIs > 1,5 m^2/m^2. Sin embargo, estos modelos se ajustan bastante bien cuando LAI < 1,5 m^2/m^2. En el caso del modelo Mod3, se observa una ligera subestimación en la mayoría de casos. El modelo Rmod3 es el que más difiere respecto a las emisividades TES,

obteniendo tan solo resultados cercanos a TES para valores de LAI elevados, esto es cuando Rmod3 toma valores similares al modelo Mod3.

Los estadísticos de la comparación entre los MTR y las emisividades TES se resumen en la Tabla 7, indicando el sesgo y el RMSE para cada MTR respecto a TES. Tal como se observaba en las Figuras 9 – 13, las diferencias entre los MTR FR97, 4SAIL, REN15 y CE-P y las medidas TES aumenta con el LAI. En cambio, para Mod3 y Rmod3, estas diferencias disminuyen con el LAI.

Tabla 7. Análisis estadístico de la comparación entre la emisividad direccional de los MTR y las medidas TES a distintos ángulos de observación cenital para los distintos valores de LAI sobre la muestra de suelo orgánico. Los estadísticos se han calculado para el conjunto de canales espectrales y ángulos de observación.

LAI	FR97		MOD3		RMOD3		4SAIL		REN15		CE-P	
(m^2/m^2)	Sesgo	RMSE	Sesgo	RMSE	Sesgo	RMSE	Sesgo	RMSE	Sesgo	RMSE	Sesgo	RMSE
2,8	0,010	0,010	-0,001	0,002	-0,001	0,002	0,011	0,011	0,011	0,011	0,012	0,012
2,4	0,006	0,007	-0,003	0,004	-0,006	0,006	0,008	0,008	0,007	0,008	0,009	0,009
2,0	0,005	0,005	-0,004	0,005	-0,008	0,008	0,006	0,007	0,006	0,006	0,007	0,007
1,5	0,003	0,004	-0,004	0,005	-0,010	0,010	0,005	0,005	0,004	0,004	0,005	0,005
0,9	-0,001	0,002	-0,005	0,006	-0,014	0,015	0,001	0,002	0,000	0,002	0,0007	0,002
0,5	-0,005	0,005	-0,007	0,007	-0,016	0,017	-0,003	0,004	-0,004	0,005	-0,003	0,003
Total	**0,003**	**0,006**	**-0,004**	**0,005**	**-0,009**	**0,011**	**0,005**	**0,007**	**0,004**	**0,007**	**0,005**	**0,007**

4.2.2.Suelo inorgánico

Sobre la muestra con SI, las medidas radiométricas para la aplicación del método TES se realizaron a dos ángulos de observación (0^o y 55^o) para los seis valores de LAI definidos en la Tabla 3. En las Figuras 14 – 18 se muestran las emisividades obtenidas con método TES y los MTR para los cinco canales estrechos del radiómetro CE312. Las emisividades TES obtenidas se encuentran en el intervalo entre 0,887 a 0,988, dependiendo del LAI, el ángulo de observación y el canal espectral. Las desviaciones estándar de las emisividades TES, mostradas como barras de error en las Figuras 14 - 18, oscilan entre ±0,002 (Figura 14) y ±0,011 (Figura 18).

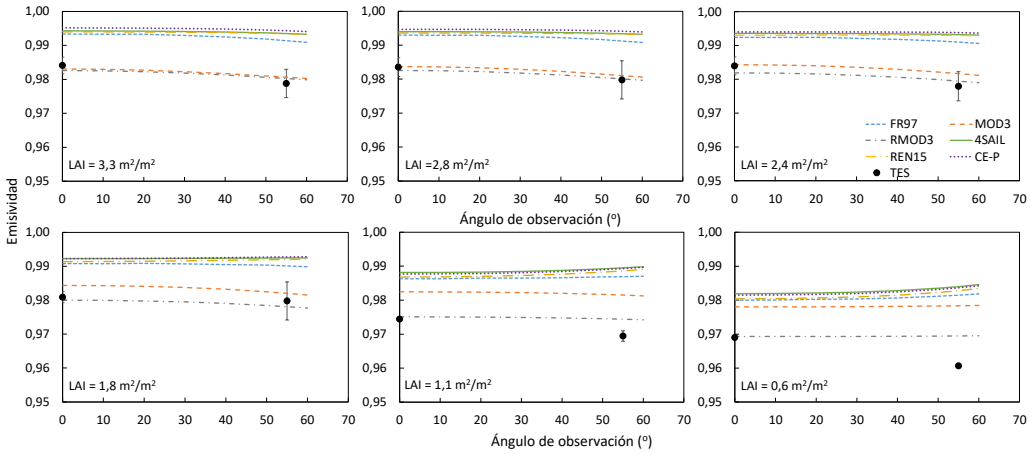

Figura 14. Emisividad obtenida de las medidas TES sobre la muestra con SI y de los MTR FR97, Mod3, Rmod3, 4SAIL, REN15 y CE-P para los siete ángulos de observación cenital y los seis valores LAI para el canal espectral de 10,9 – 11,7 µm del radiómetro CE312.

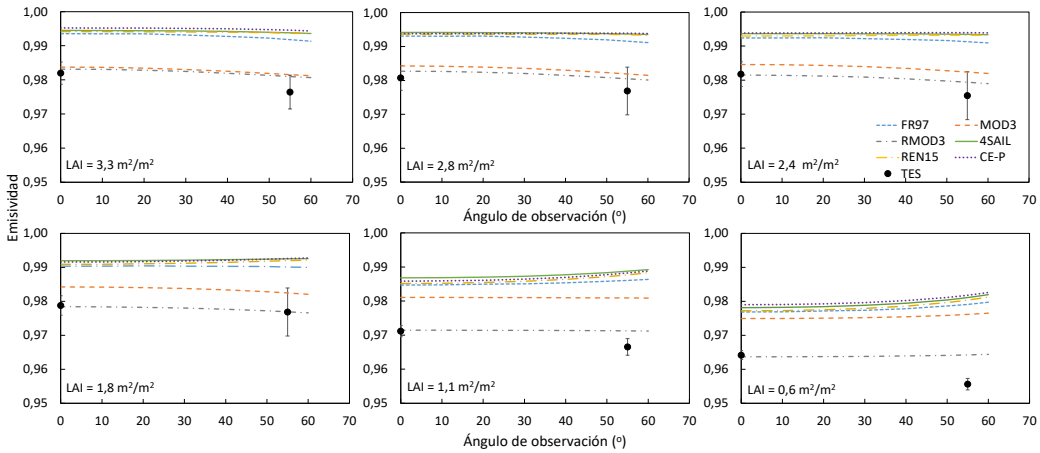

Figura 15. Emisividad obtenida de las medidas TES sobre la muestra con SI y de los MTR FR97, Mod3, Rmod3, 4SAIL, REN15 y CE-P para los siete ángulos de observación cenital y los seis valores LAI para el canal espectral de 10,2 – 11,0 µm del radiómetro CE312.

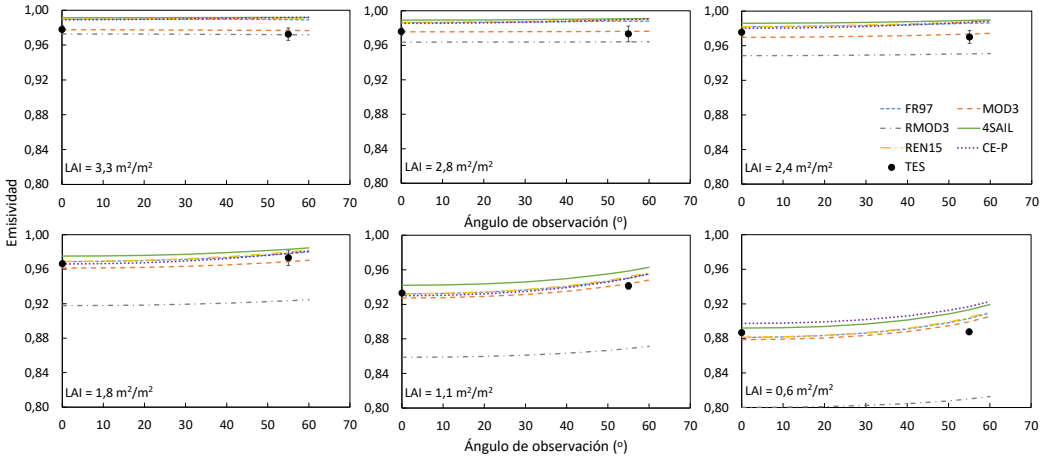

Figura 16. Emisividad obtenida de las medidas TES sobre la muestra con SI y de los MTR FR97, Mod3, Rmod3, 4SAIL, REN15 y CE-P para los siete ángulos de observación cenital y los seis valores LAI para el canal espectral de 9,0 – 9,3 µm del radiómetro CE312.

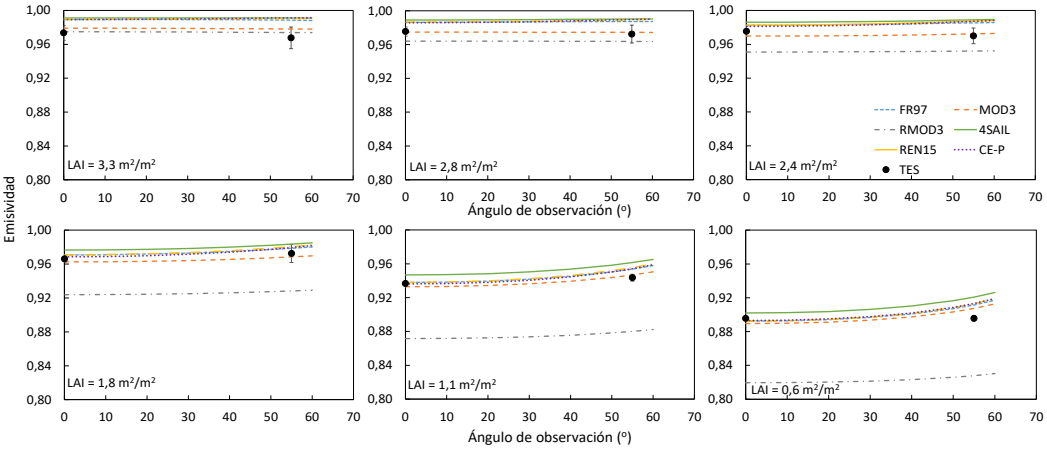

Figura 17. Emisividad obtenida de las medidas TES sobre la muestra con SI y de los MTR FR97, Mod3, Rmod3, 4SAIL, REN15 y CE-P para los siete ángulos de observación cenital y los seis valores LAI para el canal espectral de 8,5 – 8,9 µm del radiómetro CE312.

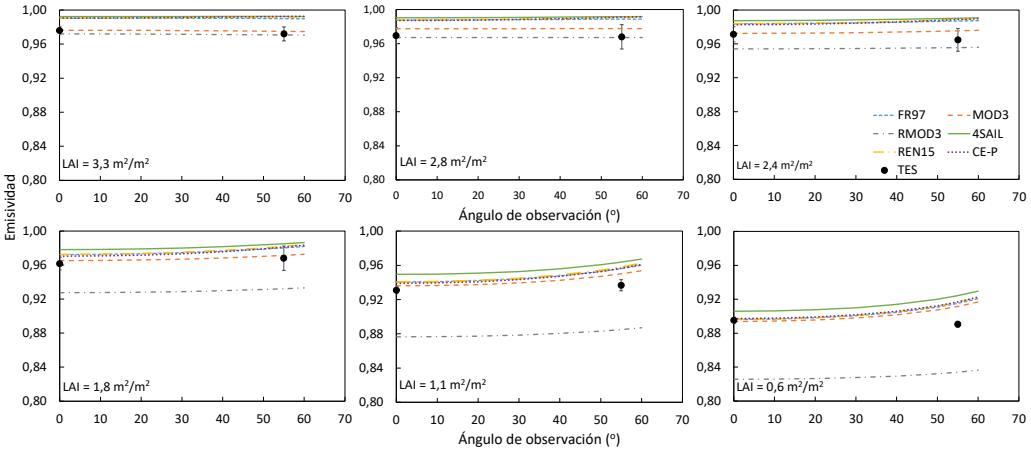

Figura 18. Emisividad obtenida de las medidas TES sobre la muestra con SI y de los MTR FR97, Mod3, Rmod3, 4SAIL, REN15 y CE-P para los siete ángulos de observación cenital y los seis valores LAI para el canal espectral de 8,3 – 8,6 µm del radiómetro CE312.

En las Figuras 14 y 15 los MTR tienen un comportamiento similar al observado para el SO, debido a que las emisividades de SI en la región espectral entre 10 – 12 µm son similares a las de SO. Sin embargo, se observan mayores diferencias en las Figuras 16 – 18, correspondientes a los canales en el intervalo espectral 8,0 – 9,5 µm, donde las diferencias entre las emisividades de ambos suelos utilizados en el estudio son más significativas. En estos canales, las diferencias entre FR97 y 4SAIL aumentan ligeramente comparando con las medidas sobre SO, pero con diferencias menores a 0,01. Los modelos Mod3 y Rmod3 siguen los mismos patrones que en las medidas de SO, entre los cuales aumentan las diferencias cuando el LAI disminuye. Estas diferencias entre Mod3 y Rmod3 llegan a ser de 0,08 para el valor de LAI más bajo.

Si comparamos la emisividad de vegetación de los MTR con la emisividad TES, los modelos FR97, 4SAIL, REN15 y CE-P sobreestiman la emisividad TES en la mayoría de casos. En contra de las observaciones realizadas con las medidas sobre la muestra con SO, el modelo Rmod3 es el que mejor se ajusta a la emisividad TES en los canales del intervalo espectral 10 – 12 µm. Sin embargo, este modelo es con diferencia el que más difiere de la emisividad TES en el intervalo espectral 8,0 – 9,5 µm para valores de LAI < 2 m^2/m^2. El modelo Mod3 es el que mejor se ajusta a los valores TES en el intervalo espectral 8,0 – 9,5 µm, pero además obtiene valores próximos a la emisividad TES en el

intervalo espectral 10 – 12 µm. La Tabla 8 muestra el sesgo y RMSE de la diferencia entre los MTR y la emisividad TES. Teniendo en cuenta todos los datos juntos, el modelo Mod3 es el que mejor resultados ofrece comparando con la emisividad TES, con un RMSE total de ±0,007. El modelo Rmod3, a pesar de obtener los mejores resultados para valores de LAI elevados, es el que peores resultados globales ofrece, debido al fuerte decrecimiento que tiene en la emisividad al reducir el LAI. En cuanto a los modelos FR97, 4SAIL, REN15 y CE-P, obtienen resultados similares entre ellos, pero con valores de RMSE superiores a los obtenidos con el modelo Mod3, siendo solamente similares para valores bajos de LAI.

Tabla 8. Análisis estadístico de la comparación entre la emisividad direccional de los MTR y las medidas TES a distintos ángulos de observación cenital para los distintos valores de LAI sobre la muestra de suelo inorgánico. Los estadísticos se han calculado para el conjunto de canales espectrales y los dos ángulos de observación.

LAI	FR97		MOD3		RMOD3		4SAIL		REN15		CE-P	
(m^2/m^2)	Sesgo	RMSE	Sesgo	RMSE	Sesgo	RMSE	Sesgo	RMSE	Sesgo	RMSE	Sesgo	RMSE
3,3	0,015	0,015	0,002	0,004	0,000	0,016	0,016	0,017	0,016	0,016	0,016	0,017
2,8	0,014	0,014	0,003	0,005	-0,004	0,015	0,016	0,017	0,015	0,015	0,015	0,016
2,4	0,013	0,014	0,002	0,005	-0,011	0,014	0,016	0,016	0,014	0,015	0,014	0,015
1,8	0,009	0,009	0,001	0,004	-0,026	0,010	0,013	0,013	0,010	0,011	0,009	0,010
1,1	0,011	0,013	0,006	0,009	-0,037	0,012	0,017	0,018	0,012	0,014	0,011	0,014
0,64	0,012	0,016	0,009	0,014	-0,042	0,012	0,018	0,021	0,012	0,017	0,013	0,017
Total	**0,012**	**0,014**	**0,004**	**0,007**	**-0,020**	**0,013**	**0,016**	**0,017**	**0,013**	**0,015**	**0,013**	**0,015**

Además de las medidas con el radiómetro CE312, se realizaron distintas medidas en el intervalo espectral entre 8 – 12 µm con el espectrómetro portable *Fourier Transform Infrared* (FT-IR) Modelo 102 de la casa *Desings & Prototypes Instruments* (Korb et al., 1996). El espectrómetro FT-IR permite obtener la emisividad direccional de la vegetación directamente con una resolución espectral de 4 cm^{-1} en frecuencia espectral. La metodología utilizada con este espectrómetro todavía debe ser refinada, pero las firmas espectrales medidas son de utilidad para comparar con los resultados obtenidos con el radiómetro CE312. Dicha metodología preliminar consiste en un método de suavizado de las líneas de emisión atmosféricas en un intervalo reducido del espectro para la obtención de la temperatura de la muestra a partir de una temperatura inicial aproximada. A partir de esta temperatura ajustada, se obtiene el espectro de emisividad de la muestra (Borel, 1998; Pérez-Planells et al., 2019a). En la Figura 19 se muestran los

espectros medidos para cuatro valores de LAI en los dos ángulos considerados sobre la muestra de rosales con el suelo inorgánico.

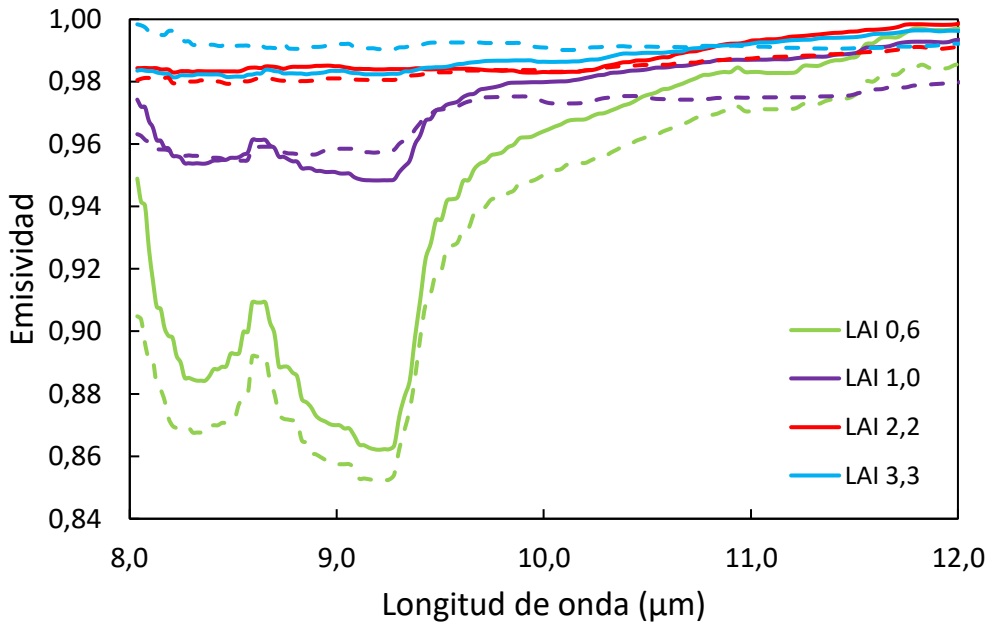

Figura 19. Emisividad de los rosales sobre el suelo inorgánico obtenida con el espectrómetro FT-IR con ángulo de observación cenital a nadir (línea continua) y a 55º (línea discontinua) para distintos valores de LAI.

Las medidas de emisividad con el espectrómetro FT-IR muestran una firma espectral similar a la observada con las emisividades TES obtenidas con el CE312. Para LAI = 0,6 m^2/m^2, podemos ver como se reproducen las curvas de absorción típicas del cuarzo presente en la arena utilizada centradas principalmente en 8,4 y 9,0 µm. A medida que aumenta el LAI, esta absorción deja de observarse, tendiendo a una firma espectral plana, típica de la vegetación. Esto ocurre para valores de LAI superiores a 1 m^2/m^2, aunque para LAI = 1,0 m^2/m^2 todavía observamos la absorción del cuarzo en el intervalo 8,0 – 9,5 µm, pero en menor medida. En estas medidas podemos observar como, para un LAI = 0,6 m^2/m^2 sí que parece haber una ligera disminución de la emisividad con el ángulo, que también puede observarse en las medidas TES de las Figuras 16 – 18, aunque estén dentro de los valores de la incertidumbre. En cambio, los MTR predicen un ligero aumento de la emisividad. Esta diferencia de comportamiento se debe a la caída de la emisividad existente con el ángulo en la muestra de SI (García-Santos et al.,

2012), la cual no se contempla en ninguno de los modelos. Sin embargo, debido al efecto de cavidad y a la disminución de la cantidad de suelo observada por el sensor, esta caída en emisividad con el ángulo deja de observarse para valores de LAI ≥ 1 m^2/m^2, obteniendo resultados muy similares para las dos observaciones angulares.

Capítulo 5

Aplicación de los modelos de emisividad a datos satelitales

En este capítulo los modelos de transferencia radiativa para la obtención de la emisividad se aplican con datos del sensor MODIS a bordo del satétlite EOS – Aqua sobre la Península Ibérica y se comparan con distintos productos de emisividad del sensor MODIS.

Para ello, se introducen los distintos productos de satélite utilizados como datos de entrada de los modelos, así como los productos de emisividad MYD11A1, MYD11B1 y MYD21A1 utilizados para la comparación.

Finalmente, se realiza la comparación de la emisividad obtenida con los distintos modelos de emisividad con los productos de emisividad MODIS sobre la zona de validación Cortes de Pallás (Valencia). Además, se compara la emisividad obtenida con los modelos con la emisividad obtenida con el producto MYD21A1 para las distintas clases de superficies vegetadas según la clasificación IGBP en la Península Ibérica.

5.1. Metodología

Los MTR para la obtención de la emisividad direccional evaluados en la sección anterior han sido utilizados para la generación de mapas de emisividad sobre la Península Ibérica. El modelo Rmod3 no se ha utilizado en esta aplicación debido a que en la evaluación previa se observaron grandes discrepancias con los otros modelos y con las medidas TES, especialmente para valores de LAI bajos. Además, este modelo conlleva un mayor coste computacional respecto a los otros modelos debido a la necesidad de calcular previamente la P_v para cada píxel de la imagen.

5.1.1. Parámetros de entrada

Para generar los mapas de emisividad direccional de la cubierta vegetal, es necesario hacer uso de productos de satélite existentes que nos permitan obtener los parámetros de entrada requeridos: emisividad de suelo y hoja, LAI y ángulo de observación. En este estudio, los mapas fueron generados para el sensor MODIS a bordo del satélite EOS – Aqua (Barnes et al., 1998), el cual tiene un periodo de revisita diario con una pasada por el día y otra por la noche. La resolución espacial nominal en el IRT es de 1 km y el ángulo de observación máximo del sensor es de 65º.

Para la obtención de los parámetros necesarios, se han utilizado distintos productos del sensor MODIS: producto de LAI a 8 días MCD15A2H (Myneni et al., 1999), producto anual de tipo de cobertura de superficie MCD12Q1 (Strahler et al., 1999), producto diario para día y noche de separación temperatura y emisividad MYD21A1D/N (Hulley et al., 2016b). Este último ha sido utilizado para obtener el ángulo de observación de cada píxel de la imagen, ya que el producto de geolocalización MYD03, el cual proporciona los datos geométricos de la medida realizada por el sensor MODIS, no está disponible en la proyección sinusoidal de MODIS. Estos productos han sido descargados con la herramienta web AppEEARS (https://lpdaacsvc.cr.usgs.gov/appeears/). Esta herramienta nos permite descargar datos del sensor MODIS de nivel 3 para un recorte entre las coordenadas seleccionadas y reproyectado a la proyección geográfica con elipsoide WGS84 y datum WGS84 (EPGS: 4326). Además, hemos hecho uso del mapa

mundial de taxonomía de suelo generado por el proyecto '*SoilGrids*' haciendo uso de los datos del Servicio de Información Mundial de Suelo (WoSIS, por sus siglas en inglés) y gestionado por el Centro Internacional de Referencia de Suelo e Información (ISRIC), basado en la clasificación de taxonomía de suelos del Departamento de Agricultura de Estados Unidos (USDA) (Batjes et al., 2017, 2020).

Producto MODIS MCD12Q1

El producto de tipo de cobertura de la superficie terrestre generado con datos del sensor MODIS a bordo de los satélites EOS – Aqua y Terra (MODIS MCD12Q1, Strahler et al., 1999) se genera anualmente desde 2001. En la versión más reciente de este producto (Colección 6), ofrecen distintos tipos de clasificaciones. En este estudio, se ha utilizado la clasificación basada en las coberturas definidas por el '*International Geosphere-Biosphere Programme*' (IGBP) por ser la más utilizada y conocida. La clasificación IGBP distingue entre 17 tipos de coberturas distintas, incluyendo distintos tipos de vegetación, superficie urbana, suelo sin vegetación, extensiones de nieve y hielo permanente y masas de agua (Loveland y Belward, 1997). A partir de la validación cruzada con los datos de entrenamiento del modelo de clasificación, Sulla-Menashe et al. (2019) obtienen una precisión del algoritmo de clasificación utilizado en la Colección 6 del 67%. El producto MCD12Q1 proporciona la clasificación de suelos IGBP en la proyección sinusoidal de MODIS con una resolución espacial de 500 m. En la Figura 20 se muestra el mapa de la Península Ibérica con la clasificación de tipo de cobertura de la superficie generado con los datos del producto MCD12Q1 del año 2015 utilizado en este estudio.

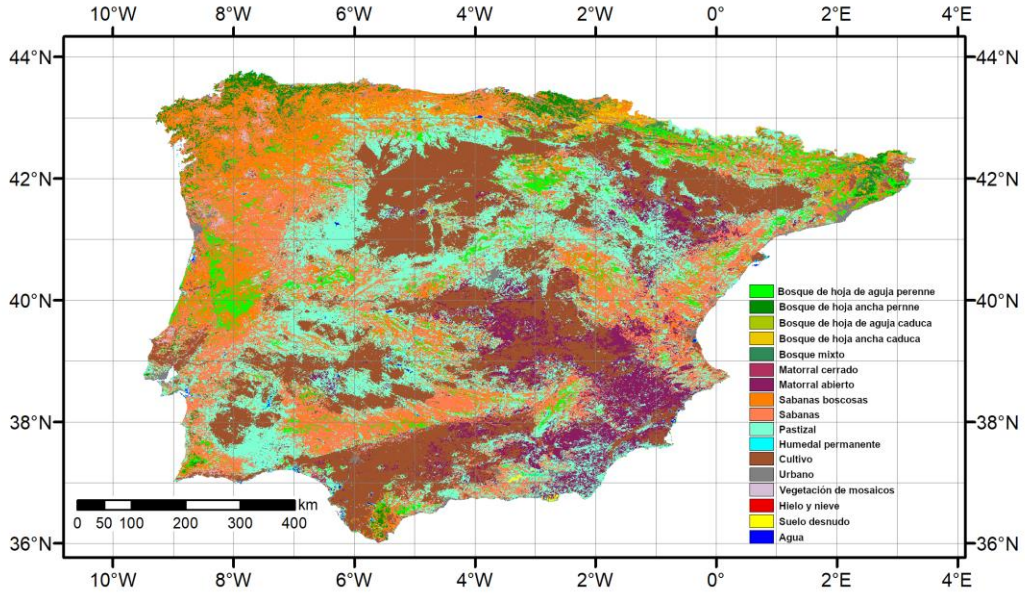

Figura 20. Mapa de tipo de cobertura de superficie del producto MODIS MCD12Q1 para el año 2015.

Producto MODIS MCD15A2H

El producto de LAI MCD15A2H (Myneni et al., 1999) es generado con datos del sensor MODIS a bordo de los satélites EOS – Aqua y Terra con una resolución temporal de 8 días. El algoritmo utilizado para obtener el LAI de este producto consiste en la aplicación de valores tabulados que relacionan el índice de diferencia normalizada de vegetación (NDVI, por sus siglas en inglés) con el LAI para distintos tipos de vegetación relacionados con los existentes en la clasificación de cobertura de superficie: hierbas, matorrales, cultivos de hoja ancha, sabana y bosques de hoja caduca/perenne y de hoja ancha/de aguja. Estas tablas son generadas haciendo uso de MTR 3D para los distintos tipos de vegetación considerados. Este producto también es ofrecido con una resolución espacial de 500 m y en la proyección sinusoidal de MODIS. La Figura 21 muestra el LAI de la Península Ibérica obtenido con el producto MCD15A2H el día 8 de julio de 2015.

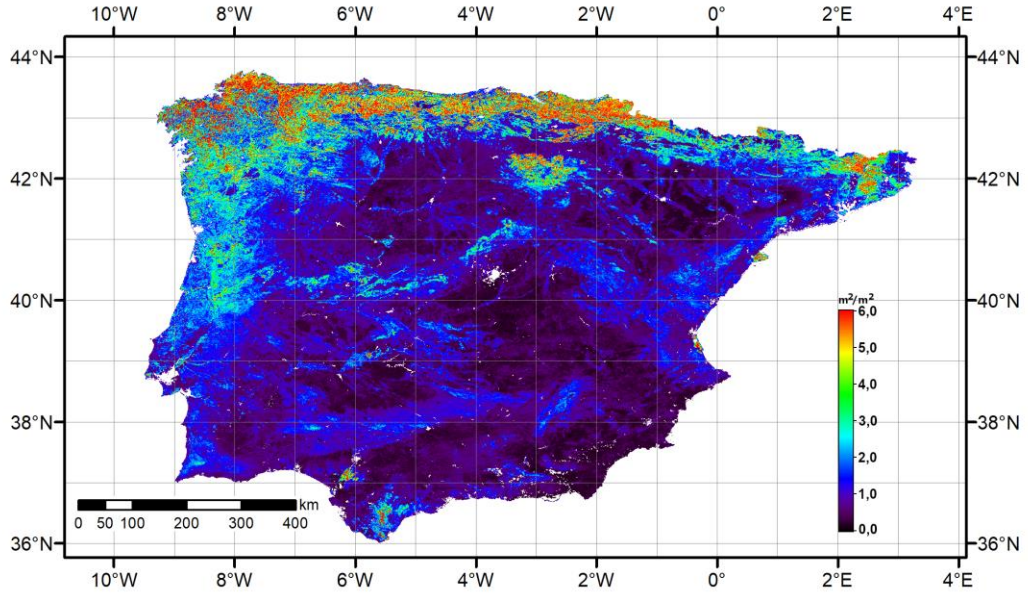

Figura 21. Mapa de LAI del producto MCD15A2H correspondiente al día 10 de julio de 2015 para la Península Ibérica.

Mapa mundial de taxonomía de suelo USDA – ISRIC

El proyecto *SoilGrids* ofrece a través de ISRIC mapas mundiales de distintas componentes del suelo, generadas a partir de datos recopilados por WoSIS y medidos por distintas entidades mundiales (Batjes et al., 2020). La recopilación, así como la generación de mapas, es un proyecto iniciado en 2016 (Batjes et al., 2017) y, a día de hoy, todavía en desarrollo. Sin embargo, la gran cantidad de datos disponibles permiten hacer uso de esta información. Además, Batjes et al. (2020) indican que los espacios donde no existen datos serán medidos en los próximos años, completando así la información en toda la extensión de la superficie terrestre. Además, se añadirá información respecto a las incertidumbres asociadas a los datos ofrecidos (Batjes et al., 2020). La generación de estos mapas se realiza mediante técnicas de 'Machine Learning' con los datos *in-situ* disponibles en la base de datos de WoSIS (https://www.isric.org/explore/soilgrids). Entre las distintas propiedades de suelo que se ofrecen, se encuentra la taxonomía de suelo según la clasificación USDA. Esta clasificación viene dada para los 12 órdenes principales: geolisol, histosol, spodosol, andisol, oxisol, vertisol, aridisol, ultisol, molisol, alfisol, inceptisol y entisol. También se

incluyen las clases de subórdenes correspondientes a cada orden principal, aunque en este estudio se han utilizado únicamente los órdenes principales por disponer de mayor estadística en los datos de emisividad a asociar a cada clase.

Estos mapas son generados a una resolución espacial de 250 m en la proyección geográfica con elipsoide WGS84 y datum WGS84 (EPGS: 4326). En la Figura 22 se muestra el mapa de clasificación de suelos según la taxonomía USDA para la Península Ibérica utilizado en este estudio. Este mapa se redimensionó a una resolución espacial de 500 m una vez asignada la emisividad a cada orden de taxonomía (ver Sección 5.1.2.), es decir, el redimensionado fue realizado en términos de emisividad. Finalmente, para la comparación directa con el producto MYD21A1, los mapas generados fueron nuevamente redimensionados a una resolución de 1 km.

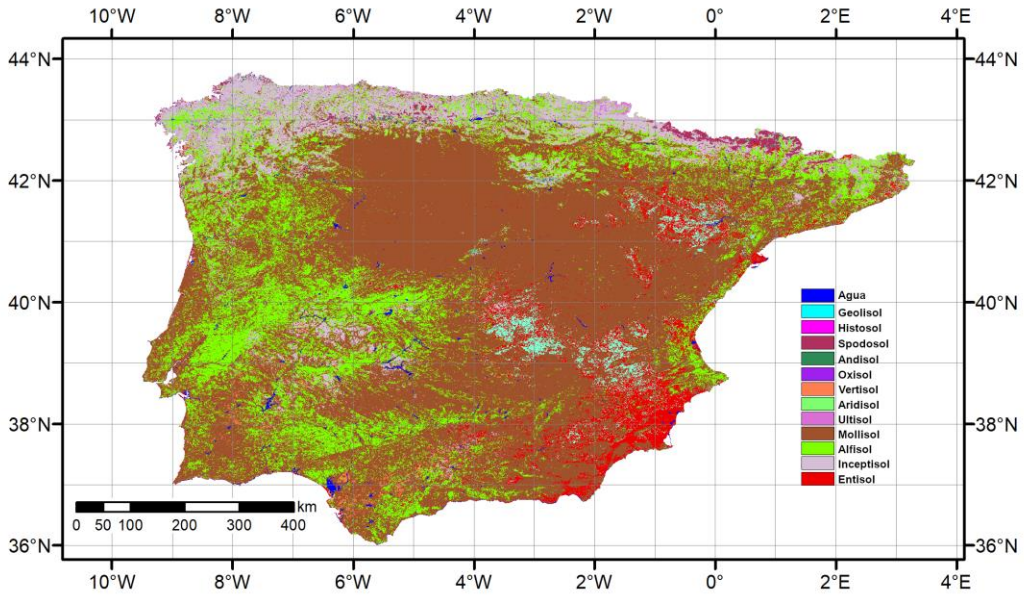

Figura 22. Mapa de la clasificación de tipo de suelo según la taxonomía USDA para la Península Ibérica ofrecida por ISRIC.

5.1.2. Selección de emisividades de suelo y vegetación

Los espectros de emisividad utilizados para la asignación de emisividad de entrada de suelo y hoja fueron obtenidos de la librería espectral ECOSTRESS (Baldridge et al., 2009; Meerdink et al., 2019). Esta librería espectral cuenta con más de 3000 espectros

medidos en laboratorio en el intervalo espectral entre 0,35 – 15,4 µm, incluyendo minerales, rocas, meteoritos, suelos terrestres y lunares, vegetación, vegetación no fotosintética, nieve, hielo, agua y materiales construidos (Meerdink et al., 2019). La librería ECOSTRESS incluye espectros de otras librerías espectrales: *John Hopkins University*, *Jet Propulsion Laboratory* y *United States Geolocogical Survey*. Para seleccionar las emisividades necesarias en este trabajo, los espectros de emisividad fueron convolucionados con la función de respuesta espectral de los canales del IRT del sensor MODIS centradas en 8,55 µm, 11,03 µm y 12,02 µm, correspondientes a los canales 29, 31 y 32, respectivamente.

Selección de emisividad de suelo

En el caso de la emisividad de suelo, se utilizaron 52 muestras de la librería ECOSTRESS identificadas con la taxonomía USDA. A pesar de que en la clasificación ISRIC de taxonomía USDA existen 12 tipos de suelo, en la librería ECOSTRESS tan solo 8 están caracterizados. Para calcular la emisividad de cada clase, se calculó el promedio de cada una de las muestras y se aplicó un filtro de una desviación estándar (±σ) para las clases con más de 3 muestras, ya que se observaron grandes diferencias entre estas. De esta manera, se usaron 35 muestras para calcular la emisividad de los 8 tipos de suelos. La emisividad obtenida para cada canal del IRT de MODIS se muestra en la Tabla 9.

Tabla 9. Emisividad de suelo (ε_s) calculada para cada tipo de taxonomía USDA y la desviación estándar (σ) obtenida con el número de muestras (N). Además, se muestra el porcentaje de píxeles que corresponden a cada tipo de suelo en la Península Ibérica.

Tipo de suelo	8,55 µm		11,03 µm		12,02 µm		N	% pixeles
	ε_s	σ	ε_s	σ	ε_s	σ		
Alfisol	0,912	0,017	0,967	0,002	0,978	0,002	5	22,3
Aridisol	0,939	0,014	0,969	0,002	0,975	0,003	9	2,9
Entisol	0,921	0,032	0,972	0,003	0,981	0,001	6	10,9
Inceptisol	0,951	0,003	0,969	0,003	0,979	0,002	4	10,9
Mollisol	0,954	0,015	0,973	0,002	0,979	0,001	7	48,2
Spodosol	0,982	-	0,969	-	0,972	-	1	1,4
Ultisol	0,848	-	0,964	-	0,981	-	1	2,6
Vertisol	0,938	-	0,974	-	0,981	-	1	0,6
Otros	0,934	0,029	0,970	0,003	0,978	0,003	35	0,2

Para los cuatro tipos de suelo no caracterizados, se realizó el promedio de todas las muestras. Las muestras no caracterizadas suponen el 0,2 % de la Península Ibérica, por lo que no tienen un gran impacto sobre los resultados generales. En cambio, el tipo de suelo más representativo en la Península Ibérica, según la clasificación de ISRIC es el suelo de tipo Mollisol, con un 48,2 %. En la Figura 23 se muestran los mapas de emisividad de suelo para cada canal espectral de MODIS utilizados como emisividad de suelo de entrada para la aplicación de los MTR.

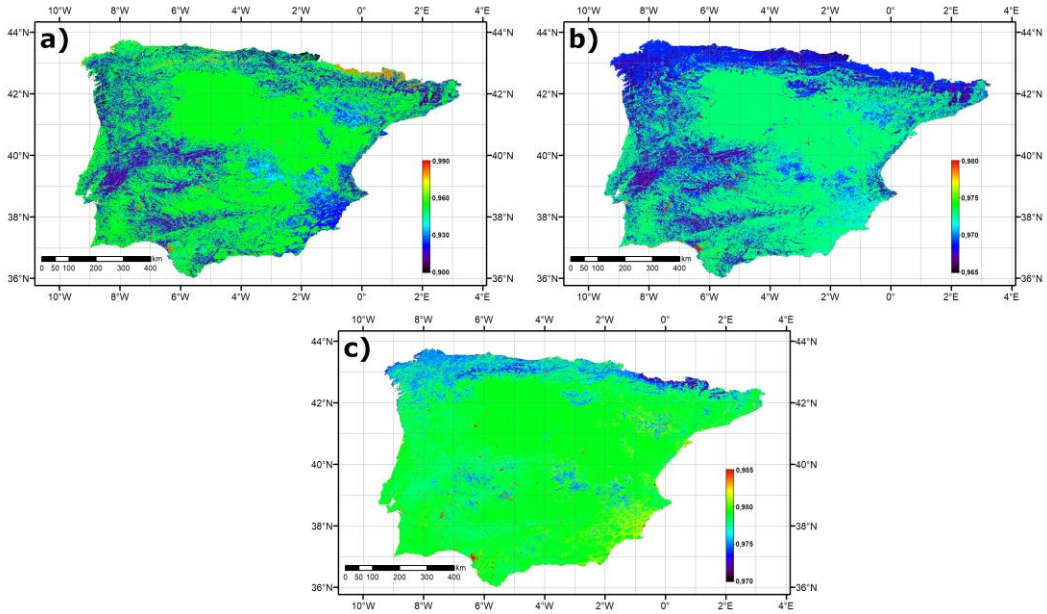

Figura 23. Emisividad de suelo para la aplicación de los MTR para los canales espectrales de MODIS centrados en 8,55 µm (a), 11,03 µm (b) y 12,02 µm (c) obtenida a partir de la clasificación de suelo ISRIC de taxonomía USDA sobre la Península Ibérica.

Selección de emisividad de hoja

Para la selección de emisividad de hojas, se ha hecho uso de los espectros de emisividad de vegetación de la librería ECOSTRESS y se han añadido los espectros de hierba verde y hierba seca de la librería espectral ASTER, los cuales no están incluidos en la librería ECOSTRESS.

De los espectros de emisividad disponibles, se consideraron tres clases: árbol, matorral y hierba. Para la clase árbol, se encontraron 264 muestras divididas en 52 subclases. Para la clase matorral, se encontraron 204 muestras divididas en 13 subclases. Y para la

clase hierba se encontraron seis muestras en un total de 4 subclases. Las muestras de árbol se utilizaron para obtener la emisividad de las clases bosque de la clasificación IGBP (clases 1 – 5, 8 y 9 de la Tabla 10) y las de matorral para las clases IGBP 6 y 7 de matorral. En el caso de dichas clases se aplicó el mismo filtrado que para las muestras de suelo, consistente en $\pm\sigma$, al realizar el promedio entre los valores de las subclases. Además, para obtener las emisividades de hoja para cada clase IGBP se han realizado las siguientes consideraciones: no se han considerado diferencias en la emisividad de los distintos tipos de bosque ya que la emisividad observada para las distintas hojas es similar, y la diferencia entre bosque de hoja caduca y hoja perenne debe observarse en el LAI. Por su definición (las definiciones de las clases IGBP están incluidas en el Anexo B), la emisividad de la clase sabanas se ha considerado igual que la clase bosque, esperando observar la diferencia en el valor del LAI. Mientras que para la clase pastizal se ha excluido la clase de hierba seca, para cultivo se han incluido todas las clases de hierba. En el caso de la clase humedal permanente, tan solo se ha considerado el espectro de hierba verde, ya que la vegetación sobre un humedal va a tener una alta emisividad. La clase vegetación de mosaicos, por su definición, se obtuvo como el promedio entre las clases bosque, matorral, pastizal y cultivo. Para la clase de suelo sin vegetación, se asignó la emisividad de hierba seca por la posibilidad de observar restos de vegetación en algunos casos. Finalmente, se consideró las muestras de hielo y nieve para el caso de los píxeles clasificados como nieve y el agua de grifo como representación de agua dulce para la clase de masas de agua, aunque no existe diferencia significativa en el IRT respecto del agua de mar. En este último caso, la emisividad asignada es atribuida al píxel sin aplicar un MTR para la obtención de la emisividad, ya que no contiene vegetación. Sin embargo, se puede obtener la emisividad direccional del agua utilizando el modelo propuesto por Niclòs et al. (2009) para el sensor MODIS. De esta manera, se obtuvo la emisividad para cada clase de la clasificación de tipos de cobertura de MODIS en cada uno de los tres canales del IRT. La emisividad obtenida y la σ de las muestras utilizadas se muestra en la Tabla 10. La Figura 24 muestra los mapas de emisividad de hoja generados para la aplicación de los MTR para los canales del sensor MODIS centrados en 8,55 μm, 11,03 μm y 12,02 μm.

Tabla 10. Emisividad de hoja (ε_v) calculada para cada clase de la clasificación MODIS de tipos de cobertura IGBP.

	Tipo de cobertura IGBP	8,55 µm		11,03 µm		12,02 µm	
		ε_v	σ	ε_v	σ	ε_v	σ
1	Bosque de hoja de aguja perenne	0,958	0,020	0,958	0,019	0,961	0,020
2	Bosque de hoja ancha perenne	0,958	0,020	0,958	0,019	0,961	0,020
3	Bosque de hoja de aguja caduca	0,958	0,020	0,958	0,019	0,961	0,020
4	Bosque de hoja ancha caduca	0,958	0,020	0,958	0,019	0,961	0,020
5	Bosque mixto	0,958	0,020	0,958	0,019	0,961	0,020
6	Matorral cerrado	0,956	0,012	0,952	0,014	0,954	0,012
7	Matorral abierto	0,956	0,012	0,952	0,014	0,954	0,012
8	Sabanas boscosas	0,958	0,020	0,958	0,019	0,961	0,020
9	Sabanas	0,958	0,020	0,958	0,019	0,961	0,020
10	Pastizal	0,983	0,002	0,975	0,008	0,980	0,008
11	Humedal permanente	0,985	0,000	0,984	0,000	0,989	0,000
12	Cultivo	0,980	0,007	0,96	0,03	0,96	0,03
13	Urbano	-	-	-	-	-	-
14	Vegetación de mosaicos	0,971	0,014	0,967	0,010	0,971	0,011
15	Hielo y nieve	0,993	0,003	0,992	0,004	0,984	0,007
16	Suelo sin vegetación	0,970	-	0,910	-	0,915	-
17	Masas de agua	0,984	-	0,991	-	0,985	-

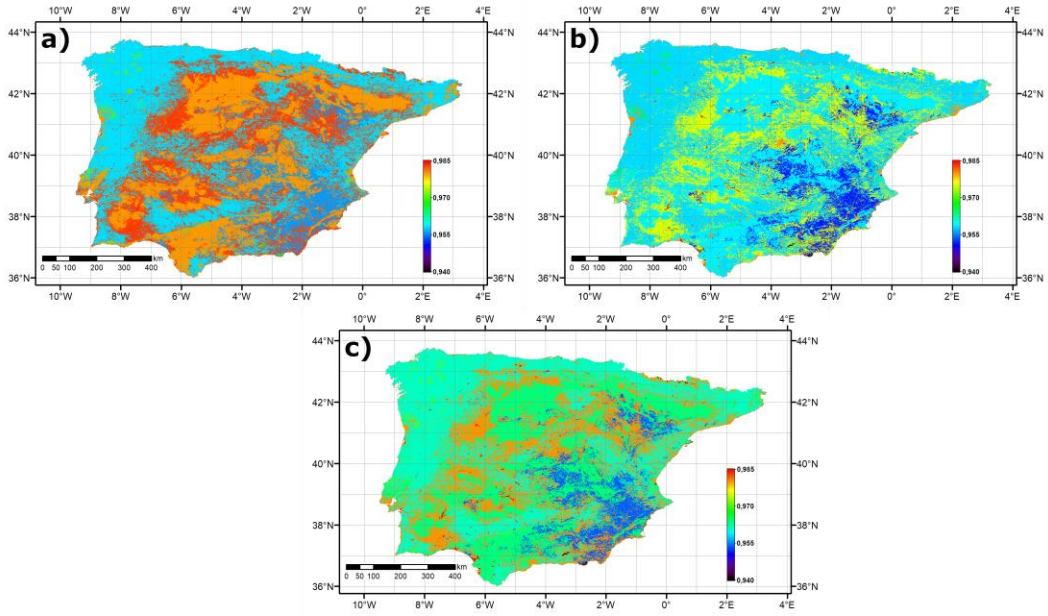

Figura 24. Emisividad de hoja para la aplicación de los MTR para los canales espectrales de MODIS centrados en 8,55 µm (a), 11,03 µm (b) y 12,02 µm (c) obtenida a partir del producto MODIS MCD12Q1 del año 2015 sobre la Península Ibérica.

5.2. Productos de emisividad MODIS

Existen tres productos operacionales del sensor MODIS que ofrecen valores de emisividad para cada píxel. Cada uno de estos productos obtiene la emisividad a partir de un algoritmo diferente. Estos productos, los cuales han sido comparados con los valores de emisividad obtenidos haciendo uso de los MTR, son el producto MXD11A, MXD11B y MXD21; MXD siendo MOD (MYD) en el caso de los productos obtenidos a partir de los datos del sensor MODIS a bordo del satélite EOS – Terra (Aqua).

5.2.1.MXD11A1

El producto de TST MXD11A1 (Wan, 1999) ofrece valores de TST de la pasada orbital diurna y nocturna y la emisividad en los canales MODIS centrados en 11,03 µm y 12,02 µm (canales 31 y 32, respectivamente). El producto MXD11A1 es de nivel 3, generado con una rejilla de coordenadas en proyección sinusoidal con una resolución espacial de 1 km. El valor para cada píxel es generado a partir del promedio de los píxeles del producto de TST MXD11_L2 (adquirido de acuerdo con la anchura de barrido a lo largo de la órbita) que forman parte de cada píxel de la rejilla de coordenadas creada. El producto MXD11_L2 obtiene la TST aplicando un algoritmo *split-window* (Wan y Dozier, 1996; Wan, 2014). Para la aplicación de este algoritmo hace uso de la emisividad de los canales 31 y 32, ofrecidas también en el producto, y que son obtenidas mediante el método basado en la clasificación de la cobertura de superficie definido por Snyder et al. (1998).

La emisividad utilizada en el producto MXD11_L2 se obtiene haciendo uso de los distintos modelos BRDF (Snyder y Wan, 1998) en función del tipo de cobertura de superficie de la clasificación de MODIS. Según la clase asignada, se hace uso del modelo BRDF geométrico, volumétrico o especular. Por lo tanto, para cada clase existe tabulada una emisividad, para cada canal en función del ángulo de observación, obtenida aplicando el modelo BRDF correspondiente. Las emisividades de entrada fueron seleccionadas para cada clase, haciendo uso de 14 espectros considerados representativos de las hojas y del suelo.

5.2.2.MXD11B1 – IREMIS

El producto de TST y emisividad MXD11B1 (Wan, 1999) es generado haciendo uso del algoritmo día/noche a partir de las radiancias obtenidas de la pasada diurna y nocturna del sensor MODIS en un mismo día sobre una zona (Wan y Li, 1997). Este producto se genera en nivel 3, a partir de la construcción de una rejilla de coordenadas con proyección sinusoidal de MODIS con una resolución espacial de 5,6 km en la actual Colección 6. A partir del par de medidas día/noche, se obtiene la TST de la pasada diurna y nocturna, así como la emisividad para 6 canales espectrales del IRT del sensor MODIS (canales 20, 22, 23, 29, 31 y 32), asumiendo una misma emisividad día y noche.

La Universidad de Wisconsin ofrece el producto global de emisividad IREMIS. Este producto es generado para valores mensuales de emisividad de la superficie terrestre, en la resolución espacial de 5 km a partir de datos de la colección 4.1 del producto MOD11B2 (promedio mensual del producto MOD11B1). Además, este producto completa los canales espectrales para los que el producto MOD11B2 no ofrece valores de emisividad, mediante la aplicación del método de ajuste de referencia (Seemann et al., 2008). Este método consiste en la obtención de la emisividad de los canales MODIS centrados en el intervalo espectral 4,4 – 7,5 µm y el canal centrado en 9,7 µm mediante ajustes lineales realizados haciendo uso de la emisividad obtenida con el producto MOD11B2 y de la emisividad de un conjunto de 123 espectros obtenidos de la librería espectral de la Universidad de California en Santa Bárbara. Por ello, la mayor relevancia de este producto, aunque en este estudio no tiene efecto, es la obtención de la emisividad para los diez canales del IRT del sensor MODIS.

5.2.3.MXD21 (MODTES)

El producto MXD21, nombrado como MODTES (Hulley et al., 2016b), aplica el método TES definido en la Sección 3.2 utilizando datos del sensor MODIS. Para la generación de este producto, es necesario realizar la corrección atmosférica a los datos tomados por el sensor para obtener las radiancias a nivel de superficie. La corrección atmosférica se realiza a partir del modelo de transferencia radiativa RTTOV, el cual precisa de distintos

perfiles atmosféricos como datos de entrada: altura, presión, temperatura del aire y humedad específica. Estos perfiles atmosféricos pueden obtenerse a partir de datos de sensores satelitales como MODIS, o a partir de la interpolación espacial y temporal de datos de reanálisis, como el producto *Global Data Asimilation System* (GDAS) generado por el *National Centers for Environmental Prediction* (NCEP) (Kalnay et al., 1990) o el producto *Modern ERA Retrospective-analysis for Research and Application* (MERRA) generado por el *Goddard Earth Observing System* (GEOS) (Bosilovich et al., 2008). Para generar el producto MXD21, inicialmente se utiliza el producto GDAS-NCEP, ya que es producido diariamente, y posteriormente se reprocesan las imágenes haciendo uso del producto MERRA-2. Tanto el producto NCEP como el MERRA-2 se generan cada 6 horas, pero la resolución espacial de NCEP es de 1^o x 1^o mientras que la de MERRA-2 es de $0,5^o$ x $0,625^o$.

En Pérez-Planells et al. (2015) (ver Anexo E) analizamos la precisión de los datos de reanálisis NCEP y los perfiles obtenidos mediante el producto MOD07 de MODIS frente a datos ofrecidos por la Universidad de Wyoming (WYO) de radiosondeos lanzados *in-situ* en tres zonas con distinta altitud: Murcia (62 m sobre el nivel del mar, s.n.m.), Zaragoza (264 m s.n.m.) y Madrid (611 m s.n.m.). Estos perfiles atmosféricos fueron utilizados para calcular los parámetros atmosféricos de radiancia ascendente, radiancia hemisférica descendente y transmisividad mediante su implementación en el modelo de transferencia radiativa MODTRAN5.2 (Berk et al., 2008) para los canales espectrales de MODIS centrados en 8,55 µm, 11,03 µm y 12,02 µm. Del análisis realizado concluimos que los datos obtenidos con los perfiles MOD07 obtenían una mayor dispersión en la comparación con los datos WYO, utilizados como referencia, además de un sesgo mayor que el obtenido con los datos NCEP. En cambio, los datos NCEP mostraron una buena correlación con los datos de referencia, con un coeficiente de correlación >0,9 en todos los casos. En la Figura 25 se muestra la comparación de los parámetros atmosféricos obtenidos con los perfiles NCEP frente a los parámetros atmosféricos obtenidos con los perfiles WYO para los tres canales MODIS y las tres zonas analizadas.

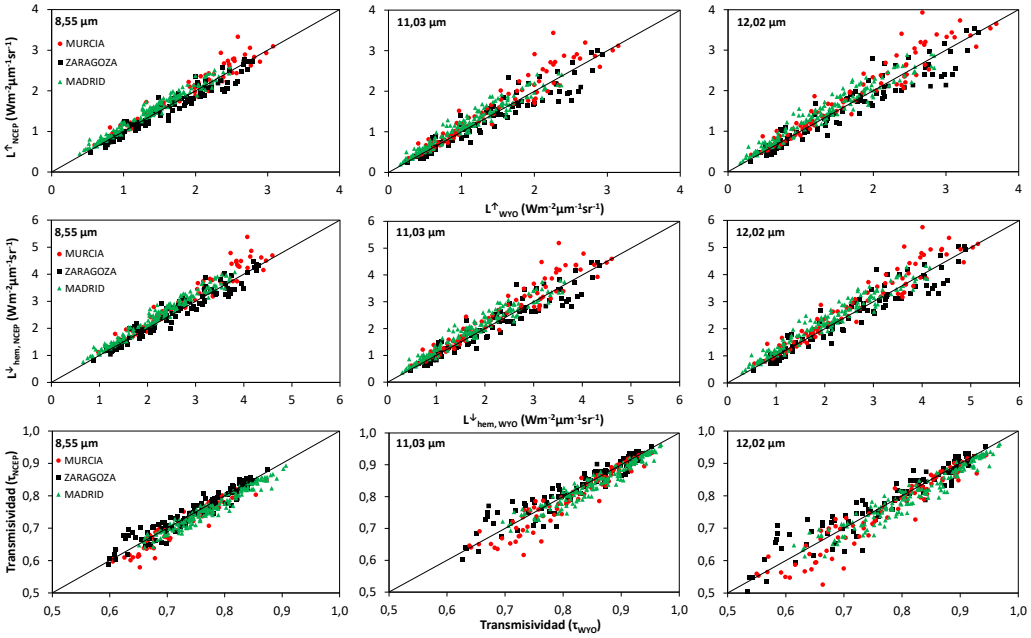

Figura 25. Radiancia ascendente ($L^{\uparrow}$), radiancia descendente hemisférica ($L^{\downarrow}_{hem}$) y transmisividad (τ) obtenida con los perfiles atmosféricos NCEP frente a la obtenida con los perfiles atmosféricos de WYO para los canales del sensor MODIS centrados en 8,55 µm, 11,03 µm y 12 µm. Los datos son mostrados para las tres zonas analizadas: Murcia (62 m s.n.m.), Zaragoza (264 m s.n.m.) y Madrid (611 m s.n.m.).

Además, en Pérez-Planells et al. (2015) realizamos un caso de simulación para analizar el efecto de los parámetros atmosféricos obtenidos con los perfiles NCEP y MOD07 en términos de temperatura, haciendo uso de estos parámetros para obtener la TST. De este análisis se concluyó que la TST obtenida a partir de los perfiles atmosféricos NCEP mostraba una mayor precisión que con los perfiles MOD07 respecto a la TST obtenida utilizando los perfiles de referencia, con valores de RMSE entre ±0,6 y ± 0,9 K según el canal de MODIS utilizado para la obtención de la TST y la zona de estudio. Mientras que la RMSE que se obtuvo con los perfiles del producto MOD07 fue entre ±1,2 K y ±3,0 K según el canal de MODIS y la zona de estudio.

Distintos autores observaron sobre datos del sensor ASTER que el método TES es muy sensible a los errores introducidos en la corrección atmosférica, especialmente sobre cuerpos grises, es decir, aquellos que tienen poco contraste espectral (Gustafson et al., 2006; Coll et al., 2007; Sabol et al., 2009; Gillespie et al., 2011). Para minimizar este efecto, Tonooka (2005) propuso el método de escalado de vapor de agua (WVS, por sus

siglas en inglés) para mejorar la precisión de los perfiles atmosféricos. Coll et al. (2016) observaron que, al aplicar esta corrección en imágenes MODIS sobre píxeles de vegetación con poco contraste espectral, la incertidumbre obtenida en la estimación de la TST respecto a medidas *in-situ* fue 1 K menor que en los casos en los que esta corrección no se realizó.

Igual que para los productos anteriores, en este trabajo se ha utilizado el producto de nivel 3 MYD21A1, el cual proporciona una imagen diurna y nocturna de la TST y la emisividad de los canales espectrales centrados en 8,55 µm, 11,03 µm y 12,02 µm. La imagen se genera para una rejilla de coordenadas con proyección sinusoidal de MODIS con resolución espacial de 1 km, a partir de los píxeles del producto MYD21_L2 que forman parte de cada píxel de la rejilla de coordenadas con proyección sinusoidal.

5.3. Comparación entre modelos y productos

La emisividad direccional obtenida con cada uno de los MTR para cada imagen diurna y nocturna del sensor MODIS – Aqua, ha sido comparada con los distintos productos de emisividad sobre la zona de validación de Cortes de Pallás (Valencia). Además, se ha comparado a nivel de imagen con el producto MYD21A1. En el Anexo C se detalla más información respecto a las imágenes de emisividad direccional generadas para la realización de este estudio.

5.3.1. Comparación sobre zona puntual: Cortes de Pallás

La zona de validación de Cortes de Pallás (39º 13’ 27” N, -0º 54’ 11” E) se encuentra situada en una planicie de ~200 km^2 a 800 m sobre el nivel del mar. Es una superficie de matorrales en la que predominan las especies de romero (*Rosmarinus oficinalis*), aliaga (*Ulex parviflorus*) y carrasca (*Quercus ilex*), con una fracción de cobertura vegetal aproximadamente constante a lo largo del año, con un valor aproximado de 0,5 en la visión a nadir (Niclòs et al., 2011, 2015). Niclòs et al. (2015) midieron la emisividad de las tres plantas predominantes y del suelo de la zona fue medido utilizando el método TES con radiómetros CE312. El promedio de la emisividad de las distintas especies y la emisividad del suelo se muestra en la Tabla 11 para los canales 29, 31 y 32 de MODIS.

Según la clasificación de tipos de cobertura del producto MODIS MCD12Q1, esta zona está clasificada como Sabanas (clase IGBP 9), mientras que en la clasificación ISRIC de tipos de suelo según la taxonomía USDA, este suelo pertenece a la orden mollisol. Estas clasificaciones determinan la emisividad de suelo y hoja asignada para la aplicación de los MTR, las cuales se muestran en la Tabla 11.

Tabla 11. Emisividad de la vegetación y suelo en la zona de Cortes de Pallás. MTR hace referencia a la emisividad de hoja y suelo utilizada para la aplicación de los MTR, asignadas a las clasificaciones. TES hace referencia a las medidas *in-situ* realizadas por Niclòs et al. (2015) sobre el suelo y las muestras de vegetación representativas de la zona.

	8,55 µm	**11,03 µm**	**12,02 µm**
$\varepsilon_{v,\,MTR}$	0,96 ± 0,02	0,958 ± 0,019	0,96 ± 0,02
$\varepsilon_{s,\,MTR}$	0,954 ± 0,015	0,973 ± 0,002	0,979 ± 0,001
$\varepsilon_{v,\,TES}$	0,966 ± 0,017	0,976 ± 0,012	0,978 ± 0,010
$\varepsilon_{s,\,TES}$	0,929 ± 0,015	0,952 ± 0,006	0,960 ± 0,006

La Tabla 11 muestra que la emisividad de hoja obtenida a partir de los espectros de la librería espectral ECOSTRESS y asignada en los MTR es menor que la emisividad de suelo para los canales de 11 y 12 µm, mientras que la emisividad medida con el método TES obtiene un valor mayor para la vegetación que para el suelo. Esto puede deberse al hecho de que las medidas TES están realizadas sobre la planta, midiendo así la emisividad del conjunto de vegetación, con un valor más elevado debido al efecto de cavidad. Los espectros de la librería espectral pertenecen a una hoja. En cuanto a los valores de la emisividad de suelo, las medidas TES obtienen valores de emisividad inferiores a los valores obtenidos a partir de la librería espectral, con una diferencia de 0,02.

Las Figuras 26 – 28 muestran la emisividad direccional obtenida por los cinco MTR y los cuatro productos de emisividad de MODIS para las fechas comprendidas entre marzo y septiembre de 2015 en la zona de validación de Cortes de Pallás.

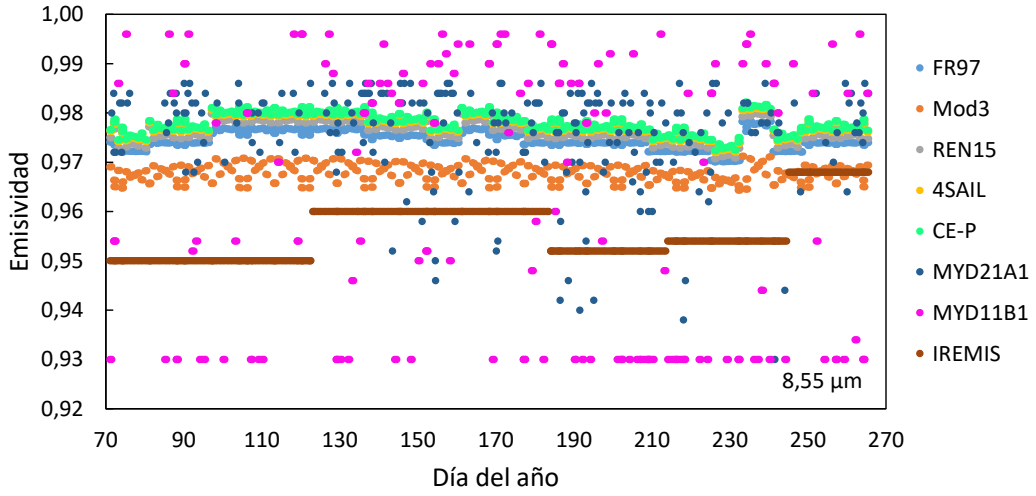

Figura 26. Emisividad del canal 29 de MODIS (8,55 µm) de la zona de validación de Cortes de Pallás. Se muestra la emisividad para los cinco MTR (FR97, Mod3, REN15, 4SAIL y CE-P), los tres productos de emisividad MODIS (MYD11A1, MYD11B1 y MYD21A1) y el producto de emisividad IREMIS.

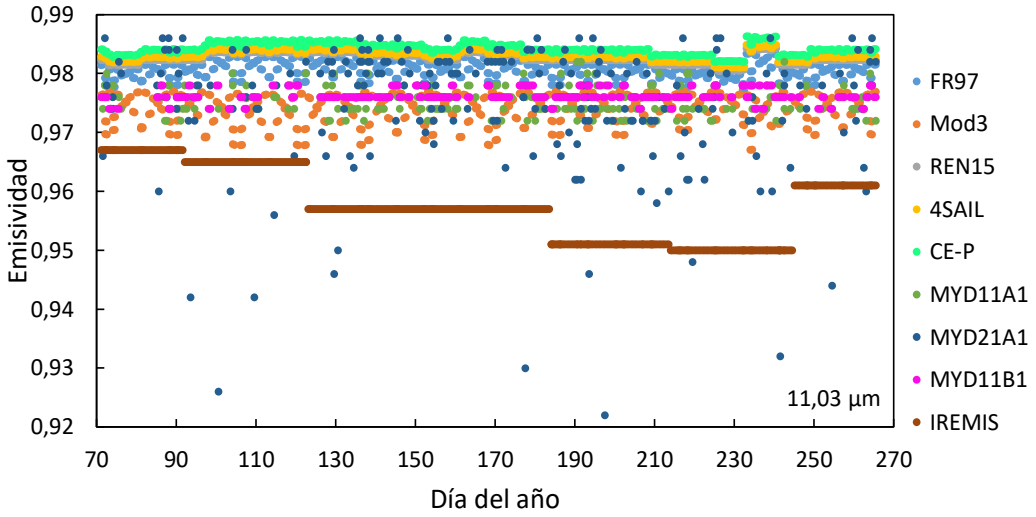

Figura 27. Emisividad del canal 31 de MODIS (11,03 µm) de la zona de validación de Cortes de Pallás. Se muestra la emisividad para los cinco MTR (FR97, Mod3, REN15, 4SAIL y CE-P), los tres productos de emisividad MODIS (MYD11A1, MYD11B1 y MYD21A1) y el producto de emisividad IREMIS.

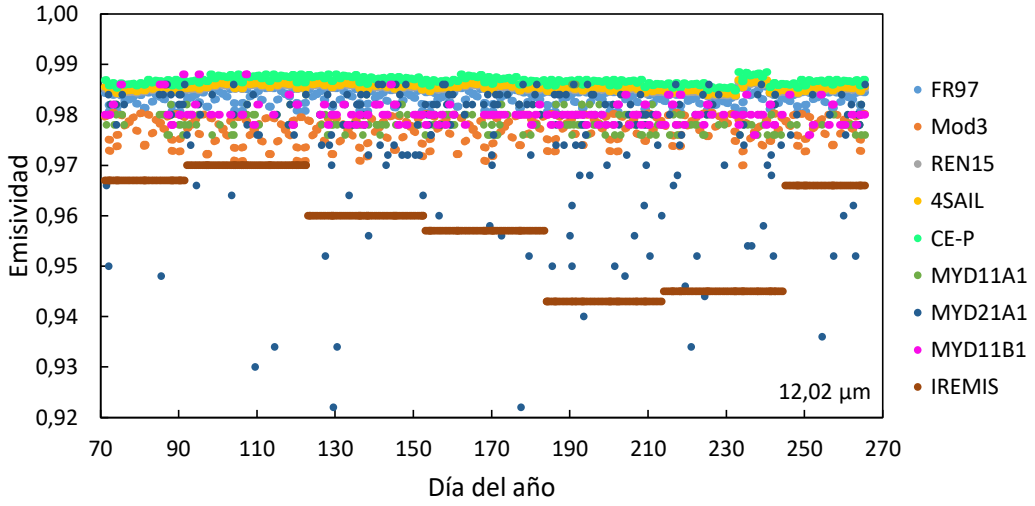

Figura 28. Emisividad del canal 32 de MODIS (12,02 µm) de la zona de validación de Cortes de Pallás. Se muestra la emisividad para los cinco MTR (FR97, Mod3, REN15, 4SAIL y CE-P), los tres productos de emisividad MODIS (MYD11A1, MYD11B1 y MYD21A1) y el producto de emisividad IREMIS.

En las Figuras 26 – 28, los valores de emisividad obtenidos por los MTR varían entre 0,965 y 0,986 según el canal espectral. Estos valores son más elevados en el caso de los MTR REN15, 4SAIL y CE-P, siendo este último el que obtiene la emisividad más alta. Los modelos FR97 y Mod3 muestran un mayor efecto de la variación del ángulo de observación por parte del satélite de la zona de estudio para con el día del año de acuerdo a su periodo de revisita. Ello conlleva a que en la evolución temporal de la emisividad de estos modelos se observa un patrón de una ligera oscilación en la emisividad.

En las Figuras 27 y 28, correspondientes a la emisividad de los canales de 11 y 12 µm, los productos MODIS MYD11A1 y MYD11B1 muestran unos valores de emisividad estables alrededor de 0,980. Sin embargo, el producto MYD21A1 muestra una mayor dispersión en los datos, posiblemente debido a la mayor sensibilidad a la corrección atmosférica del método TES con el que se obtiene dicho producto. Esta dispersión es mayor en la Figura 26, para la emisividad del canal centrado en 8,55 µm, ya que este canal tiene una mayor absorción atmosférica y, como consecuencia, un mayor impacto en los datos. Por este mismo motivo, la dispersión en los valores del producto MYD11B1 aumenta en la Figura 26. El producto de emisividad IREMIS muestra unos valores de

emisividad inferiores a los esperados, siendo considerablemente inferiores tanto a los productos MYD11/MYD21 como a los MTR.

Dado que la zona de estudio mantiene una cantidad de vegetación constante a lo largo del año, no se observa ninguna variación significativa en la emisividad en ninguno de los canales. Los valores de LAI obtenidos del producto MCD15A2H oscilan entre 0,6 m^2/m^2 y 1,0 m^2/m^2, por lo que estas diferencias no llevan a una variación en emisividad significativa.

5.3.2.Comparación sobre imágenes: Península Ibérica

Las imágenes de emisividad direccional generadas con los MTR para las imágenes de satélite MODIS han sido comparadas con la emisividad dada por el producto MODIS MYD21A1 sobre la Península Ibérica. En este caso no se han considerado otros productos para la comparación, como por ejemplo el producto MYD11A1, ya que el producto MYD21A1 se genera haciendo uso del método TES, el cual no depende de los parámetros de entrada utilizados en los MTR y, además, nos permite observar los posibles cambios que puedan tener lugar en la superficie terrestre (Hulley et al., 2014). En cambio, el producto MYD11A1 utiliza valores tabulados en función el tipo de cobertura obtenidos a partir de modelos BRDF, con parámetros de entrada similares a los utilizados en los MTR, por lo que no refleja los posibles cambios sobre la superficie terrestre. Para ello, se han seleccionado todos los píxeles del año 2015 clasificados como vegetación en la Península Ibérica y calificados como “libre de nubes” por la máscara de nubes del sensor MODIS. Las clases de vegetación han sido agrupadas según la clasificación IGBP del producto MCD12Q1 según: Bosque (IGBP 1 - 5), Matorral (IGBP 6 – 7), Sabana (IGBP 8 – 9), Pastizal (IGBP 10), humedal permanente (IGBP 11), Cultivo (IGBP 12) y vegetación de mosaicos (IGBP 14). Además, se ha añadido la clase de suelo sin vegetación (IGBP 16), ya que esta puede contener vegetación en ciertos periodos del año. La Figura 29 muestra los mapas de emisividad de vegetación obtenidos con los MTR FR97 y Mod3 para la pasada nocturna del sensor MODIS del día 10 de julio de 2019 y los canales de MODIS centrados en 8,55 µm, 11,03 µm y 12,02 µm. En la Figura 30 se

muestran las diferencias obtenidas entre el MTR FR97 y el MTR Mod3 mostrados en la Figura 29 con la emisividad producto MYD21 de cada canal.

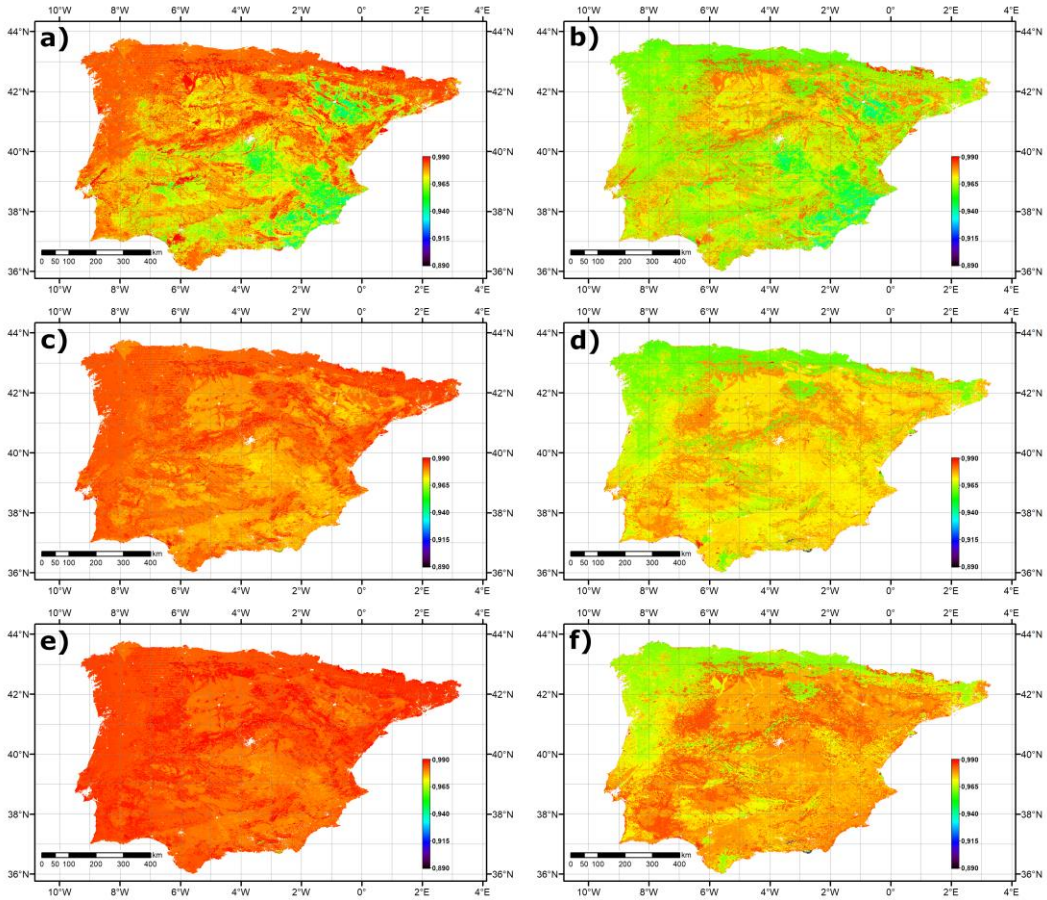

Figura 29. Emisividad obtenida con los MTR FR97 (a, c, e) y Mod3 (b, d, f) para los canales espectrales de MODIS centrados en 8,55 µm (a y b), 11,03 µm (c y d) y 12,02 µm (e, f) sobre la Península Ibérica para el día 10 de julio de 2015.

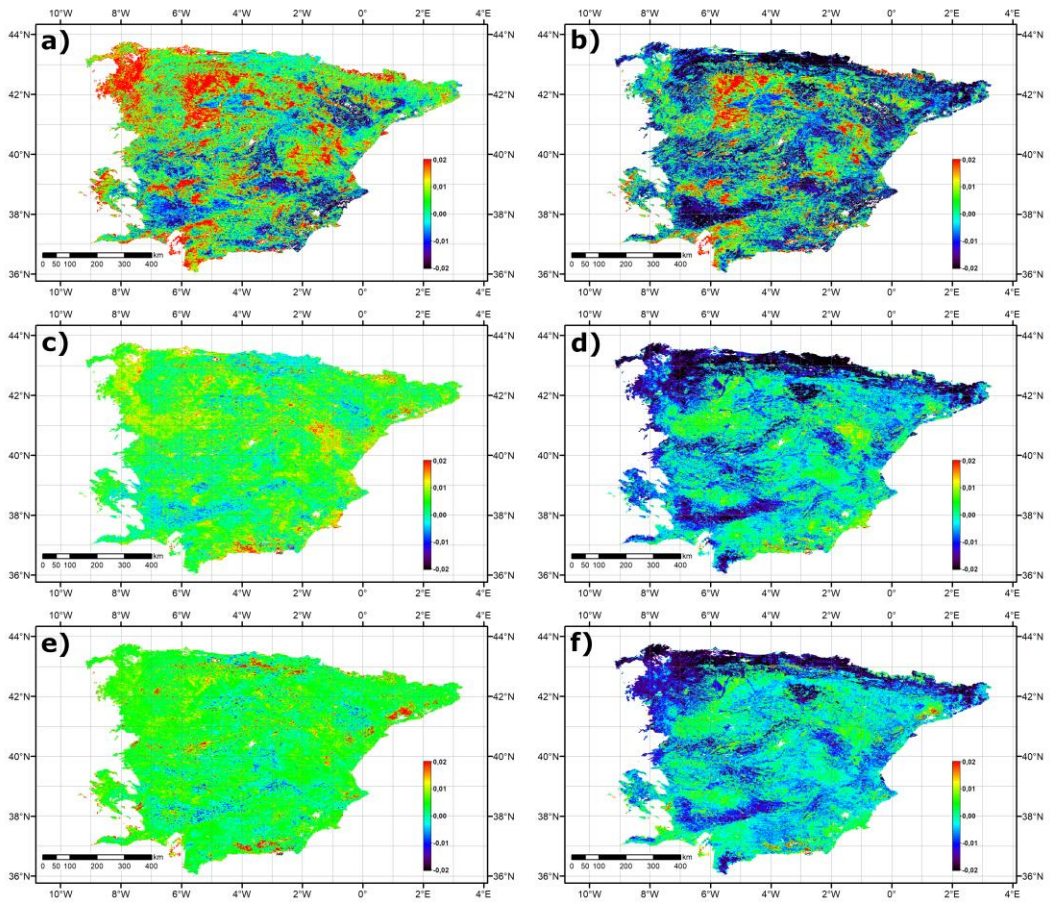

Figura 30. Diferencia entre la emisividad obtenida con los MTR FR97 (a, c, e) y Mod3 (b, d, f) y la emisividad del producto MYD21 para los canales espectrales de MODIS centrados en 8,55 µm (a y b), 11,03 µm (c y d) y 12,02 µm (e, f) sobre la Península Ibérica para el día 10 de julio de 2015.

Dada la cantidad de datos, se han utilizado los estadísticos robustos (Wilrich, 2007) para el análisis de la diferencia entre la emisividad direccional obtenida a partir de los MTR y del producto MYD21, ya que estos estadísticos minimizan el efecto de posibles valores atípicos en los datos. En los estadísticos robustos se considera la mediana de los datos, la desviación estándar robusta (RSD = mediana$|(T_{MTR}-T_{MYD21})_i$ - mediana$(T_{MTR}-T_{MYD21})_i|$ x 1,4826) y la raíz del error cuadrático medio robusto (R-RMSE) calculado como la raíz de la suma cuadrática de la mediana y la RSD. La mediana y la RSD representan el error sistemático y aleatorio, respectivamente, mientras que el R-RMSE representa la incertidumbre total de la variable observada respecto a la referencia considerada. La mediana y la RSD de las diferencias obtenidas de la comparación se muestran en las

Tablas 12 – 14 para los canales espectrales de MODIS centrados en 8,55 µm, 11,03 µm y 12,02 µm, respectivamente.

Tabla 12. Mediana y desviación estándar robusta (RSD) obtenidos de la diferencia entre la emisividad direccional obtenida con cada MTR y el producto MYD21A1 para el canal de 8,55 µm (canal 29) del sensor MODIS. Se muestran los estadísticos para dichas diferencias sobre cada tipo de cobertura vegetal y suelo sin vegetación en la Península Ibérica, así como para el conjunto global de los datos. El número total de datos utilizados en la comparación de cada clase es >10^4 para todas las clases.

	FR97		Mod3		REN15		4SAIL		CE-P	
	Mediana	RSD	Mediana	RSD	Mediana	RSD	Mediana	RSD	Mediana	RSD
Bosque	0,002	0,007	-0,015	0,006	0,004	0,007	0,005	0,006	0,005	0,007
Matorral	-0,011	0,017	-0,014	0,017	-0,010	0,018	-0,008	0,017	-0,008	0,017
Sabana	-0,002	0,009	-0,012	0,008	0,000	0,009	0,002	0,009	0,002	0,009
Pastizal	0,004	0,012	0,000	0,011	0,005	0,012	0,006	0,012	0,005	0,012
Humedal	0,005	0,012	0,002	0,011	0,006	0,012	0,007	0,012	0,006	0,012
Cultivo	0,005	0,018	0,002	0,016	0,005	0,018	0,007	0,018	0,006	0,018
Mosaico	0,007	0,010	-0,002	0,010	0,009	0,010	0,010	0,010	0,010	0,010
Suelo sin vegetación	0,03	0,03	0,03	0,03	0,03	0,03	0,03	0,03	0,03	0,03
Global	**0,002**	**0,014**	**-0,003**	**0,015**	**0,003**	**0,014**	**0,004**	**0,014**	**0,004**	**0,014**

Tabla 13. Mediana y desviación estándar robusta (RSD) obtenidos de la diferencia entre la emisividad direccional con cada MTR y el producto MYD21A1 para el canal de 11 µm (canal 31) del sensor MODIS. Se muestran los estadísticos para dichas diferencias sobre cada tipo de cobertura vegetal y suelo sin vegetación en la Península Ibérica, así como para el conjunto global de los datos. El número total de datos utilizados en la comparación de cada clase es >10^4 para todas las clases.

	FR97		Mod3		REN15		4SAIL		CE-P	
	Mediana	RSD	Mediana	RSD	Mediana	RSD	Mediana	RSD	Mediana	RSD
Bosque	0,004	0,005	-0,012	0,006	0,007	0,005	0,007	0,004	0,009	0,005
Matorral	0,003	0,006	0,000	0,006	0,005	0,006	0,005	0,006	0,006	0,006
Sabana	0,004	0,005	-0,006	0,006	0,006	0,005	0,007	0,005	0,008	0,005
Pastizal	0,008	0,005	0,004	0,005	0,009	0,005	0,010	0,005	0,010	0,005
Humedal	0,009	0,006	0,006	0,005	0,009	0,006	0,010	0,006	0,010	0,006
Cultivo	0,006	0,006	0,001	0,006	0,007	0,006	0,008	0,006	0,009	0,006
Mosaico	0,008	0,005	-0,001	0,005	0,010	0,005	0,010	0,005	0,011	0,005
Suelo sin vegetación	0,004	0,012	0,001	0,012	0,005	0,012	0,005	0,012	0,006	0,011
Global	**0,006**	**0,006**	**0,001**	**0,007**	**0,007**	**0,006**	**0,008**	**0,006**	**0,009**	**0,006**

Tabla 14. Mediana y desviación estándar robusta (RSD) obtenidos de la diferencia entre la emisividad direccional con cada MTR y el producto MYD21A1 para el canal de 12 μm (canal 32) del sensor MODIS. Se muestran los estadísticos para dichas diferencias sobre cada tipo de cobertura vegetal y suelo sin vegetación en la Península Ibérica, así como para el conjunto global de los datos. El número total de datos utilizados en la comparación de cada clase es >10^4 para todas las clases.

	FR97		Mod3		REN15		4SAIL		CE-P	
	Mediana	RSD	Mediana	RSD	Mediana	RSD	Mediana	RSD	Mediana	RSD
Bosque	0,004	0,003	-0,011	0,005	0,006	0,003	0,006	0,003	0,007	0,003
Matorral	0,002	0,004	-0,001	0,004	0,003	0,004	0,003	0,004	0,005	0,004
Sabana	0,003	0,003	-0,006	0,005	0,005	0,003	0,005	0,003	0,007	0,003
Pastizal	0,007	0,004	0,004	0,004	0,008	0,004	0,009	0,004	0,009	0,004
Humedal	0,011	0,005	0,009	0,004	0,011	0,005	0,012	0,005	0,012	0,005
Cultivo	0,004	0,004	0,000	0,004	0,005	0,004	0,006	0,004	0,007	0,004
Mosaico	0,007	0,003	-0,001	0,004	0,009	0,004	0,009	0,003	0,010	0,004
Suelo sin vegetación	0,002	0,007	0,001	0,007	0,003	0,007	0,003	0,007	0,005	0,007
Global	**0,004**	**0,004**	**0,001**	**0,005**	**0,006**	**0,004**	**0,006**	**0,004**	**0,007**	**0,004**

Las Tablas 12 – 14 muestran la mediana (error sistemático) y la desviación estándar robusta (error aleatorio) del total de datos utilizados para cada clase. Estos resultados son similares a los obtenidos en las medidas experimentales para la mayoría de superficies, observándose la sobreestimación de los modelos FR97, REN15, 4SAIL y CE-P en los canales de 11 y 12 μm. En el canal de 8,55 μm, FR97, 4SAIL, REN15 y CE-P también sobreestiman la emisividad MYD21A1 en todas las superficies, excepto en la clase matorral y, en el caso de los MTR FR97 y REN15, en la clase sabana. En cambio, el MTR Mod3 subestima la emisividad MYD21A1 en las clases bosque, matorral, sabana y mosaico, mientras que sobreestima ligeramente la emisividad obtenida sobre las otras superficies. En términos globales, el MTR Mod3 obtiene los resultados más cercanos a los dados por el producto MYD21A1, con valores de error sistemático global de +0,001 para los canales de 11 y 12 μm. En cuanto a la desviación estándar robusta, todos los MTR muestran valores similares, los cuales varían entre ±0,004 y ±0,007 en los canales de 11 y 12 μm. En el canal de 8,55 μm, las desviaciones obtenidas son mayores, debido a la mayor variabilidad de las muestras en este intervalo espectral, obteniendo valores entre ±0,014 y ±0,015, excepto para el caso del suelo sin vegetación, donde el error aleatorio obtenido es de ±0,03 para todos los modelos. En este último caso, el error sistemático muestra valores de +0,03, siendo mucho mayores que para las otras superficies. Esto puede ser debido a una incorrecta estimación del LAI que cause el aumento de la emisividad determinada por los modelos, una sobreestimación de la

emisividad de suelo utilizada como parámetro de entrada o una disminución de la emisividad del suelo sin vegetación con el ángulo. Esta última no es contemplada por los MTR, ya que estos son generados para la obtención de la emisividad direccional sobre superficies vegetadas.

Capítulo 6

Efecto de los modelos de emisividad sobre la TST

En este capítulo se evalúa el efecto en la estimación de la temperatura de la superficie terrestre haciendo uso de la emisividad obtenida con los modelos de transferencia radiativa. Para ello, se ha calculado la temperatura de la superficie utilizando un algoritmo split-window y la emisividad obtenida tanto de los modelos como de los distintos productos de emisividad MODIS. Los datos de temperatura obtenidos han sido validados frente a datos de temperatura tomados in-situ en la zona de validación de Cortes de Pallás (Valencia). Además, se ha realizado la validación R-based de los datos obtenidos sobre una zona de olivos y una zona de viña.

Los productos satelitales de TST requieren de una continua validación de sus datos. Estos datos pueden ser validados mediante distintas técnicas: validación usando datos de referencia medidos *in-situ* (Niclòs et al., 2018), validación *R-based* (Coll et al., 2012) o validación cruzada frente a datos de otros sensores (Guillevic et al., 2014). La emisividad tiene un papel fundamental en la generación de los algoritmos que generan estos productos, especialmente en los de tipo *Split-Window* (SW). Los algoritmos SW pueden presentar una dependencia implícita con la emisividad (Prata, 2002; Ghent et al., 2017) o bien explícita (Coll et al., 2005; Niclòs et al., 2011; Pérez-Planells 2020). En el primero de los casos, los coeficientes del algoritmo SW son generados para cada tipo de superficie haciendo uso de una clasificación de tipos de superficie, teniendo en cuenta los valores de emisividad para dicha superficie durante la simulación de los datos de entrada que se utilizan para determinar los coeficientes, generalmente mediante regresión. Por tanto, estos son dependientes de la cobertura terrestre, también denominada bioma. En cambio, en los algoritmos con dependencia explícita de la emisividad, los coeficientes son calculados independientemente de la misma, asignando el valor de la emisividad a cada píxel como parámetro de entrada en la ecuación SW. En este caso, se requiere hacer uso de mapas de emisividad para poder aplicar el algoritmo a las imágenes satelitales.

En esta sección validamos la TST obtenida con el algoritmo SW propuesto por Wan (2014), el cual está basado en el algoritmo SW generalizado (Wan y Dozier, 1996), y haciendo uso de la emisividad obtenida con los MTR y los distintos productos MODIS de emisividad. El algoritmo SW propuesto por Wan (2014) es actualmente utilizado para generar la última versión (Colección 6) del producto MYD11. Dado que los coeficientes del producto operacional MYD11 no se encuentran disponibles, se utilizaron los coeficientes generados por Wang et al. (2019) para este mismo algoritmo. De esta manera, el algoritmo utilizado viene definido por la ecuación 16.

$$T = c_1 + \left(c_2 + c_3\frac{1-\bar{\varepsilon}}{\bar{\varepsilon}} - c_4\frac{\Delta\varepsilon}{\bar{\varepsilon}^2}\right)\frac{T_{31}+T_{32}}{2} + \left(c_5 + c_6\frac{1-\bar{\varepsilon}}{\bar{\varepsilon}} + c_7\frac{\Delta\varepsilon}{\bar{\varepsilon}^2}\right)\frac{T_{31}-T_{32}}{2} + c_8(T_{31}-T_{32})^2 \qquad (16)$$

donde T es la TST, T_{31} y T_{32} son las temperaturas de brillo de los canales 31 (centrado en 11 μm) y 32 (centrado en 12 μm) del sensor MODIS, respectivamente, $\bar{\varepsilon} = (\varepsilon_{31} + \varepsilon_{32})/2$ es la emisividad promedio de los canales 31 y 32 de MODIS, $\Delta\varepsilon = \varepsilon_{31} - \varepsilon_{32}$ es la diferencia entre la emisividad de los canales 31 y 32 de MODIS y c_i con i desde 1 a 8 son los coeficientes del algoritmo SW. Estos coeficientes tienen los siguientes valores: c_1=-4,1190 K, c_2=1,0166, c_3=0,1578, c_4=-0,2142, c_5=2,8572, c_6=-10,0586, c_7=-54,3715, c_8=0,6535 K^{-1}. Para la obtención de la TST aplicando el algoritmo SW, se utilizó el producto MYD021KM que ofrece la radiancia medida por el sensor MODIS a nivel de satélite.

En Niclòs et al. (2018) (ver Anexo F) validamos el producto TST operacional del sensor VIIRS, a bordo de la plataforma *Suomi National Polar-orbiting Partnership* (SNPP), el cual fue diseñado como predecesor del sensor MODIS utilizado en este estudio. Este producto se obtiene a partir de un algoritmo SW con dependencia implícita de la emisividad. La validación del producto operacional del sensor VIIRS se realizó sobre la zona de validación de TST de Valencia. Se trata de una zona homogénea de arrozales de ~100 km^2 centrada en las coordenadas 39º16'22" N, -0º19'7" E (Coll et al., 2005). Debido a las labores agrícolas del cultivo del arroz, esta zona varía el tipo de superficie de forma cíclica a lo largo del año, contando así con tres tipos de superficie distintas: suelo sin vegetación desde febrero a mayo, agua (suelo inundado) en enero, junio y diciembre, y vegetación (arroz) desde julio a septiembre. En esta zona contamos con una estación de medidas fija para el seguimiento continuo de la TST. La estación cuenta con dos radiómetros de banda ancha Apogee SI-121 (8 – 14 μm). Estos radiómetros tienen un campo de visión de 36º y una incertidumbre de medida de ±0,2 ºC según el fabricante (www.apogeeinstruments.com). Estos radiómetros fueron calibrados regularmente frente a la fuente de cuerpo negro Landcal P80P en nuestro laboratorio obteniendo una precisión de ±0,2 ºC para el intervalo de temperaturas entre 273 K y 323 K. Además, durante la campaña internacional organizada por el *Committee on Earth Observation Satellites* (CEOS) en 2009 para la comparación de radiómetros del IRT, estos radiómetros fueron comparados frente a un cuerpo negro de referencia del *National Institute of Standards and Technology* (NIST) con temperaturas entre 283 y 303 K, obteniendo una

precisión mejor que ±0,2 ºC (Theocharous et al., 2010; Niclòs et al., 2015). Los radiómetros están instalados a tres metros de altura, uno de ellos observando la superficie con visión a nadir y el otro instalado con un ángulo de observación de 53º desde el cenit, tomando medidas representativas de la radiancia hemisférica descendente (Garcia-Santos et al., 2013; Guillevic et al., 2018). Además, en el caso de la validación del sensor VIIRS se utilizó un sistema angular de adquisición permanente de datos instalado en la misma estación, el cual tomaba datos a 11 ángulos cenitales distintos (entre 0º y 180º) y 10 ángulos azimutales (entre 18º y 342º) (Niclòs et al., 2015). En este último caso, la radiancia hemisférica descendente se obtuvo a partir de la integración de las radiancias observadas con los ángulos cenitales de observación de cielo (es decir, ángulo cenital > 90º) y todos los ángulos azimutales.

Para la validación se usaron como referencia las medidas de los dos radiómetros SI-121 adquiridas dentro del periodo comprendido entre los tres minutos anteriores y posteriores a la pasada del satélite. A partir de estas medidas, la temperatura de brillo (T_b) fue corregida de la emisividad y de la radiancia hemisférica descendente reflejada en la superficie. Para la corrección de emisividad, se utilizaron valores conocidos para cada superficie, todas ellas previamente caracterizadas mediante las técnicas descritas en la Sección 1.2.1. Estas correcciones fueron realizadas mediante la ecuación (10), obteniendo la temperatura de cada medida con la inversión de la ley de Planck. La TST utilizada para la validación se obtiene del promedio de la temperatura obtenida de cada una de las medidas simultáneas a la pasada del satélite.

Para la validación del producto TST del sensor VIIRS – SNPP se utilizaron datos del sistema angular de la estación fija simultáneos a las pasadas del satélite entre los años 2012 y 2016. Dado que el algoritmo del producto TST de VIIRS fue generado mediante regresiones tomando datos de simulación para ángulos de observación ≤ 40º, la validación del producto se realizó separando el conjunto de datos en ángulos de observación mayores y menores que 40º. En total, se utilizaron 235 datos coincidentes con píxeles libres de nubosidad para el ángulo de observación ≤ 40º. La Tabla 15 muestra

los estadísticos robustos (Wilrich, 2007) de la validación del sensor VIIRS – SNPP para el ángulo de observación ≤ 40º.

Tabla 15. Mediana, desviación estándar robusta (RSD) y raíz del error cuadrático medio robusto (R-RMSE) la TST del producto operativo del sensor VIIRS – SNPP con la TST observada por la estación fija en la zona de validación de Valencia. Los valores estadísticos están expresados en K. N es el número de datos coincidentes.

	Día				Noche			
	MEDIANA	RSD	R-RMSE	N	MEDIANA	RSD	R-RMSE	N
Todas coberturas	0,4	1,1	1,1	123	-0,03	1,1	1,1	112
Agua	1,0	0,8	1,3	36	-0,4	0,8	0,9	36
Suelo sin vegetación	0,3	1,0	1,0	42	1,0	0,8	1,2	39
Vegetación	-0,03	1,1	1,1	45	-0,6	0,7	0,9	37

En la Tabla 15 se muestran los resultados que se obtuvieron en la validación del producto operativo de VIIRS – SNPP. Los resultados obtenidos para las tres superficies se encuentran dentro del umbral propuesto por el Sistema Global de Observación del Clima (GCOS) para el error sistemático (mediana) y aleatorio (RSD) inferior a 1 K (GCOS, 2016).

El algoritmo SW de Wan (2014) utilizado en este estudio fue aplicado al sensor *Sea and Land Surface Temperature Radiometer* (SLSTR) a bordo de los satélites Sentinel-3A y Sentinel-3B por Zheng et al. (2019) y al sensor Thermal Infrared Radiometer Sensor (TIRS) a bordo del satélite Landsat-8 por Meng et al. (2019). Este algoritmo lo validamos sobre la zona de validación de TST de Valencia en Pérez-Planells et al. (2020) (Anexo J) para datos del sensor SLSTR, obteniendo un error sistemático de +0,2 K y un error aleatorio de ±1,4 K con el global de datos sobre todas las superficies. Y en Niclòs et al. (2020) (Anexo K) lo validamos para datos del sensor TIRS, obteniendo un error sistemático (aleatorio) de +0,7 K (±0,7 K). Los detalles de la validación del producto operacional de TST del sensor SLSTR, así como del algoritmo SW de (Wan, 2014) con datos de los sensores SLSTR y TIRS se muestran en el Anexo D.

6.1. Evaluación con datos *in-situ*

Para evaluar el efecto de la emisividad de los distintos MTR en la obtención de la TST mediante el algoritmo SW, los valores de emisividad mostrados en la Sección 5.3.1.

fueron utilizados para obtener la TST en la zona de validación de Cortes de Pallás. Además, también se obtuvo la TST con la emisividad obtenida con los distintos productos de emisividad del sensor MODIS (MYD11A1, MYD11B1 y MYD21A1) y el producto IREMIS de la Universidad de Wisconsin. Para esta evaluación, se utilizaron los datos comprendidos entre marzo y septiembre de 2015 mostrados en la Sección 5.3. En este periodo se encuentran disponibles tanto datos adquiridos con el sistema angular sobre una estación fija, y dos radiómetros Apogee SI-121 instalados en esta misma estación: uno en observación cercana a nadir y otro midiendo la radiancia hemisférica descendente con observación a 53º desde el cenit. El tratamiento de estos datos sigue el mismo proceso descrito anteriormente para la validación del producto operacional del sensor VIIRS – SNPP. Los valores de emisividad utilizados para la corrección de emisividad fueron asignados por Niclòs et al. (2015), tomando valores entre 0,985 y 0,989, según el ángulo de observación del sistema angular.

La TST calculada utilizando la emisividad de cada MTR o producto MODIS fue comparada frente a la TST obtenida con el sistema angular y con la obtenida de los radiómetros fijos. Los datos del sistema angular fueron filtrados de nubes haciendo uso de las medidas radiométricas de cielo del propio sistema mientras que para los datos de los radiómetros fijos fueron filtrados de nubes utilizando los bits de calidad de los productos MYD11A1 y MYD21A1. En la Tabla 16 se muestran los valores estadísticos de la evaluación de la TST obtenida con cada fuente de emisividad frente a los datos obtenidos con el sistema angular. Además, se han incluido en la evaluación los valores de TST dados en los productos MYD11A1 y MYD21A1. Estos mismos valores se muestran comparando la TST obtenida con la emisividad de distintas fuentes frente a la TST obtenida con los radiómetros fijos de la estación.

La evaluación de los datos mostrados en la Tabla 16 muestran en el conjunto de datos un error sistemático inferior a 1 K para todos los productos. El error sistemático permanece inferior a 0,7 K en todos los productos, excepto para el producto de emisividad IREMIS. En cuanto al error aleatorio, este es elevado, siendo igual o superior a ±1,3 K en todos los casos. Sin embargo, al observar los datos diurnos y nocturnos, los

últimos muestran un error sistemático y aleatorio inferior que el obtenido con los datos diurnos. La RSD observada con los datos nocturnos muestra valores entre ±0,8 K y ±1,2 K en todos productos. Esta diferencia en el caso de los datos de día puede ser debido a efectos de sombra en los datos observados por el sensor MODIS y por los sistemas de la estación.

Tabla 16. Mediana, desviación estándar robusta (RSD), raíz del error cuadrático medio robusto (R-RMSE) y número de datos (N) obtenido de la evaluación de la TST obtenida haciendo uso de las distintas fuentes de emisividad frente a la TST obtenida *in-situ*. La evaluación ser realiza frente a datos obtenidos con el sistema angular de medidas radiométricas y con los radiómetros de observación fija. Los valores estadísticos están expresados en K. MYDXXA1$_{\varepsilon}$ es la TST calculada utilizando la emisividad de los productos MODIS, mientras que MYDXXA1$_{TST}$ es la TST dada por el producto MODIS.

	Sistema angular				Sistema fijo			
	MEDIANA	RSD	R-RMSE	N	MEDIANA	RSD	R-RMSE	N
FR97	0,0	1,7	1,7	53	0,2	1,6	1,6	107
Mod3	0,4	1,8	1,8	53	0,6	1,6	1,7	107
REN15	-0,1	1,7	1,7	53	0,1	1,5	1,5	107
4SAIL	-0,1	1,7	1,7	53	0,1	1,5	1,5	107
CE-P	-0,2	1,7	1,7	53	0,0	1,5	1,5	107
MYD11A1$_{\varepsilon}$	0,3	1,7	1,7	53	0,4	1,6	1,6	107
MYD21A1$_{\varepsilon}$	0,1	1,8	1,8	53	0,3	1,6	1,7	107
MYD11B1	0,3	1,8	1,8	53	0,4	1,6	1,6	107
IREMIS	0,9	1,8	2,1	53	1,2	1,7	2,0	107
MYD11A1$_{TST}$	0,3	1,5	1,5	53	0,3	1,4	1,4	107
MYD21A1$_{TST}$	0,7	1,3	1,4	53	0,4	1,6	1,6	107

En cuanto a las diferencias entre la TST obtenida con la emisividad de cada uno de los MTR, las mayores diferencias se dan entre los modelos CE-P y Mod3, siendo de 0,6 K en términos de mediana. Esta diferencia puede asociarse a las diferencias observadas en emisividad en la Sección 5.3.1, donde la diferencia entre estos dos modelos era próxima a 0,015. En cuanto al producto MYD11, debido a que las emisividades obtenidas por este producto son concordantes a las obtenidas por los MTR (ver Sección 5.3.1), la TST que se obtiene haciendo uso de la emisividad del producto MYD11 es similar a la obtenida con la emisividad de los MTR. En cambio, podría esperarse mayores diferencias en el caso del producto MYD21, ya que la emisividad de este producto tiene una mayor dispersión, especialmente obteniendo valores de emisividad menores. Pero los valores obtenidos no difieren en gran medida ya que la cantidad de puntos que obtienen una emisividad menor no tienen un gran peso estadístico.

Por lo tanto, debido a la homogeneidad de la zona a lo largo del año no se han observado diferencias notables entre los distintos productos MODIS y los MTR. Se puede observar que, entre los MTR, el modelo Mod3 muestra la mayor diferencia en términos de mediana respecto a los datos *in-situ*. Mientras que entre el resto de modelos obtuvieron diferencias próximas a 0,2 K.

6.2. Validación *R-based*

Siguiendo la metodología empleada en la sección 6.1. para la obtención de la TST en la zona de validación de Cortes de Pallás, se obtuvo la TST sobre una zona de olivos (*Olea europea*) ubicada en las coordenadas geográficas 37º 49' 00'' N, -3º 58' 00'' E y una zona de viña ubicada en las coordenadas geográficas 39º 34' 48'' N, -1º 16' 12'' E. Dado que para estas coordenadas no se disponía de datos *in-situ*, se realizó una validación *R-based* (Wan y Li, 2008) haciendo uso de los propios datos del satélite MODIS y de perfiles atmosféricos NCEP para obtener la temperatura de referencia. En las Figuras 31 y 32 se muestra la emisividad obtenida con los MTR y los productos de emisividad de MODIS para los canales centrados en 11 y 12 µm sobre la zona de olivos y de viña, respectivamente. Estas emisividades han sido utilizadas para la estimación de la TST sobre dichas zonas.

La emisividad obtenida por los MTR varía sobre la zona de olivos con valores entre 0,964 y 0,987 según el canal espectral, siendo este intervalo más acotado en la zona de viña, donde se obtienen valores entre 0,969 y 0,984, similar al observado en la zona de Cortes de Pallás. El producto de emisividad MYD21A1 muestra valores concordantes con los obtenidos con los MTR, siendo más cercanos al Mod3 en el caso de viña y al FR97 en el caso de los olivos. En cambio, el producto MYD11A1 obtiene valores similares y ligeramente superiores a los obtenidos por los MTR CE-P y 4SAIL en la zona de olivos, mientras que este producto obtiene valores muy elevados en la zona de viña. Estos valores difieren de los valores esperados ya que la zona de viña tiene un LAI entre 0,4 y 0,7 m^2/m^2 a lo largo del año, por lo que el suelo sin vegetación predomina respecto a la vegetación. De esta manera, no se esperaría una emisividad superior a 0,98, propia de una zona completamente vegetada. En ambas zonas, observamos como el producto de

emisividad IREMIS muestra un valor considerablemente más bajo que los productos MODIS y los MTR, siendo estos valores inferiores a los esperados, tal como ocurría en la zona de Cortes de Pallás.

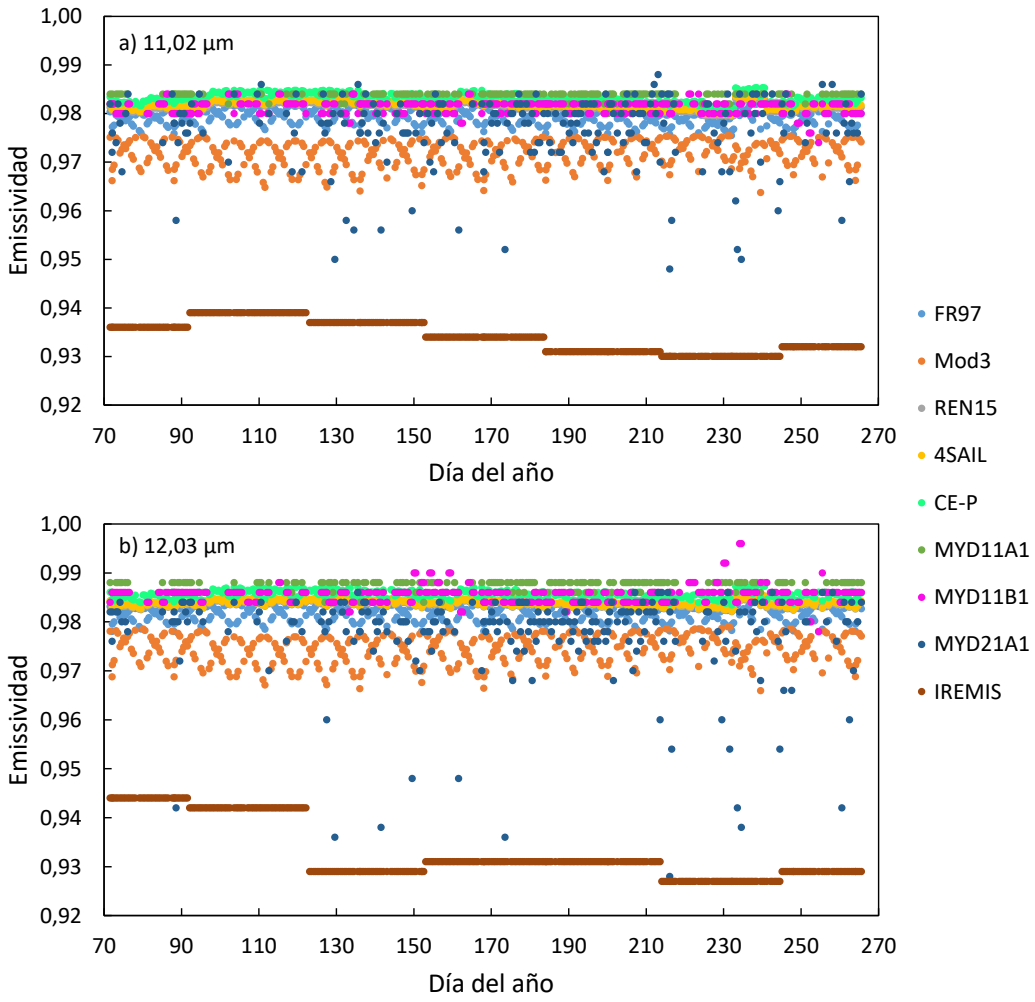

Figura 31. Emisividad sobre la zona de olivos utilizada para la validación *R-based* de los canales de MODIS a) 31 (centrado en 11,03 µm) y b) 32 (centrado en 12,02 µm). Se muestra la emisividad para los cinco MTR (FR97, Mod3, REN15, 4SAIL y CE-P) y cuatro productos de emisividad MODIS (MYD11A1, MYD11B1 y MYD21A1) y el producto de emisividad IREMIS.

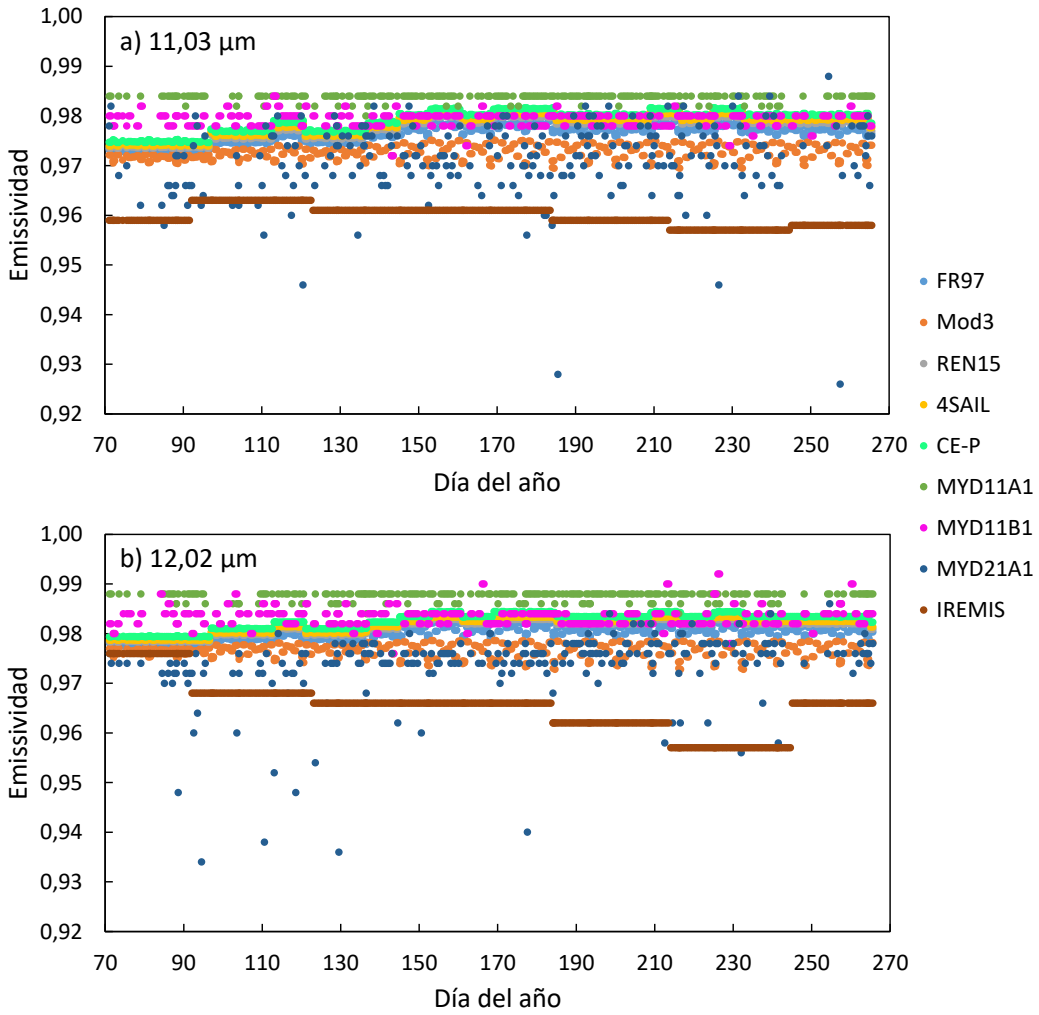

Figura 32. Emisividad sobre la zona de viña utilizada para la validación *R-based* de los canales de MODIS a) 31 (centrado en 11,03 µm) y b) 32 (centrado en 12,02 µm). Se muestra la emisividad para los cinco MTR (FR97, Mod3, REN15, 4SAIL y CE-P) y cuatro productos de emisividad MODIS (MYD11A1, MYD11B1 y MYD21A1) y el producto de emisividad IREMIS.

La validación *R-based* utiliza como temperatura de referencia la temperatura del canal de 11 µm observada por el satélite y corregida de la absorción atmosférica y de la emisividad de la superficie. Por ello, esta validación requiere de una buena precisión en la corrección atmosférica, así como en el uso de la emisividad para la obtención de las temperaturas de superficie en los canales de 11 y 12 µm (T_{11} y T_{12}, respectivamente). Ante una corrección atmosférica ideal y el uso una emisividad correcta, ambas temperaturas deberían obtener el mismo valor. Pero debido a las incertidumbres de los

parámetros utilizados y el mayor efecto atmosférico sobre el canal de 12 µm, esta igualdad no se observa en los datos.

Para la validación *R-based* se realiza el Test ΔT (Coll et al., 2009, 2012), el cual permite seleccionar los datos adecuados puesto que detecta los perfiles atmosféricos utilizados que muestran una mayor precisión, suponiendo una correcta asignación de la emisividad. El parámetro ΔT se define como la diferencia entre las dos temperaturas obtenidas ($\Delta T = T_{11} - T_{12}$). El Test ΔT considera como válidos aquellos valores de temperatura en los que ΔT toma valores dentro de la incertidumbre asociada a su estimación (Coll et al., 2009). Esta incertidumbre se obtiene como la raíz de la suma cuadrática de las incertidumbres introducidas por la emisividad y los perfiles atmosféricos en la estimación de ΔT. Para ello, se consideraron las siguientes incertidumbres de los perfiles atmosféricos: ±1 K en la temperatura de aire y ±10 % en la humedad relativa (Coll et al., 2012; Pérez-Planells et al., 2015; Niclòs et al., 2020). Para el cálculo de los parámetros atmosféricos se utilizó el modelo de transferencia radiativa MODTRAN5.2 (Berk et al., 2008).

En cuanto a la emisividad, para la zona de olivos se ha utilizado un valor de emisividad de 0,98 (Rubio et al., 2003; Sepulcre-Cantó et al., 2006) y una incertidumbre de ±0,01 para los canales 31 y 32 de MODIS. Para la zona de viña, la emisividad fue obtenida a partir de medidas *in-situ* con un radiómetro CE312 haciendo uso del método TES sobre hojas de vid y el suelo. El valor de emisividad para las hojas de vid fue de 0,972 ± 0,008 y 0,973 ± 0,008 para los canales de 11 y 12 µm, respectivamente. Para el suelo se obtuvieron valores de emisividad de 0,967 ± 0,006 y 0,959 ± 0,010 para los canales de 11 y 12 µm, respectivamente. Utilizando los valores de estas medidas, se aplicó el método de cobertura vegetal (Valor y Caselles, 2005) para obtener la emisividad:

$$\varepsilon_i = \varepsilon_{v,i} P_v + \varepsilon_{s,i}(1 - P_v) + 4 < d\varepsilon > (1 - P_v) P_v \quad (17)$$

$$< d\varepsilon > = -0{,}435\varepsilon_{s,i} + 0{,}4343 \quad (18)$$

La P_v fue obtenida del producto de P_v ofrecido por EUMETSAT y generado con datos del sensor *Advanced Very High Resolution Radiometer* (AVHRR) a bordo del satélite MetOp

(García-Haro et al., 2018). Este producto se genera con una resolución temporal de 10 días y una resolución espacial de 1,1 km. Los valores de P_v obtenidos para el píxel de estudio varían entre 0,07 ± 0,06 en la temporada sin hojas de vegetación (diciembre – febrero) y 0,27 ± 0,09 en la temporada de mayor vegetación (mayo – agosto). La incertidumbre de la emisividad ha sido calculada mediante la propagación de errores.

La contribución de cada fuente de incertidumbre sobre las temperaturas T_{11} y T_{12} y ΔT se muestran en la Tabla 17. Además, se muestra la RSC de las tres contribuciones, la cual determina la incertidumbre asociada a la temperatura en cada canal y a ΔT.

Tabla 17. Contribución de la incertidumbre de la emisividad (ε) y de los perfiles atmosféricos de temperatura de aire (Taire) y humedad relativa (HR) en la estimación de las temperaturas T_{11} y T_{12} y de ΔT en la zona de olivos y de viña. RSC es la raíz de la suma cuadrática de las tres contribuciones anteriores en cada temperatura.

	Olivos			**Viña**		
	T_{11} (K)	T_{12} (K)	ΔT (K)	T_{11} (K)	T_{12} (K)	ΔT (K)
$\boldsymbol{\varepsilon}$	0,3	0,3	0,4	0,3	0,4	0,4
Taire	1,1	1,7	0,6	0,6	0,8	0,2
HR	0,5	0,7	0,2	0,3	0,4	0,1
RSC	**1,2**	**1,9**	**0,7**	**0,7**	**1,0**	**0,5**

La incertidumbre obtenida para T_{11} se encuentra alrededor de ±1 K en las dos zonas, siendo este el error asociado a la temperatura de referencia para la validación. La incertidumbre obtenida para la temperatura T_{12} es mayor que para T_{11} ya que este canal tiene un mayor efecto atmosférico que afecta a la precisión en su obtención. La incertidumbre obtenida para ΔT es similar en ambos casos, con valor de ±0,7 K en la zona de olivos y ±0,5 K en la de viña. Esta incertidumbre es el umbral del valor ΔT para el cual se han considerado válidos los datos de validación, es decir, se han utilizado en la validación todos aquellos datos que cumplen la condición $-0,7\ K < \Delta T < 0,7\ K$ para los olivos y $-0,5\ K < \Delta T < 0,5\ K$ para la viña.

Una vez realizada la selección de datos para la validación mediante el Test ΔT, se dispuso de 130 datos para la zona de olivos y de 139 datos para la zona de viña. La Tabla 18 muestra los resultados obtenidos de la validación *R-based* de la temperatura obtenida con el algoritmo SW y la emisividad obtenida de cada MTR y producto MODIS en las dos zonas propuestas.

Tabla 18. Mediana, desviación estándar robusta (RSD), raíz del error cuadrático medio robusto (R-RMSE) obtenidos de la validación *R-based* de la TST obtenida haciendo uso de las distintas fuentes de emisividad sobre las zonas de olivos y de viña. Los valores estadísticos están expresados en K. MYDXXA1$_{\varepsilon}$ es la TST calculada utilizando la emisividad de los productos MODIS, mientras que MYDXXA1$_{TST}$ es la TST dada por el producto MODIS.

	Olivos			Viña		
	Mediana	RSD	R-RMSE	Mediana	RSD	R-RMSE
FR97	-0,5	0,9	1,1	0,0	0,8	0,8
Mod3	-0,1	0,8	0,8	0,2	0,9	0,9
REN15	-0,6	0,9	1,1	-0,1	0,9	0,9
4SAIL	-0,6	0,9	1,1	-0,1	0,9	0,9
CE-P	-0,7	0,9	1,1	-0,1	0,9	0,9
MYD11A1$_{\varepsilon}$	-0,6	0,9	1,1	-0,3	0,9	0,9
MYD21A1$_{\varepsilon}$	-0,5	1,1	1,2	0,2	1,3	1,3
MYD11B1	-0,6	1,1	1,2	0,0	0,8	0,8
IREMIS	1,4	1,1	1,8	0,9	0,9	1,3
MYD11A1$_{TST}$	-0,7	0,9	1,1	-0,3	0,9	0,9
MYD21A1$_{TST}$	0,1	0,8	0,8	0,6	0,6	0,9

La Tabla 18 muestra los estadísticos obtenidos de la validación *R-based* en las zonas de olivos y viña. En la zona de olivos, la TST obtenida con la emisividad del MTR Mod3 muestra un menor error sistemático que la obtenida con los los demás MTR y productos de emisividad MODIS, así como un error aleatorio ligeramente inferior. Las temperaturas obtenidas haciendo uso de la emisividad de los otros MTR y de los productos de emisividad MYD11A1, MYD21A1 y MYD11B1 muestran un error sistemático similar, con valores entre -0,5 y -0,7 K. En este caso, los MTR y el producto MYD11A1 obtienen un error aleatorio de ±0,9 K, mientras que para los productos MYD21A1 y MYD11B1 este es ligeramente superior, ±1,1.

Los resultados obtenidos en la zona de viña muestran un error aleatorio inferior a ±1 K en todos los casos excepto para la TST obtenida con la emisividad del producto MYD21A1. Además, las TST obtenidas tanto con la emisividad de los MTR como de los productos MODIS muestran una buena relación con los datos de referencia, con un error sistemático entre -0,3 y +0,2 K.

En cuanto a la temperatura obtenida con la emisividad del producto IREMIS, esta sobreestima la temperatura de referencia tanto en la zona de olivos (+1,4 K) como en la zona de viña (+0,9 K), mostrando un error aleatorio cercano a ±1K en ambos casos. Esta

sobreestimación es debida a los bajos valores de emisividad observados en este producto.

Los valores de TST dados por los productos MYD11A1 y MYD21A1 también han sido validados bajo las mismas condiciones, obteniendo un error tanto sistemático como aleatorio inferior a 1 K en todos los casos. El producto MYD11A1 obtiene unos resultados similares a los obtenidos haciendo uso de la emisividad de los MTR y la emisividad del propio producto junto con los coeficientes del algoritmo SW de Wang et al. (2019). En cuanto al producto MYD21A1, este muestra el mejor error sistemático junto al modelo Mod3 sobre la zona de olivos (+0,1 K), pero sobre la zona de viña sobreestima la temperatura de referencia en mayor medida (+0,6 K). Sin embargo, en ambas zonas muestra el menor error aleatorio: ±0,8 y ±0,6 K sobre las zonas de olivos y viña, respectivamente.

Capítulo 7

Conclusiones

En este capítulo se exponen las conclusiones más relevantes obtenidas de la realización de esta tesis.

En esta sección se muestran las conclusiones más relevantes de los análisis realizados en este estudio. De la evaluación de los MTR con la emisividad TES sobre las muestras de rosales con SO y SI se obtuvieron las siguientes conclusiones:

- En las medidas con visión a nadir no se observó ninguna variación de la emisividad con el LAI sobre la muestra de SO. En cambio, sobre la muestra de SI, la emisividad mostró el crecimiento con el LAI predicho por los MTR, el cual fue más pronunciado en el intervalo espectral de 8,0 – 9,5 µm, debido a la mayor diferencia entre la emisividad de suelo y hojas en dicho intervalo.
- Cuando los datos de la emisividad obtenida experimentalmente con el método TES sobre el SI fueron ajustados mediante regresión frente al LAI, se obtuvo un coeficiente de correlación del ajuste de 0,986 para los canales del radiómetro CE312 en el intervalo 10 – 12 µm y de 0,999 para los canales en el intervalo 8,0 – 9,5 µm, con un RMSE en la estimación inferior a ±0,002.
- Sobre la muestra de SO, el MTR que mejor se ajustó a las emisividades TES fue el FR97 para valores de LAI < 1,5 m^2/m^2 y el MTR Mod3 para LAI > 1,5 m^2/m^2. En cambio, sobre la muestra de SI, el MTR Mod3 se ajustó mejor a los datos obtenidos con las medidas TES en todos los casos.
- No se observó ninguna variación de la emisividad con el ángulo de observación en el intervalo de 0^o – 60^o sobre la muestra de SO.
- Sobre la muestra de SI, tan solo para el valor de LAI = 0,6 m^2/m^2 se observó una ligera disminución de la emisividad con el ángulo de observación, aunque dentro de la incertidumbre de las medidas TES. Mientras que para los demás valores de LAI no se observó ninguna variación angular significativa.
- En las medidas realizadas con el espectrómetro FT-IR se observó que las curvas de absorción típicas del cuarzo dejan de apreciarse para valores de LAI > 1 m^2/m^2.

Las conclusiones más relevantes obtenidas de la comparación entre los mapas de emisividad direccional generados haciendo uso de los MTR y los productos de emisividad MODIS son:

- Sobre la zona de Cortes de Pallás (Valencia), los MTR mostraron poca variación temporal en la serie utilizada (marzo – septiembre de 2015), debido a que esta zona tiene una cantidad de vegetación constante durante todo el año.
- En los MTR FR97 y Mod3 se observó un mayor efecto del ángulo de observación por parte del satélite. Este efecto se reflejó en una oscilación periódica de la emisividad de la vegetación coincidente con el periodo de revisita del satélite.
- Los productos de emisividad MYD11A1, MYD11B1 y MYD21A1 obtuvieron valores concordantes con los obtenidos por los MTR, aunque el producto MYD21A1, así como el producto MYD11B1 para el canal 29 (centrado en 8,55 µm), mostraron una gran variabilidad de los datos, con valores entre 0,92 y 0,99.
- El producto IREMIS de la Universidad de Wisconsin obtuvo valores de emisividad inferiores a los esperados, subestimando en gran medida los valores obtenidos con los productos MODIS y los MTR.
- La comparación por clases de superficie realizada sobre la Península Ibérica mostró que, para los canales 31 y 32 (centrados en 11 y 12 µm, respectivamente), los MTR FR97, REN15, 4SAIL y CE-P sobreestiman la emisividad obtenida por el producto MYD21A1. Mientras, el MTR Mod3 mostró distintos resultados dependiendo de la clase de superficie, subestimando para las clases bosque, matorral, sabana y mosaico de vegetación.
- Para el canal de 8,55 µm, los MTR FR97, REN15, 4SAIL y CE-P subestimaron la emisividad MYD21A1 en las clases de superficie matorral y, en el caso del FR97, también en la clase sabana. El MTR Mod3 subestimó las mismas clases que en el caso de los canales centrados en 11 y 12 µm: bosque, matorral, sabana y mosaico de vegetación.
- Incluyendo todas las clases de superficie para la comparación con el producto MYD21A1, para el canal centrado en 8,55 µm, todos los MTR obtuvieron un error tanto sistemático como aleatorio similar. Se obtuvieron valores de error sistemático entre -0,003 y +0,004, y valores de error aleatorio entre ±0,014 y ±0,015.

- En la comparación global para todas las superficies en los canales centrados en 11 y 12 µm, el MTR Mod3 mostró los mejores resultados comparando con el producto MYD21A1, con un error sistemático (aleatorio) de +0,001 (±0,007) para el canal de 11 µm, y un error sistemático (aleatorio) de +0,001 (±0,005) para el canal de 12 µm. Mientras, los otros MTR obtuvieron un error sistemático entre +0,004 y +0,009, y un error aleatorio entre ±0,004 y ±0,006.

Finalmente, los mapas de emisividad direccional obtenidos con los MTR y los distintos productos MODIS fueron utilizados para obtener la TST sobre la Península Ibérica. Esta TST fue validada frente a datos de TST tomados *in-situ* sobre la zona de Cortes de Pallás y mediante la técnica de validación *R-based* sobre una zona de olivos y otra de viña, obteniendo las siguientes conclusiones:

- Considerando los datos diurnos y nocturnos en conjunto, tanto la temperatura obtenida con la emisividad de los MTR como de los productos de emisividad de MODIS llevó a un error sistemático inferior a 1 K sobre la zona de validación de Cortes de Pallás.
- El error aleatorio observado sobre la zona de Cortes de Pallás frente a los datos *in-situ* fue entre ±1,7 K y ±1,8 K, tanto para la temperatura obtenida con la emisividad de los MTR como de los productos MODIS.
- En la zona de validación de Cortes de Pallás, dado que la emisividad obtenida por los productos MODIS era concordante con los valores de emisividad de los MTR, la temperatura determinada con la emisividad de los productos MODIS no mostró diferencias significativas con la temperatura resultante de utilizar la emisividad de los MTR.
- Los MTR Mod3 y CE-P obtuvieron una diferencia en el error sistemático de +0,6 K. Esta diferencia se relaciona con la diferencia observada en la emisividad sobre la zona, la cual es de 0,015 entre los dos modelos.
- La emisividad obtenida por el producto MYD11A1 sobre la zona de viña es superior a la esperada, ya que muestra una emisividad típica de una zona completamente vegetada (0,984 y 0,988 para los canales de 11 y 12 µm,

respectivamente), cuando la cantidad de vegetación de la viña es reducida (P_v ≤ 0,27 y LAI ≤ 0,7 m^2/m^2). Los MTR reproducen valores de emisividad más realistas teniendo en cuenta el tipo de superficie en dicha zona, como así refleja la emisividad obtenida por el producto MYD21A1, el cual muestra valores concordantes con los obtenidos con el MTR Mod3, con valores cercanos a 0,975.

- En el caso de la validación *R-based* sobre la zona de olivos, la temperatura obtenida con la emisividad del MTR Mod3 obtuvo el menor error sistemático (-0,1 K) y el menor error aleatorio (±0,8 K). La temperatura obtenida con la emisividad de los otros MTR y de los productos MODIS obtuvo un error sistemático entre -0,7 y -0,5 K y un error aleatorio entre ±0,9 y ±1,1 K.
- Sobre la zona de viña, el error sistemático fue similar en términos de la temperatura obtenida con todos los MTR y productos MODIS, obteniendo valores entre -0,3 K y +0,2 K. El error aleatorio sobre la zona de viña contó con valores similares a los obtenidos en la zona de olivos. Sobre esta zona, a pesar de que el MTR Mod3 muestra valores de emisividad más acordes con el tipo de superficie, no se refleja en términos de TST ya que la diferencia en emisividad lleva a una diferencia en TST de ~0,5 K. Esta diferencia es observada en términos de error sistemático entre Mod3 y MYD11A1, pero ambos se encuentran cercanos a los valores de referencia.
- La TST obtenida directamente de los productos MYD11A1 y MYD21A1 mostró un error sistemático inferior a 1 K en las tres zonas utilizadas para la validación. En cambio, el error aleatorio observado fue inferior a ±1 K en la validación *R-based* sobre las zonas de olivos y viña, pero fue superior a ±1 K en la validación con datos *in-situ* sobre la zona de validación de Cortes de Pallás.
- Los MTR han demostrado un buen resultado en la estimación de la emisividad sobre superficies vegetadas, proporcionando buenos resultados en su implementación para la estimación de la TST desde el sensor MODIS, siendo iguales o mejores a los obtenidos mediante los datos de los productos operativos del sensor MODIS. En concreto, el MTR Mod3 mostró el mejor

funcionamiento considerando los resultados obtenidos tanto en términos de emisividad como de TST. Además, este modelo tiene, junto al MTR FR97, una mayor simplicidad de aplicación, que se hace especialmente notable en la aplicación a imágenes de satélite. Por ello, los resultados obtenidos hacen interesante la extensión de estos MTR, especialmente el Mod3, a otros sensores satelitales, ya que permitirían obtener la emisividad de la cubierta vegetal teniendo en cuenta las posibles variaciones en la vegetación de la superficie.

Conclusions

The most relevant conclusions are summarized in this section.

First, the conclusions extracted from the evaluation of the RTM emissivities against the TES emissivities measured over the rose samples with organic and inorganic soils (OS and IS, respectively) are:

- No significant emissivity variation with LAI was observed at nadir for the sample with OS. However, for the sample with IS, the increase of emissivity with LAI predicted by the RTMs was also observed on the TES measurements. This increase was more pronounced in the 8.0 – 9.5 µm spectral range, due to the higher difference between the soil and leaf emissivity in this range.
- A non-linear regression fitting was applied to the emissivity data obtained from the TES measurements over the IS sample. It was obtained a correlation coefficient of 0.986 for the CE312 channels located in the 10 – 12 µm spectral range and of 0.999 for the channels located in the 8.0 – 9.5 µm spectral range, and a RMSE on the estimation lower than ±0.002.
- For the sample with OS, the FR97 model showed the best agreement with TES emissivity for LAIs < 1.5 m^2/m^2, but the Mod3 model was the best for LAIs > 1.5 m^2/m^2. However, for the sample with IS, the Mod3 RTM showed the best agreement with TES emissivity for any LAI.
- No significant emissivity variation with the viewing angle was observed for the studied range from 0^o to 60^o for the sample with OS.
- For the sample with IS, a slight decrease of emissivity with the viewing angle was observed for LAI = 0.6 m^2/m^2, but this difference was lower than the TES emissivity uncertainty. No significant angular variation was observed for higher LAIs.
- The emissivity measurements taken with the FT-IR spectrometer showed that the typical absorption curves of the quartz in the 8.5 – 9.5 µm spectral range were no longer visible for LAI > 1 m^2/m^2.

The most relevant conclusions drawn from the comparison of the directional canopy emissivity maps generated with the emissivity RTMs and the MODIS emissivity products are presented next:

- The emissivity derived from the RTMs showed little variation for the time series used (March – September, 2015) at the Cortes de Pallás validation site, because the fraction of vegetation cover is fairly constant throughout the year at this site.
- A higher effect of the satellite viewing angle was observed on maps for FR97 and Mod3 RTMs. This effect was observed as a periodic oscillation of the canopy emissivity, which was coincident with the satellite revisit period.
- The emissivity values obtained from the MYD11A1, MYD11B1 and MYD21A1 MODIS products were in agreement with the emissivity values obtained by the canopy emissivity RTMs. However, the MYD21A1 product, as well as the MYD11B1 product at channel 29 (centered at 8.55 μm), showed a high variability, with emissivity values between 0.92 and 0.99.
- The IREMIS product of the University of Wisconsin obtained emissivity values lower than the expected emissivity, underestimating the emissivities obtained with the MODIS products and the canopy emissivity RTMs.
- The FR97, REN15, 4SAIL and CE-P RTMs overestimated the MYD21A1 product for each land cover type over the Iberian Peninsula at MODIS channels 31 and 32 (centered at 11 and 12 μm, respectively). However, Mod3 showed different results depending on the land cover type, underestimating the MYD21A1 emissivity for the types: forest, shrubland, savanna and vegetation mosaic.
- For the channel centered at 8.55 μm, FR97, REN15, 4SAIL and CE-P underestimated the MYD21A1 emissivity for the shrubland type, but also for savanna in the case of the FR97. The Mod3 RTM underestimated the same land covers than those for the channels centered at 11 and 12 μm.
- In a global comparison, i.e. taking into account all land covers together, all RTMs showed a similar systematic and random uncertainties for the channel centered

at 8.55 µm when compared with the MYD21 product. These systematic uncertainties ranged from -0.003 to +0.004 and random uncertainties ranged from ±0.014 to ±0.015.

- The Mod3 RTM showed the best results in the global comparison with the MYD21A1 emissivity for channels centered at 11 and 12 µm. They obtained systematic (random) uncertainties of +0.001 (±0.007) and +0.001 (±0.005) for the channels at 11 µm and 12 µm, respectively. The other canopy emissivity RTMs obtained systematic uncertainties from +0.004 to +0.009, and random uncertainties from ±0.004 to ±0.006.

Finally, I summarized the main conclusions obtained when these emissivity maps and products were used to estimate the LST over the Iberian Peninsula and these LSTs were validated against ground LST data. Ground measurements acquired in-situ at the Cortes de Pallás validation site and R-based estimates over an olive orchard and a vineyard were used as reference data for the calibration.

- Considering all data, the systematic uncertainty observed for the LST obtained with the RTMs emissivity and the MODIS emissivity products was lower than 1 K over the Cortes de Pallás validation site.
- Random uncertainties from ±1.7 to ±1.8 K were observed at the Cortes de Pallás validation site for the LSTs obtained with the RTMs emissivities and the MODIS emissivity products.
- LSTs retrieved with emissivities of the MODIS products showed a good agreement with the LSTs retrieved with the RTM emissivities, due to the similarities in both emissivities at the site.
- The difference between the systematic uncertainty observed for the Mod3 and CE-P RTMs was of +0.6 K. This difference agrees with the difference observed between the emissivities of the Mod3 and CE-P models, which was of 0.015.
- The MYD11A1 emissivity at the vineyard site was higher than expected, with emissivity values typical for full vegetation cover (0.984 and 0.988 for 11 and

12 µm spectral channels), although there is low vegetation cover at the site (P_v ≤ 0.27 and LAI ≤ 0.7 m^2/m^2). More realistic emissivity values were derived by the RTMs for each surface cover, as it was also reflected by the MYD21A1 emissivity, which was in agreement with the Mod3 RTM, with emissivity values close to 0.975.

- From the R-based validation at the olive orchard, the LST obtained with the emissivity of the Mod3 RTM showed the lowest systematic uncertainty (-0.1 K) and the lowest random uncertainty (±0.8 K). The LST obtained with the emissivity retrieved by the other RTMs and the MODIS emissivity products showed systematic uncertainties from -0.7 to -0.5 K and random uncertainties from ±0.9 to ±1.1 K.
- At the vineyard site, the systematic uncertainty was similar in terms of the LST retrieved with the emissivity of all RTMs and MODIS products, with values between -0.3 and +0.2 K. The random uncertainties at the vineyard were similar to those at the olive orchard site. Although Mod3 showed emissivity values according to the surface cover, this was not the case in LST since this emissivity difference implied a difference of ~0.5 K. This difference was observed in the systematic uncertainty obtained by the Mod3 and MYD11A1, but both obtained similar values to the reference LST.
- The LST retrieved with the Mod3 RTM obtained a better result than the LST retrieved with the other RTMs or the MODIS products at the olive orchard site. However, similar results were obtained for all the RTMs and MODIS products over the Cortes de Pallás site and the vineyard site.
- The LST given by the MYD11A1 and MYD21A1 products showed a systematic uncertainty lower than 1 K at the three sites. However, the random uncertainty was lower than ±1 K at the olive orchard site and the vineyard site, but it was higher than ±1 K using the in-situ data at the Cortes de Pallás validation site.
- The RTMs showed a good performance on the canopy emissivity estimation, providing good results in their application for the LST retrieval with MODIS data, which were similar or better than those obtained with the MODIS

operational products data. Specifically, the Mod3 showed the best performance considering the results both in terms of emissivity and LST. In addition, this model has, like the FR97 RTM, a greater simplicity of application, which is especially notable in its application to satellite images. These results make interesting the extension of the RMTs, especially the Mod3 RTM, to other satellite thermal sensors, since they allow estimating the canopy emissivity taking into account changes over time in the surface vegetation.

Bibliografía

Baldridge, A.M., Hook, S.J., Grove, C.I., Rivera, G., 2009. The ASTER spectral library version 2.0. Remote Sens. Environ. 113, 711–715. https://doi.org/10.1016/j.rse.2008.11.007

Barnes, W.L., Pagano, T.S., Salomonson, V. V., 1998. Prelaunch characteristics of the moderate resolution imaging spectroradiometer (MODIS) on EOS-AMI. IEEE Trans. Geosci. Remote Sens. 36, 1088–1100. https://doi.org/10.1109/36.700993

Batjes, N.H., Ribeiro, E., Van Oostrum, A., Leenaars, J., Hengl, T., Mendes De Jesus, J., 2017. WoSIS: Providing standardised soil profile data for the world. Earth Syst. Sci. Data 9, 1–14. https://doi.org/10.5194/essd-9-1-2017

Batjes, N.H., Ribeiro, E., Van Oostrum, A., 2020. Standardised soil profile data to support global mapping and modelling (WoSIS snapshot 2019). Earth Syst. Sci. Data 12, 299–320. https://doi.org/10.5194/essd-12-299-2020

Berk, A., Anderson, G.P., Acharya, P.K., Shettle, E.P., 2008. MODTRAN5. 2.0. 0 user's manual. Spectr. Sci. Inc., Burlingt. MA, Air Force Res. Lab. Hanscom MA.

Bian, Z., Roujean, J.L., Lagouarde, J.P., Cao, B., Li, H., Du, Y., Liu, Q., Xiao, Q., Liu, Q., 2020. A semi-empirical approach for modeling the vegetation thermal infrared directional anisotropy of canopies based on using vegetation indices. ISPRS J. Photogramm. Remote Sens. 160, 136–148. https://doi.org/10.1016/j.isprsjprs.2019.12.004

Borel, C.C., 1998. Surface emissivity and temperature retrieval for a hyperspectral sensor. Int. Geosci. Remote Sens. Symp. 1, 546–549. https://doi.org/10.1109/igarss.1998.702966

Bosilovich, M.G., Chen, J., Robertson, F.R., Adler, R.F., 2008. Evaluation of global precipitation in reanalyses. J. Appl. Meteorol. Climatol. 47, 2279–2299. https://doi.org/10.1175/2008JAMC1921.1

Campos-Taberner, M., García-Haro, F.J., Confalonieri, R., Martínez, B., Moreno, Á., Sánchez-Ruiz, S., Gilabert, M.A., Camacho, F., Boschetti, M., Busetto, L., 2016. Multitemporal monitoring of plant area index in the valencia rice district with PocketLAI. Remote Sens. 8, 1–17. https://doi.org/10.3390/rs8030202

Cao, B., Guo, M., Fan, W., Xu, X., Peng, J., Ren, H., Du, Y., Li, H., Bian, Z., Hu, T., Xiao, Q., Liu, Q., 2018. A new directional canopy emissivity model based on spectral invariants. IEEE Trans. Geosci. Remote Sens. 56, 6911–6926. https://doi.org/10.1109/TGRS.2018.2845678

Cao, B., Liu, Q., Du, Y., Roujean, J.L., Gastellu-Etchegorry, J.P., Trigo, I.F., Zhan, W., Yu, Y., Cheng, J., Jacob, F., Lagouarde, J.P., Bian, Z., Li, H., Hu, T., Xiao, Q., 2019. A review of earth surface thermal radiation directionality observing and modeling: Historical development, current status and perspectives. Remote Sens. Environ.

232, 111304. https://doi.org/10.1016/j.rse.2019.111304

Caselles, E., Valor, E., Abad, F., Caselles, V., 2012. Automatic classification-based generation of thermal infrared land surface emissivity maps using AATSR data over Europe. Remote Sens. Environ. 124, 321–333. https://doi.org/10.1016/j.rse.2012.05.024

Chehbouni, A., Nouvellon, Y., Kerr, Y.H., Moran, M.S., Watts, C., Prevot, L., Goodrich, D.C., Rambal, S., 2001. Directional effect on radiative surface temperature measurements over a semiarid grassland site. Remote Sens. Environ. 76, 360–372. https://doi.org/10.1016/S0034-4257(01)00183-3

Coll, C., Valor, E., Caselles, V., Niclòs, R., 2003. Adjusted Normalized Emissivity Method for surface temperature and emissivity retrieval from optical and thermal infrared remote sensing data. J. Geophys. Res. D Atmos. 108, 1–14. https://doi.org/10.1029/2003jd003688

Coll, C., Caselles, V., Galve, J.M., Valor, E., Niclòs, R., Sánchez, J.M., Rivas, R., 2005. Ground measurements for the validation of land surface temperatures derived from AATSR and MODIS data. Remote Sens. Environ. 97, 288–300. https://doi.org/10.1016/j.rse.2005.05.007

Coll, C., Caselles, V., Valor, E., Niclòs, R., Sánchez, J.M., Galve, J.M., Mira, M., 2007. Temperature and emissivity separation from ASTER data for low spectral contrast surfaces. Remote Sens. Environ. 110, 162–175. https://doi.org/10.1016/j.rse.2007.02.008

Coll, C., Wan, Z., Galve, J.M., 2009. Temperature-based and radiance-based validations of the V5 MODIS land surface temperature product. J. Geophys. Res. Atmos. 114, 1–15. https://doi.org/10.1029/2009JD012038

Coll, C., Valor, E., Galve, J.M., Mira, M., Bisquert, M., García-Santos, V., Caselles, E., Caselles, V., 2012. Long-term accuracy assessment of land surface temperatures derived from the Advanced Along-Track Scanning Radiometer. Remote Sens. Environ. 116, 211–225. https://doi.org/10.1016/j.rse.2010.01.027

Coll, C., García-Santos, V., Niclòs, R., Caselles, V., 2016. Test of the MODIS land surface temperature and emissivity separation algorithm with ground measurements over a rice paddy. IEEE Trans. Geosci. Remote Sens. 54, 3061–3069. https://doi.org/10.1109/TGRS.2015.2510426

Coll, C., Niclòs, R., Puchades, J., García-Santos, V., Galve, J.M., Pérez-Planells, L., Valor, E., Theocharous, E., 2019. Laboratory calibration and field measurement of land surface temperature and emissivity using thermal infrared multiband radiometers. Int. J. Appl. Earth Obs. Geoinf. 78, 227–239. https://doi.org/10.1016/j.jag.2019.02.002

Confalonieri, R., Foi, M., Casa, R., Aquaro, S., Tona, E., Peterle, M., Boldini, A., De Carli, G., Ferrari, A., Finotto, G., Guarneri, T., Manzoni, V., Movedi, E., Nisoli, A., Paleari, L., Radici, I., Suardi, M., Veronesi, D., Bregaglio, S., Cappelli, G., Chiodini, M.E., Dominoni, P., Francone, C., Frasso, N., Stella, T., Acutis, M., 2013. Development of an app for estimating leaf area index using a smartphone. Trueness and precision determination and comparison with other indirect methods. Comput. Electron. Agric. 96, 67–74. https://doi.org/10.1016/j.compag.2013.04.019

François, C., Ottle, C., Prevot, L., 1997. Analytical parameterization of canopy directional emissivity and directional radiance in the thermal infrared. Application on the retrieval of soil and foliage temperatures using two directional measurements. Int. J. Remote Sens. 18, 2587–2621. https://doi.org/10.1080/014311697217495

François, C., 2002. The potential of directional radiometric temperatures for monitoring soil and leaf temperature and soil moisture status. Remote Sens. Environ. 80, 122–133. https://doi.org/10.1016/S0034-4257(01)00293-0

García-Haro, F.J., Campos-Taberner, M., Muñoz-Marí, J., Laparra, V., Camacho, F., Sánchez-Zapero, J., Camps-Valls, G., 2018. Derivation of global vegetation biophysical parameters from EUMETSAT Polar System. ISPRS J. Photogramm. Remote Sens. 139, 57–74. https://doi.org/10.1016/j.isprsjprs.2018.03.005

García-Santos, V., Valor, E., Caselles, V., Burgos, M.A., Coll, C., 2012. On the angular variation of thermal infrared emissivity of inorganic soils. J. Geophys. Res. Atmos. 117, 1–18. https://doi.org/10.1029/2012JD017931

Garcia-Santos, V., Valor, E., Caselles, V., Mira, M., Galve, J.M., Coll, C., 2013. Evaluation of different methods to retrieve the hemispherical downwelling irradiance in the thermal infrared region for field measurements. IEEE Trans. Geosci. Remote Sens. 51, 2155–2165. https://doi.org/10.1109/TGRS.2012.2209891

García-Santos, V., Valor, E., Caselles, V., Doña, C., 2016. Validation and comparison of two models based on the Mie theory to predict 8–14µm emissivity spectra of mineral surfaces. J. Geophys. Res. Solid Earth 121, 1739–1757. https://doi.org/10.1002/2015JB012654

GCOS, 2016. The Global Observing System for Climate: Implementation Needs. World Meteorol. Organ. 200, 341.

Ghent, D., Corlett, G.K., Göttsche, F.M., Remedios, J.J., 2017. Global Land Surface Temperature From the Along-Track Scanning Radiometers. J. Geophys. Res. Atmos. 122, 12,167-12,193. https://doi.org/10.1002/2017JD027161

Gillespie, A.R., 1986. Lithologic Mapping of Silicate Rocks Using TIMS; TIMS Data User'sWorkshop Jet Propulsion Laboratory: Pasadena, CA, USA; pp. 29–44.

Gillespie, A.R., Rokugawa, S., Matsunaga, T., Steven Cothern, J., Hook, S., Kahle, A.B.,

1998. A temperature and emissivity separation algorithm for advanced spaceborne thermal emission and reflection radiometer (ASTER) images. IEEE Trans. Geosci. Remote Sens. 36, 1113–1126. https://doi.org/10.1109/36.700995

Gillespie, A.R., Abbott, E.A., Gilson, L., Hulley, G., Jiménez-Muñoz, J.C., Sobrino, J.A., 2011. Residual errors in ASTER temperature and emissivity standard products AST08 and AST05. Remote Sens. Environ. 115, 3681–3694. https://doi.org/10.1016/j.rse.2011.09.007

Guillevic, P.C., Biard, J.C., Hulley, G.C., Privette, J.L., Hook, S.J., Olioso, A., Göttsche, F.M., Radocinski, R., Román, M.O., Yu, Y., Csiszar, I., 2014. Validation of Land Surface Temperature products derived from the Visible Infrared Imaging Radiometer Suite (VIIRS) using ground-based and heritage satellite measurements. Remote Sens. Environ. 154, 19–37. https://doi.org/10.1016/j.rse.2014.08.013

Guillevic, P., Göttsche, F., Nickeson, J., Hulley, G., Ghent, D., Yu, Y., Trigo, I., Hook, S., Sobrino, J.A., Remedios, J., Román, M., Camacho, F., 2018. Land surface temperature product validation best practice protocol version 1.1. Best Pract. Satell. L. Prod. Valid. (p. 60) L. Prod. Valid. Subgr. doi, 58. https://doi.org/10.5067/doc/ceoswgcv/lpv/lst.001

Guo, M., Cao, B., Fan, W., Ren, H., Cui, Y., Du, Y., Liu, Q., 2019. Scattering Effect Contributions to the Directional Canopy Emissivity and Brightness Temperature Based on CE-P and CBT-P Models. IEEE Geosci. Remote Sens. Lett. 16, 957–961. https://doi.org/10.1109/LGRS.2018.2886606

Gustafson, W., Gillespie, A., Yamada, G., 2006. Revisions to the ASTER temperature/emissivity separation algorithm. Recent Adv. Quant. Remote Sens. 1–7.

Hapke, B., 2011. Theory of Reflectance and Emittance Spectroscopy. Cambridge University Press, Cambridge. https://doi.org/10.1017/CBO9781139025683

Hollmann, R., Merchant, C.J., Saunders, R., Downy, C., Buchwitz, M., Cazenave, A., Chuvieco, E., Defourny, P., De Leeuw, G., Forsberg, R., Holzer-Popp, T., Paul, F., Sandven, S., Sathyendranath, S., Van Roozendael, M., Wagner, W., 2013. The ESA climate change initiative: Satellite data records for essential climate variables. Bull. Am. Meteorol. Soc. 94, 1541–1552. https://doi.org/10.1175/BAMS-D-11-00254.1

Hulley, G.C., Hook, S.J., 2009. The North American ASTER Land Surface Emissivity Database (NAALSED) Version 2.0. Remote Sens. Environ. 113, 1967–1975. https://doi.org/10.1016/j.rse.2009.05.005

Hulley, G., Veraverbeke, S., Hook, S., 2014. Thermal-based techniques for land cover change detection using a new dynamic MODIS multispectral emissivity product (MOD21). Remote Sens. Environ. 140, 755 – 765.

Hulley, G., Islam, T., Freepartner, R., Malakar, N., 2016a. Visible Infrared Imaging Radiometer Suite (VIIRS) Land Surface Temperature and Emissivity Product Collection 1 Algorithm Theoretical Basis Document 1–25.

Hulley, G., Malakar, N., Freepartner, R., 2016b. Moderate Resolution Imaging Spectroradiometer (MODIS) Land Surface Temperature and Emissivity Product (MxD21) Algorithm Theoretical Basis Document Collection-6. JPL Publ. 12–17.

Islam, T., Hulley, G.C., Malakar, N.K., Radocinski, R.G., Guillevic, P.C., Hook, S.J., 2017. A Physics-Based Algorithm for the Simultaneous Retrieval of Land Surface Temperature and Emissivity From VIIRS Thermal Infrared Data. IEEE Trans. Geosci. Remote Sens. 55, 563–576. https://doi.org/10.1109/TGRS.2016.2611566

Jacob, F., Lesaignoux, A., Olioso, A., Weiss, M., Caillault, K., Jacquemoud, S., Nerry, F., French, A., Schmugge, T., Briottet, X., Lagouarde, J.P., 2017. Reassessment of the temperature-emissivity separation from multispectral thermal infrared data: Introducing the impact of vegetation canopy by simulating the cavity effect with the SAIL-Thermique model. Remote Sens. Environ. 198, 160–172. https://doi.org/10.1016/j.rse.2017.06.006

Jimenez-Munoz, J.C., Sobrino, J.A., Mattar, C., Hulley, G., Gottsche, F.M., 2014. Temperature and emissivity separation from MSG/SEVIRI data. IEEE Trans. Geosci. Remote Sens. 52, 5937–5951. https://doi.org/10.1109/TGRS.2013.2293791

Joint Committee For Guides In Metrology, 2008. Evaluation of measurement data — Guide to the expression of uncertainty in measurement, International Organization for Standardization Geneva ISBN. https://doi.org/10.1373/clinchem.2003.030528

Kalnay, E., Kanamitsu, M., Baker, W.E., 1990. Global numerical weather prediction at the National Meteorological Center. Bull. Amer. Meteor. Soc. 71, 1410–1428. https://doi.org/10.1175/1520-0477(1990)071<1410:GNWPAT>2.0.CO;2

Korb, A.R., Dybwad, P., Wadsworth, W., Salisbury, J.W., 1996. Portable Fourier transform infrared spectroradiometer for field measurements of radiance and emissivity. Appl. Opt. 35, 1679. https://doi.org/10.1364/ao.35.001679

Legrand, M., Pietras, C., Brogniez, G., Haeffelin, M., Abuhassan, N.K., Sicard, M., 2000. A high-accuracy multiwavelength radiometer for in situ measurements in the thermal infrared. Part I: Characterization of the instrument. J. Atmos. Ocean. Technol. 17, 1203–1214. https://doi.org/10.1175/1520-0426(2000)017<1203:AHAMRF>2.0.CO;2

Li, Z.L., Tang, B.H., Wu, H., Ren, H., Yan, G., Wan, Z., Trigo, I.F., Sobrino, J.A., 2013a. Satellite-derived land surface temperature: Current status and perspectives. Remote Sens. Environ. 131, 14–37. https://doi.org/10.1016/j.rse.2012.12.008

Li, Z.L., Wu, H., Wang, N., Qiu, S., Sobrino, J.A., Wan, Z., Tang, B.H., Yan, G., 2013b. Land surface emissivity retrieval from satellite data. Int. J. Remote Sens. 34, 3084–3127. https://doi.org/10.1080/01431161.2012.716540

Loveland, T.R., Belward, A.S., 1997. The international geosphere biosphere programme data and information system global land cover data set (DIScover). Acta Astronaut. 41, 681–689. https://doi.org/10.1016/S0094-5765(98)00050-2

Meerdink, S., Roberts, D., Hulley, G., Gader, P., Pisek, J., Adamson, K., King, J., Hook, S.J., 2019. Plant species' spectral emissivity and temperature using the hyperspectral thermal emission spectrometer (HyTES) sensor. Remote Sens. Environ. 224, 421–435. https://doi.org/10.1016/j.rse.2019.02.009

Meng, X., Cheng, J., Zhao, S., Liu, S., Yao, Y., 2019. Estimating Land Surface Temperature from Landsat-8 Data using the NOAA JPSS Enterprise Algorithm. Remote Sens., 11, 155. doi:10.3390/rs11020155

Mira, M., Schmugge, T.J., Valor, E., Caselles, V., Coll, C., 2009. Comparison of thermal infrared emissivities retrieved with the two-lid box and the TES methods with laboratory spectra. IEEE Trans. Geosci. Remote Sens. 47, 1012–1021. https://doi.org/10.1109/TGRS.2008.2008901

Myneni, R.B., Knyazikhin, Y., Privette, J.L., Running, S.W., Nemani, R., Zhang, Y., Tian, Y., Wang, Y., Morissette, J.T., Glassy, J., Votava, P., 1999. MODIS Leaf Area Index (LAI) And Fraction Of Photosynthetically Active Radiation Absorbed By Vegetation (FPAR) Product. MODIS ATBD Version 4., 130. https://doi.org/http://eospso.gsfc.nasa.gov/atbd/modistables.html

Niclòs, R., Valor, E., Caselles, V., Coll, C., Sánchez, J.M., 2005. In situ angular measurements of thermal infrared sea surface emissivity - Validation of models. Remote Sens. Environ. 94, 83–93. https://doi.org/10.1016/j.rse.2004.09.002

Niclòs, R., Caselles, V., Valor, E., Coll, C., Sánchez, J.M., 2009. A simple equation for determining sea surface emissivity in the 3-15 µm region. Int. J. Remote Sens. 30, 1603–1619. https://doi.org/10.1080/01431160802541523

Niclòs, R., Galve, J.M., Valiente, J.A., Estrela, M.J., Coll, C., 2011. Accuracy assessment of land surface temperature retrievals from MSG2-SEVIRI data. Remote Sens. Environ. 115, 2126–2140. https://doi.org/10.1016/j.rse.2011.04.017

Niclòs, R., Valiente, J.A., Barberà, M.J., Coll, C., 2015. An autonomous system to take angular thermal-infrared measurements for validating satellite products. Remote Sens. 7, 15269–15294. https://doi.org/10.3390/rs71115269

Niclòs, R., Pérez-Planells, L., Coll, C., Valiente, J.A., Valor, E., 2018. Evaluation of the S-NPP VIIRS land surface temperature product using ground data acquired by an autonomous system at a rice paddy. ISPRS J. Photogramm. Remote Sens. 135.

https://doi.org/10.1016/j.isprsjprs.2017.10.017

Niclòs, R., Puchades, J., Coll, C., Barberà, M.J., Pérez-Planells, L., Valiente, J.A., Sánchez, J.M., 2020. Evaluation of Landsat-8 TIRS data recalibrations and land surface temperature split-window algorithms over a homogeneous crop area with different phenological land covers. ISPRS J. Photogramm. Remote Sens. *Under review (Revision).*

Norman, J.M., Becker, F., 1995. Terminology in thermal infrared remote sensing of natural surfaces. Agric. For. Meteorol. 77, 153–166. https://doi.org/10.1016/0168-1923(95)02259-Z

Orlando, F., Movedi, E., Paleari, L., Gilardelli, C., Foi, M., Dell'Oro, M., Confalonieri, R., 2015. Estimating leaf area index in tree species using the PocketLAI smart app. Appl. Veg. Sci. 18, 716–723. https://doi.org/10.1111/avsc.12181

Pérez-Planells, L., García-Santos, V., Caselles, V., 2015. Comparing different profiles to characterize the atmosphere for three MODIS TIR bands. Atmos. Res. 161–162. https://doi.org/10.1016/j.atmosres.2015.04.001

Pérez-Planells, L., Valor, E., Coll, C., Niclòs, R., 2017. Comparison and evaluation of the TES and ANEM algorithms for land surface temperature and emissivity separation over the area of Valencia, Spain. Remote Sens., 9(12), 1251. https://doi.org/10.3390/rs9121251

Pérez-Planells, L., Niclòs, R., Valor, E., Puchades, J., Coll, C., García-Santos, V., Caselles, V., 2019a. Spectral characterization of surface emissivities in the thermal infrared, in: Instituto Nacional de Técnica Aeroespacial (INTA), Seminario: Protocolos y Librerías Espectrales En Espectroscopía de Campo. 17 de Marzo de 2019. Torrejón de Ardoz, Madrid.

Pérez-Planells, L., Valor, E., Niclòs, R., Coll, C., Puchades, J., Campos-Taberner, M., 2019b. Evaluation of Six Directional Canopy Emissivity Models in the Thermal Infrared Using Emissivity Measurements. Remote Sens., 11(24), 3011. https://doi.org/10.3390/rs11243011.

Pérez-Planells, L., Niclòs, R., Puchades, J., Coll, C., Göttsche, F.M., Valiente, J. A., Valor, E., Galve, J.M., 2020. Validation of the Sentinel-3 SLSTR operational land surface temperature product and emissivity-dependent split-window algorithms over a rice paddy site. Remote Sens. Environ. *Under review*.

Prata, F., 2002. Land Surface Temperature Measurement from Space: AATSR Algorithm Theoretical Basis Document. Contract Rep. to ESA, CSIRO Atmos. Res. Aspendale, Victoria, Aust. 2002, 1–34.

Prévot, L., 1985. Modélisation des échanges radiatifs au sein des couverts végétaux. Application à la Télédétection. Validation sur un Couvert de Maïs. University of

Paris VI, Paris, France.

Ren, H., Liu, R., Yan, G., Li, Z.-L., Qin, Q., Liu, Q., Nerry, F., 2015. Performance evaluation of four directional emissivity analytical models with thermal SAIL model and airborne images. Opt. Express 23, A346. https://doi.org/10.1364/oe.23.00a346

Rubio, E., Caselles, V., Badenas, C., 1997. Emissivity measurements of several soils and vegetation types in the 8-14 µm wave band: Analysis of two field methods. Remote Sens. Environ. 59, 490–521. https://doi.org/10.1016/S0034-4257(96)00123-X

Rubio, E., Caselles, V., Coll, C., Valor, E., Sospedra, F., 2003. Thermal-infrared emissivites of natural surfaces: Improvements on the experimental set-up and new measurements. Int. J. Remote Sens. 24, 5379–5390. https://doi.org/10.1080/0143116031000102412

Sabol, D.E., Gillespie, A.R., Abbott, E., Yamada, G., 2009. Field validation of the ASTER Temperature-Emissivity Separation algorithm. Remote Sens. Environ. 113, 2328–2344. https://doi.org/10.1016/j.rse.2009.06.008

Salisbury, J.W., D'Aria, D.M., 1994. Emissivity of terrestrial materials in the 3-5 µm atmospheric window. Remote Sens. Environ. 47, 345–361. https://doi.org/10.1016/0034-4257(94)90102-3

Sánchez, J.M., López-Urrea, R., Doña, C., Caselles, V., González-Piqueras, J., Niclòs, R., 2015. Modeling evapotranspiration in a spring wheat from thermal radiometry: crop coefficients and E/T partitioning. Irrig. Sci. 33, 399–410. https://doi.org/10.1007/s00271-015-0476-2

Seemann, S.W., Borbas, E.E., Knuteson, R.O., Stephenson, G.R., Huang, H.L., 2008. Development of a global infrared land surface emissivity database for application to clear sky sounding retrievals from multispectral satellite radiance measurements. J. Appl. Meteorol. Climatol. 47, 108–123. https://doi.org/10.1175/2007JAMC1590.1

Sentinel-3 Optical Products and Algorithm Definition: SLSTR Land Surface Temperarure Algorithm Theoretical Basis Document (ATBD)., 2012. University of Leicester/NILU. Doc. Ref: S3-L2-SD-03-T03-ULNILU-ATBD_L2LST.

Sepulcre-Cantó, G., Zarco-Tejada, P.J., Jiménez-Muñoz, J.C., Sobrino, J.A., Miguel, E., Villalobos, F.J., 2006. Detection of water stress in an olive orchard with thermal remote sensing imagery. Agric. For. Meteorol. 136, 31–44. https://doi.org/10.1016/j.agrformet.2006.01.008

Shi, Y., 2011. Thermal infrared inverse model for component temperatures of mixed pixels. Int. J. Remote Sens. 32, 2297–2309. https://doi.org/10.1080/01431161003698252

Snyder, W.C., Wan, Z., 1998. BRDF models to predict spectral reflectance and emissivity

in the thermal infrared. IEEE Trans. Geosci. Remote Sens. 36, 214–225. https://doi.org/10.1109/36.655331

Snyder, W.C., Wan, Z., Zhang, Y., Feng, Y.Z., 1998. Classification-based emissivity for land surface temperature measurement from space. Int. J. Remote Sens. 19, 2753–2774. https://doi.org/10.1080/014311698214497

Sobrino, J.A., Jiménez-Muñoz, J.C., Verhoef, W., 2005. Canopy directional emissivity: Comparison between models. Remote Sens. Environ. 99, 304–314. https://doi.org/10.1016/j.rse.2005.09.005

Strahler, A., Gopal, S., Lambin, E., Moody, A., 1999. MODIS Land Cover Product Algorithm Theoretical Basis Document (ATBD) MODIS Land Cover and Land-Cover Change. Change 72.

Sulla-Menashe, D., Gray, J.M., Abercrombie, S.P., Friedl, M.A., 2019. Hierarchical mapping of annual global land cover 2001 to present: The MODIS Collection 6 Land Cover product. Remote Sens. Environ. 222, 183–194. https://doi.org/10.1016/j.rse.2018.12.013

Theocharous, E., Usadi, E., Fox, N.P., 2010. CEOS Comparison of IR Brightness Temperature Measurements in Support of Satellite Validation. Part I: Laboratory and Ocean Surface Temperature Comparison of Radiation Thermometers; National Physical Laboratory: Teddington, UK.

Theocharous, E., Barker-Snook, I., Fox, N.P., 2017. 2016 Comparison of IR Brightness Temperature Measurements in Support of Satellite Validation. Part 1: Blackbody Laboratory Comparison. NPL REPORT ENV 12. National Physical Laboratory, Teddington, UK.

Tonooka, H., 2005. Accurate atmospheric correction of ASTER thermal infrared imagery using the WVS method. IEEE Trans. Geosci. Remote Sens. 43, 2778–2792. https://doi.org/10.1109/TGRS.2005.857886

Ullah, S., Skidmore, A.K., Ramoelo, A., Groen, T.A., Naeem, M., Ali, A., 2014. Retrieval of leaf water content spanning the visible to thermal infrared spectra. ISPRS J. Photogramm. Remote Sens. 93, 56–64. https://doi.org/10.1016/j.isprsjprs.2014.04.005

Valor, E., Caselles, V., 1996. Mapping land surface emissivity from NDVI: Application to European, African, and South American areas. Remote Sens. Environ. 57, 167–184. https://doi.org/10.1016/0034-4257(96)00039-9

Valor, E., Caselles, V., 2005. Validation of the vegetation cover method for land surface emissivity estimation, in: Recent Research Developments in Thermal Remote Sensing. Research Signpost, Kerala, India.

Verhoef, W., 1984. Light Scattering by Leaf layers with Application to Canopy

Reflectance Modeling: the SAIL Model. Remote Sens. Environ. 141, 125–141.

Verhoef, W., Jia, L., Xiao, Q., Su, Z., 2007. Unified optical-thermal four-stream radiative transfer theory for homogeneous vegetation canopies. IEEE Trans. Geosci. Remote Sens. 45, 1808–1822. https://doi.org/10.1109/TGRS.2007.895844

Wan, Z., Dozier, J., 1996. A generalized split-window algorithm for retrieving land surface temperature from GF-5 thermal infrared data. IEEE Trans. Geosci. Remote Sens. 34, 892–905. https://doi.org/10.1109/36.508406

Wan, Z., Li, Z.L., 1997. A physics-based algorithm for retrieving land-surface emissivity and temperature from eos/modis data. IEEE Trans. Geosci. Remote Sens. 35, 980–996. https://doi.org/10.1109/36.602541

Wan, Z., 1999. MODIS Land-Surface Temperature Algorithm Theoretical Basis Document (LST ATBD).

Wan, Z., Li, Z.L., 2008. Radiance-based validation of the V5 MODIS land-surface temperature product. Int. J. Remote Sens. 29, 5373–5395. https://doi.org/10.1080/01431160802036565

Wan, Z., 2014. New refinements and validation of the collection-6 MODIS land-surface temperature/emissivity product. Remote Sens. Environ. 140, 36–45. https://doi.org/10.1016/j.rse.2013.08.027

Wang, C., Duan, S.B., Zhang, X., Wu, H., Gao, M.F., Leng, P., 2019. An alternative split-window algorithm for retrieving land surface temperature from Visible Infrared Imaging Radiometer Suite data. Int. J. Remote Sens. 40, 1640–1654. https://doi.org/10.1080/01431161.2018.1492180

Warren, S.G., Wiscombe, W.J., 1980. A Model for the Spectral Albedo of Snow. II: Snow Containing Atmospheric Aerosols. J. Atmos. Sci. 37, 2734–2745. https://doi.org/https://doi.org/10.1175/1520-0469(1980)037<2734:AMFTSA>2.0.CO;2

Wilrich, P.T., 2007. Robust estimates of the theoretical standard deviation to be used in interlaboratory precision experiments. Accredit. Qual. Assur. 12, 231–240. https://doi.org/10.1007/s00769-006-0240-7

Zheng, Y., Ren, H., Guo, J., Ghent, D., Tansey, K., Hu, X., Nie, J., Chen, S., 2019. Land Surface Temperature Retrieval from Sentinel-3A Sea and Land Surface Temperature Radiometer, Using a Split-Window Algorithm. Remote Sens. 11, 650. https://doi.org/10.3390/rs11060650

Anexos

Anexo A

Análisis de sensibilidad de los modelos de transferencia radiativa para la obtención de la emisividad direccional sobre superficies vegetadas

En este anexo se complementa el análisis de incertidumbres mostrado en la Sección 2.7. Para ello, se muestran las contribuciones a la incertidumbre obtenida mostrada por cada MTR en la estimación de la emisividad de superficies vegetadas a distintos ángulos de observación.

La metodología descrita en la Sección 2.7 para la estimación de la incertidumbre asociada a cada MTR para la obtención de la emisividad direccional se ha aplicado a cada uno de los modelos para los 7 ángulos utilizados en el estudio. En las Figuras A.1 – A.6 se muestra la contribución de la incertidumbre de cada uno de los parámetros de entrada en los MTR de emisividad direccional para los ángulos de observación de 0º, 20º, 40º y 60º.

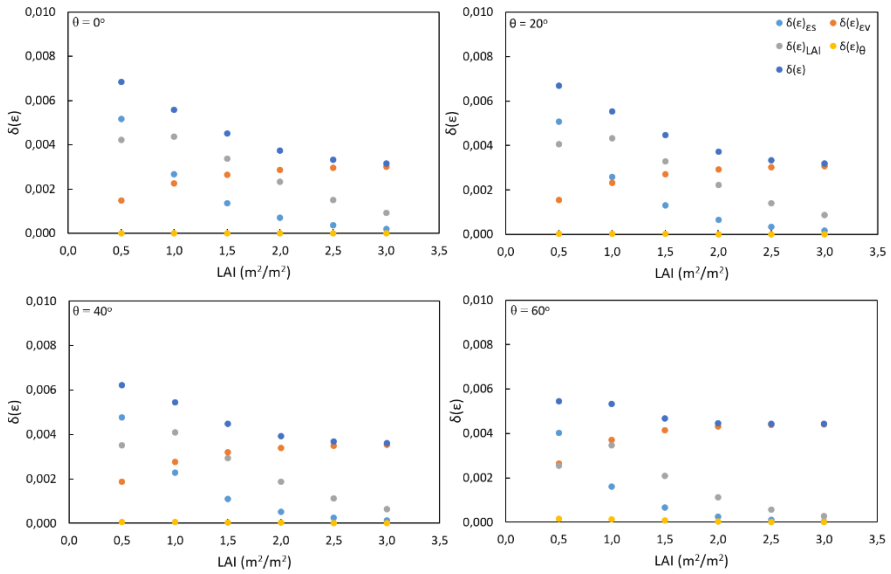

Figura A.1. Contribución de la incertidumbre de emisividad de suelo ($\delta(\varepsilon)_{\varepsilon s}$), de emisividad de hoja ($\delta(\varepsilon)_{\varepsilon v}$), del LAI ($\delta(\varepsilon)_{LAI}$) y del ángulo de observación ($\delta(\varepsilon)_{\theta}$) a la incertidumbre asociada a la emisividad del MTR ($\delta(\varepsilon)$) FR97 para cada LAI y los ángulos de observación de 0º, 20º, 40º y 60º.

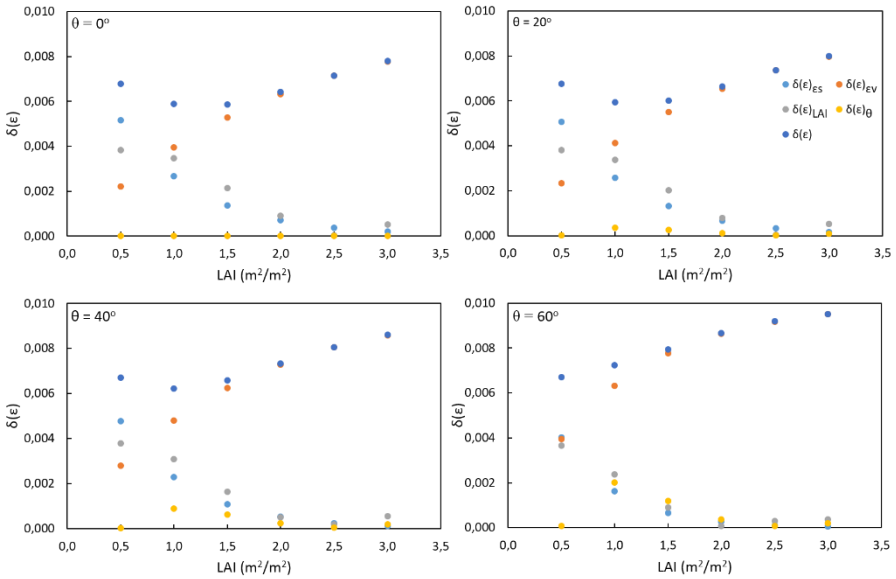

Figura A.2. Contribución de la incertidumbre de emisividad de suelo ($\delta(\varepsilon)_{\varepsilon s}$), de emisividad de hoja ($\delta(\varepsilon)_{\varepsilon v}$), del LAI ($\delta(\varepsilon)_{LAI}$) y del ángulo de observación ($\delta(\varepsilon)_{\theta}$) a la incertidumbre asociada a la emisividad del MTR ($\delta(\varepsilon)$) Mod3 para cada LAI y los ángulos de observación de 0º, 20º, 40º y 60º.

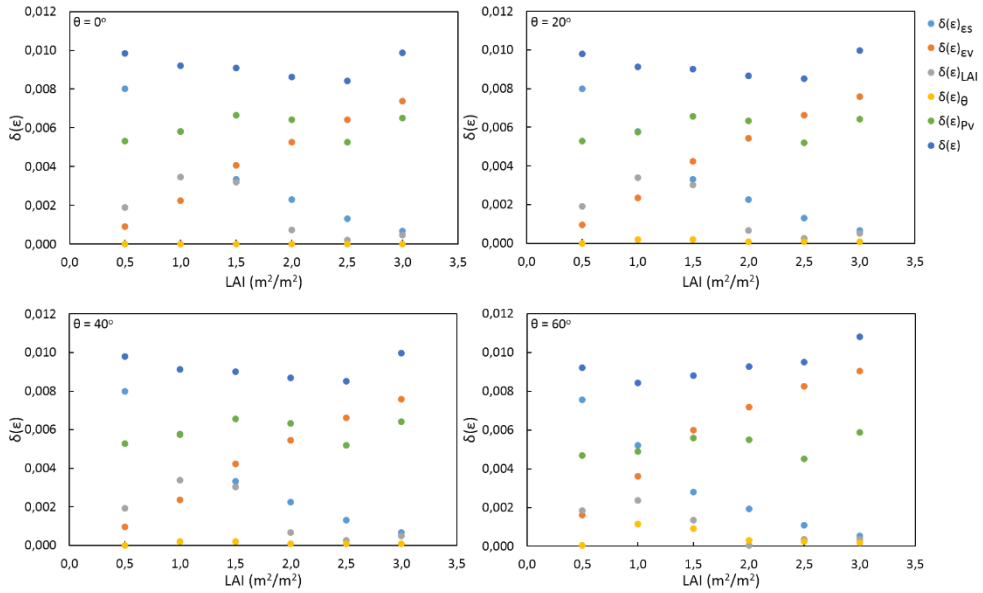

Figura A.3. Contribución de la incertidumbre de emisividad de suelo ($\delta(\varepsilon)_{\varepsilon s}$), de emisividad de hoja ($\delta(\varepsilon)_{\varepsilon v}$), del LAI ($\delta(\varepsilon)_{LAI}$), de la proporción de vegetación ($\delta(\varepsilon)_{Pv}$) y del ángulo de observación ($\delta(\varepsilon)_{\theta}$) a la incertidumbre asociada a la emisividad del MTR ($\delta(\varepsilon)$) Rmod3 para cada LAI y los ángulos de observación de 0º, 20º, 40º y 60º.

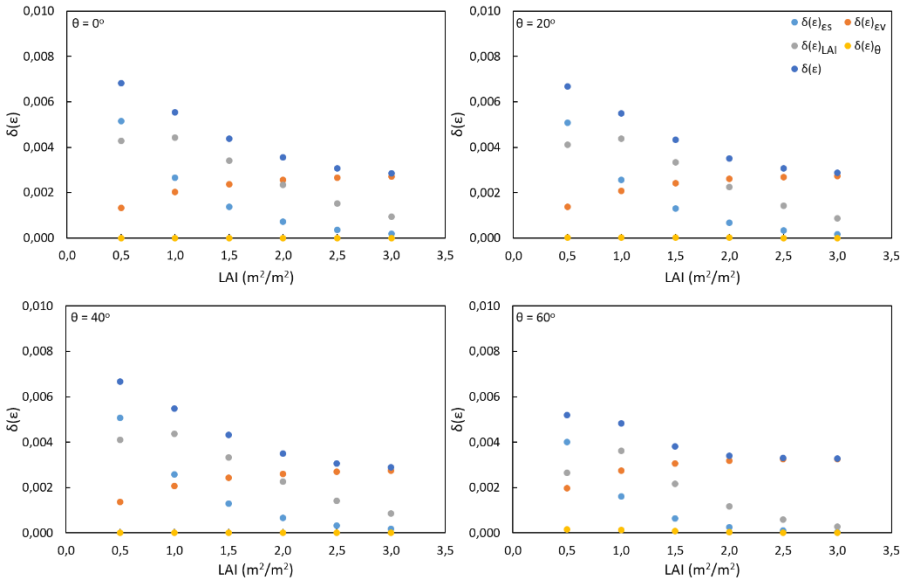

Figura A.4. Contribución de la incertidumbre de emisividad de suelo ($\delta(\varepsilon)_{\varepsilon s}$), de emisividad de hoja ($\delta(\varepsilon)_{\varepsilon v}$), del LAI ($\delta(\varepsilon)_{LAI}$) y del ángulo de observación ($\delta(\varepsilon)_{\theta}$) a la incertidumbre asociada a la emisividad del MTR ($\delta(\varepsilon)$) REN15 para cada LAI y los ángulos de observación de 0º, 20º, 40º y 60º.

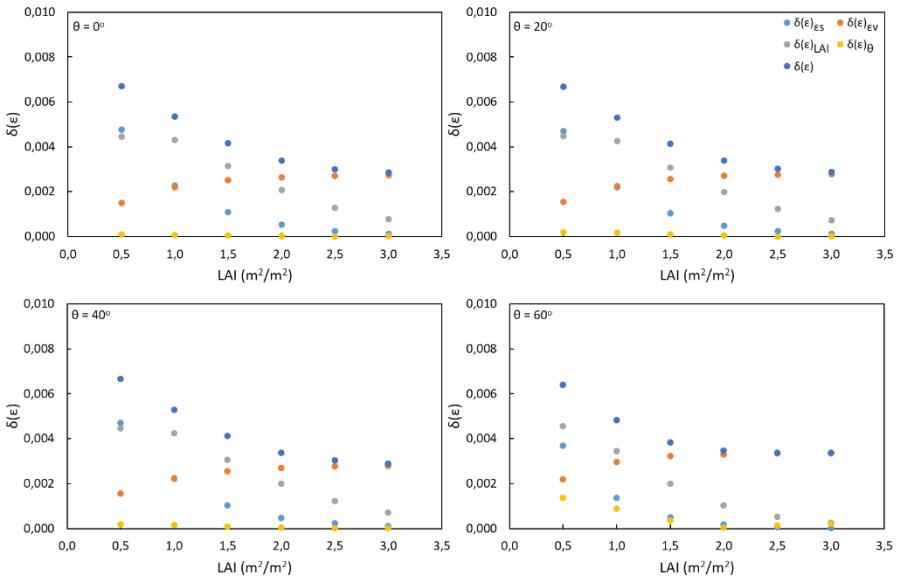

Figura A.5. Contribución de la incertidumbre de emisividad de suelo ($\delta(\varepsilon)_{\varepsilon s}$), de emisividad de hoja ($\delta(\varepsilon)_{\varepsilon v}$), del LAI ($\delta(\varepsilon)_{LAI}$) y del ángulo de observación ($\delta(\varepsilon)_{\theta}$) a la incertidumbre asociada a la emisividad del MTR ($\delta(\varepsilon)$) 4SAIL para cada LAI y los ángulos de observación de 0º, 20º, 40º y 60º.

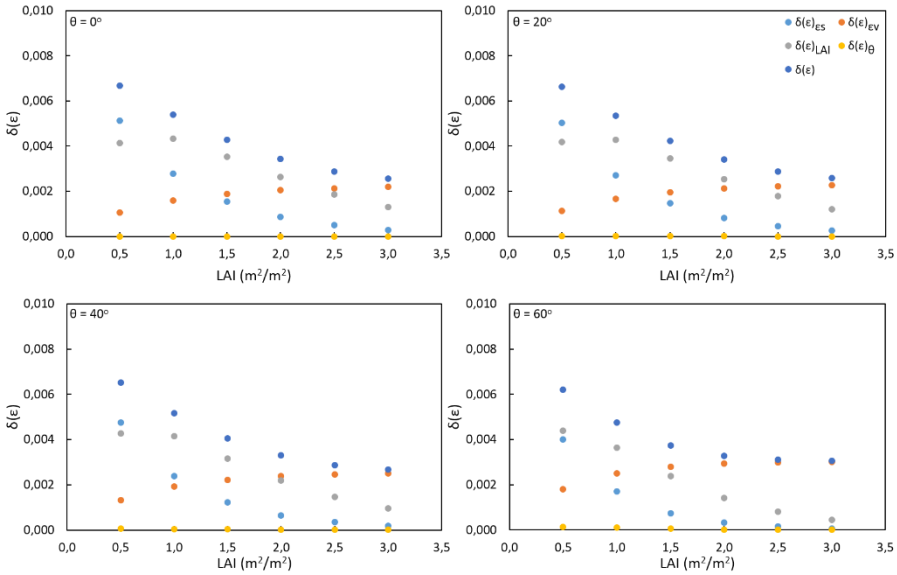

Figura A.6. Contribución de la incertidumbre de emisividad de suelo ($\delta(\varepsilon)_{\varepsilon s}$), de emisividad de hoja ($\delta(\varepsilon)_{\varepsilon v}$), del LAI ($\delta(\varepsilon)_{LAI}$) y del ángulo de observación ($\delta(\varepsilon)_{\theta}$) a la incertidumbre asociada a la emisividad del MTR ($\delta(\varepsilon)$) CE-P para cada LAI y los ángulos de observación de 0º, 20º, 40º y 60º.

Anexo B

Definiciones de las clases de superficie IGBP

En este anexo se definen las clases de tipo de superficie del producto MCD12Q1 de MODIS basadas en la clasificación del International Geosphere-Biosphere Programme (IGBP).

El producto MODIS MCD12Q1 está basado en las 17 clases de superficie definidas por el *International Geosphere-Biosphere Programme* (IGBP, Loveland y Belward, 1997). En la Tabla B. 1 se muestra la definición de estas 17 clases.

Tabla B. 1. Definición de las 17 clases de superficie terrestre de la clasificiación IGBP. Tabla extraída de Loveland y Belward (1997) y mostrada también en el documento de base teórica del algoritmo (ATBD) del producto MODIS MCD12Q1 (Strahler et al., 1999).

Natural Vegetation		
1	Evergreen Needleleaf Forests	Lands dominated by woody vegetation with a percent cover >60% and height exceeding 2 meters. Almost all trees remain green all year. Canopy is never without green foliage.
2	Evergreen Broadleaf Forests	Lands dominated by woody vegetation with a percent cover >60% and height exceeding 2 meters. Almost all trees and shrubs remain green year round. Canopy is never without green foliage.
3	Deciduous Needleleaf Forests	Lands dominated by woody vegetation with a percent cover >60% and height exceeding 2 meters. Consists of seasonal needleleaf tree communities with an annual cycle of leaf-on and leaf-off periods.
4	Deciduous Broadleaf Forests	Lands dominated by woody vegetation with a percent cover >60% and height exceeding 2 meters. Consists of broadleaf tree communities with an annual cycle of leaf-on and leaf-off periods.
5	Mixed Forests	Lands dominated by trees with a percent cover >60% and height exceeding 2 meters. Consists of tree communities with interspersed mixtures or mosaics of the other four forest types. None of the forest types exceeds 60% of landscape.
6	Closed Shrublands	Lands with woody vegetation less than 2 meters tall and with shrub canopy cover >60%. The shrub foliage can be either evergreen or deciduous.
7	Open Shrublands	Lands with woody vegetation less than 2 meters tall and with shrub canopy cover between 10-60%. The shrub foliage can be either evergreen or deciduous.
8	Woody Savannas	Lands with herbaceous and other understory systems, and with forest canopy cover between 30-60%. The forest cover height exceeds 2 meters.
9	Savannas	Lands with herbaceous and other understory systems, and with forest canopy cover between 10-30%. The forest cover height exceeds 2 meters.
10	Grasslands	Lands with herbaceous types of cover. Tree and shrub cover is less than 10%.
11	Permanent Wetlands	Lands with a permanent mixture of water and herbaceous or woody vegetation. The vegetation can be present in either salt, brackish, or fresh water.
Developed and Mosaic Lands		
12	Croplands	Lands covered with temporary crops followed by harvest and a bare soil period (e.g., single and multiple cropping systems). Note that perennial woody crops will be classified as the appropriate forest or shrub land cover type.
13	Urban and Built-Up Lands	Land covered by buildings and other man-made structures.
14	Cropland/Natural Vegetation Mosaics	Lands with a mosaic of croplands, forests, shrubland, and grasslands in which no one component comprises more than 60% of the landscape.
Non-Vegetated Lands		
15	Snow and Ice	Lands under snow/ice cover throughout the year.
16	Barren	Lands with exposed soil, sand, rocks, or snow and never has more than 10% vegetated cover during any time of the year.
17	Water Bodies	Oceans, seas, lakes, reservoirs, and rivers. Can be either fresh or salt-water bodies.

Anexo C

Mapas generados de emisividad direccional de la superficie vegetada

En este anexo se muestran los mapas de emisividad direccional de la Península Ibérica generados haciendo uso de los MTR FR97, Mod3, REN15, 4SAIL y CE-P analizados en este estudio. Para generar los mapas de emisividad direccional de la Península Ibérica se han utilizado los productos mostrados en la Sección 5.1. Estos mapas se han generado para todos los días del año 2015, generando dos imágenes diarias correspondientes a la pasada diurna y nocturna del sensor MODIS – Aqua para los canales centrados en 8,55 µm (canal 29), 11,02 µm (canal 31) y 12,03 (canal 32). En total se han obtenido 10950 imágenes. En este anexo se muestran los mapas obtenidos por los distintos MTR para los canales 29 y 31 del sensor MODIS y para 4 días del año 2015 en distintas estaciones: 24 de febrero – invierno, 14 de mayo – primavera, 12 de agosto – verano y 10 de noviembre – otoño.

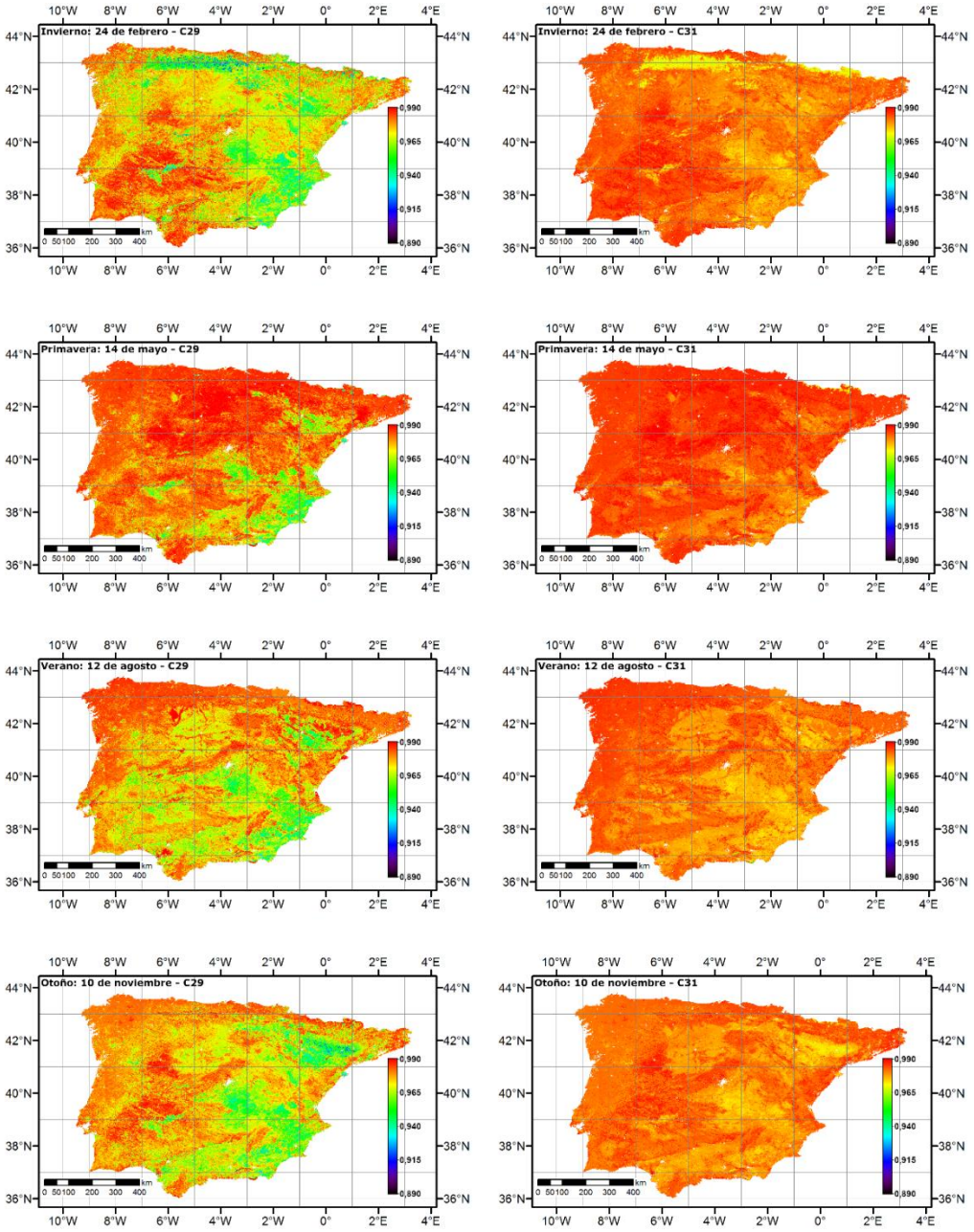

Figura C.1. Emisividad direccional obtenida con el MTR FR97 para los canales MODIS 29 (izquierda) y 31 (derecha) para cuatro días del año 2015.

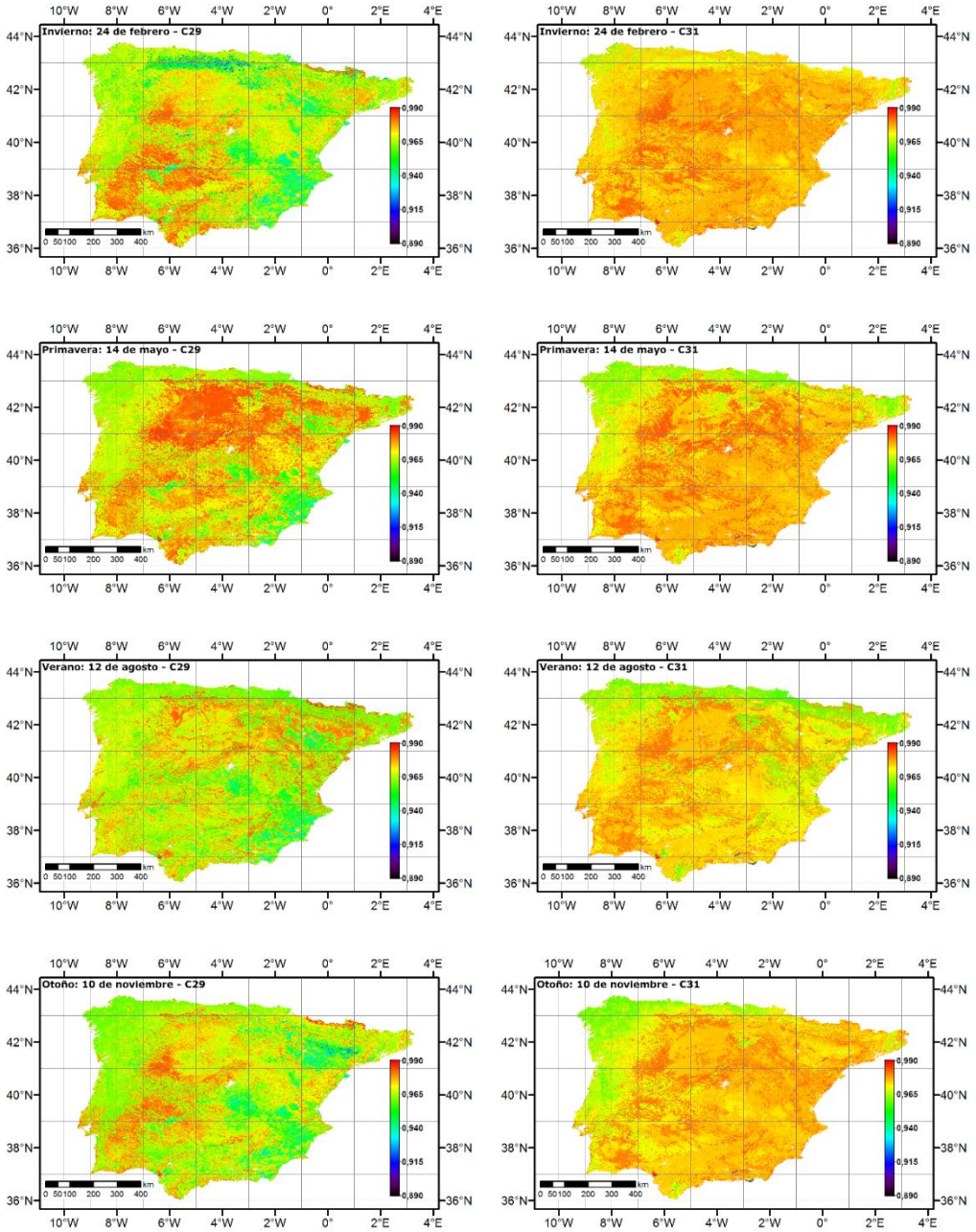

Figura C.2. Emisividad direccional obtenida con el MTR Mod3 para los canales MODIS 29 (izquierda) y 31 (derecha) para cuatro días del año 2015.

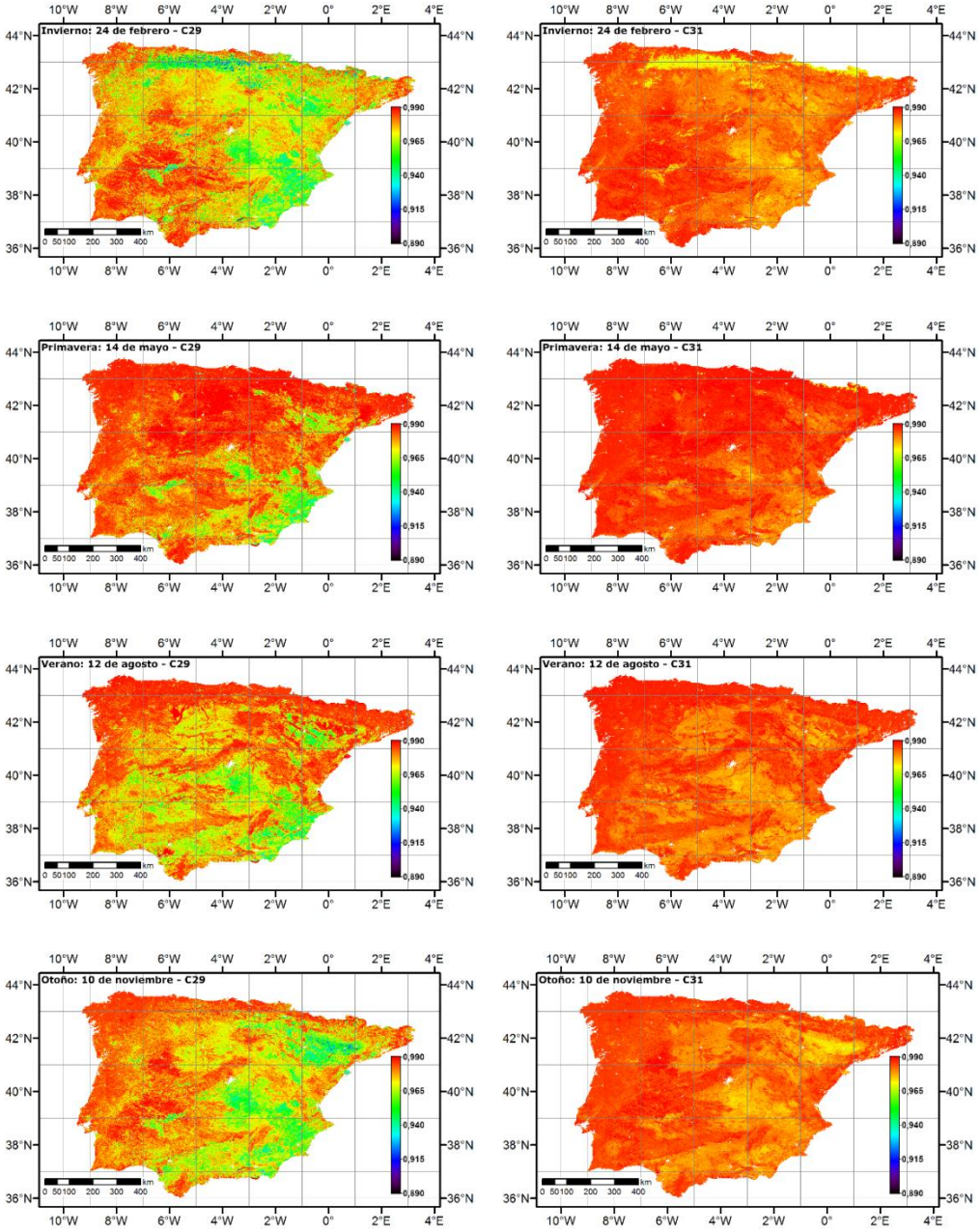

Figura C.3. Emisividad direccional obtenida con el MTR REN15 para los canales MODIS 29 (izquierda) y 31 (derecha) para cuatro días del año 2015.

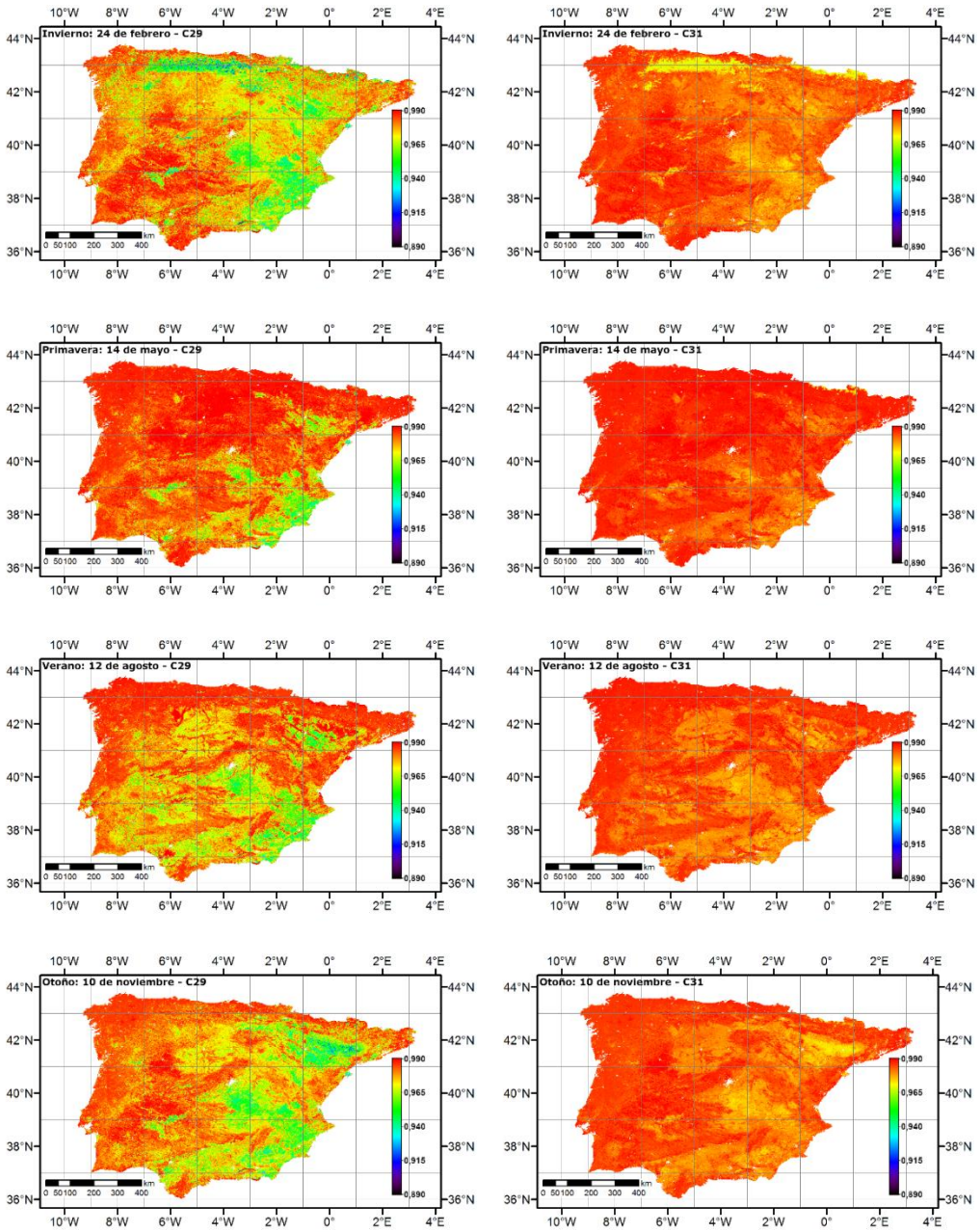

Figura C.4. Emisividad direccional obtenida con el MTR 4SAIL para los canales MODIS 29 (izquierda) y 31 (derecha) para cuatro días del año 2015.

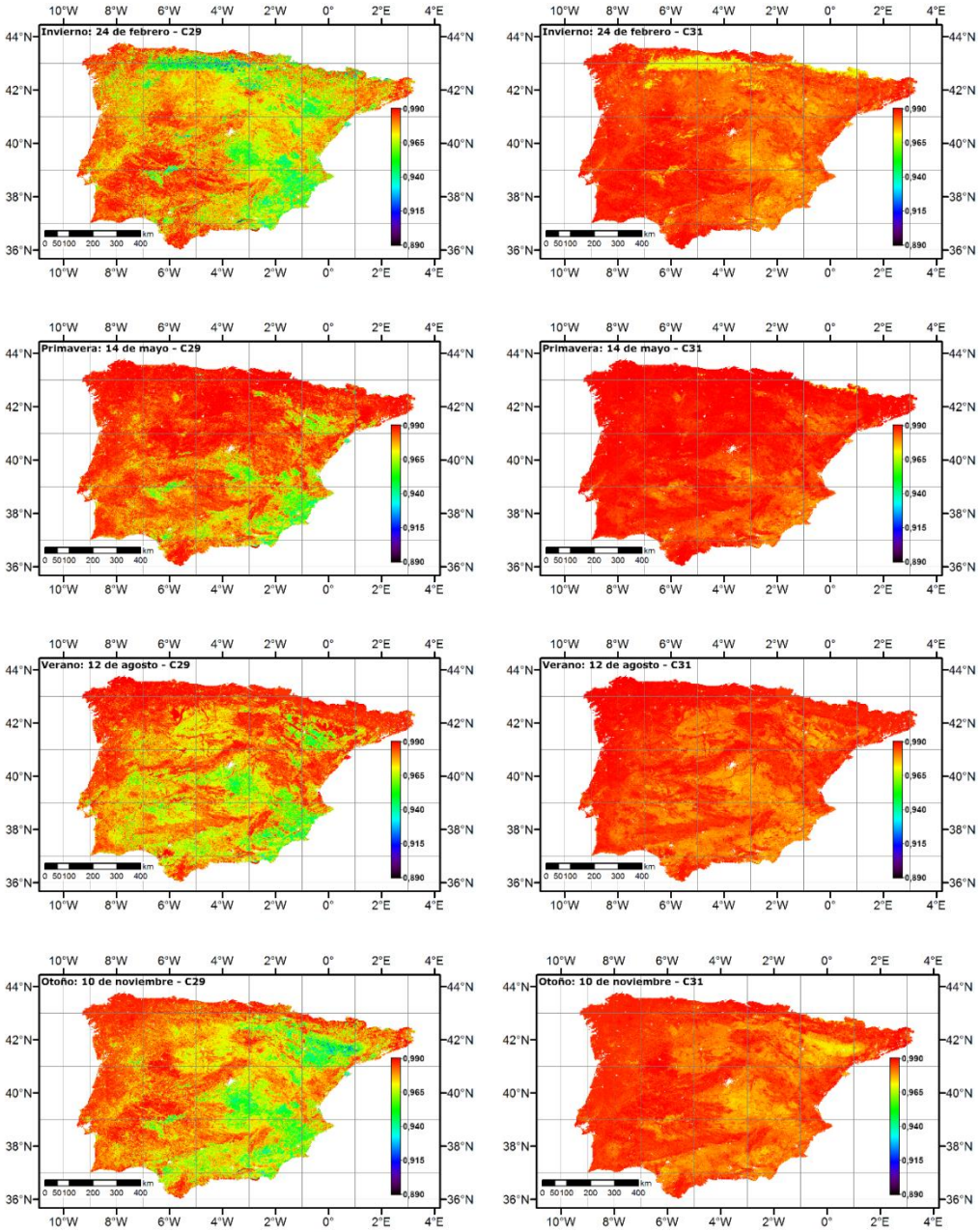

Figura C.5. Emisividad direccional obtenida con el MTR CE-P para los canales MODIS 29 (izquierda) y 31 (derecha) para cuatro días del año 2015.

Anexo D

Validación del algoritmo *split-window* generalizado refinado para los sensores SLSTR y TIRS

En este anexo se muestra la validación del algoritmo split-window utilizado para la obtención de la TST en la Sección 6. Esta validación se ha realizado con datos del sensor SLSTR a bordo del satélite Sentinel-3A y con datos del sensor TIRS a bordo del satélite Landsat-8. Estas validaciones se muestran en los trabajos Pérez-Planells et al. (2020) y Niclòs et al. (2020).

El algoritmo split-window (SW) generalizado fue propuesto por Wan y Dozier (1996). Este algoritmo SW ha sido utilizado en el producto operativo MOD11 para la obtención de la TST del sensor MODIS. La última versión de este producto, correspondiente a la Colección 6, fue generada utilizando el algoritmo SW generalizado refinado propuesto por Wan (2014). Dicho algoritmo es una actualización de la versión original del algoritmo SW de Wan y Dozier (1996), la cual añade un término con la diferencia al cuadrado de las temperaturas de los canales de 11 y 12 µm multiplicadas por un coeficiente (ecuación (16), Sección 6). El algoritmo SW generalizado refinado fue aplicado por Zheng et al. (2019; Zheng19) a datos del sensor *Sea and Land Surface Temperature Radiometer* (SLSTR) a bordo del satélite Sentinel-3A. Asimismo, fue aplicado por Meng et al. (2019) a datos del sensor *Thermal Infrared Radiometer Sensor* (TIRS) a bordo del satélite Landsat-8. Los coeficientes propuestos por Meng et al. (2019) para TIRS, fueron generados tanto para distintos intervalos de contenido de vapor de agua (Meng19_W), como para contenidos de vapor de agua entre 0 y 7 cm (Meng19).

Los algoritmos Zheng19, Meng19 y Meng19_W los validamos utilizando datos del sensor SLSTR en Pérez-Planells et al. (2020) y datos del sensor TIRS en Niclòs et al. (2020) sobre la zona de validación de TST de Valencia (Coll et al., 2005). Además, en Pérez-Planells et al. (2020) se validó el algoritmo utilizado por el producto operativo del sensor SLSTR, el cual asigna coeficientes al algoritmo según el tipo de bioma asignado a cada píxel (SLSTR LST ATBD, 2012).

Zona de validación de Valencia

La zona de validación de TST de Valencia consiste en una zona homogénea de arrozales de ~100 km^2 centrada en las coordenadas 39º16’22” N, 0º19’7” W (Coll et al., 2005). Debido a las labores agrícolas del cultivo del arroz, esta zona varía el tipo de superficie de forma cíclica a lo largo del año, contando así con tres tipos de superficie distintas: suelo sin vegetación desde febrero a mayo, agua (suelo inundado) en enero, junio y diciembre, y vegetación (arroz) desde julio a septiembre. En esta zona contamos con una estación de medidas fija para el seguimiento continuo de la TST. La estación cuenta con dos radiómetros de banda ancha Apogee SI-121 (8 – 14 µm). Estos radiómetros

tienen un campo de visión de 36º y una incertidumbre de medida de ±0,2 K según el fabricante (www.apogeeinstruments.com). Estos radiómetros fueron calibrados regularmente frente a la fuente de cuerpo negro Landcal P80P en nuestro laboratorio obteniendo una precisión de ±0,2 K para el intervalo de temperaturas entre 273 K y 323 K. Además, durante la campaña internacional organizada por el *Committee on Earth Observation Satellites* (CEOS) en 2009 para la comparación de radiómetros del IRT, estos radiómetros fueron comparados frente a un cuerpo negro de referencia del *National Institute of Standards and Technology* (NIST) con temperaturas entre 283 y 303 K, obteniendo una precisión mejor a ±0,2 K (Theocharous et al., 2010; Niclòs et al., 2015). Los radiómetros están instalados a tres metros de altura, uno de ellos observando la superficie con visión a nadir y el otro instalado con un ángulo de observación de 53º desde el cenit, tomando medidas representativas de la radiancia hemisférica descendente (García-Santos et al., 2013; Guillevic et al., 2018).

Tratamiento de los datos *in-situ*

Para la validación de productos TST obtenidos con datos del sensor SLSTR, se utilizaron como referencia las medidas de los dos radiómetros SI-121 adquiridas dentro del periodo comprendido entre los tres minutos anteriores y posteriores a la pasada del satélite Sentinel-3A. A partir de estas medidas, la temperatura de brillo (T_b) fue corregida de la emisividad y de la radiancia hemisférica descendente reflejada en la superficie. Para la corrección de emisividad, se utilizaron valores medidos *in-situ* sobre cada superficie mediante las técnicas descritas en la Sección 1.2.1. La ecuación (10) (Sección 3.2) fue aplicada para la obtención de la radiancia corregida del efecto atmosférico y de la emisividad, a partir de la cual se obtuvo la TST correspondiente a cada medida mediante la inversión de la ley de Planck. La TST utilizada para la validación se obtuvo del promedio de las TSTs obtenidas de cada una de las medidas adquiridas.

En cuanto a la validación del algoritmo SW con datos del sensor TIRS, esta fue realizada haciendo uso de medidas de radiancia tomadas durante la realización de transectos de ~300 m sobre la zona de validación con los radiómetros multicanal CE312. A partir de las medidas de radiancia adquiridas con estos radiómetros, se siguió el mismo

procedimiento de corrección atmosférica y de emisividad utilizado para los radiómetros de banda ancha SI-121. En este caso, la radiancia descendente hemisférica fue medida haciendo uso de un panel de oro de alta reflectividad en el IRT (IRT-94-100) de la casa Labsphere (García-Santos et al., 2013).

El sensor SLSTR tiene un periodo de revisita diario, por lo que hacer uso de los datos adquiridos con la estación fija nos permite disponer de una mayor cantidad de datos coincidentes, ya que contamos tanto con datos diurnos como nocturnos que estén libres de nubosidad. Por ello, para la validación del producto operativo del sensor SLSTR a bordo de la plataforma Sentinel-3A se utilizaron datos de la estación fija de medidas de TST entre agosto 2016 y abril 2020. En total, se dispuso de 194 datos coincidentes con las pasadas del satélite Sentinel-3A libres de nubosidad en el caso del producto operativo de TST del sensor SLSTR, y de 201 datos coincidentes de datos de temperatura de brillo (nivel 1) utilizados para la aplicación del algoritmo SW. En ambos casos, los datos con presencia de nubes fueron identificados y eliminados haciendo uso de la máscara de nubes del producto operativo del sensor SLSTR. Además, para asegurar la representatividad de las medidas tomadas por la estación fija sobre la zona, sus datos fueron comparados con datos de transectos sobre la zona de estudio. Para ello, se utilizó un conjunto de doce transectos coincidentes con la adquisición de datos de TST de la estación fija y con la pasada del sensor SLSTR. De esta comparación se obtuvo un sesgo de -0,15 K y una desviación estándar de ±0,35 K, determinando así la representatividad sobre la zona de estudio de los datos tomados por la estación fija.

En el caso del sensor TIRS, aunque el periodo de revisita es de 16 días, sobre la zona de validación de Valencia se superponen dos órbitas (órbitas 198 y 199), permitiendo así la adquisición de dos escenas sobre esta zona cada 16 días. Debido a la menor resolución temporal (mayor periodo de revisita) de este sensor, la cantidad de días libres de nubosidad coincidentes con la pasada del sensor son menores. Esto nos permitió hacer un seguimiento continuo de las pasadas del satélite Landsat-8 en días completamente libres de nubosidad y condiciones superficiales óptimas en cuanto a homogeneidad espacial entre los años 2014 y 2019, realizando transectos coincidentes con dichas

pasadas en aquellos días que reunieron dichas condiciones óptimas para la validación de la TST. En total se obtuvo 25 transectos representativos sobre la zona de validación coincidentes con las pasadas del satélite Landsat-8 en días libres de nubosidad.

Resultados

Los estadísticos obtenidos de la validación del producto TST operativo del sensor SLSTR y del algoritmo Zheng19 aplicado a datos de este sensor se muestran en la Tabla D.1.

Tabla D.1. Sesgo, desviación estándar (SD) y raíz del error cuadrático medio (RMSE) de la TST del producto operativo del sensor SLSTR a bordo del satélite Sentinel-3A y del algoritmo Zheng19 frente a datos *in-situ* en la zona de validación de Valencia. N es el número de datos utilizados en el estudio.

	Sesgo (K)	SD (K)	RMSE (K)	N
Producto TST Operativo	1,3	1,3	1,8	194
Zheng19	0,2	1,4	1,4	201

La validación del producto operativo de TST del sensor SLSTR muestra una sobreestimación del producto de TST sobre la zona de validación de Valencia (Tabla D.1), con un error tanto sistemático como aleatorio superior a los umbrales propuestos por el GCOS para la validación de la TST (< 1 K). En el caso del algoritmo Zheng19, el error sistemático es de +0,2 K, mejorando considerablemente el valor obtenido por el producto operativo, mientras que muestra un error aleatorio similar al obtenido por el algoritmo operativo. Esta diferencia en errores sistemáticos puede ser debida al ajuste realizado en la emisividad en el algoritmo SW generalizado, ya que el algoritmo operativo tiene el mismo bioma asignado (cultivo de regadío) para las tres superficies presentes en la zona de estudio.

En la Tabla D.2 se muestran los estadísticos obtenidos de la validación de los algoritmos Meng19 y Meng19_W aplicados al sensor TIRS sobre la zona de validación de Valencia.

Tabla D.2. Sesgo, desviación estándar (SD) y raíz del error cuadrático medio (RMSE) de la TST del algoritmo Meng19 y Meng19_W frente a datos de transectos tomados *in-situ* en la zona de validación de Valencia. N es el número de datos utilizados en el estudio.

	Sesgo (K)	SD (K)	RMSE (K)	N
Meng19	0,7	0,7	1,0	25
Meng19_W	0,4	0,7	0,8	25

De la validación de los algoritmos Meng19 y Meng19_W mostrada en la Tabla D.2 se puede observar que ambos algoritmos obtienen resultados similares, con un error sistemático y aleatorio dentro de los umbrales propuestos por el GCOS (2016) para la validación de la TST (< 1 K), determinando así el buen funcionamiento del algoritmo y de los coeficientes generados.

Anexo E

Comparing different profiles to characterize the atmosphere for three MODIS TIR bands

El siguiente trabajo fue publicado en Atmospheric Research en abril del 2015. Esta revista tiene un factor de impacto de 3,38 y ocupa la posición 18 de 84 revistas en la categoría Meteorology and Atmospheric Sciences según Journal Citation Reports en la edición de 2015.

Atmospheric Research 161–162 (2015) 108–115

Contents lists available at ScienceDirect

Atmospheric Research

journal homepage: www.elsevier.com/locate/atmos

Comparing different profiles to characterize the atmosphere for three MODIS TIR bands

Lluís Pérez-Planells, Vicente García-Santos, Vicente Caselles *

Department of Earth Physics and Thermodynamics, Faculty of Physics, University of Valencia, 46100 Valencia, Spain

ARTICLE INFO

Article history:
Received 19 November 2014
Received in revised form 24 March 2015
Accepted 9 April 2015
Available online 15 April 2015

Keywords:
NCEP
MOD07
Radiosoundings
LST
Atmospheric profiles
MODTRAN

ABSTRACT

Accurate land surface temperature (LST) retrievals from sensors aboard orbiting satellites are dependent on the corresponding atmospheric correction, especially in the thermal infrared (TIR) spectral domain (8–14 μm). To remove the atmospheric effects from at-sensor measured radiance in the TIR range it is needed to characterize the atmosphere by means of three specific variables: the upwelling path and the hemispherical downwelling radiances plus the atmospheric transmissivity. Those variables can be derived from the previous knowledge of vertical atmospheric profiles of air temperature and relative humidity at different geo-potential heights and pressures.

In this work, the above mentioned atmospheric variables were analyzed for three specific weather station sites located in Spain, at three different altitudes. These variables were calculated with atmospheric profiles retrieved from three different sources: The National Centers for Environmental Prediction (NCEP) web-tool atmospheric profiles calculator, the MODIS (MOD07) product and the radiosoundings available on the web of the University of Wyoming (WYO), which are launched by the Agencia Estatal de Meteorologia (AEMET), in the particular case of Spain. Atmospheric profiles from 2010 to 2013 were obtained to carry out the present study.

Results from comparison of these three different atmospheric profiles show that the NCEP profiles characterize the atmosphere in a better manner than MOD07. Average result values of the three MODIS spectral bands 29, 31 and 32 show a BIAS of 0.06 $Wm^{-2}\,\mu m^{-1}\,sr^{-1}$ and RMSE of ± 0.2 $Wm^{-2}\,\mu m^{-1}\,sr^{-1}$ for upwelling radiance, a BIAS of 0.13 $Wm^{-2}\,\mu m^{-1}\,sr^{-1}$ and RMSE of ± 0.3 $Wm^{-2}\,\mu m^{-1}\,sr^{-1}$ for the donwelling radiance and a BIAS of -0.008 and RMSE of ± 0.03 for the atmospheric transmissivity.

In terms of simulated LST, these errors yield a deviation of ± 0.9 K when applying a single-channel method.

1. Introduction

Surface radiance measurements taken by remote sensing instruments aboard satellites are affected by the atmosphere. In the particular case of the thermal infrared region (3–14 μm), there exists two specific spectral ranges located at 3.7–4.1 μm and 8–14 μm, where the atmosphere shows the lowest radiative effect, mainly due to the water vapor content (W).

The land surface temperature (LST) is a variable of great interest in numerous meteorological and climatological studies, and its accurate retrieval is of prime interest to estimate energy and water fluxes budgets between the surface and atmosphere (Sánchez et al., 2011, 2014). The main concerns in retrieving LST from satellite data are the atmospheric and emissivity correction (Jiang and Liu, 2014). Currently LST can be obtained from several algorithms dependent on the sensor specifications (Zhou et al., 2012). Two of these techniques are the single-channel (SC; Vlassova et al., 2014) and the temperature and emissivity separation (TES; Hulley et al., 2014) methods. Both algorithms derive the LST from inversion of the radiative transfer equation (RTE), which at the same time needs the previous knowledge of a characterized atmosphere, among other factors. The radiation measured with a radiometric sensor is composed of a double contribution: first, the radiation directly emitted by the surface, and secondly, the radiation reflected in the surface, coming from the surroundings and the atmosphere. In addition, if the measurement is taken from satellite, the atmosphere contributes in two different ways: on the one hand, absorbing part of the surface radiation and in the other, emitting radiation directly to the sensor. RTE connects the at-sensor radiation and the radiation emitted by the surface through an energy balance defined as:

$$L_i^{TOA} = \tau_i\left[\varepsilon_i B_i(T) + (1-\varepsilon_i)L_{i,hem}^{\downarrow}\right] + L_i^{\uparrow}(\theta) \quad (1)$$

where τ_i is the atmospheric transmissivity at the spectral range i, ε_i is the surface spectral emissivity, $B_i(T)$ is the Planck function for black body spectral radiance at temperature T, $L_{i,hem}^{\downarrow}$ is the downwelling hemispheric radiance, $L_i^{\uparrow}(\theta)$ is the upwelling path radiance at zenith angle θ, and L_i^{TOA} is the radiance measured by the sensor at the top of the atmosphere. All the surface and atmospheric factors exposed in Eq. (1) can be found explicitly defined in the reviewing publication of García-Santos

* Corresponding author.
E-mail address: Vicente.Caselles@uv.es (V. García-Santos).

http://dx.doi.org/10.1016/j.atmosres.2015.04.001
0169-8095/

et al. (2010). The W present in the atmosphere affects directly to the value of these atmospheric parameters (τ_i, $L^{\downarrow}_{i,hem}$, $L^{\uparrow}_{i}(\theta)$).

Nowadays, the most suitable way to characterize the atmosphere is by using a radiative transfer code (RTC; Berk et al., 2011), which calculates the atmospheric factors from introducing vertical profiles of pressure, air temperature and humidity at different levels of altitude. Probably, the best representative profile of the corresponding atmosphere is obtained from radiosounding data, acquired with a launched balloon. However, this data is rarely available at the time and location of the measurements acquisition. As an alternative, there exists the possibility to obtain an atmospheric profile derived from the spectral features of overpassing satellite sensor as well as with interpolating models (in space and time) based on radiosounding data acquired close to a selected point (Jiménez-Muñoz et al., 2010).

The objective of this paper is to analyze differences on the atmospheric variables, τ_i, $L^{\downarrow}_{i,hem}$, $L^{\uparrow}_{i}(\theta)$, after applying on MODTRAN RTC (Berk et al., 2011) different vertical profiles of cloudless days. These profiles are obtained from three different sources: a) modeled MODIS spectral measured radiances (MOD07; Borbas et al., 2011) profiles, b) spatial and temporal interpolated National Centers for Environmental Prediction (NCEP) atmospheric profiles (Barsi et al., 2005), c) radiosounding data measured by balloons launched by AEMET and showed on the web of the Department of Atmospheric Science in the University of Wyoming (WYO).

In previous studies carried out by Coll et al. (2012) and Li et al. (2013), the LST obtained from satellite data using SC methods were compared with in situ ground LST measurements, after applying different atmospheric profiles obtained from the NCEP and the MOD07 product. In both cases, these studies obtained good results for the LST comparison, but MOD07 introduced greater errors in the LST retrievals ($\pm$1.0 K for NCEP and MOD07 in Coll et al., 2012 and $\pm$1.1 K for NCEP and $\pm$1.2 K for MOD07 in Li et al., 2013). This paper faces the same objective pursued by Coll et al. (2012) and Li et al. (2013) but in a different and profuse manner. The most important contribution in this paper is that the comparison of atmospheric parameters obtained from NCEP and MOD07 profiles with in situ radiosounding data has been done for a period of 4 years (from 2010 to 2013), and for three different sites with differences in the heights above sea level as well as in the distances from the corners used by NCEP to interpolate the profiles, yielding to more representative statistical results. In addition, results and statistics from MODIS band 29 (8.4–8.7 μm) are included. This band, which is not analyzed before in the other papers, is added to the study. It is important an accurate atmospheric correction between 8.4 and 8.7 μm, which is required in mineralogical and geological research purposes. For instance, mapping geological presence of minerals, like quartz, based on measurements in the reststrahlen region 8–9 μm, where the emissivity of quartz decreases in a very pronounced manner.

Section 2 describes the methodology applied to reach the fixed objective. Section 3, shows the results obtained and the corresponding discussions. A simulation study was carried out in Section 4 to evaluate the effect in terms of LST when applying SC method with NCEP and MOD07 profiles if in-situ radiosounding data is not available. Finally, the main conclusions of the study are given in Section 5.

2. Materials and methods

2.1. Site

The three selected sites for the study are located at Spain (Murcia, Zaragoza and Madrid). They have been chosen because, from the different Wyoming radiosounding data available, they represent different altitudes above sea level.

The site situated at lesser height above the sea level is Murcia (62 m). The radiosoundings are launched at the Territorial Center of AEMET of Murcia, located at 3.5 km from the city (38°N, 1°9′W).

Another region analyzed is focused on the airport of Zaragoza (41°39′N, 1°1′W) at 264 meters of altitude above sea level, and 10 km west from the city.

Finally, as in the case of Zaragoza, in the Madrid area the radiosoundings are launched at the Airport Adolfo Suarez–Barajas (40°30′N, 3°34′W), located at 611 m above sea level and 12 km from the city, in north–east direction.

2.2. Atmospheric profiles

The spatial and temporal representativeness of radiosounding data is a questionable point in some studies. It is used to consider radiosounding data with a spatial representativeness of 250 km (Huntrieser et al., 1997) and temporal representativeness of 12 h. But these values could be lower in some cases due to the variability of the atmosphere, as happens in mountain areas as Ebro valley (Merino et al., 2013). Different atmospheric profiles are proposed to analyze in these study.

2.2.1. NCEP

The on-line atmospheric correction tool (http://atmcorr.gsfc.nasa.gov, last accessed on February 2015) provides the atmospheric parameters needed to make the atmospheric correction in the thermal band of the satellites Landsat-5, Landsat-7 and Landsat-8. The NCEP provides $1^{\circ} \times 1^{\circ}$ representative spatial resolution atmospheric profiles every 6 h, as result of four dimensional meteorological data assimilation, including radiosonde (different from WYO soundings), ground and satellite sounder measurements (Barsi et al, 2005). These profiles are processed at 28 different pressure, air temperature and relative humidity, independently of the surface elevation. The corresponding NCEP outputs of temperature (°C) and relative humidity (%), have assigned errors of $\pm$2 K and $\pm$10%, respectively.

2.2.2. WYO radiosounding data

The Atmospheric Science Department of the University of Wyoming (Laramie, WY, USA) has a database of soundings launched every day at 00:00 and 12:00 UTC at different stations distributed around the world (http://weather.uwyo.edu/upperair/sounding.html, last accessed on February 2015).

From this database, vertical profiles of height (km), pressure (hPa), temperature (°C), relative humidity (%) and mixing ratio (g/kg), provided at 64 levels, were downloaded for the selected site between 2010 and 2013.

These measured variables have uncertainties of $\pm$1 K for the air temperature and $\pm$10% for relative humidity.

2.2.3. MODIS

MODIS (Moderate Resolutions Imaging Spectroradiometer), aboard Terra platform, operates in 36 spectral bands between 0.645 and 14.235 μm, at 705 km of the Earth's surface. Because the characteristics of its spectral bands, MODIS can be used to generate profiles of temperature, relative humidity and dew point at 20 levels of pre-established pressures. Estimations of W are also provided in the atmospheric product named MOD07 (Borbas et al., 2011). Attributed errors to atmospheric parameters provided by MOD07 product are: $\pm$1.9 °C to the temperature, $\pm$4 °C to the dew point, $\pm$10% to relative humidity (Borbas et al., 2011).

2.3. Filtering and processing of atmospheric profiles

For a period from 2010 to 2013, a total of 86 scenes for Murcia, 94 for Zaragoza and 164 for Madrid have been introduced in the MODTRAN5.2.1 (Berk et al., 2011) RTC to carry out the study. To pick the selected scenes, some restrictions have been taken into account.

First we consider as a valid time those days where the satellite passed within 30 min of the balloon launching. After this first filtering,

free of clouds MOD07 scenes over our study region were selected by using the byte codification offered by the MOD07 product, which qualify each pixel as cloudless or not. In a range of 5 × 5 pixels (Borbas et al., 2011), we require a minimum of 20 cloudless pixels.

Finally, only those days for which the three different profiles were available were selected for this study, obtaining the results that are compared in the next section.

The atmospheric parameters obtained from running MODTRAN5 are presented in the corresponding spectral range to the MODIS bands 29 (8.55 μm), 31 (11 μm) and 32 (12 μm).

3. Results and discussions

3.1. Sensitivity analysis

The uncertainty for each of the retrieved parameters is calculated from the uncertainties associated to the different parameters of the profiles commented in Section 2.2. The process to calculate the uncertainty associated to the different parameters that characterize the atmosphere is explained. First, MODTRAN is run with the original profiles, then, MODTRAN is run again with profiles that include the original profiles plus the uncertainty associated to their parameters. Finally, the uncertainty associated to each parameter τ_i, $L^{\downarrow}_{i,hem}$, $L^{\uparrow}_{i}(\theta)$ and W is obtained calculating the difference of the parameters retrieved from the original profiles and the parameters retrieved from the profiles with the associated error.

Table 1 shows some statistics rescued from the uncertainties calculated for the atmospheric parameters τ_i, $L^{\downarrow}_{i,hem}$, $L^{\uparrow}_{i}(\theta)$ of the three sources. These values are calculated taking all data available per band and parameter, not dividing the data for each site.

The average uncertainty associated to each parameter is lesser for the parameters obtained from MOD07 product, with average values lesser than ± 0.5 Wm^{-2} μm^{-1} sr^{-1} for $L^{\uparrow}_{i}(\theta)$, ± 0.6 Wm^{-2} μm^{-1} sr^{-1} for $L^{\downarrow}_{i,hem}$ and ± 0.07 for τ_i. For these cases, the 75% of the uncertainties are under values of ± 0.7 Wm^{-2} μm^{-1} sr^{-1} for $L^{\uparrow}_{i}(\theta)$, ± 0.8 Wm^{-2} μm^{-1} sr^{-1} for $L^{\downarrow}_{i,hem}$ and ± 0.09 for τ_i. In the case of NCEP parameters, the uncertainties are higher, with average values lesser than ± 0.8 Wm^{-2} μm^{-1} sr^{-1}, ± 1.1 Wm^{-2} μm^{-1} sr^{-1} and ± 0.11 for $L^{\uparrow}_{i}(\theta)$, $L^{\downarrow}_{i,hem}$ and τ_i, respectively. For these cases, the 75% of the uncertainties are minor than ± 1.13 Wm^{-2} μm^{-1} sr^{-1}, ± 1.5 Wm^{-2} μm^{-1} sr^{-1} and ± 0.14 for $L^{\uparrow}_{i}(\theta)$, $L^{\downarrow}_{i,hem}$ and τ_i, respectively. And for WYO parameters, average uncertainties are lesser than ± 0.6 Wm^{-2} μm^{-1} sr^{-1}, ± 0.8 Wm^{-2} μm^{-1} sr^{-1} and ± 0.08 for $L^{\uparrow}_{i}(\theta)$, $L^{\downarrow}_{i,hem}$ and τ_i, respectively. For these cases, the 75% of the uncertainties are down to ± 0.8 Wm^{-2} μm^{-1} sr^{-1}, ± 1.1 Wm^{-2} μm^{-1} sr^{-1} and ± 0.11 for $L^{\uparrow}_{i}(\theta)$, $L^{\downarrow}_{i,hem}$ and τ_i, respectively.

All this uncertainties values correspond to band 32 of each parameter and source, since it is the band with greater associated uncertainties.

Table 2
Statistics of the uncertainties obtained for the water vapour content each source. Max and Min represents the maximum and minor value obtained, Av is the average uncertainty and Q1, Q2, Q3 are the first, second and third quartile, respectively.

	W (cm)					
	Max	Min	Av	Q1	Q2	Q3
NCEP	1.4	0.19	0.7	0.5	0.7	0.9
MOD07	0.7	0.004	0.2	0.10	0.19	0.3
WYO	1.1	0.13	0.6	0.4	0.5	0.7

Moreover, the average values are in most cases equal or very close to the median (Q_2).

The results of uncertainties obtained for W are shown in Table 2.

As happens with the other parameters, W retrieved from NCEP profiles provide the greater uncertainties, with an average of ± 0.7 cm, while for MOD07 and WYO they are of 0.23 cm and 0.55 cm. In these cases, the 75% of the parameters have an associated uncertainty lower than ± 0.9 cm, ± 0.3 cm and 0.7 cm for NCEP, MOD07 and WYO, respectively.

3.2. Total column water vapor content

The quantity of water vapor at the atmosphere in a column per unit area (W) is a factor not used directly in the RTE, but with a key importance in the transmissivity, the upwelling and downwelling radiances retrievals. For instance, in García-Santos et al. (2012) the W is obtained through a relationship of downwelling atmospheric radiances, measured at the TIR region in two different angles (0° and 55°).

Therefore, when no radiosounding data are available from a launched balloon, it is important to assure that the selected alternative atmospheric profile is able to characterize the atmosphere by means of a realistic W.

Fig. 1 shows the comparison of the W values from NCEP and MOD07 profiles with those from WYO soundings for the full dataset of each site. Comparing results of Fig. 1 and Table 3, it can be observed that W_{NCEP} fit better with W_{WYO} than W_{MOD07} values for the three areas, with an average correlation of 0.93, a BIAS of 0.02 cm and a RMSE of ± 0.2 cm for Zaragoza and a BIAS of 0.2 cm and a RMSE of ± 0.3 cm for Murcia and Madrid, while W_{MOD07} and W_{WYO} present an average correlation of 0.76, a BIAS of -0.05 cm and a RMSE of ± 0.4 cm for Zaragoza, a BIAS of $+0.09$ and a RMSE of ± 0.3 cm for Murcia and a BIAS of -0.11 and a RMSE of ± 0.3 cm for Madrid. Note that atmospheric MOD07 profiles show a significant underestimation in the W retrievals respect to W_{WYO} values for wet atmospheres ($W_{WYO} \geq 2.5$ cm) on the sites of Zaragoza and Madrid while NCEP profiles retrieve well-correlated W values even for very humid atmospheres ($W_{WYO} \geq 3$ cm), although for Murcia they are overestimated.

Table 1
Statistics of the uncertainties obtained for the different atmospheric parameters (Lup, Ldown, τ) in each MODIS spectral band and for the three sources. Max and Min represents the maximum and minor value obtained, Av is the average uncertainty and Q1, Q2, Q3 are the first, second and third quartile, respectively.

	NCEP						MOD07						WYO					
	BAND 29						**BAND 29**						**BAND 29**					
	Max	Min	Av.	Q1	Q2	Q3	Max	Min	Av.	Q1	Q2	Q3	Max	Min	Av.	Q1	Q2	Q3
Lup (Wm^{-2} μm^{-1} sr^{-1})	1.1	0.13	0.5	0.3	0.5	0.7	0.8	0.08	0.3	0.2	0.5	0.4	0.7	0.07	0.4	0.2	0.3	0.5
Ldown (Wm^{-2} μm^{-1} sr^{-1})	1.5	0.2	0.8	0.5	0.8	1.0	1.0	0.11	0.5	0.3	0.8	0.6	1.1	0.12	0.5	0.3	0.5	0.7
τ	0.11	0.02	0.06	0.05	0.06	0.08	0.09	0.01	0.04	0.03	0.06	0.05	0.09	0.01	0.05	0.04	0.05	0.06
	BAND 31						**BAND 31**						**BAND 31**					
Lup (Wm^{-2} μm^{-1} sr^{-1})	1.7	0.09	0.7	0.4	0.7	1.0	1.3	0.05	0.5	0.2	0.4	0.6	1.2	0.06	0.5	0.3	0.5	0.7
Ldown (Wm^{-2} μm^{-1} sr^{-1})	2.0	0.15	1.0	0.6	1.1	1.4	1.4	0.08	0.6	0.3	0.5	0.7	1.6	0.10	0.7	0.4	0.7	1.0
τ	0.17	0.01	0.09	0.05	0.09	0.12	0.14	0.01	0.06	0.03	0.05	0.08	0.13	0.01	0.06	0.04	0.06	0.09
	BAND 32						**BAND 32**						**BAND 32**					
Lup (Wm^{-2} μm^{-1} sr^{-1})	1.7	0.12	0.8	0.5	0.9	1.1	1.3	0.07	0.5	0.3	0.5	0.7	1.3	0.08	0.6	0.3	0.6	0.8
Ldown (Wm^{-2} μm^{-1} sr^{-1})	2.1	0.2	1.13	0.8	1.2	1.5	1.4	0.10	0.6	0.4	0.6	0.8	1.6	0.13	0.8	0.5	0.8	1.1
τ	0.33	0.02	0.11	0.07	0.12	0.14	0.15	0.01	0.07	0.04	0.07	0.09	0.16	0.01	0.08	0.05	0.08	0.11

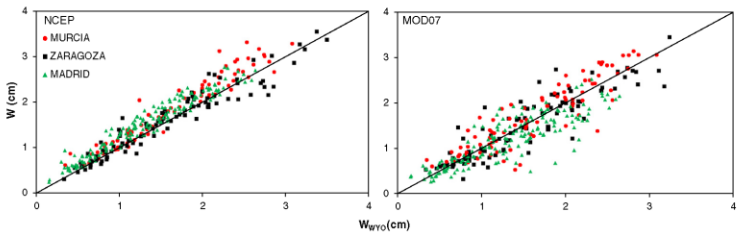

Fig. 1. Differences of NCEP-WYO, and MOD07-WYO, versus W.

Table 3
Linear regression parameters obtained from the comparison of W retrieved between the NCEP-WYO and MOD07-WYO (Fig. 1). From the fitting, m represents the slope, n is the offset, r^2 is the regression coefficient and σ is the standard deviation. In addition, it ishowns the average BIAS and RMSE of the depicted points.

		m	n	r^2	σ	BIAS	RMSE
NCEP-WYO	(cm)						
Murcia		1.07	0.08	0.93	0.2	0.2	0.3
Zaragoza		0.93	0.13	0.92	0.2	0.018	0.2
Madrid		0.99	0.22	0.94	0.15	0.2	0.3
MOD07-WYO	(cm)						
Murcia		0.99	0.11	0.80	0.3	0.09	0.3
Zaragoza		0.80	0.26	0.74	0.4	−0.05	0.4
Madrid		0.76	0.20	0.74	0.3	−0.11	0.3

3.3. Atmospheric transmissivity

The atmospheric transmissivity (τ) retrieved from the NCEP and MOD07 profiles are also compared with the corresponding values, calculated from radiosounding of the University of Wyoming (τ_{WYO}). Fig. 2 shows this comparison between the three selected profiles for the three MODIS thermal bands 29 (8.55 μm), 31 (11 μm) and 32 (12 μm).

Results of τ comparison depicted in Fig. 2 and statistics in Table 4, show clearly again a better agreement between NCEP profiles and WYO data than MOD07 profiles. Average regression coefficients for NCEP are 0.93 for band 29, and 0.91 for bands 31 and 32. For Murcia and Madrid, τ is underestimated, with BIAS among −0.013 and −0.019, depending on the MODIS band analyzed, while for Zaragoza it is overestimated, with BIAS among 0.006 and 0.007. RMSE values are among ±0.02 and ±0.04. Corresponding statistics for MOD07 are: average regression coefficient of 0.71, 0.69 and 0.70 for bands 29, 31 and 32, respectively. In the case of Murcia, τ retrieved is underestimated, with BIAS among −0.07 and −0.05, while for Zaragoza and Madrid it is overestimated, with BIAS values among 0.001 and 0.06. RMSE values for MOD07 are among 0.03 and 0.08. Note that for MOD07 values of BIAS and RMSE values are close to zero as the altitude of the meteorological station is higher. However, for NCEP they are similar for the three areas.

NCEP reproduces transmissivity values closer to those obtained from radiosounding data. This is probably due to the good agreement observed between the water vapor retrieved with NCEP and that calculated from WYO soundings data, since W is indirectly included in the transmissivity exponential expression, through W concentration factor (ρ) and the water spectral absorption coefficient (k, see Eq. (4) in García-Santos et al., 2010).

3.4. Upwelling path radiance

The upwelling radiance ($L_\lambda^{\uparrow}(\theta)$ or Lup), retrieved from NCEP and MOD07 atmospheric profiles, is compared with that from the radiosoundings of University of Wyoming (Lup_{WYO}). The results are shown in Fig. 3 for the three thermal bands of sensor MODIS.

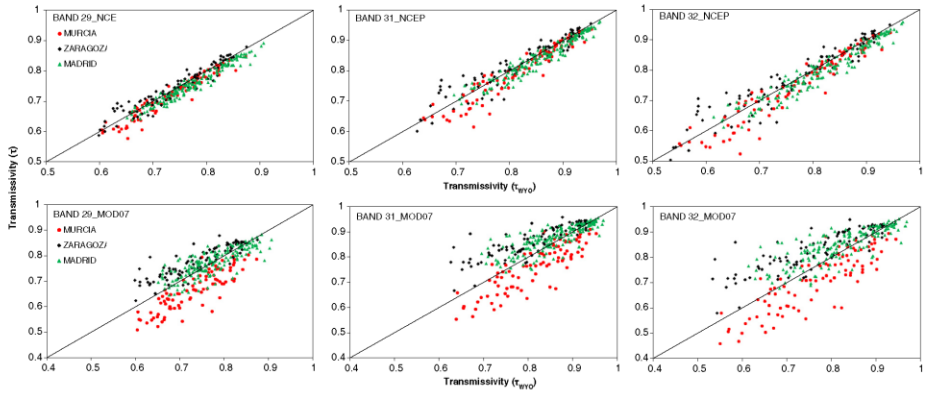

Fig. 2. Linear regression of the comparison between NCEP and WYO (three top graphs) and MODIS-WYO (three bottom graphs), in terms of estimated τ for the three MODIS thermal bands 29 (8.55 μm), 31 (11 μm) and 32 (12 μm).

Table 4
Linear regression parameters obtained from the comparison of transmissivity retrieved for three MODIS TIR bands between the NCEP-WYO and MOD07-WYO (Fig. 2), for three different sites. From the fitting, m represents the slope, n is the offset, r^2 is the regression coefficient and σ is the standard deviation. In addition, it shows the average BIAS and RMSE of the depicted points.

	NCEP						MOD07					
	MURCIA						MURCIA					
	m	n	r^2	σ	BIAS	RMSE	m	n	r^2	σ	BIAS	RMSE
τ_{29}	1.01	−0.02	0.93	0.02	−0.013	0.02	0.98	−0.05	0.74	0.04	−0.07	0.08
τ_{31}	1.04	−0.05	0.91	0.03	−0.016	0.03	0.99	−0.04	0.74	0.05	−0.05	0.07
τ_{32}	1.04	−0.05	0.91	0.03	−0.019	0.04	0.96	−0.03	0.74	0.06	−0.06	0.08
	ZARAGOZA						ZARAGOZA					
τ_{29}	0.92	0.06	0.92	0.02	0.006	0.02	0.71	0.25	0.76	0.03	0.04	0.05
τ_{31}	0.90	0.09	0.89	0.03	0.007	0.03	0.61	0.37	0.72	0.03	0.05	0.06
τ_{32}	0.91	0.08	0.89	0.04	0.009	0.04	0.63	0.35	0.73	0.04	0.06	0.08
	MADRID						MADRID					
τ_{29}	0.94	0.03	0.95	0.013	−0.015	0.02	0.71	0.22	0.63	0.03	0.0014	0.03
τ_{31}	0.95	0.03	0.93	0.017	−0.013	0.02	0.61	0.35	0.62	0.03	0.02	0.04
τ_{32}	0.94	0.03	0.93	0.02	−0.016	0.03	0.62	0.34	0.63	0.04	0.03	0.05

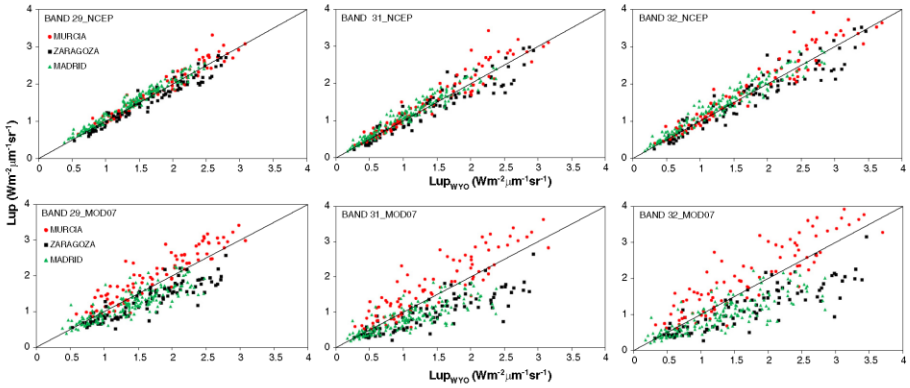

Fig. 3. Linear regression of the comparison between NCEP and WYO (three top graphs) and MODIS-WYO (three bottom graphs), in terms of estimated Lup for the three MODIS thermal bands 29 (8.55 μm), 31 (11 μm) and 32 (12 μm).

Graphics of Fig. 3 show a better agreement for NCEP results than for MOD07, when comparing with Lup calculated from WYO profiles. From statistics in Table 5, the average regression coefficient for NCEP is 0.95 for band 29 and 0.92 for bands 31 and 32. For Murcia and Madrid, BIAS values are among 0.08 $Wm^{-2}\ \mu m^{-1}\ sr^{-1}$ and 0.15 $Wm^{-2}\ \mu m^{-1}\ sr^{-1}$, and RMSE among $\pm 0.13\ Wm^{-2}\ \mu m^{-1}\ sr^{-1}$ and $\pm 0.3\ Wm^{-2}\ \mu m^{-1}\ sr^{-1}$. For Zaragoza, BIAS is of $-0.06\ Wm^{-2}\ \mu m^{-1}\ sr^{-1}$ and $-0.07\ Wm^{-2}\ \mu m^{-1}\ sr^{-1}$, depending of the spectral band, and RMSE among $\pm 0.16\ Wm^{-2}\ \mu m^{-1}\ sr^{-1}$ and $\pm 0.3\ Wm^{-2}\ \mu m^{-1}\ sr^{-1}$. Considering MOD07, the average regression coefficients for each band are: 0.78, 0.73 and 0.73 for bands 29, 31 and 32, respectively. For Murcia, BIAS is among

Table 5
Linear regression parameters obtained from the comparison of upwelling radiance retrieved for three MODIS TIR bands between the NCEP-WYO and MOD07-WYO (Fig. 2), for three different sites. From the fitting, m represents the slope, n is the offset, r^2 is the regression coefficient and σ is the standard deviation. In addition, it shows the average BIAS and RMSE of the depicted points.

		NCEP						MOD07					
		MURCIA						MURCIA					
		m	n	r^2	σ	BIAS	RMSE	m	n	r^2	σ	BIAS	RMSE
Lup_{29}	($Wm^{-2}\ \mu m^{-1}\ sr^{-1}$)	1.03	0.03	0.95	0.15	0.08	0.17	1.02	0.24	0.85	0.3	0.3	0.4
Lup_{31}		1.05	0.05	0.92	0.2	0.13	0.3	1.01	0.31	0.80	0.4	0.3	0.5
Lup_{32}		1.04	0.07	0.92	0.3	0.15	0.3	0.98	0.39	0.79	0.4	0.4	0.6
		ZARAGOZA						ZARAGOZA					
Lup_{29}	($Wm^{-2}\ \mu m^{-1}\ sr^{-1}$)	0.93	0.05	0.94	0.15	−0.06	0.16	0.72	0.13	0.80	0.2	−0.3	0.4
Lup_{31}		0.91	0.06	0.90	0.2	−0.06	0.2	0.61	0.12	0.74	0.3	−0.4	0.5
Lup_{32}		0.91	0.08	0.90	0.3	−0.07	0.3	0.62	0.13	0.75	0.3	−0.5	0.6
		MADRID						MADRID					
Lup_{29}	($Wm^{-2}\ \mu m^{-1}\ sr^{-1}$)	1.00	0.11	0.97	0.10	0.11	0.15	0.70	0.26	0.70	0.2	−0.16	0.3
Lup_{31}		0.98	0.13	0.94	0.14	0.11	0.18	0.59	0.22	0.65	0.2	−0.2	0.3
Lup_{32}		0.97	0.17	0.94	0.16	0.13	0.13	0.59	0.24	0.65	0.3	−0.3	0.4

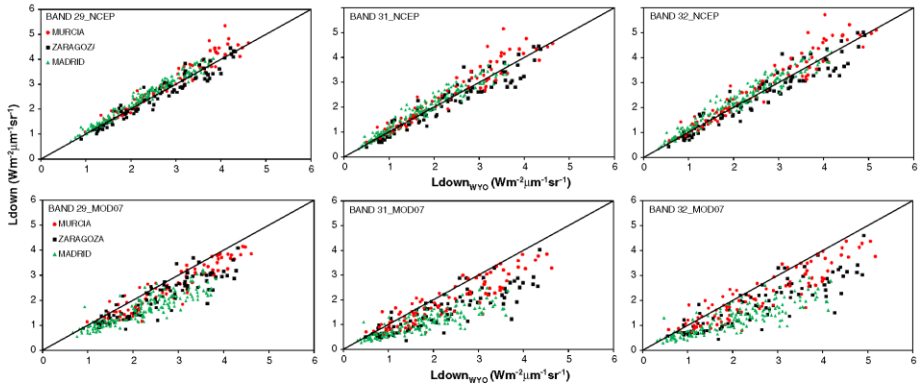

Fig. 4. Linear regression of the comparison between NCEP and WYO (three top graphs) and MODIS-WYO (three bottom graphs), in terms of estimated Ldown for the three MODIS thermal bands 29 (8.55 μm), 31 (11 μm) and 32 (12 μm).

0.27 $Wm^{-2}\ \mu m^{-1}\ sr^{-1}$ and 0.35 $Wm^{-2}\ \mu m^{-1}\ sr^{-1}$, and RMSE among ± 0.4 $Wm^{-2}\ \mu m^{-1}\ sr^{-1}$ and ± 0.6 $Wm^{-2}\ \mu m^{-1}\ sr^{-1}$. In the cases of Zaragoza and Madrid, BIAS is among -0.16 $Wm^{-2}\ \mu m^{-1}\ sr^{-1}$ and -0.49 $Wm^{-2}\ \mu m^{-1}\ sr^{-1}$, and RMSE among ± 0.3 $Wm^{-2}\ \mu m^{-1}\ sr^{-1}$ and ± 0.6 $Wm^{-2}\ \mu m^{-1}\ sr^{-1}$.

In this case, NCEP data seems to fit better to the curve 1:1. This might be linked to the better agreement in terms of transmissivity shown above. Moreover, it is noticed that the BIAS and RMSE values obtained from both sources are better for high altitudes.

3.5. Downwelling hemispheric radiance

The results of the downwelling hemispherical radiances ($L^{\downarrow}_{\lambda,hem}$ or Ldown) retrieved from the NCEP and product MOD07 profiles, are compared with the radiosoundings of the University of Wyoming (WYO), and they are depicted on Fig. 4.

Results from graphics of Fig. 4 show a better fitting of NCEP than for MODIS compared with WYO data. From information in Table 6, the average regression coefficients for NCEP in each band are 0.95 for band 29 and 0.95 for bands 31 and 32. In the case of NCEP, the BIAS obtained for each site ranges among 0.21 $Wm^{-2}\ \mu m^{-1}\ sr^{-1}$ and 0.23 $Wm^{-2}\ \mu m^{-1}\ sr^{-1}$ for Murcia, -0.014 $Wm^{-2}\ \mu m^{-1}\ sr^{-1}$ and 0.07 $Wm^{-2}\ \mu m^{-1}\ sr^{-1}$ for Zaragoza and 0.19 $Wm^{-2}\ \mu m^{-1}\ sr^{-1}$ and 0.23 $Wm^{-2}\ \mu m^{-1}\ sr^{-1}$ for Madrid. RMSE values for the three sites ranges among ± 0.2 $Wm^{-2}\ \mu m^{-1}\ sr^{-1}$ and ± 0.4 $Wm^{-2}\ \mu m^{-1}\ sr^{-1}$. Respect to MOD07, average regression coefficients are 0.82, 0.76 and 0.76 for bands 29, 31 and 32, respectively. For Murcia, BIAS is among -0.26 $Wm^{-2}\ \mu m^{-1}\ sr^{-1}$ and -0.33 $Wm^{-2}\ \mu m^{-1}\ sr^{-1}$, -0.41 $Wm^{-2}\ \mu m^{-1}\ sr^{-1}$ and -0.65 $Wm^{-2}\ \mu m^{-1}\ sr^{-1}$ for Zaragoza and -0.51 $Wm^{-2}\ \mu m^{-1}\ sr^{-1}$ and -0.73 $Wm^{-2}\ \mu m^{-1}\ sr^{-1}$ for Madrid. RMSE for the three sites are among ± 0.4 $Wm^{-2}\ \mu m^{-1}\ sr^{-1}$ and ± 0.7 $Wm^{-2}\ \mu m^{-1}\ sr^{-1}$.

Similar to Lup, the Ldwn depends on the atmospheric transmissivity, so the undervaluation realized for the W in wet atmosphere is here reflected again, for the cases of Zaragoza and Madrid. This effect is stressed for band 32 since water vapor absorption is higher in this spectral range.

4. Simulation study

In order to analyze the uncertainties in terms of temperature retrieved using the atmospheric parameters calculated in this paper, through different sources, a simulation study was carried out using the SC method (Vlassova et al., 2014). The procedure is as follows:

First, for a defined T (in this study three different temperatures were selected: 273 K, 293 K and 313 K) a $B_i(T)$ is calculated and a L_i^{TOA} is retrieved trough Eq. (1) at the three MODIS bands 29, 31 and 32. Atmospheric parameters from the WYO profiles are used to obtain L_i^{TOA} and

Table 6
Linear regression parameters obtained from the comparison of downwelling hemispheric radiance retrieved for three MODIS TIR bands between the NCEP-WYO and MOD07-WYO (Fig. 2), for three different sites. From the fitting, m represents the slope, n is the offset, r^2 is the regression coefficient and σ is the standard deviation. In addition, it shows the average BIAS and RMSE of the depicted points.

		NCEP						MOD07					
		MURCIA						MURCIA					
		m	n	r^2	σ	BIAS	RMSE	m	n	r^2	σ	BIAS	RMSE
$Ldown_{29}$	($Wm^{-2}\ \mu m^{-1}\ sr^{-1}$)	1.08	0.00	0.94	0.26	0.2	0.3	0.90	0.02	0.89	0.30	−0.3	0.4
$Ldown_{31}$		1.06	0.07	0.92	0.34	0.2	0.4	0.78	0.19	0.83	0.37	−0.3	0.5
$Ldown_{32}$		1.05	0.09	0.92	0.37	0.2	0.4	0.79	0.22	0.83	0.43	−0.3	0.5
		ZARAGOZA						ZARAGOZA					
$Ldown_{29}$	($Wm^{-2}\ \mu m^{-1}\ sr^{-1}$)	0.98	0.05	0.94	0.23	−0.014	0.2	0.78	0.15	0.81	0.36	−0.4	0.5
$Ldown_{31}$		0.93	0.08	0.91	0.32	−0.06	0.3	0.66	0.15	0.75	0.40	−0.6	0.7
$Ldown_{32}$		0.94	0.08	0.91	0.35	−0.07	0.4	0.68	0.16	0.76	0.46	−0.7	0.8
		MADRID						MADRID					
$Ldown_{29}$	($Wm^{-2}\ \mu m^{-1}\ sr^{-1}$)	1.04	0.14	0.97	0.15	0.2	0.3	0.65	0.26	0.78	0.28	−0.5	0.6
$Ldown_{31}$		0.99	0.20	0.95	0.20	0.19	0.3	0.50	0.24	0.70	0.27	−0.6	0.7
$Ldown_{32}$		0.98	0.26	0.95	0.23	0.2	0.3	0.51	0.26	0.70	0.33	−0.7	0.8

Table 7
BIAS and RMSE calculated from the comparison between the original LST and those retrieved using NCEP or MOD07 atmospheric parameters for three MODIS bands (29, 31, 32) in each one of the selected sites.

	NCEP		MOD07	
Band	BIAS (K)	RMSE (K)	BIAS (K)	RMSE (K)
MURCIA				
29	0.08	0.6	3	3
31	−0.05	0.6	1.2	1.9
32	−0.05	0.8	1.6	3
ZARAGOZA				
29	0.15	0.6	0.15	1.3
31	0.011	0.7	−0.03	1.4
32	−0.004	0.9	−0.07	2
MADRID				
29	0.03	0.6	1.3	1.7
31	−0.09	0.6	0.6	1.2
32	−0.09	0.7	0.8	2

the surface emissivity (ε_i) used in this case, is corresponding to a rice crop, which has a well characterized value of 0.983 ± 0.005 (Coll et al., in review). Moreover, this value is almost constant in the thermal region.

In a second step, a new $B_i(T)$ is calculated through Eq. (1), using the corresponding atmospheric variables obtained from NCEP or MOD07 profiles and the previously calculated L_i^{TOA}. This new $B_i(T)$ is inverted and a new T is retrieved. Table 7 shows the average BIAS between original T and those temperatures (for the three selected temperatures) obtained from NCEP and MOD07 profiles and RMSE calculated from all the cases analyzed, at the three MODIS thermal bands.

Average results for these three temperatures show that the lowest errors are obtained for bands 29 (8.55 μm) and 31 (11 μm). Taking average results of the three sites per MODIS band, band 29 shows a BIAS of +1.3 K and RMSE of ±0.6 K for NCEP and 1.2 K and ±1.9 K for MOD07. For band 31, NCEP shows a BIAS of −0.04 K and RMSE of ±0.6 K and for MOD07 the study shows a BIAS of +0.6 K and RMSE of ±1.5 K. The greatest error is obtained for band 32 (12 μm) where the NCEP profiles show a BIAS of −0.05 K and RMSE of ±0.8 K, and BIAS of 0.7 K and RMSE of ±2 K for MOD07, this is reasonable since this band is the most sensitive to water vapor.

In summary, the well characterization obtained for the atmospheric parameters τ_i, $L_{i,hem}^{\downarrow}$, $L_i^{\uparrow}(\theta)$, especially for bands 29 and 31, affects directly to the LST retrieval, obtaining lower uncertainties in these cases. Moreover, for MOD07 band 31 obtains better results for LST since it is the less affected band by the water vapor. It is noticed that RMSE obtained are lower in the cases from Madrid, where the altitude is higher and the atmosphere might be better characterized, particularly in profile got from satellite data. These results are in agreement with Coll et al. (2012) for which band 31 has BIAS of −0.3 K and RMSE of ±0.6 K for NCEP and BIAS of −0.5 K and RMSE of ±0.8 K for MOD07, and Li et al. (2013) with BIAS of 0.37 K and RMSE of ±1.16 K for NCEP using the IRS thermal band (10.5–12.5 μm) and BIAS of 0.20 K and RMSE of ±1.2 K for MOD07, concluding that NCEP offers less error than MOD07 profiles.

5. Conclusions

This work has analyzed the differences appeared when characterizing the atmosphere from different atmospheric profiles: NCEP, MOD07_L2 product and radiosoundings from the University of Wyoming (used as reference).

Atmospheric parameters in the TIR region 8–14 μm (upwelling radiance, downwelling hemispheric radiance and atmospheric transmissivity) were obtained for three thermal bands (29, 31 and 32) of sensor MODIS.

It is concluded that both NCEP and MOD07 profiles show an acceptable agreement with results from WYO profiles. However, despite NCEP profiles show greater uncertainties estimating the atmospheric parameter, because their spatial and temporal interpolation procedure, results show a better fit with the reference WYO values at the three spectral bands. Conversely, the values obtained from MOD07 show lower uncertainties than the NCEP, but their results are more scattered and less correlated with WYO results. So water vapor content is usually underestimated for MOD07, in particular for wet atmospheres (w > 2.5 cm) and high altitudes. This underestimation is propagated to the others parameters, underestimating in the same way upwelling and downwelling radiance and overestimating the atmospheric transmissivity.

A simulation study was carried out to analyze the effect of each atmospheric profile retrieving the surface temperature when applying the SC method. Results showed RMSE between ±0.6 and ±0.9 K for NCEP and between ±1.3 and ±3 K for MOD07, depending on the spectral band and the altitude of the study site. So for bands 29 and 31, temperature uncertainties show the best results, probably because band 32 is more affected by the water vapor. Moreover, it is observed better results on the LST retrievals for high altitudes, leading to lower errors in the way that the altitude is greater. This is probably due to MOD07 product get less data for lower altitudes. For example, in the case of Murcia, the first data level is around 120 m, 60 m over the ground altitude. While for higher altitudes, that measure is more accurate.

Radiosounding data is probably the best way to characterize the atmosphere, but rarely there are radiosoundings available at the time and location of interest. This study has shown that using as alternative NCEP profiles leads to optimal results when characterizing the atmosphere. In addition, good results are obtained for MODIS band 29 (8.55 μm), which has not been studied previously in other works, with uncertainties similar to those obtained for MODIS band 31 (11 μm).

Acknowledgments

This study was supported by the Spanish Ministry of Economy and Competitiveness, through projects CGL2013-46862-C2-1-P and CGL2011-30433-C02-02. We also want to thank the Government of Generalitat Valenciana for the support this study through the project PROMETEOII/2014/086.

References

Barsi, J.A., Schott, J.R., Palluconi, F.D., Hook, S.J., 2005. Validation of a Web-Based Atmospheric Correction Tool for Single Thermal Band Instruments. Earth Observing Systems X, Proc. SPIE Vol. 5882, August 2005, San Diego, CA.
Berk, Anderson, G.P., Acharya, P.K., Shettle, E.P., 2011. MODTRAN®5.2.1 USER'S MANUAL.
Borbas, E.E., Seemann, S.W., Kern, A., Moy, L., Li, J., Gumley, L., Menzel, P., 2011. Modis Atmospheric Profile Retrieval Algorithm Theoretical Basis Document, Collection 6, Version 7. University of Wisconsin-Madison.
Coll, C., Caselles, V., Valor, E., Niclòs, R., 2012. Comparison between different sources of atmospheric profiles for land surface temperature retrieval from single channel thermal infrared data. Remote Sens. Environ. 117, 199–210.
Coll, C., García-Santos, V., Niclòs, R., Caselles, V., 2014w. Validation of the new MODIS land surface and emissivity algorithm (MOD21) with ground measurements at the Valencia test site. Remote Sensing of Environment (in review).
García-Santos, V., Valor, E., Caselles, V., 2010. Determination of the surface temperature by remote sensing. Tethys 7, 67–75.
García-Santos, V., Galve, J.M., Valor, E., Caselles, V., Coll, C., 2012. Estimation of atmospheric water vapour content from direct measurements of radiance in the thermal infrared region. Remote Sens. Lett. 3 (1), 31–38. http://dx.doi.org/10.1080/01431161.2010.531060.
Hulley, G., Veraverbeke, S., Hook, S., 2014. Thermal-based techniques for land cover change detection using a new dynamic MODIS multispectral emissivity product (MOD21). Remote Sens. Environ. 140, 755–765.
Huntrieser, H., Schiesser, H.H., Schmid, W., Waldvogel, A., 1997. Comparison of traditional and newly developed thunderstorm indices for Switzerland. Weather Forecast. 12, 108–125.
Jiang, G.-M., Liu, R., 2014. Retrieval of sea and land surface temperature from SVISSR/FY-2C/D/E measurements. IEEE Trans. Geosci. Remote Sens. 52, 10.
Jiménez-Muñoz, J.C., Sobrino, J.A., Mattar, C., Franch, B., 2010. Atmospheric correction of optical imagery from MODIS and Reanalysis atmospheric products. Remote Sens. Environ. 114, 2195–2210.
Li, H., Liu, Q., Du, Y., Jiang, J., Wang, H., 2013. Evaluation of the NCEP and MODIS atmospheric products for single channel land surface temperature retrieval with ground measurements: a case study of HJ-1B IRS data. IEEE J. Sel. Top. Appl. Earth Obs. Remote Sens. 6 (3).

Merino, A., García-Ortega, E., López, L., Sánchez, J.L., Guerrero-Higueras, A.M., 2013. Synoptic environment, mesoscale configurations and forecast parameters for hailstorms in Southwestern Europe. Atmos. Res. 122, 183–198.
Sánchez, J.M., López-Urrea, R., Rubio, E., Caselles, V., 2011. Determining water use of sorghum from two-source energy balance and radiometric temperatures. Hydrol. Earth Syst. Sci. 15, 3061–3070.
Sánchez, J.M., López-Urrea, R., Rubio, E., González-Piqueras, J., Caselles, V., 2014. Assessing crop coefficients of sunflower and canola using two.source energy balance and thermal radiometry. Agric. Water Manag. 137, 23–29.
Vlassova, L., Perez-Cabello, F., Nieto, H., Martín, P., Riaño, D., Riva, J., 2014. Assesment of methods for land surface temperature retrieval from Landsat-5 TM images applicable to multiscale tree-grass ecosystem modeling. Remote Sens. 6, 4345–4368.
Zhou, J., Li, J., Zhang, L., Hu, D., Zhan, W., 2012. Intercomparison of methods for esmating land surface temperature from a Landsat-5 TM image in an arid region with low water vapour in the atmosphere. Int. J. Remote Sens. 33, 2582–2602.

Anexo F

Comparison and Evaluation of the TES and ANEM Algorithms for Land Surface Temperature and Emissivity Separation over the Area of Valencia, Spain

El siguiente trabajo fue publicado en Remote Sensing en diciembre del 2017. Esta revista tiene un factor de impacto de 3,41 y ocupa la posición 8 de 30 revistas en la categoría Remote Sensing según Journal Citation Reports en la edición de 2017.

remote sensing

MDPI

Article

Comparison and Evaluation of the TES and ANEM Algorithms for Land Surface Temperature and Emissivity Separation over the Area of Valencia, Spain

Lluís Pérez-Planells *, Enric Valor, César Coll and Raquel Niclòs

Earth Physics and Thermodynamics Department, University of Valencia, 50 Dr. Moliner, E-46100 Burjassot-Valencia, Spain; enric.valor@uv.es (E.V.); cesar.coll@uv.es (C.C.); raquel.niclos@uv.es (R.N.)
* Correspondence: lluis.perez@uv.es; Tel.: +34-963-543-249; Fax: +34-963-543-385

Received: 10 October 2017; Accepted: 30 November 2017; Published: 2 December 2017

Abstract: Land Surface temperature (LST) is a key magnitude for numerous studies, especially for climatology and assessment of energy fluxes between surface and atmosphere. Retrieval of accurate LST requires a good characterization of surface emissivity. Both quantities are coupled in a single radiance measurement; for this reason, for N spectral bands available in a remote sensor, there will always be N + 1 unknowns. To solve the indeterminacy, temperature-emissivity separation methods have been proposed, among which the Temperature Emissivity Separation (TES) algorithm is one of the most widely used. The Adjusted Normalized Emissivity Method (ANEM) was proposed as a modification of the Normalized Emissivity Method (NEM) algorithm by adjusting the initial emissivity guess using an estimation provided by the Vegetation Cover Method (VCM). In this work, both methods were applied to a set of five ASTER scenes over the area of Valencia, Spain, which were recalibrated and atmospherically corrected using local radiosoundings and ground measurements. These scenes were compared to the ASTER temperature and emissivity standard products (AST08 and AST05, respectively). The comparison to reference measurements showed a better agreement of ANEM LST in low spectral contrast surfaces, with biases of +0.4 K, +0.8 K for TES and +1.4 K for the AST08 product in a rice crop site. For sea surface temperature, bias was −0.1 K for ANEM, +0.3 K for TES and +1.3 K for the AST08 product. The larger differences of the AST08 product could be ascribed mainly to the atmospheric correction based on NCEP profiles in contrast to the local correction used in TES and ANEM and to a lesser extent the Maximum-Minimum Difference (MMD) empirical relationship used by TES. In terms of emissivity, ANEM obtained biases up to ±0.007 (positive over vegetation and negative over water), while TES biases were up to −0.015. The AST05 product showed differences up to −0.050, although for high contrast areas, such as sand surfaces, it showed better accuracy than both TES and ANEM. A comparison between TES and ANEM on four different classes within the scene showed a systematic difference between both algorithms, which was more pronounced for low spectral contrast surfaces. Therefore, ANEM improves the accuracy at low spectral contrast surfaces, while obtaining similar results to TES at higher spectral contrast surfaces, such as urban areas. The combination of both methods could provide a procedure benefiting from the strengths shown by each of them.

Keywords: TES; ANEM; land surface temperature; emissivity; ASTER; thermal infrared

1. Introduction

Land Surface Temperature (LST) is one of the most important magnitudes for numerous climatological and meteorological processes, as the energy fluxes between surface and atmosphere for

instance [1–3]. Retrieving accurate LSTs from remote sensing measurements depends on two essential issues: firstly, to make a correct characterization of the atmosphere, in order to remove the atmospheric effects on the at-sensor measurements; secondly, the Land Surface Emissivity (LSE) must be well known, with appropriate values for the analyzed bands [4]. However, LSE is commonly an unknown magnitude. For this reason, obtaining accurate LST and LSE values is a challenging goal in Thermal Infrared (TIR) remote sensing.

The main problem lays in the fact that for N TIR spectral bands, there exist N + 1 unknowns, corresponding to the respective emissivity channels and the LST value. Different temperature-emissivity separation algorithms, based on quasi-empirical models, have been proposed to solve this indetermination in the last two decades, e.g., [5–11]. Generally, these models assume an initial emissivity to make a first approach, which later is adjusted or improved.

One of the most used methods is the Temperature and Emissivity Separation (TES) algorithm, which has been studied in depth by different authors for different multispectral sensors [12–16]. This method starts from an initial emissivity guess for all pixels and channels (Normalized Emissivity Method or NEM module) and uses an empirical relationship (Maximum-Minimum Difference, or MMD module) that allows estimating the minimum emissivity of the spectrum by taking into account the spectral contrast, thus to obtain the emissivity for all channels.

Coll et al. proposed in [17,18] the Adjusted Normalized Emissivity Method (ANEM) based on the NEM [19], which is estimated using the vegetation cover method proposed in [20], which relates for each pixel the effective emissivity to the fractional vegetation cover calculated previously from a vegetation index.

Presently, most remote sensing missions tend to integrate hyperspectral sensors, with several spectral bands in the thermal infrared region. In this manner, these empirical models will contribute to the LST and LSE retrieval from thermal infrared measurements in near future hyperspectral missions, like the HyspIRI mission. In this context, the comparison of the TES and ANEM algorithms, which has not been performed before, can be of interest.

ASTER, launched on 19 December 1999 aboard the Terra satellite, is a multispectral sensor provided with 15 spectral bands (4 Visible and Near-Infrared Bands (VNIR), 6 Shortwave Infrared Bands (SWIR) and 5 Thermal Infrared Bands (TIR)). ASTER offers high resolution imagery for the TIR region (90 m), with LST and emissivity products (AST08 and AST05, respectively) based on the TES method. Validation studies [16,21–23] have shown the agreement of these products within the predicted uncertainty values of ± 1.5 K for temperature and ± 0.015 for emissivity. Despite this, some authors suggest improvements to the product algorithm in order to reduce that uncertainty, most of them related to atmospheric correction [13,24,25].

In this paper, ASTER products AST05 and AST08 were compared with TES and ANEM algorithms applied to ASTER L1 scenes, which were previously calibrated and corrected atmospherically using local radiosoundings and ground measurements. The aim of this work is to evaluate the ANEM algorithm in comparison to the TES algorithm in ASTER scenes over different surface types. To reach the objective, five ASTER L1 scenes and ASTER LST and LSE and emissivity products over the Valencia area, Spain, were used, covering different surface types such as rice crops and other agricultural sites, water and urban areas.

The paper proceeds as follows. Section 2 presents the study area and data. Then, in Section 3, the methodology applied to carry out the study, corresponding to TES and ANEM methods, is presented. Section 4 shows the results obtained, while the corresponding discussion is presented in Section 5. Finally, the main conclusions of the work are given in Section 6.

Remote Sens. **2017**, *9*, 1251

2. Study Area & Data

2.1. Study Area

This study was carried out over the Mediterranean coast near the city of Valencia, Spain (see Figure 1). This area covers different surface types including Valencia city, many smaller urban centers and industrial areas (seen in gray in Figure 1), the Albufera Lake with rice crops around it, agricultural areas corresponding to other crops (mainly orange groves, seen in orange-red in Figure 1), Mediterranean forest areas (seen in brown in Figure 1) and the Mediterranean Sea.

Figure 1. Scene over the study area on 3 August 2004 using VNIR ASTER Channels 3n (0.81 μm), 2 (0.66 μm) and 1 (0.56 μm) to compose the RGB image, respectively.

The study area is characterized by the Mediterranean climate. It is a typically hot climate during the summer season. Maximum temperatures are close to 308 K; the minimum ones are around 293 K; and rain is scarce in this period of the year. The orography of the area is varied, with altitudes from sea level to 800 m, although most part of the zone is below 300 m.

2.2. Data

Five ASTER L1B scenes that provided the Top of Atmosphere (TOA) radiances required to apply the analyzed methods were used. These scenes were selected from all ASTER L1B scenes available for the study area taking into account two main reasons, which make the evaluation conditions optimum: the homogeneity of the surface existing during the summer period at the rice crops and the availability of in situ radiosounding profiles launched concurrently with the ASTER overpasses. They were recorded on 3 August 2004, 12 August 2004, 21 July 2005, 24 July 2006 and 11 July 2007. The atmospheric correction was applied to the different scenes and channels in order to obtain the corresponding at-surface radiances required by the methods. The results were compared with ground data measured over the rice fields concurrent to the satellite overpass, with the Sea Surface Temperature

(SST) product from the MODIS sensor and also with the ASTER emissivity and temperature standard products (AST05 and AST08, respectively).

2.2.1. ASTER Sensor

ASTER provides high resolution images of the Earth at 14 different bands of the electromagnetic spectrum, with two Visible and two Near-Infrared (VNIR) bands, six Shortwave Infrared (SWIR) bands and five Thermal Infrared (TIR) bands. The viewing angle is close to nadir (<8.5°). The spatial resolution depends on the sensor spectral band, with 15 m for VNIR, 30 m for SWIR and 90 m for the TIR (see Table 1).

Table 1. Wavelength and spatial resolution of each ASTER band.

Spectral Range	ASTER Band	Wavelength (μm)	Spatial Resolution (m)
VNIR	1	0.520–0.600	15
	2	0.630–0.690	
	3n	0.760–0.860	
	3b	0.760–0.860	
SWIR	4	1.600–1.700	30
	5	2.145–2.185	
	6	2.185–2.225	
	7	2.235–2.285	
	8	2.295–2.365	
	9	2.360–2.430	
TIR	10	8.125–8.475	90
	11	8.475–8.825	
	12	8.925–9.275	
	13	10.250–10.950	
	14	10.950–11.650	

The VNIR data (ASTER Bands 2 and 3n) were used to calculate the NDVI needed to retrieve the ANEM emissivity as shown in the next section. The digital numbers were transformed to at-sensor radiances according to:

$$L_{TOA,i} = (DN_i - 1)UCC_i \quad (1)$$

where UCC_i are the unit conversion coefficients given in the scene metadata, which take values of 0.708 and 0.862 W m^{-2} sr^{-1} μm^{-1} for Bands 2 and 3, respectively. Then, $L_{TOA,i}$ was converted to at-surface reflectance using the image-based atmospheric correction model of Chavez et al. proposed in [26], based on Dark-Object Subtraction (DOS model). This model corrects the at-sensor radiance subtracting the path radiance, before calculating the at-surface reflectance.

For the TIR bands, at-surface radiances are needed to apply the TES and ANEM methods. To increase the precision and accuracy of the at-surface radiances, the local calibration and atmospheric correction proposed in [21] were applied instead of the ASTER standard calibration. This combined local calibration and atmospheric correction was given by a linear function of DN_i:

$$L_{surf,i} = a_i DN_i + b_i \quad (2)$$

where coefficients a_i and b_i depend on the band and date of the scene, $L_{surf,i}$ being the at-surface recalibrated and atmospherically-corrected radiances at band i. These coefficients were retrieved using simulated radiances from the radiative transfer code MODTRAN 4 [27] with atmospheric profiles of pressure, temperature and moisture measured using an RS80 radiosonde balloon launched at the study area at the time of satellite overpass (details are given in [21]). The use of ground measurements reduces the $L_{surf,i}$ uncertainties due to calibration and atmospheric correction, so the application of

the ANEM and TES methods should provide, in principle, more accurate results than the standard ASTER products. Coefficients used in Equation (2) for all dates are presented in Table 2 for each band.

Table 2. Coefficients a_i (W m^{-2} sr^{-1} μm^{-1}/DN) and b_i (W m^{-2} sr^{-1} μm^{-1}) to apply the combined local calibration and atmospheric correction for the scenes used in the present study (given in [21]) for 2004 and 2005 and derived here for 2006 and 2007. The correlation coefficients of each linear function are also provided.

Date	Band	a_i	b_i	r^2
3 August 2004	10	0.012908	−5.982	0.9996
	11	0.010369	−3.682	0.9998
	12	0.009087	−2.687	0.9997
	13	0.007389	−2.451	1.0000
	14	0.007210	−3.057	0.9989
12 August 2004	10	0.012796	−6.113	0.9994
	11	0.010419	−3.859	0.9997
	12	0.008995	−2.640	0.9994
	13	0.007430	−2.587	1.0000
	14	0.007320	−3.378	1.0000
21 July 2005	10	0.013155	−6.639	0.9993
	11	0.010774	−4.480	1.0000
	12	0.009265	−3.131	0.9996
	13	0.007538	−2.831	1.0000
	14	0.007602	−3.908	0.9986
24 July 2006	10	0.013970	−7.445	0.9995
	11	0.011175	−4.933	0.9986
	12	0.009451	−3.379	0.9998
	13	0.007779	−3.221	1.0000
	14	0.007852	−4.313	0.9996
11 July 2007	10	0.014565	−7.297	0.9956
	11	0.011427	−4.663	0.9991
	12	0.009836	−3.523	0.9989
	13	0.008485	−3.940	1.0000
	14	0.008629	−5.136	0.9993

ASTER L2 standard products of emissivity and temperature (AST05 and AST08, respectively) were used as a reference to compare with the images obtained with the analyzed methods. AST05 and AST08 products are obtained by the TES algorithm, with a spatial resolution of 90 m. The nominal accuracy of these products are ±1.5 K for AST 08 and ±0.015 for AST05 [28]. These products use the radiative transfer model MODTRAN 3.5 with required atmospheric parameters obtained from the National Center of Environmental Prediction and the National Center of Atmosphere Research (NCEP and NCAR) and satellite data [23,29].

2.2.2. Reference Measurements

In order to evaluate the results obtained with the different methodologies, temperature and emissivity values for different surface types measured by Coll et al. [21] and Niclòs et al. [30] in the field were used.

One of the major difficulties with the evaluation of remote sensing data is the difference between the spatial scales of satellite and ground measurements. In this case, that ASTER sensor has a spatial resolution of 90 m in the TIR, but the spatial scale of ground radiometric measurements is usually lower than 1 m. In order to make the two types of measurements compatible, it is necessary to consider wide and homogeneous reference areas, both in temperature and emissivity. Consequently,

water (Mediterranean Sea) and vegetation with complete cover (rice fields around Albufera Lake) were used for the evaluation and comparison.

The temperature of rice-covered surfaces was obtained through in situ radiometric measurements concurrent to the ASTER overpass, between 10:54 and 11:00 UTC depending on the data. Two CIMEL 312 radiometers [31] were used, for which the temperature measurements corresponding to 3 min around the satellite overpass were considered for evaluation. The mean value and standard deviation of those temperatures were calculated, the latter giving an estimate of the natural variability of ground temperatures in the area. The average radiometric temperature was corrected for emissivity and atmospheric effects using measurements of emissivity and atmospheric downwelling irradiance. The uncertainty associated with the in situ-measured LST includes the radiometer calibration uncertainties, the emissivity correction uncertainties and the natural variation of the surface temperature (see [21] for details). The retrieved LSTs and uncertainties for the rice field evaluation site are shown in Table 3. Additionally, Table 4 shows the emissivity of the rice crops and also of the sand at the nearby beach that were measured in situ for the five bands of the CIMEL 312-2 radiometer through the TES method adapted to that radiometer [32].

Table 3. Ground LST values and uncertainties measured in situ at the rice field concurrent to the ASTER overpass. MODIS-Terra SST product values (mean and standard deviation for 3 × 3 pixels centered at the location shown as latitude/longitude) from the Mediterranean Sea and the total precipitable water (TPW) are also given.

Date	TPW (cm)	Rice Field			Mediterranean Sea		
		LST (K)	δ (K)	Location	SST (K)	δ (K)	Location
3 August 2004	2.35	303.6	0.7	39.250°N, 0.295°W	299.3	0.4	39.250°N, 0.295°W
12 August 2004	2.05	302.0	0.5	39.250°N, 0.295°W	299.6	0.5	39.250°N, 0.295°W
21 July 2005	2.03	301.6	0.6	39.265°N, 0.308°W	299.8	0.4	39.250°N, 0.295°W
24 July 2006	2.39	302.4	0.9	39.265°N, 0.308°W	301.0	0.4	39.250°N, 0.295°W
11 July 2007	2.90	300.3	0.3	39.265°N, 0.308°W	297.9	0.4	39.250°N, 0.295°W

Table 4. Rice and sand beach emissivity values with their standard deviations (Std) retrieved from ground measurements using Temperature Emissivity Separation (TES) with CIMEL 312-2 and Mediterranean Sea emissivity using CIMEL CE312-2 and Negative Temperature Coefficient (NTC) thermistors.

CE 312 Band	λ_i (μm)	Rice Field		Sand Beach		Mediterranean Sea	
		ε	Std	ε	Std	ε	Std
6	8.42	0.970	0.012	0.820	0.011	0.980	0.006
5	8.68	0.980	0.015	0.813	0.009	0.984	0.005
4	9.15	0.978	0.015	0.796	0.010	0.984	0.004
3	10.57	0.982	0.010	0.951	0.005	0.990	0.004
2	11.30	0.982	0.008	0.956	0.003	0.991	0.004

To compare the ASTER-derived water temperature, the MODIS-Terra SST product MOD28 [33] with 1 km of spatial resolution was used. The SST was obtained for a window 3 × 3 of each MODIS scene and compared against a window of 33 × 33 pixels of ASTER centered on the same coordinates. Table 3 shows the MOD28 SST values together with their uncertainty, calculated as the quadratic sum of the SST standard deviation for the 3 × 3 pixels and the product uncertainty established by Niclòs et al. in [34]. This last uncertainty has a value of ±0.37 and was obtained as a result of a MOD28 product validation with in situ measurements. Water emissivity values, shown in Table 4, were measured in [30] for the six CE312-2 bands. A sample of Mediterranean Sea water was used to obtain the emissivity from measurements of the surface and sky radiance with two CE312-2 radiometers and the surface temperature with several Negative Temperature Coefficient (NTC) thermistors (see [30] for more details).

3. Methodology

3.1. TES Algorithm

The Temperature-Emissivity Separation (TES) method was first proposed in [10] to obtain LST and LSE from the five TIR ASTER channels. TES is applied to channel i at-surface radiance ($L_{surf,i}$), as given by Equation (3):

$$L_{surf,i} = \varepsilon_i B_i(T) + \frac{(1-\varepsilon_i)F_{atm,i}}{\pi} \quad (3)$$

where $B_i(T)$ is Planck's function for the effective wavelength λ_i of each ASTER band at surface temperature T, ε_i is the channel emissivity and $F_{atm,i}$ is the downwelling atmospheric irradiance. TES starts with the Normalized Emissivity Method (NEM) module [19], in which the at-surface radiances obtained from the atmospherically-corrected at-sensor radiances are introduced into Equation (3) using an initial surface emissivity value, generally 0.99, for all channels and pixels, and the Planck radiance $B_i(T)$ is retrieved for each band:

$$B_i(T) = \frac{\left[L_{surf,i} - \frac{(1-\varepsilon_i)F_{atm,i}}{\pi}\right]}{\varepsilon_i} \quad (4)$$

Planck radiances are then inverted obtaining five temperature values. The maximum temperature value (T_{NEM}) is chosen as the first approximation to the LST. Using T_{NEM} in Equation (3), new emissivity values are retrieved for each band ($\varepsilon_{NEM,i}$):

$$\varepsilon_{NEM,i} = \frac{\left(L_{surf,i} - \frac{F_{atm,i}}{\pi}\right)}{\left(B_i(T_{NEM}) - \frac{F_{atm,i}}{\pi}\right)} \quad (5)$$

$\varepsilon_{NEM,i}$ values are used to retrieve the temperature-independent β_i index (β spectrum):

$$\beta_i = \frac{\varepsilon_{NEM,i}}{\bar{\varepsilon}} \quad (6)$$

where $\bar{\varepsilon}$ is the mean value of NEM emissivities of the five TIR bands. Then, the difference between maximum and minimum β values is calculated (maximum-minimum difference or *MMD*). The *MMD* is related to the minimum value of the emissivity spectrum (ε_{min}) in accordance with an empirical relationship (calibration curve), which is obtained using a set of spectra of rocks, soils, vegetation, snow and water given in the ASTER library [35]. Hulley and Hook in [12] obtained a new expression, which adjusts better to vegetated covers since they used a larger number of vegetated cover types to estimate the *MMD* regression curve, which is:

$$\varepsilon_{min} = 0.9951 - 0.7264 \times MMD^{0.7873} \quad (7)$$

This expression was compared with the one given by Gillespie et al. in [10]. The difference between both expressions according to the *MMD* value is shown in Figure 2. This difference is higher for *MMD* values between 0.05 and 0.15, showing a maximum disagreement up to 1% in the minimum emissivity estimation.

Finally, the emissivity spectrum is calculated using ε_{min} together with the β spectrum.

$$\varepsilon_i = \varepsilon_{min}\frac{\beta_i}{min(\beta_i)} \quad (8)$$

The emissivity spectra obtained from Equation (8) are then used in Equation (4), from which five new temperatures are retrieved. These new temperatures should be equal, but often, they present small differences. If these differences are lower than the noise equivalent temperature difference (NEΔT)

of ASTER (±0.3 K), then the maximum of the obtained temperature values is considered as the best estimate of LST.

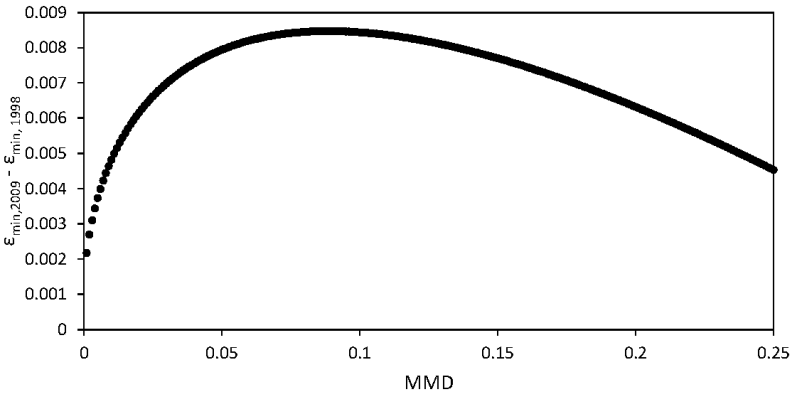

Figure 2. Difference between minimum emissivity retrieved using the empirical expression proposed in [12] and the one proposed in [10] depending on the maximum-minimum difference (*MMD*).

3.2. *ANEM Algorithm*

The Adjusted Normalized Emissivity Method (ANEM) was proposed in [18] as a combination of the Vegetation Cover Method (VCM) [20,36] and NEM [19], explained in Section 3.1. In ANEM, the emissivity introduced as the input in NEM is retrieved with VCM depending on the vegetation fraction of each pixel in the scene. As a consequence, a different value of emissivity is used for each pixel as initial emissivity for NEM, instead of a unique value for all pixels.

To apply ANEM, it is required to distinguish between natural areas, urban areas and water using the corresponding masks in the scene. They were obtained using ASTER Shortwave Infrared (SWIR) bands (Bands 4–9) with a supervised classification using a Mahalanobis distance of 30 m. We selected the following regions of interest: natural areas including different types of agricultural fields (mainly rice paddies and orange groves) and forested areas; urban areas such as the city of Valencia and other smaller towns around it; and water areas of the Mediterranean Sea and the Albufera Lake. The VCM is applied for natural areas. The effective emissivity of a heterogeneous and rough surface is calculated as:

$$\varepsilon_i = \varepsilon_{vi} P_v + \varepsilon_{si}(1 - P_v) + 4\langle d\varepsilon_i \rangle P_v (1 - P_v) \quad (9)$$

where ε_{vi} and ε_{si} are the emissivities of vegetation and soil pixels in band i, respectively, P_v is the vegetation fractional cover and $\langle d\varepsilon_i \rangle$ is a term related to the internal reflections between vegetation and soil that depend on the surface structure (cavity term), which is given in [37]:

$$\langle d\varepsilon_i \rangle = -0.435\varepsilon_{si} + 0.4343 \quad (10)$$

The ε_{vi} and ε_{si} values (see Table 5) were estimated from the spectra provided in the ASTER spectral library. For vegetation, ε_{vi} was calculated as the average emissivity of green vegetation samples (grass and conifer) for each of the five ASTER TIR bands; while for soil, the procedure is the same, but using 65 soil samples, including 23 aridisols, 11 entisols, 10 mollisols, 9 alfisols, 8 inceptisols, 2 vertisols, 1 spodosol and 1 ultisol. Before the estimation, the different emissivity spectra were integrated with the filter functions of the five ASTER TIR channels to get band-integrated emissivities corresponding to each spectrum.

Table 5. Emissivity of vegetation (ε_{vi}), soil (ε_{si}) and cavity term ($\langle d\varepsilon_i \rangle$) to be used in the Vegetation Cover Method (VCM) for the different ASTER TIR channels (see Equation (9)). The indicated uncertainties correspond to the standard deviation of the emissivity values for all the considered samples.

Band	ε_{vi}	ε_{si}	$\langle d\varepsilon_i \rangle$
10	0.990 ± 0.002	0.92 ± 0.05	0.03 ± 0.02
11	0.986 ± 0.005	0.93 ± 0.05	0.03 ± 0.02
12	0.979 ± 0.015	0.93 ± 0.04	0.031 ± 0.017
13	0.985 ± 0.005	0.970 ± 0.006	0.012 ± 0.003
14	0.988 ± 0.003	0.971 ± 0.005	0.012 ± 0.002

Different values of vegetation fraction between 0 and 1 were introduced into Equation (9) together with the coefficients given in Table 5. For each value of P_v, five different effective emissivity values were retrieved, one per band, then the maximum value was taken. The obtained emissivity maximum values were adjusted against P_v, with a correlation coefficient of 0.987, resulting in Equation (11), which directly provides the maximum emissivity value to be introduced into NEM as a function of the vegetation fraction:

$$\varepsilon_{max} = 0.9938P_v + 0.9699(1 - P_v) + 0.044P_v(1 - P_v) \quad (11)$$

The vegetation fraction needed in Equation (11) was calculated following the procedure proposed in [20]:

$$P_v = \frac{\left(1 - \frac{i}{i_s}\right)}{\left(1 - \frac{i}{i_s}\right) - K\left(1 - \frac{i}{i_v}\right)} \quad (12)$$

where i is the Normalized Difference Vegetation Index (NDVI) [38] of each pixel, i_s and i_v are the minimum and maximum NDVI values of the area, which are representative of bare soil and dense vegetation, respectively, and $K = (\rho_{3v} - \rho_{2v})/(\rho_{3s} - \rho_{2s})$, where ρ_{is} (ρ_{iv}) is the at-surface reflectance value in the red (ASTER Band 2) and near-infrared (ASTER band 3) over pixels where the values i_s (i_v) are found. Then, the NDVI image was resized to the SWIR pixel size in order to take the i_s and i_v values from the histogram of the scene taking into consideration only the pixels belonging to the natural areas mask. Using the cumulative histogram, the mean value of the pixels between percentiles 4 and 7 was used to calculate i_s, while the mean of the pixels with percentiles between 93 and 96 of the NDVI distribution was used to obtain i_v.

Since the previous procedure is not applicable in the case of urban zones and water surfaces, an input emissivity value for the NEM module was determined for them. For water, the emissivity values for the ASTER channels were obtained from Niclòs et al. in [30] (see Table 4). The maximum value was taken as $\varepsilon_{max} = 0.991$ corresponding to ASTER Band 14.

For urban areas, the ASTER library spectra of manmade materials were divided into three groups: construction concrete (to estimate the emissivity of building walls), road asphalts and tars (to estimate the emissivity of streets) and roofing materials (emissivity of building tops). All the spectra in these groups were integrated with the filter functions. For each group, the average and the standard deviation were calculated, obtaining three values of emissivity with a given uncertainty (see Table 6). With these values, the effective emissivity of the urban areas was determined using the model of Caselles and Sobrino described in [39]:

$$\varepsilon_{urban\ area} = \varepsilon_t P_t + \varepsilon_g(1 - P_t) + \varepsilon_w(1 - \varepsilon_g)(1 - P_t)\left[\left(1 + \frac{H}{S}\right) - \sqrt{1 + \left(\frac{H}{S}\right)^2}\right] \quad (13)$$

where ε_t is the roofing materials emissivity (building tops), ε_g is road asphalts and tars emissivity (streets), ε_w is construction concrete emissivity (building walls), P_t is the roof proportion, H is the height of components in the urban area and S is the separation between these components.

In the calculations, different combinations of the aspect ratio H/S (from 0.5–10, at intervals of 0.5) and P_t (from 0.2–0.8, at intervals of 0.05) were considered for the possible urban structures. Using these values, urban emissivity values were simulated using a random procedure considering that the different variables in Equation (13) were normally distributed around a mean value, given by the mean values in Table 6, with a standard deviation given by the corresponding uncertainties in that table. Each simulation in this procedure gives as a result an emissivity for the urban area. The procedure was repeated 25 times, from which the final urban emissivity value was calculated as the average of the 25 different obtained values. It was checked that the use of a larger number of repetitions did not change the obtained average value and the standard deviation. The final values and uncertainties for the urban emissivity at the ASTER bands are shown in Table 6.

Table 6. Emissivity of urban areas ($\varepsilon_{urban\ area}$) used by the VCM algorithm for the ASTER TIR bands. The values of the emissivities and uncertainties of building tops (ε_t), streets (ε_g) and building walls (ε_w) used to retrieve the emissivity of urban areas are also shown. See the main text for additional details.

ASTER Band	ε_g	ε_w	ε_t	$\varepsilon_{urban\ area}$
10	0.941 ± 0.013	0.92 ± 0.03	0.94 ± 0.07	0.96 ± 0.03
11	0.945 ± 0.013	0.92 ± 0.03	0.92 ± 0.09	0.95 ± 0.04
12	0.942 ± 0.014	0.90 ± 0.04	0.88 ± 0.11	0.92 ± 0.05
13	0.956 ± 0.014	0.96 ± 0.02	0.94 ± 0.03	0.970 ± 0.013
14	0.956 ± 0.012	0.959 ± 0.007	0.954 ± 0.019	0.973 ± 0.010

In the ANEM algorithm, the VCM emissivity values for the natural areas must be calculated for each scene; however, the estimated values for water and urban areas can be used for every ASTER scene and do not need to be estimated again.

4. Results

4.1. Land Surface Temperature and Emissivity Evaluation

The values retrieved from TES and ANEM algorithms and the ASTER AST08 product were compared with ground measurements at the rice fields around the Albufera Lake and water from the Mediterranean Sea. LST values retrieved with each source are shown in Table 7.

Table 7. LST values retrieved at evaluation points of rice crops and water from TES, Adjusted Normalized Emissivity Method (ANEM) and AST08 scenes, together with reference values measured at the ground for each analyzed day. The standard deviation (Std) of each measurement is also shown.

	Date	TES		ANEM		AST08		REFERENCE	
		LST (K)	Std (K)	LST (K)	Std (K)	LST (K)	Std (K)	LST (K)	Std (K)
RICE	3 August 2004	304.2	0.4	303.8	0.4	304.3	0.3	303.6	0.7
	12 August 2004	302.5	0.5	302.2	0.5	303.0	0.5	302.0	0.5
	21 July 2005	302.5	0.6	302.0	0.5	302.5	0.5	301.6	0.6
	24 July 2006	303.0	0.6	302.5	0.5	304.5	0.5	302.4	0.9
	11 July 2007	301.6	0.6	301.3	0.5	302.6	0.4	300.3	0.3
WATER	3 August 2004	299.3	0.2	298.8	0.1	299.9	0.3	299.3	0.2
	12 August 2004	300.4	0.2	300.1	0.2	301.3	0.3	299.6	0.3
	21 July 2005	300.2	0.3	299.7	0.2	300.9	0.3	299.8	0.2
	24 July 2006	300.7	0.3	300.3	0.2	302.2	0.3	301.0	0.2
	11 July 2007	298.5	0.3	298.1	0.2	299.6	0.3	297.9	0.2

From the comparison of LST and SST values in Table 7, a better agreement between ANEM and the reference values is obtained in both areas, rice crops and the Mediterranean Sea. For the rice crops area, the three products overestimate the LST reference value, with a mean bias of +0.8 K for TES, +0.4 K for ANEM and +1.4 K for the AST08 product. While for seawater, the mean bias for TES is

+0.3 K, −0.1 K for ANEM and +1.3 K for the AST08 product. In these cases, TES and the AST08 product overestimate the references values while ANEM shows a slight underestimation of them, although on some days, such as 3 August 2004 and 11 July 2007, ANEM overestimates the SST value. It was checked that the standard deviation of SST did not depend significantly on the number of pixels used for the calculation (with similar results for 3 × 3 and 33 × 33 pixel boxes).

The emissivity at the same points was retrieved for the ASTER thermal bands using the TES and ANEM algorithms and also the AST05 product. These emissivity values were compared with the reference measurements for rice crops and water. A comparison for the sand beach was added in this analysis.

The obtained rice crop emissivity spectra corresponding to the days analyzed in this paper are shown in Figure 3. Vertical bar errors depicted in Figure 3 represent the standard deviation of the 3 × 3 window centered on the pixel of the evaluation point.

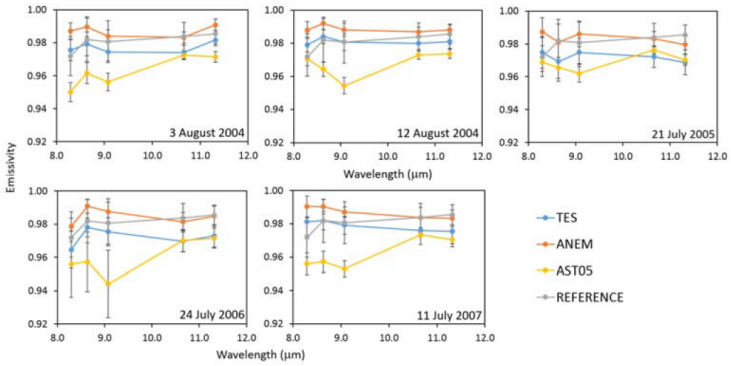

Figure 3. Rice crop emissivity for each studied day measured in the field (REFERENCE), obtained with TES and ANEM methods, and provided by the standard product AST05.

Results show a better agreement between TES values and the reference for shorter wavelength bands, while for ASTER Bands 13 and 14, ANEM emissivity is closer to the reference values. Average differences between TES, ANEM and AST05 with reference values are, respectively: 0.003, 0.014 and −0.012 for Band 10; −0.003, 0.007 and −0.021 for Band 11; −0.004, 0.006 and −0.027 for Band 12; −0.009, 0.0 and −0.011 for Band 13; and finally, −0.010, 0.0 and −0.014 for Band 14. The underestimated values of TES and AST05 emissivity are in accordance with the LST bias observed before. Moreover, the larger LST difference observed in AST08 is shown again in Figure 3 in terms of emissivity differences in the AST05 product.

In Figure 4, water spectral emissivity is depicted for each studied day. Vertical bar errors in Figure 4 represent the standard deviation of the 33 × 33 window centered on the pixel of the evaluation point.

Results in Figure 4 show better agreement between ANEM and reference emissivity, with differences under 1%. Differences between TES, ANEM and the AST05 product and reference values are, respectively: −0.014, −0.005 and −0.047 for Band 10; −0.016, −0.007 and −0.048 for Band 11; −0.011, −0.002 and −0.049 for Band 12; −0.012, −0.003 and −0.023 for Band 13; and −0.013, −0.004 and −0.026 for Band 14. These results are in accordance with the SST values of Table 7, which determined that the ANEM SST was the most accurate compared to the reference. The largest differences were shown, as with LST, by the AST05 product, with differences up to 5%. It is noticed that all of them underestimate reference emissivity as was observed previously over low-contrast surfaces [21]. This underestimation is more pronounced at Bands 10–12, as was observed in [13].

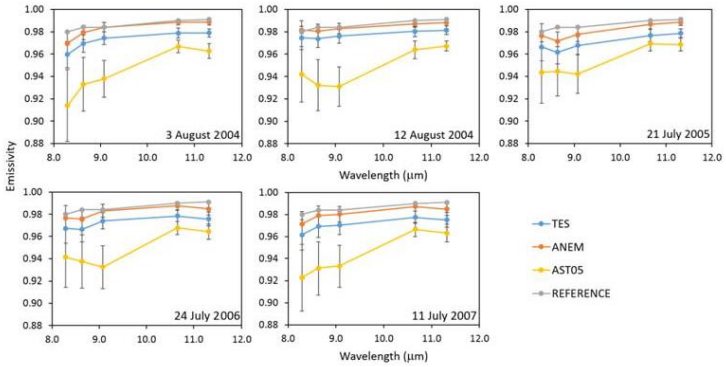

Figure 4. Water emissivity for each studied day provided by Niclòs et al. in [34] (REFERENCE), obtained with TES and ANEM methods and provided by the standard product AST05.

The emissivity comparison was also made using pixels along the beach coastline, since the sand emissivity spectrum was also measured in situ. In Figure 5, the retrieved emissivity spectra are depicted together with the reference emissivity of sand beach measured using the TES method with the CIMEL 312-2 radiometer.

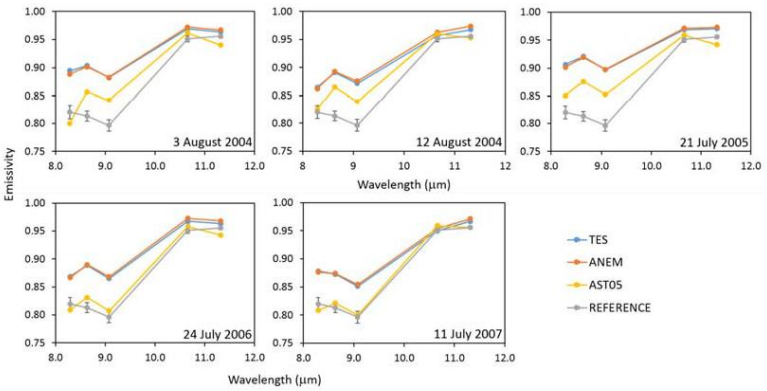

Figure 5. Sand emissivity spectra retrieved with the different methods compared to the ground reference measurements carried out on the sand beach.

Results in Figure 5 show a better agreement of the AST05 product, with differences below 1% in some cases with respect to the reference values. Average differences between TES, ANEM and AST05 with reference values are, respectively: 0.063, 0.059 and −0.001 for Band 10; 0.082, 0.083 and 0.037 for Band 11; 0.077, 0.079 and 0.032 for Band 12; 0.011, 0.015 and 0.008 for Band 13; and 0.011, 0.015 and −0.009 for Band 14. For sand, the ASTER product AST05 works better than TES and ANEM, with values closer to the reference. These results show that the ASTER product is working pretty well for this high contrast surface (sand beach), but shows significant errors in relation to low contrast surfaces (i.e., vegetation and water). The atmospherically-adjusted and -recalibrated TES used in this work and the ANEM algorithm supply very similar values in the case of sand, although they are overestimating significantly the emissivity in Channels 10–12, giving better results in Bands 13 and 14.

4.2. Comparison between TES and ANEM

To compare both methods over different surface types, four different cover types characteristic of the area were chosen: rice crop, water, orange fields and urban areas. Emissivity spectra for the four classes are presented in Figures 6–9.

Rice crop emissivity for ASTER bands is depicted in Figure 6. This emissivity was calculated as the average value of all pixels classified as rice crop; vertical bar errors show the emissivity standard deviation. These spectra show ANEM emissivities higher than TES ones, with differences $\varepsilon_{TES} - \varepsilon_{ANEM}$ ranging between -0.009 and -0.012 depending on the spectral band and the analyzed scene, with larger differences for lower wavelengths. In comparison to the reference spectrum in Figure 3, TES underestimates emissivity, while ANEM overestimates it, but in both cases, the differences are within the measurement errors. As shown in Figure 3, TES adjusted better for lower wavelengths, with differences smaller than ± 0.005 in ASTER Bands 10, 11 and 12, while for Bands 13 and 14, these differences are up to ± 0.013. For ANEM emissivity, Band 10 shows a difference up to ± 0.015; Bands 11 and 12 show differences lower than ± 0.008; and for Bands 13 and 14, the emissivity values are closer, with differences below ± 0.003. The standard deviation obtained for each channel emissivity is higher for shorter wavelengths than for longer ones, taking values from ± 0.006–± 0.013 for TES and from ± 0.004–± 0.011 for ANEM, showing a reasonable homogeneity within this class.

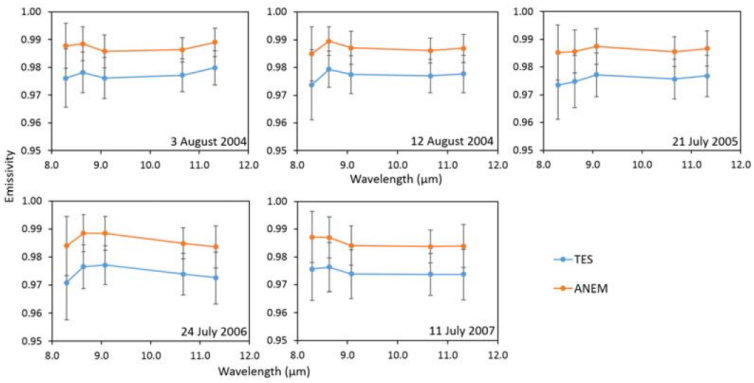

Figure 6. Mean emissivity retrieved with TES and ANEM methods using the pixels classified as rice crop for the five thermal ASTER bands.

The same analysis was performed for pixels classified as water, which include the Mediterranean Sea and the Albufera Lake, and the results are shown in Figure 7. ANEM produces emissivity values higher than TES. There is a constant difference between them for all bands of $\varepsilon_{TES} - \varepsilon_{ANEM} = -0.009$, which means a consistency in the spectral shape retrieved from both methods. This shape is in accordance with the reference spectra shown in Figure 4, although both methods underestimated the reference values, with higher differences for TES, which are up to -0.022, than for ANEM with differences up to -0.011. The standard deviations depicted with the error bars present values between ± 0.004 and ± 0.015 for TES and between ± 0.003 and ± 0.012 for ANEM, showing lower deviations for Bands 13 and 14 and higher for Bands 10 and 11.

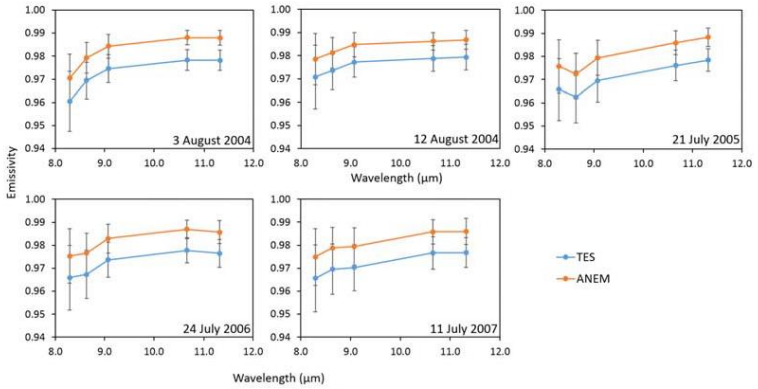

Figure 7. Mean emissivity retrieved with TES and ANEM methods using the pixels classified as water for the five thermal ASTER bands.

Since the agricultural area is the most extensive class, an orange field area common for the five scenes was selected to provide a surface with constant vegetation fractional cover over time (trees are green-leaved and have no fruits in the summer season). Figure 8 shows the emissivity spectra for this class. For each scene, the TES and ANEM methods provide the same spectral shape for each day, with emissivity differences $\varepsilon_{TES} - \varepsilon_{ANEM}$ of −0.010 for 3 August 2004, −0.009 for 12 August 2004, −0.014 for 21 July 2005 and 24 July 2006 and −0.011 for 11 July 2007. The standard deviation for TES ranges between ±0.004 and ±0.012, and for ANEM, it does between ±0.003 and ±0.010.

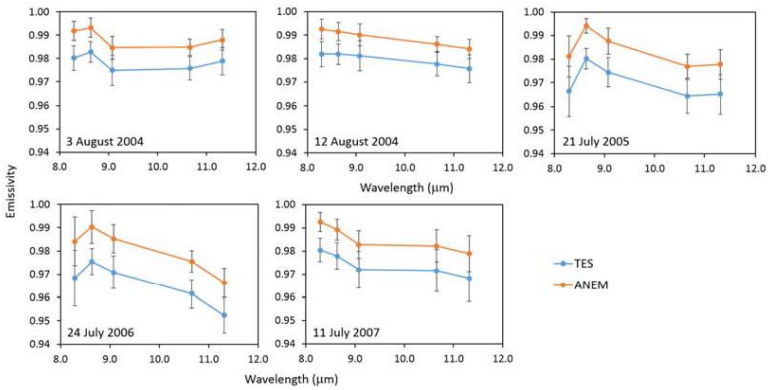

Figure 8. Mean emissivity retrieved with TES and ANEM methods using the pixels selected over orange fields for the five thermal ASTER bands.

Figure 9 shows the emissivity corresponding to urban areas, which include cities, towns, industrial zones and other urbanized sites. For urban surfaces, emissivity spectra retrieved from TES and ANEM provide closer values, with differences below ±0.004. For ASTER Bands 10, 11 and 12, TES overestimates ANEM values, with differences $\varepsilon_{TES} - \varepsilon_{ANEM}$ up to +0.007. For Bands 13 and 14, it depends on the scene, but the differences are very close to zero. The standard deviation obtained

for TES is between ±0.009 and ±0.018, and for ANEM, it is between ±0.008 and ±0.020, with higher differences for lower wavelengths.

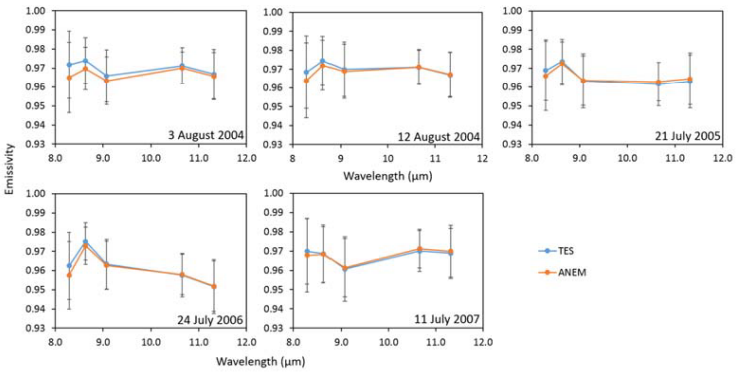

Figure 9. Mean emissivity retrieved with TES and ANEM methods using the pixels classified as urban area for the five thermal ASTER bands.

5. Discussion

5.1. Advantages and Limitations of TES and ANEM

TES and ANEM algorithms have as a common point the use of the NEM method. TES uses NEM as the initial module starting from a single emissivity value for every pixel and channel to get a first-guess relative spectrum, which is then spectrally tuned using the MMD empirical relationship getting finally the LST. ANEM obtains a maximum emissivity value different for each pixel (contrary to TES) using the VCM algorithm, then obtains the emissivity spectrum using this first-guess emissivity in the NEM method.

Both methods need the use of at-surface radiances corrected for the atmospheric effects as input data. For this reason, atmospheric correction with radiosounding profiles spatially and temporally coincident to the ASTER data recordings and local recalibration of the ASTER radiances were used. This procedure assured that both methods were compared under optimal conditions.

A rough classification is required in the VCM module of ANEM to separate the vegetated surfaces from urban and water areas (and eventually, ice/snow where needed). For water and urban areas, the maximum emissivity is estimated once (as in this paper) and can be applied to different scenes and areas. For the vegetated surface, the maximum emissivity for NEM needs an estimation of the fractional vegetation cover that can be calculated easily from VNIR data using the proposed methodology with low dependence on the atmospheric correction and two average emissivity coefficients, namely bare soil and vegetation emissivity. A mean emissivity is enough for vegetation, but it could be insufficient to describe the variation of all soil types, especially in the 8–10-μm range. However, the soil emissivity usually peaks within 10–12 μm just where soil emissivities show much lower variability as can be seen in the standard deviation of the soil coefficients for ASTER Channels 13 and 14 in Table 5 (below ±0.006). Note that in ANEM, the VCM is used to get a first-guess maximum emissivity as the input to the NEM module and not to obtain the final spectrum. In addition, the VCM allows adjusting this first-guess considering the temporal changes in the surface introduced by the vegetation phenology; these changes can be significant through the year especially for senescent vegetation and agricultural areas.

The matrix confusion of the classification was used to check its accuracy, and it showed an overall accuracy of 97.3% and an index kappa of 0.967. In any case, an estimation of the emissivity error in

ANEM due to misclassified pixels was also made. It would cause a difference in the initial emissivity at the NEM module. If a pixel of the urban area were misclassified as water or vegetated area, or vice versa, this difference in the initial emissivity would be ±0.015. This difference at the initial emissivity would lead to errors up to ±0.7 K in the final LST following the described methodology.

In contrast, TES applies the NEM module with a single emissivity value to get a first relative emissivity spectrum and LST value. They are then refined by using the MMD empirical relationship that places the absolute value of the emissivity spectrum providing the final LST. The main drawback of TES is the MMD relationship that was initially derived with a strong predominance of soil and rock samples, although it was modified by Hulley and Hook in [12] by adding simulated samples with different degrees of vegetation cover; and the high sensitivity of the MMD to residual errors in the atmospheric correction that makes this relationship provide too low minimum emissivities, thus lowering the whole spectrum. For that reason, TES provides in general excellent results over high contrast surfaces (almost all the validation exercises have been conducted till present over desert areas), but more modest results over vegetated or water surfaces.

5.2. *Quality of Reference Data*

Different data were used as the reference for validating the results obtained. For rice crops, LST data were measured with several CIMEL 312 radiometers deployed in the field concurrent to the scene acquisition, providing accurate ground reference values. For water, no radiometric or contact temperatures provided by sea buoys were available at the time of scene acquisitions; thus, the MODIS L2 SST product (MOD28) was taken as the reference, or at least as a cross-comparison for the TES and ANEM results. Although the MOD28 SST product is not a ground reference strictly speaking, the SST values are obtained using a split-window algorithm devised specifically for the sea surface and has been extensively validated [40–43], in particular including buoys in the Mediterranean Sea in the comparison [34], providing an overall accuracy of ±0.37 K (for MODIS viewing angles $\leq 40°$) that gives confidence to these data as a valid reference for TES and ANEM. The difference in spatial resolution of MODIS (1 km) and ASTER (90 m) is not a limiting condition for the comparison, since SST usually varies smoothly in space as can be seen in the low standard deviations of the MODIS SST data collected in 3 × 3 pixel boxes (<0.2 K) and the corresponding TES and ANEM SST values for 33 × 33 pixel windows (<0.3 K).

5.3. *LSE and LST Evaluation*

With regard to the LST evaluation using the reference measurements, the ASTER AST08 product retrieved values within the uncertainty established in [10], as other previous works have pointed out [13,22]. However, the LSTs obtained from the applied TES and ANEM algorithms showed a better accuracy in this paper when applied to data with a more site-specific atmospheric correction, the results being slightly better for ANEM than for TES.

With regard to emissivity, it is observed that for surfaces with low spectral contrast such as water or rice crops, AST05 provides less accurate values than ANEM or TES out of the predicted uncertainty range proposed in [10]. These differences could be due to the empirical expression to retrieve the minimum emissivity from MMD at the AST05 product algorithm, which is not fitted to low contrast surfaces [12], as well as to the atmospheric correction applied at the product AST05, since NCEP atmospheric profiles are less accurate than profiles obtained by in situ radiosoundings [44,45]. As an example, Pérez-Planells et al. in [45] showed that using interpolated NCEP profiles instead of radiosoundings yielded errors of ±0.6 K for sites close to sea level, which would be equivalent to ±0.01 in terms of emissivity. Moreover, previous studies pointed out that ASTER product atmospheric correction loses accuracy in warm and humid areas close to sea level [23,24]. Despite using an MMD relationship including additional samples for vegetated surfaces and a local recalibration and atmospheric correction, the results of emissivity for these surfaces are systematically lower for TES than

for ANEM (see Figures 3 and 4), which confirms the existence of an impact of residual atmospheric correction errors that may be affecting TES emissivities more than ANEM ones.

Nevertheless, for a high contrast surface as the sand beach is, the AST05 product fits much better to the ground reference measurement than the TES applied in this paper and ANEM, especially for spectral bands from 8–10 μm. It is difficult to find an explanation of this result, provided that the AST05 product and the TES version applied in this work should at least give similar results, since a local radiosounding was used in the latter. By contrast, TES provides virtually the same results as ANEM for that surface type.

5.4. TES and ANEM Comparison over Time

The comparison between TES and ANEM algorithms on different surfaces over time shows that the obtained spectra are consistent for all surfaces, with little differences, which are always within the uncertainty. For rice crop, water and orange field, ANEM emissivity values are higher than TES by 1%, ANEM results being closer to the ground reference values.

For urban areas, an overestimation of TES emissivity is observed, which does not appear in the previous classes, so urban area is a class that provides pixels with positive differences between TES and ANEM. In this class, moreover, the spectra show again temporal consistency over the years, as was the case of rice crops and water.

It is worth showing that two different areas can be distinguished inside the urban class. Using TES emissivities in ASTER Bands 10, 12 and 14, emissivity bands in the RGB composition shown in Figure 10 for the scene on 3 August 2004, city areas (red pixels) can be clearly distinguished from industrial areas (green pixels); a difference that cannot be clearly observed with the VNIR and SWIR bands. The same effect was observed using ANEM emissivities. For each scene, a set of 3×3 pixels (selected from visual inspection of Figure 10) was used to retrieve the emissivity spectra of each area for the five TES scenes used in this work, obtaining the results shown in Figure 11.

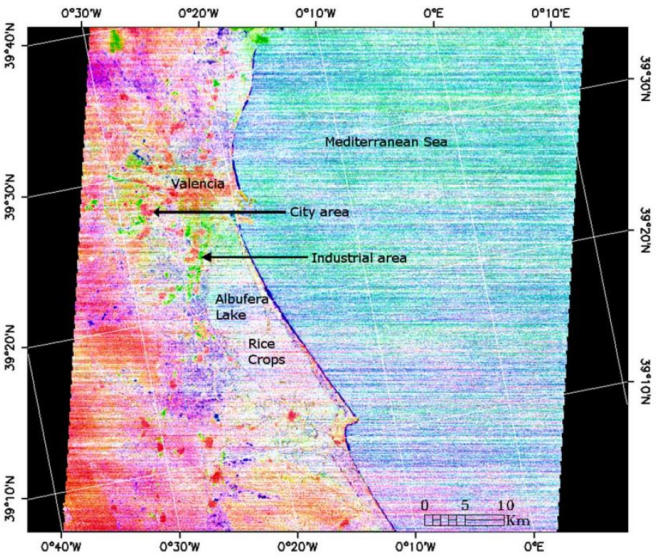

Figure 10. Scene over the study area on 3 August 2004 using TES emissivity from ASTER Channels 10 (8.29 μm), 12 (9.08 μm) and 14 (11.32 μm) to compose the RGB image, respectively.

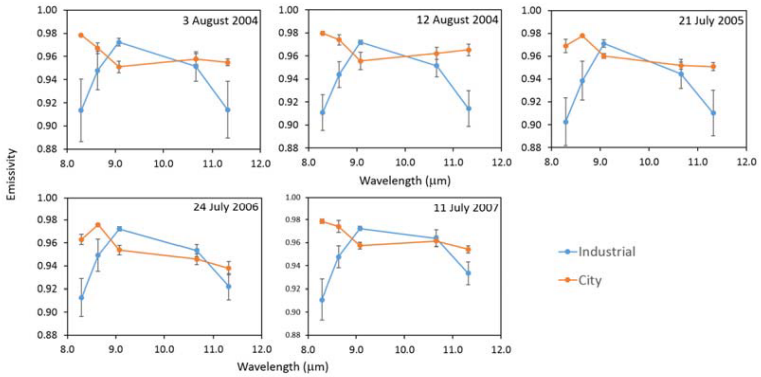

Figure 11. Mean emissivity retrieved with the TES method in 3 × 3 windows over the industrial area (centered on coordinates: 39°14′1″N 0°29′25″W) and the urban area (centered on coordinates: 39°11′35″N 0°26′2″W) for the five thermal ASTER bands.

A clearly different spectrum for each area is observed. The main construction materials for the city area are red bricks, terra cotta tiles and asphalt for building roofing and streets. The emissivity spectra of these materials were retrieved from the ASTER Spectral Library and integrated for the TIR ASTER bands (see Figure 12). The same process was done for the industrial area, considering concrete, galvanized steel, oxidized galvanized steel and asphalt as the main construction materials for this area (see Figure 13). Oxidized galvanized steel was also included because galvanized steel oxidizes after a time outdoors.

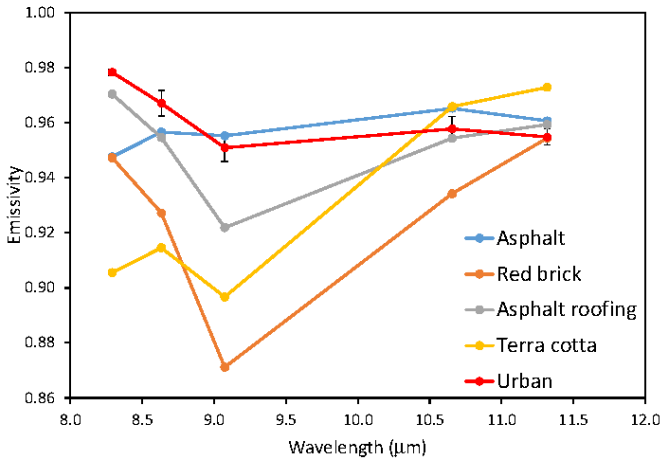

Figure 12. Mean emissivity of urban construction materials retrieved from the ASTER Spectral Library and integrated for the five thermal ASTER bands.

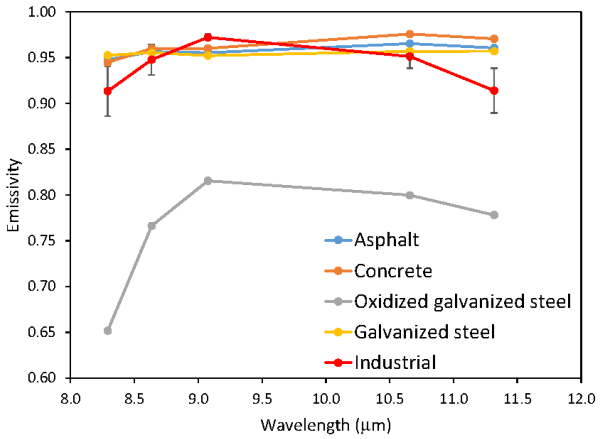

Figure 13. Mean emissivity of industrial construction materials retrieved from the ASTER Spectral Library and integrated for the five thermal ASTER bands.

The TES emissivity spectra obtained for the city area (Figure 11) resemble the spectra of red brick and asphalt roofing (Figure 12), showing similar shapes. This is reasonable, since red brick is one of the materials most used in buildings. It is observed that the city spectra show values higher than any material; this may be due to the cavity effect caused by the city structure. Looking at the industrial area, the TES emissivity spectra shown in Figure 11 are very similar to the shape of the oxidized galvanized steel spectrum shown in Figure 13. It should be noted that this last spectrum does not fit the MMD regression curve used by TES, showing lower values ($\varepsilon_{min} = 0.65$) than those predicted by Equation (7) ($\varepsilon_{min} = 0.82$) for $MMD = 0.16$ observed in Figure 13. Taking into account the spectra of the other materials used in these zones, which have higher emissivity values and a lower spectral contrast, and taking into account the cavity effect, the spectra compare reasonably well.

6. Conclusions

This paper compared the TES and ANEM algorithms using L1 ASTER data that were recalibrated and atmospherically corrected using concurrent local atmospheric profiles. The algorithms were applied to a set of five ASTER scenes over the area of Valencia, Spain, which included water, agricultural and urban areas. The results were compared to the ASTER temperature and emissivity standard products (AST08 and AST05 products, respectively).

The surface temperatures obtained from TES, ANEM and AST08 product were validated with reference measurements taken on a rice paddy located near the Albufera Lake of Valencia and also with the sea surface temperature provided by Terra MODIS (MOD28 product). From these comparisons, it is concluded that ANEM shows the best agreement, with a bias of +0.4 K and −0.01 K for LST and SST, respectively. For TES, biases are +0.8 K and +0.3 K, respectively. Both methods provide good results since their accuracy is less than 1 K. Results shown by the AST08 product are worse, with biases of +1.4 K for LST and +1.3 K for SST; this may be due largely to the use of NCEP profiles for atmospheric correction in AST08 in comparison to the local recalibration and atmospheric correction performed in ANEM and TES.

The emissivity spectra obtained with both methods and provided by the AST05 product were compared on two land surfaces, rice and sand, for which ground measurements were made, and on the sea surface using the water spectra provided by the ASTER spectral library. It was observed that in the case of rice crops, TES provided values closer to the reference spectra in ASTER Bands 10–12,

while ANEM showed better accuracy for ASTER Bands 13 and 14. For water, both the TES and ANEM methods underestimated the emissivity. ANEM results were closer to the reference with differences lower than 0.005, while for TES, these differences were up to 0.015. In comparison, the AST05 product showed less agreement in these two low-contrast surfaces, yielding differences up to −0.027 for rice crops and −0.050 for water. For sand, differences between TES and ANEM were less than 0.005, and they disagreed with the reference measurement by 0.06–0.08 for Bands 10–12 and by 0.011–0.015 for Bands 13 and 14. In contrast, the results shown by the AST05 product in this case were much better, showing biases of −0.001 for Band 10, +0.037 for Band 11, +0.032 for Band 12, +0.008 for Band 13 and −0.009 for Band 14. These were out of the uncertainty predicted for the AST05 product, which could be attributed to residual errors in the atmospheric correction used in the ASTER products, as has been pointed out previously [21,23,25], as well as to the deficient adjustment for low-contrast surfaces in the MMD empirical relationship [21]. However, results showed a better agreement of the AST05 product over high spectral contrast areas, such as a sandy beach.

The TES and ANEM results were also compared to each other using four known surface types common for the scenes. For surfaces with low spectral contrast, such as water or vegetated areas, ANEM systematically overestimated TES emissivity, yielding closer values to the reference emissivity. However, for surfaces with a high spectral difference, such as urban areas, ANEM obtained values lower than TES, but close to them. Both methods were capable of separating surfaces with different spectral behaviors, as shown in the analysis of the urban areas. In addition, the temporal evolution of the obtained emissivity spectra in both cases could be used to monitor changes in the observed surfaces as has been also indicated by Hulley et al. in [46].

Future work will be addressed to analyzing the use of more efficient atmospheric correction algorithms in TES and ANEM, such as the Water Vapor Scaling (WVS) method [24] or the Single-Band Atmospheric Correction (SBAC) [47], and the eventual combination of TES and ANEM in a single algorithm that could benefit from the strengths shown by both methods.

Acknowledgments: This work was funded by the Spanish Ministerio de Economía y Competitividad and the European Regional Development Fund (FEDER) through the project CGL2015-64268-R (MINECO/FEDER, UE), by the Ministerio de Economía y Competitividad under the project CGL2013-46862-C2-1-P and by the Generalitat Valenciana under Contract PROMETEOII/2014/086.

Author Contributions: Lluís Pérez-Planells is the main author of this research work and wrote the manuscript. Enric Valor, César Coll and Lluís Pérez-Planells proposed the ANEM methodology, and performed the data processing and analysis. Raquel Niclòs contributed to the satellite data evaluation and the results analysis.

Conflicts of Interest: The authors declare no conflict of interest.

References

1. Zhang, R.; Tian, J.; Su, H.; Sun, X.; Chen, S.; Xia, J. Two improvements of an operational two-layer model for terrestrial surface heat flux retrieval. *Sensors* **2008**, *8*, 6165–6187. [CrossRef] [PubMed]
2. Anderson, M.C.; Kustas, W.P.; Norman, J.M.; Hain, C.R.; Mecikalski, J.R.; Schultz, L.; González-Dugo, M.P.; Cammalleri, C.; D'Urso, G.; Pimstein, A.; et al. Mapping daily evapotranspiration at field to continental scales using geostationary and polar orbiting satellite imagery. *Hydrol. Earth Syst. Sci.* **2011**, *15*, 223–239. [CrossRef]
3. Sánchez, J.M.; López-Urrea, R.; Rubio, E.; González-Piqueras, J.; Caselles, V. Assessing crop coefficients of sunflower and canola using two-source energy balance and thermal radiometry. *Agric. Water Manag.* **2014**, *137*, 23–29. [CrossRef]
4. Li, Z.; Tang, B.; Wu, H.; Ren, H.; Yan, G.; Wan, Z.; Trigo, I.F.; Sobrino, J.A. Satellite-derived land surface temperature: Current status and perspectives. *Remote Sens. Environ.* **2013**, *131*, 14–37. [CrossRef]
5. Watson, K. Two-temperature method for measuring emissivity. *Remote Sens. Environ.* **1992**, *42*, 117–121. [CrossRef]
6. Li, Z.L.; Becker, F. Feasibility of land surface temperature and emissivity determination from AVHRR data. *Remote Sens. Environ.* **1993**, *43*, 67–85. [CrossRef]

7. Barducci, A.; Pippi, I. Temperature and emissivity retrieval from remotely sensed images using the "grey body emissivity" method. *IEEE Trans. Geosci. Remote Sens.* **1996**, *34*, 681–695. [CrossRef]
8. Borel, C. Iterative Retrieval of Surface Emissivity and Temperature for a Hyperspectral Sensor. In Proceedings of the 1st JPL Workshop on Remote Sensing of Land Surface Emissivity, Pasadena, CA, USA, 6–8 May 1997.
9. Wan, Z.; Li, Z.L. A physics-based algorithm for retrieving land-surface emissivity and temperature from eos/modis data. *IEEE Trans. Geosci. Remote Sens.* **1997**, *35*, 980–996.
10. Gillespie, A.; Rokugawa, S.; Matsunaga, T.; Cothern, J.S.; Hook, S.; Kahle, A.B. A Temperature and Emissivity Separation Algorithm for Advanced Spaceborne Thermal Emission and Reflection Radiometer (ASTER) Images. *IEEE Trans. Geosci. Remote Sens.* **1998**, *36*, 1113–1126. [CrossRef]
11. Wang, N.; Wu, H.; Nerry, F.; Li, C.; Li, Z.L. Temperature and emissivity retrievals from hyperspectral thermal infrared data using linear spectral emissivity constraint. *IEEE Trans. Geosci. Remote Sens.* **2011**, *49*, 1291–1303. [CrossRef]
12. Hulley, G.C.; Hook, S.J. The North American ASTER Land Surface Emissivity Database (NAALSED) Version 2.0. *Remote Sens. Environ.* **2009**, *113*, 1967–1975. [CrossRef]
13. Sabol, D.E.; Gillespie, A.R.; Abbott, E.; Yamada, G. Field validation of the ASTER Temperature-Emissivity Separation algorithm. *Remote Sens. Environ.* **2009**, *113*, 2328–2344. [CrossRef]
14. Jiménez-muñoz, J.C.; Sobrino, J.A.; Mattar, C.; Hulley, G.; Göttsche, F. Temperature and Emissivity Separation from MSG/SEVIRI Data. *IEEE Trans. Geosci. Remote Sens.* **2013**, *52*, 1–15. [CrossRef]
15. Coll, C.; García-Santos, V.; Niclòs, R.; Caselles, V. Test of the MODIS Land Surface Temperature and Emissivity Separation Algorithm with ground measurements over a rice paddy. *IEEE Trans. Geosci. Remote Sens.* **2016**, *54*, 3061–3069. [CrossRef]
16. Islam, T.; Hulley, G.; Malakar, N.; Radocinski, R.; Guillevic, P.; Hook, S. A physics-based algorithm for the simultaneous retrieval of land surface temperature and emissivity from VIIRS thermal infrared data. *IEEE Trans. Geosci. Remote Sens.* **2017**, *55*, 563–576. [CrossRef]
17. Coll, C.; Caselles, V.; Rubio, E.; Sospedra, F.; Valor, E. Temperature and emissivity separation from calibrated data of the Digital Airborne Imaging Spectrometer. *Remote Sens. Environ.* **2001**, *76*, 250–259. [CrossRef]
18. Coll, C.; Valor, E.; Caselles, V.; Niclo, R. Adjusted Normalized Emissivity Method for surface temperature and emissivity retrieval from optical and thermal infrared remote sensing data. *J. Geophys. Res.* **2003**, *108*, 1–14. [CrossRef]
19. Gillespie, A.R. *Lithologic Mapping of Silicate Rocks Using TIMS*; TIMS Data User's Workshop Jet Propulsion Laboratory: Pasadena, CA, USA, 1986; pp. 29–44.
20. Valor, E.; Caselles, V. Mapping Land Surface Emissivity from NDVI: Application to European, African, and South American Areas. *Remote Sens. Environ.* **1996**, *184*, 167–184. [CrossRef]
21. Coll, C.; Caselles, V.; Valor, E.; Niclòs, R.; Sánchez, J.M.; Galve, J.M.; Mira, M. Temperature and emissivity separation from ASTER data for low spectral contrast surfaces. *Remote Sens. Environ.* **2007**, *110*, 162–175. [CrossRef]
22. Barreto, Á.; Arbelo, M.; Hernández-Leal, P.A.; Núez-Casillas, L.; Mira, M.; Coll, C. Evaluation of surface temperature and emissivity derived from ASTER data: A case study using ground-based measurements at a volcanic site. *J. Atmos. Ocean. Technol.* **2010**, *27*, 1677–1688. [CrossRef]
23. Gillespie, A.R.; Abbott, E.A.; Gilson, L.; Hulley, G.; Jiménez-Muñoz, J.C.; Sobrino, J.A. Residual errors in ASTER temperature and emissivity standard products AST08 and AST05. *Remote Sens. Environ.* **2011**, *115*, 3681–3694. [CrossRef]
24. Tonooka, H. Accurate atmospheric correction of ASTER thermal infrared imagery using the WVS method. *IEEE Trans. Geosci. Remote Sens.* **2005**, *43*, 2778–2792. [CrossRef]
25. Gustafson, W.; Gillespie, A.; Yamada, G. Revisions to the ASTER temperature/emissivity separation algorithm. In Proceedings of the 2nd Recent Advances in Quantitative Remote Sensing, Torrent, Spain, 25–29 September 2006; pp. 770–775.
26. Chavez, P.S. Image-Based Atmospheric Corrections—Revisited and Improved. *Photogramm. Eng. Remote Sens.* **1996**, *62*, 1025–1036.
27. Berk, A.; Anderson, G.P.; Acharya, P.K.; Chetwynd, J.H.; Bernstein, L.S.; Shettle, E.P.; Matthew, M.W. *MODTRAN4 User's Manual*; Air Force Research Laboratory: Hanscom AFB, Bedford, MA, USA, 1999.
28. Gillespie, A.R.; Rokugawa, S.; Hook, S.J.; Matsunaga, T.; Kahle, A.B. *Temperature/Emissivity Separation Algorithm Theoretical Basis Document, Version 2.4*; NASA: Washington, DC, USA, 1999; Volume 4, pp. 1–64.

29. Thome, K.; Palluconi, F.; Takashima, T.; Masuda, K. Atmospheric correction of ASTER. *IEEE Trans. Geosci. Remote Sens.* **1998**, *36*, 1199–1211. [CrossRef]
30. Niclòs, R.; Doña, C.; Valor, E.; Bisquert, M.; Niclòs, R.; Doña, C.; Valor, E.; Bisquert, M. Thermal-Infrared Spectral and Angular Characterization of Crude Oil and Seawater Emissivities for Oil Slick Identification. *IEEE Trans. Geosci. Remote Sens.* **2014**, *52*, 5387–5395.
31. Legrand, M.; Pietras, C.; Brogniez, G.; Haeffelin, M.; Abuhassan, N.K.; Sicard, M. A high-accuracy multiwavelength radiometer for in situ measurements in the thermal infrared. Part I: Characterization of the instrument. *J. Atmos. Ocean. Technol.* **2000**, *17*, 1203–1214. [CrossRef]
32. Payan, V.; Royer, A. Analysis of Temperature Emissivity Separation (TES) algorithm applicability and sensitivity. *Int. J. Remote Sens.* **2004**, *25*, 15–37. [CrossRef]
33. Brown, O.B.; Minnett, P.J. *MODIS Infrared Sea Surface Temperature Algorithm Algorithm Theoretical Basis Document*; University of Miami: Miami, FL, USA, 1999.
34. Niclòs, R.; Caselles, V.; Coll, C.; Valor, E. Determination of sea surface temperature at large observation angles using an angular and emissivity-dependent split-window equation. *Remote Sens. Environ.* **2007**, *111*, 107–121. [CrossRef]
35. Baldridge, A.M.; Hook, S.J.; Grove, C.I.; Rivera, G. The ASTER spectral library version 2.0. *Remote Sens. Environ.* **2009**, *113*, 711–715. [CrossRef]
36. Caselles, E.; Valor, E.; Abad, F.; Caselles, V. Automatic classification-based generation of thermal infrared land surface emissivity maps using AATSR data over Europe. *Remote Sens. Environ.* **2012**, *124*, 321–333. [CrossRef]
37. Valor, E.; Caselles, V. Validation of the vegetation cover method for land surface emissivity estimation. In *Recent Research Developments in Thermal Remote Sensing*; Research Signpost: Kerala, India, 2005.
38. Rouse, J.W.; Haas, R.H.; Schell, J.A.; Deering, D.W.; Harlan, J.C. *Monitoring the Vernal Advancement and Retrogradation (Greenwave Effect) of Natural Vegetation*; Type III, Final Report; NASA/GSFC: Greenbelt, MD, USA, 1974; p. 371.
39. Caselles, V.; Sobrino, J.A. Determination of frost in orange groves from NOAA-9 AVHRR data. *Remote Sens. Environ.* **1989**, *29*, 135–146. [CrossRef]
40. Marcello, J.; Eugenio, F.; Hernandez, A. Validation of MODIS and AVHRR/3 Sea Surface Temperature Retrieval Algorithms. In Proceedings of the IEEE International Geoscience and Remote Sensing Symposium (IGARSS '04), Anchorage, AK, USA, 20–24 September 2004; pp. 839–842.
41. Lee, M.-A.; Tzeng, M.-T.; Hosoda, K.; Sakaida, F.; Kawamura, H.; Shieh, W.; Yang, Y.; Chang, Y. Validation of JAXA/MODIS Sea Surface Temperature in Water around Taiwan Using the Terra and Aqua Satellites. *Terr. Atmos. Ocean. Sci.* **2010**, *21*, 727–736. [CrossRef]
42. Qin, H.; Chen, G.; Wang, W.; Wang, D.; Zeng, L. Validation and application of MODIS-derived SST in the South China Sea. *Int. J. Remote Sens.* **2014**, *35*, 4315–4328. [CrossRef]
43. Hao, Y.; Cui, T.; Singh, V.P.; Zhang, J.; Yu, R.; Zhilei, Z. Validation of MODIS Sea Surface Temperature Product in the Coastal Waters of the Yellow Sea. *IEEE J. Sel. Top. Appl. Earth Obs. Remote Sens.* **2017**, *10*, 1667–1680. [CrossRef]
44. Coll, C.; Caselles, V.; Valor, E.; Niclòs, R. Comparison between different sources of atmospheric profiles for LST retrieval from single channel thermal infrared data. *Remote Sens. Environ.* **2012**, *117*, 199–210. [CrossRef]
45. Pérez-Planells, L.; García-Santos, V.; Caselles, V. Comparing different profiles to characterize the atmosphere for three MODIS TIR bands. *Atmos. Res.* **2015**, *161–162*, 108–115. [CrossRef]
46. Hulley, G.; Veraverbeke, S.; Hook, S. Thermal-based techniques for land cover change detection using a new dynamic MODIS multispectral emissivity product (MOD21). *Remote Sens. Environ.* **2014**, *140*, 755–765. [CrossRef]
47. Galve, J.M.; Coll, C.; Sánchez, J.M.; Valor, E.; Niclòs, R.; Pérez-Planells, L.; Doña, C.; Caselles, V. Single band atmospheric correction tool for thermal infrared data: Application to Landsat 7 ETM+. In Proceedings of the SPIE 10004, Image and Signal Processing for Remote Sensing XXII, Edinburgh, UK, 26–29 September 2016. [CrossRef]

Anexo G

Evaluation of the S-NPP VIIRS land surface temperature product using ground data acquired by an autonomous system at a rice paddy

El siguiente trabajo fue publicado en ISPRS Journal of Photogrammetry and Remote Sensing en enero del 2018. Esta revista tiene un factor de impacto de 6,94 y ocupa la posición 3 de 30 revistas en la categoría Remote Sensing según Journal Citation Reports en la edición de 2018.

ISPRS Journal of Photogrammetry and Remote Sensing 135 (2018) 1–12

Contents lists available at ScienceDirect

ISPRS Journal of Photogrammetry and Remote Sensing

journal homepage: www.elsevier.com/locate/isprsjprs

Evaluation of the S-NPP VIIRS land surface temperature product using ground data acquired by an autonomous system at a rice paddy

Raquel Niclòs [a,*], Lluís Pérez-Planells [a], César Coll [a], José A. Valiente [b], Enric Valor [a]

[a] Department of Earth Physics and Thermodynamics, Faculty of Physics, University of Valencia., 50 Dr. Moliner, E-46100 Burjassot, Spain
[b] Instituto Universitario Centro de Estudios Ambientales del Mediterráneo – CEAM-UMH, 14 Charles Darwin, E-46980 Paterna, Spain

ARTICLE INFO

Article history:
Received 5 June 2017
Received in revised form 30 October 2017
Accepted 30 October 2017

Keywords:
Land surface temperature
Emissivity
S-NPP VIIRS
Validation
Accuracy
Multiangular ground measurements

ABSTRACT

The S-NPP VIIRS Land Surface Temperature (LST) product attained the stage V1 of validation maturity (provisional validated) at the end of 2014. This paper evaluates the current VIIRS V1 LST product versus concurrent ground data acquired at a rice paddy site from December 2014 to August 2016. The experimental site has three different seasonal and homogeneous land covers through the year, which makes the site interesting for validation activities. An autonomous and multiangular system was used to record continuous ground data at the site. The data acquired at zenith angles similar to the VIIRS viewing angles were used for the validation to avoid possible differences between satellite and ground views due to angular dependences of the LSTs. Concurrently to surface data, downwelling sky radiances were measured at different incidence angles by the system, which were used to improve the cloud screening of the validation dataset, since cloud leakage was identified in previous validation studies as an important issue for further improvement. The validation results show good performance for the VIIRS V1 LST product at zenith angles $\leq 40°$, with systematic uncertainties within ±0.5 K and accuracies around 1.2 K. These values are within the threshold requirements established for the VIIRS LST product, and they are better than the validation results published previously for the beta version of the product or using VIIRS data reprocessed with the calibrated algorithm coefficients implemented from April 2014. As the VIIRS LST algorithm has regression coefficients dependent on land cover type, the impact of land cover misclassifications on VIIRS LST data accuracy was also evaluated. It was expected that changing the surface type assigned by the VIIRS product to more appropriate types at the site pixels should improve the validation results. However, the improvement was limited, likely due to the reduced range of variability of the emissivities considered for the different land cover types in the regression process of the VIIRS LST algorithm coefficients. The results reveal the difficulties and uncertainties involved in the LST retrieval when using a LST algorithm with surface type dependent coefficients.

1. Introduction

Land surface temperature (LST) and emissivity are key variables to assess the longwave flux exchange between land surfaces and the atmosphere, and therefore they are essential variables in meteorology, climatology and hydrology (Weng, 2009; Ghent et al., 2010; Schneider and Hook, 2010; Anderson et al., 2012; Sánchez et al., 2015).

The aim of this paper is to evaluate the LST product of the Suomi National Polar-Orbiting Partnership (S-NPP) Visible Infrared Imaging Radiometer Suite (VIIRS) using concurrent ground measurements. The VIIRS LST product is generated with a split-window algorithm with different sets of coefficients for daytime and nighttime overpasses and for 17 surface land cover types, which are assigned to each VIIRS pixel according to classification maps (Yu et al., 2005; VIIRS LST ATBD, 2013). The threshold requirements for VIIRS LSTs are bias between satellite and ground-based LSTs of 1.4 K and standard deviation (SD) of 2.5 K, although the objective is to attain bias of 0.8 K and SD of 1.5 K (Justice et al., 2013; Joint Polar Satellite System (JPSS) Program, 2014). In this paper, the current V1 version of the product (i.e., JPSS defined "provisional validated") was evaluated from mid-December 2014 to mid-August 2016 using data acquired by an autonomous and multiangular system deployed on a permanent station in a ~100 km^2 flat and homogeneous area of rice fields (39.274°N, −0.317°E in

* Corresponding author.
E-mail address: raquel.niclos@uv.es (R. Niclòs).

https://doi.org/10.1016/j.isprsjprs.2017.10.017

WGS-84; 2.5 m above sea level) near Valencia city, Spain. Due to changes in crop phenology, the site has different seasonal land covers throughout the year (water, bare soil and full vegetation cover), all of them being thermally homogeneous (Coll et al., 2005, 2007; Niclòs et al., 2015).

There exist several methods for the validation of satellite-derived LSTs. One is the temperature-based method, which directly compares satellite LSTs with concurrent ground measurements in a test site. In this case, the test site must be thermally homogeneous at the spatial scales of the ground measurements (m^2) and the satellite data (km^2), a condition which is difficult to meet for most land surfaces. Another validation method is the radiance-based method (Wan and Li, 2008; Coll et al., 2009) where ground-measured LSTs are not necessary, but requires emissivity estimates and atmospheric profiles over the validation site concurrent with the satellite overpass, together with an atmospheric radiative transfer model. Although the radiance-based method does not strictly provide a direct LST validation, it can be applied to much more surface types than the temperature-based method. However, the efficiency of the radiance-based method depends on the quality of the emissivity data and the atmospheric profiles required. Finally, LST estimates from a satellite under study can be compared to LSTs provided by another well documented, validated satellite sensor, what is known as the cross-validation method (Tang et al., 2015; Duan et al., 2017). However, when comparing LST products from different satellites, there are important sources of discrepancies (overpass times, view angles, cloud cover, resolutions and spectral response functions) that can affect the performance evaluations.

The characterization of uncertainties on existing LST products is not possible without independent and traceable sites (Hulley et al., 2012). Thus, accurate in situ LST measurements at dedicated, homogeneous validation sites provide the most reliable validation results (Guillevic et al., 2014).

Several studies have evaluated the previous versions of the VIIRS LST product (Justice et al., 2013; Li et al., 2014; Guillevic et al., 2014). Guillevic et al. (2014) presented validation results against ground measurements for the version previous to V1 (with the JPSS defined "beta maturity stage", i.e., minimally validated) of the VIIRS LST product. They used VIIRS LST data from August 2012 to October 2013, provided by both the NOAA's Comprehensive Large Array-data Stewardship System (CLASS) and the NASA's Land Product Evaluation and Analysis Tool Element (LPEATE), which contains subsets of the VIIRS data. Ground data were acquired from 8 stations (7 from the SURFace RADiation (SURFRAD) network and the Karlsruhe Institute of Technology (KIT) Gobabeb station in Namibia) and by NASA JPL at Lake Tahoe, California. The validation showed that the VIIRS beta LST product performed accordingly to the threshold requirements over most vegetated and inland water surfaces, with overall mean differences lower than ±0.8 K and SD values from 0.4 to 2.7 K depending on the site. However, stronger biases and SDs were obtained when results were analyzed separately for nighttime and daytime overpasses. Moreover, an overall bias of −4.6 K, with SD of 2.5 K, was obtained for the Gobabeb station. Other studies over arid and semi-arid validation sites (Justice et al., 2013; Li et al., 2014) also showed a systematic underestimation of the VIIRS beta LST product by up to 5 K.

Liu et al. (2015) used ground measurements acquired by the SURFRAD observing network to evaluate the product with new calibrated algorithm coefficients implemented from April 2014 (those of the current version V1). They also used ground data acquired by the Gobabeb station in Namibia for the evaluation, similarly to that shown by Guillevic et al. (2014). The SURFRAD stations provide ground data of upwelling and downwelling thermal infrared (TIR) irradiances measured by pyrgeometers in the spectral range from 3.5 to 50 μm (Augustine et al., 2005). These irradiances were used in the abovementioned references to estimate ground LSTs. According to Guillevic et al. (2012), the SURFRAD instrumental error alone gives rise to a LST uncertainty less than 1 K. Ground observations at Gobabeb, Namibia, are collected with a thermal infrared radiometer in the 9.6–11.5 μm spectral domain set up in a permanent station located at a homogeneous gravel plain sparsely covered by dry grass. There, the downwelling thermal radiance is estimated using another radiometer facing the sky at an effective angle of 53° (from zenith). However, the effective angle depends on the atmospheric conditions and the measurement spectral band; so the use of a fixed angle can introduce uncertainties (Niclòs et al., 2005a; Guillevic et al., 2014). The main uncertainties in the derived ground LSTs are due to the accuracy of the surface emissivity and the downwelling radiance (Hook et al., 2007). In general, directional measurements of sky downwelling radiance are not routinely sampled in the field, yielding LST uncertainties, especially for humid and warm atmospheres. However, directional sky downwelling data are measured by our autonomous and multiangular system, avoiding this problem.

Liu et al. (2015) showed validation results for the VIIRS LST data obtained from LPEATE. They reprocessed a dataset of VIIRS LST data (from February 2012 to April 2015) by using the calibrated algorithm coefficients implemented from April 2014. An overall bias of −0.4 K and SD of 2.4 K were shown in the case of the reprocessed dataset when compared with ground LSTs derived from the SURFRAD data. Better results were obtained at nighttime (bias of −0.2 K and SD of 2.0 K) compared to daytime (bias of −0.7 K and SD of 2.9 K). Liu et al. (2015) also showed a VIIRS LST overall bias of −1.6 K and a SD of 2.1 K when comparing with ground LSTs from the Gobabeb station. Therefore, the VIIRS reprocessed data provided better results for such arid area, but an underestimation was still observed.

Additionally, previous studies evaluated the VIIRS LST product performance by comparing with other satellite LST products, like the MODIS one (Guillevic et al., 2013, 2014; Liu et al., 2015), showing both large biases and SDs (e.g., larger than 3 K in Guillevic et al. (2014)).

The paper follows with a brief description of the S-NPP VIIRS LST product in Section 2. Section 3 shows the ground measurements acquired by the system and a new cloud screening procedure based on the system data. In Section 4, the product (version V1) validation is shown and compared with the results from Liu et al. (2015), together with an evaluation of the effect of assigning different surface types and thus different coefficient sets in the VIIRS LST algorithm at the rice paddy site. Finally, the main conclusions of the study and some suggestions for future algorithm refinements are summarized in Section 5.

2. S-NPP VIIRS land surface temperature product

The VIIRS Environmental Data Record (EDR) LST product is derived at pixel level (spatial resolution of ~750 m at nadir and around 1.5 km at the edge of the swath) using the following split-window algorithm (Yu et al., 2005):

$$LST = a_0 + a_1 T_{15} + a_2 (T_{15} - T_{16}) + a_3 (sec\theta_v - 1) + a_4 (T_{15} - T_{16})^2 \quad (1)$$

which uses brightness temperatures (T_i) measured in two VIIRS spectral bands: M15 placed at 10.76 μm (i = 15) and M16 placed at 12.01 μm (i = 16). Different sets of coefficients (a_j, with j = 0–4) are used for daytime and nighttime and for 17 surface types of the International Geosphere-Biosphere Programme (IGBP) classification maps (VIIRS LST ATBD, 2013; Guillevic et al., 2014; Liu et al., 2015). The coefficient sets were obtained using simulations with the MODTRAN radiative transfer model (Berk et al., 2006)

and globally representative atmospheric and surface conditions. Atmospheric parameters were derived from the National Center for Environmental Prediction (NCEP) global data. The emissivity values for each surface type were derived based on the MOSART spectra database (VIIRS LST ATBD, 2013). The regression coefficients were trained for VIIRS zenith angles (θ_v) less than 40°. The VIIRS EDR LST products can be downloaded from CLASS. Newly calibrated algorithm coefficients were implemented from April 2014. The VIIRS EDR LST product attained the V1 stage of validation maturity (provisional validated) at the end of 2014. This stage was defined as "using a limited set of samples, the algorithm output is shown to meet the threshold performance attributes identified in the JPSS level 1 requirements" (Liu et al., 2015). As mentioned before, the threshold requirements for VIIRS LSTs are bias between satellite and ground-based LSTs of 1.4 K and SD of 2.5 K, although the objective is to attain bias of 0.8 K and SD of 1.5 K (Justice et al., 2013; JPSS Program, 2014). According to the JPSS VIIRS-LST-EDR team, further validation studies are required to attain better maturity stages, extending the LST validation effort to different regions.

Hereafter, this paper will focus on the evaluation of the VIIRS V1 LST product, distributed by NOAA's CLASS, versus the concurrent ground data acquired at the rice paddy site, with view angles similar to the VIIRS ones, from December 2014 to August 2016.

3. Ground data acquired by the autonomous and multiangular system

3.1. System and experimental site

As described in Niclòs et al. (2015), we developed an autonomous system that permits continuous acquisition of ground-truth LST data. The system takes angular measurements of both the land surface and the sky using just one radiometer in the TIR spectral region: the *Apogee Instruments* SI-121 (8–14 μm, half angle field of view of 18°). The device can rotate automatically to achieve complete scans using a set of zenith and azimuth viewing angles (with a total of ~100 viewing directions in the two hemispheres) at which the SI-121 radiometer takes measurements. Another SI-121 radiometer was additionally set up to provide continuous LST measurements at nadir.

The experimental site is a seasonal rice paddy with complete vegetation cover during the summer months. The site is completely inundated in December, January and June, and the land type is bare soil (initially wet and then dried) from February to May. Therefore, the site can be considered especially suitable for validation purposes because it has three different land types (i.e., bare soil, full vegetation cover and water, which are spatially homogeneous) to be studied by the system throughout the year (Fig. 1). The radiometer was placed at the top of a three-meter vertical mast, observing a footprint area of 5 (13) m^2 for zenith angle of 36° (54°). The footprint area can be considered as thermally homogenous for the three surface types of the site, containing one single surface element in each case (soil, vegetation or water).

Due to the large dissimilarity between the area covered by the ground and VIIRS data, we assessed the thermal homogeneity of the test site at different spatial scales. Previous studies (Coll et al., 2005, 2007, 2012; Niclòs et al., 2011, 2015) used daytime, summer data from Landsat-5 TM (resolution of 60 m) and EOS ASTER (90 m) showing SDs less than 0.5 K for an area of ~16 km^2 over the site. Additionally, measurements were taken in the site along transects covering areas of ~250 × 250 m^2 with several hand-held Cimel Electronique multiband radiometers (model CE-312, Legrand et al., 2000), showing SDs for the LST values less than ±0.6 K in daytime, summer conditions (Coll et al., 2005, 2007). We also used four hand-held CE-312 radiometers to measure LST along transects in the test site area concurrently to the system daytime acquisitions for the three seasonal land covers: flooded soil (water; January 20, February 1 and June 1, 2016), full vegetation (July 6 and 18, 2016), and bare soil (wet bare soil; February 23, 2016, and dry bare soil; April 21, 2016). SDs of 0.5 K and 0.4 K were obtained for the LST data measured along transects in the full vegetation and flooded soil cases, respectively. SDs less than 0.9 K were obtained in the bare soil cases. We obtained average differences between the transect LST measurements and the LSTs assessed from concurrent system acquisitions of +0.16 K, +0.15 K, and −0.3 K for full vegetation cover, flooded soil, and bare soil, respectively. These results show the thermal homogeneity of the area and that the ground LST measurements performed by the automated system are suitable for the validation of the VIIRS LST product.

3.2. Ground LST retrieval from the system data

An spectral channel (i) of a TIR radiometer observing the land surface near it at direction (θ, ϕ) measures the surface radiance, $L_i(\theta, \phi)$, which is given as follow:

$$L_i(\theta, \phi) = \varepsilon_i(\theta, \phi) B_i(LST) + (1 - \varepsilon_i(\theta, \phi)) L^{\downarrow}_{i\ a,hem} \quad (2)$$

where $\varepsilon_i(\theta, \phi)$ is the emissivity of the observed surface, $B_i(LST)$ is the channel Planck's function for the LST, and $L^{\downarrow}_{i\ a,hem}$ is the sky downwelling irradiance divided by π, also called hemispheric downwelling radiance. $L^{\downarrow}_{i\ a,hem}$ is the angular integration of the sky radiance coming from every sky zenith and azimuthal angles.

3.2.1. Hemispheric downwelling radiance and cloud screening

As mentioned before, directional measurements of downwelling sky radiance are not usually routinely sampled in field measurements (Guillevic et al., 2014). However, our system collects sky directional measurements and the downwelling thermal irradiance can be better determined concurrently with surface radiance measurements, and not estimated from atmospheric radiative transfer simulations, like in Lake Tahoe (Hook et al., 2003), or measured for an approximated effective angle of 53°, like in the Gobabeb station (Göttsche et al., 2013). Using a fixed angle can introduce uncertainties since the effective angle depends on the atmospheric conditions and the radiometer spectral band (Kondratyev, 1969; Rubio et al., 1997; Niclòs et al., 2005a). In addition, measuring the sky just at one single angle cannot discern partial cloud contamination.

Usually, the filtering of pixels affected by clouds for validation purposes is typically based on the satellite data themselves, but there may be some ambiguity in the determination of cloud contamination. The use of image quality flag (QF) from cloud masks for cloud filtering appears sometimes insufficient for validation studies (Guillevic et al., 2014; Liu et al., 2015). The VIIRS cloud mask is defined as less than 10% cloud coverage. Cloud leakage in validation results has been reported by EDR teams and has been identified as an important issue for further improvement. Besides the VIIRS QFs, we additionally used the system sky directional measurements to improve cloud screening in the validation of the VIIRS LST product. Improving the validation data quality with a strong cloud screening procedure significantly reduces the number of matchups but minimizes the cloud impacts in the results.

The sky radiances can be approximated in case of horizontal homogeneity of the atmosphere (Kondratyev, 1969; Rubio et al., 1997; Niclòs et al., 2005a). In fact, the retrieval of LSTs from satellite TIR data needs cloud-free atmospheres, which can be considered horizontally homogeneous. In this case, the directional sky radiance can be assumed as independent on the azimuth angle and approximated as

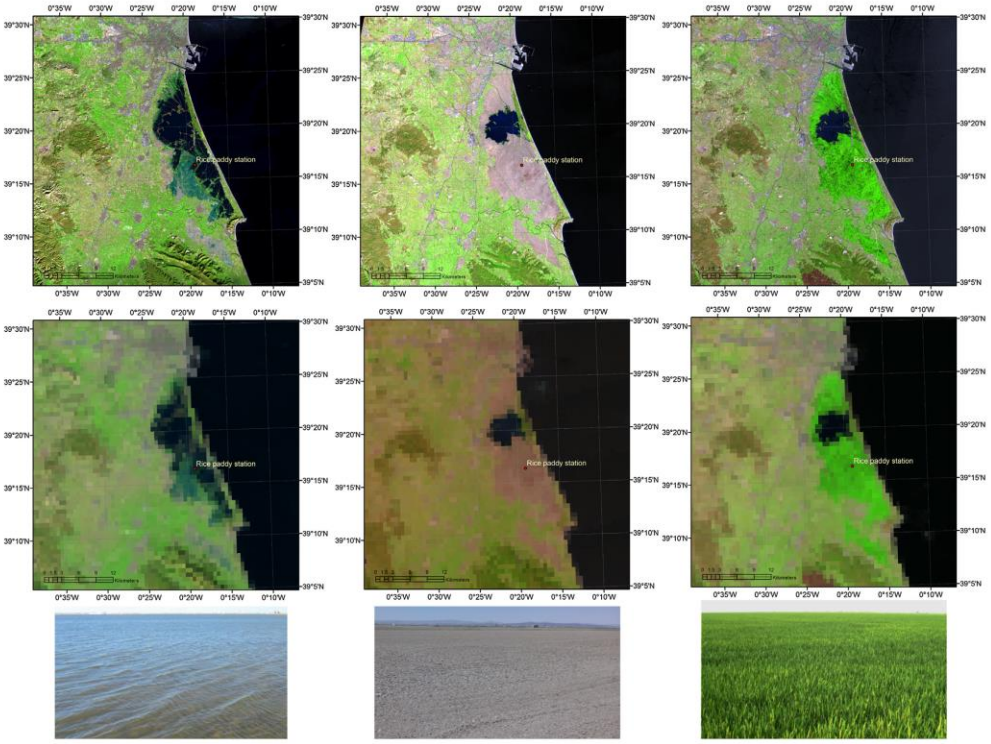

Fig. 1. Seasonal land type variation at the rice paddy site. Site views on January (flooded soil), May (bare soil) and July (full vegetation cover). False color composites of Landsat-8 OLI (R-G-B 6-5-4; top) and VIIRS SDR (R-G-B M10-M7-M5; middle) reflectance data are shown. (For interpretation of the references to colour in this figure legend, the reader is referred to the web version of this article.)

$$L^{\downarrow}_{i\ a}(\theta,\phi) = L^{\downarrow}_{i\ a}(\theta) \approx L^{\downarrow}_{i\ a}(0^{\circ})\cos^{-x_i}(\theta) \quad (3)$$

where x_i is a parameter depending on the radiometer band and the atmospheric conditions. Therefore, the integration of Eq. (3) to the upper hemisphere to obtain $L^{\downarrow}_{i\ a,hem}$ yields

$$L^{\downarrow}_{i\ a,hem} = \frac{2}{2-x_i} L^{\downarrow}_{i\ a}(0^{\circ}) \quad (4)$$

For each scan, the sky data can be linearly regressed using logarithms in Eq. (3). Thus, $-x_i$ is the slope of the regression equation and $L^{\downarrow}_{i\ a}(^{\circ})$ can be obtained from the regression offset. Then $L^{\downarrow}_{i\ a,hem}$ is obtained with Eq. (4). The data offsets from the fitting line are negligible for cloud-free scans. Anyway, they are considered in the uncertainty estimates for x_i, $L^{\downarrow}_{i\ a}(^{\circ})$, and $L^{\downarrow}_{i\ a,hem}$. In case of partial cloud contamination, the approximations are not suitable and the determination coefficient (r^2) of the linear regression using a complete sky scan data drops considerably. The data acquired by the system in scans with r^2 lower than 0.9 were filtered and removed for the validation, which entails an additional cloud screening to the filtering using the VIIRS related QF information. Fig. 2 shows plots of the data measured by the system for the sky hemisphere for three VIIRS overpass times with different cloud conditions: (a) completely cloud-free sky (20 May 2016, 01:55 UTC), with r^2 = 0.998; (b) sky slightly affected by clouds (18 May 2016, 02:40 UTC), with r^2 = 0.857; and (c) partially cloudy sky (21 May 2016, 01:40 UTC), with r^2 = 0.423. The VIIRS – ground LST matchups in cases (b) and (c) were discarded for the validation. However, the QFs of the VIIRS products, i.e., those coming from cloud masks, indicate cloud-free conditions for the three cases. Additionally, SDs of 0.4 K and 0.15 K were shown for the neighbouring 3 × 3 pixel box (centred at the station location) in the VIIRS LSTs and M15 brightness temperatures, respectively, for case (b). Similarly, SDs of 0.7 K and 0.5 K, respectively, were obtained for case (c). Consequently, spatial variation tests applied to the VIIRS data as an additional cloud filter, e.g., with a SD threshold of ~1.5 K (Li et al., 2014; Liu et al., 2015), are not always enough for cloud screening in validation studies. Therefore, the developed multiangular system permits to improve the constraint of matchups to be confidently clear, and reduce cloud leakage in the validation results.

3.2.2. Ground emissivity measurements

Emissivity measurements were taken at the different seasonal covers at the rice site. For the emissivity measurements we used the multiband radiometer CE-312 (Legrand et al., 2000), which has a wide band (8–13 μm) and five narrow bands within the wide band. We used two different emissivity measurement methods: the Temperature-Emissivity Separation method (TES) (Gillespie et al., 1998) applied to ground radiometers (Mira et al., 2009) and the box method (Rubio et al., 2003). The TES method was used

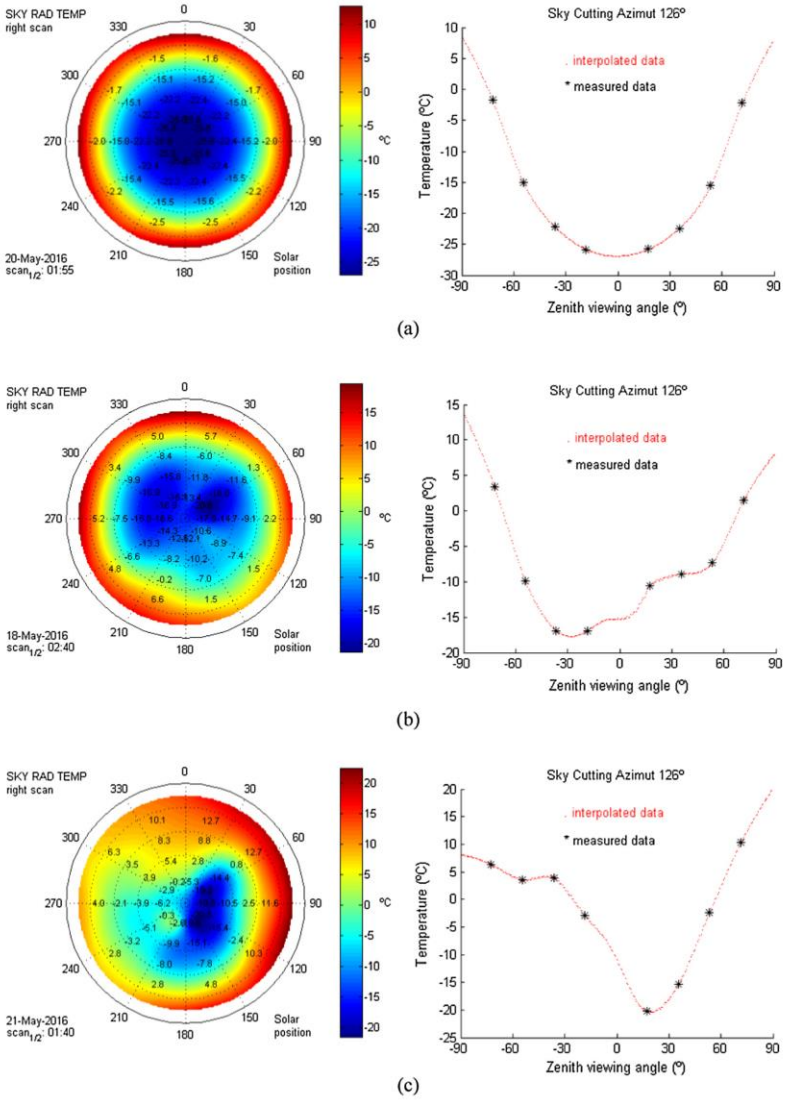

Fig. 2. Polar projections of the data acquired by the system in the sky hemisphere, together with the corresponding azimuthal cuts (for an azimuth angle of 126°) to show the sky brightness temperature dependence with the zenith angle. The sky data measured by the system for three VIIRS overpass times with different cloud conditions are shown: (a) a completely cloud-free sky (20 May 2016, 01:55), with $r^2 = 0.998$; (b) a sky slightly affected by clouds (18 May 2016, 02:40), with $r^2 = 0.857$; and (c) a partially cloud sky (21 May 2016, 01:40), with $r^2 = 0.423$. The SI-121 brightness temperature distributions shown in the polar projections were made by interpolation of the actual measurements, which are also shown with numbers.

for flooded soil and wet to dry bare soils, i.e., for surfaces with significant emissivity spectral and/or angular variations, while the box method was used for the full vegetation cover. The TES method uses at-surface radiances measured simultaneously over a given sample in the different bands of the CE-312 instrument, the downwelling sky radiance in each band and an initial emissivity guess to retrieve the apparent spectral contrast or the maximum-minimum emissivity difference (MMD) between the radiometer bands. Then, an empirical relationship between the MMD and the minimum band emissivity is used to re-scale the apparent band emissivities to the actual values. The empirical relationship was obtained by integrating the spectra contained in the ASTER spectral library

(Baldridge et al., 2009) with the response functions of the CE-312 bands.

On the other hand, the box method uses a box (height of 80 cm, base of 30 cm × 30 cm) with inner walls made of highly reflecting polished aluminum (ideally ε = 0) and two interchangeable top lids; the "cold" lid of the same material and the "hot" lid made of highly emitting material (corrugated aluminum painted in Parson's black, ideally ε = 1), which can be heated to about 60 °C and is equipped with a thermostat. To ensure thermal stability within the box, the walls and lids are externally covered by a 3 cm thick sheet of a thermally insulating material. Both lids have a small aperture for the radiometer to observe the radiance coming from the bottom of the box. The bottom can be open or closed with another "cold" lid. The measurement of emissivity requires a series of radiance measurements for the sample-box system in different configurations. In the first measurement, the box (bottom open) is placed over the sample with the cold lid at top. In the second measurement, the hot lid at high temperature is used at top instead of the cold lid. For the third measurement, the hot lid is still at top but the box is closed with a cold lid at the bottom. In the ideal box, those three measurements are sufficient to calculate the sample emissivity. However, for the real box typical values of emissivity for the cold and hot lids are 0.03 and 0.98, instead of 0 and 1 respectively. For these reasons, a correcting term must be introduced, which requires a fourth measurement with cold lids both at top and bottom of the box. Further details on the emissivity measurement method and the correcting term are given in Rubio et al. (2003).

According to the measurements, a near-gray body spectrum was shown for the full vegetation cover. An emissivity of 0.985 ± 0.005 was obtained, and no angular or spectral variations were observed between 8 and 13 μm (Coll et al., 2007, 2012; Niclòs et al., 2011, 2015). Niclòs et al. (2015) showed, in Fig. 6, the spectra obtained with the TES method for flooded and bare soils. The angular dependences of the emissivities of the bare soil and flooded soil (water) in the rice paddy site were characterized by García-Santos et al. (2014) and Niclòs et al. (2005b, 2009, 2014), respectively. García-Santos et al. (2014) also analyzed the bare soil emissivity dependence on soil moisture. Table 1 shows the angular emissivity values used to obtain LSTs from the data measured by the system SI-121 radiometer. Emissivities in Table 1 correspond to the wide band (8–13 μm) of the CE-312 radiometer, thus existing a spectral mismatch with SI-121. The effect of the spectral mismatch was analyzed using spectral emissivity measurements for eleven samples of water, vegetation and soils from the ASTER library (Baldridge et al., 2009; https://speclib.jpl.nasa.gov/), which were integrated with the spectral response of the CE-312 and SI-121 bands considered. The comparison showed emissivity differences lower than 0.002 between the two bands for all covers, which is lower than the experimental emissivity uncertainties in Table 1 and is equivalent to a LST difference lower than 0.10 K for the conditions of the dataset.

3.2.3. Ground LST uncertainties

Ground LSTs were assessed using Eq. (2). The radiance data acquired by the system at the zenith angles closest to the VIIRS viewing zenith angle and at a selection of azimuth angles were averaged to obtain reference ground LST values for the validation. The system angles at which the radiometer footprints were found entirely over the rice crop (i.e., avoiding the viewing of a narrow agricultural ridge) were selected for this end (Niclòs et al., 2015). Despite the site homogeneity reported in Section 3.1, possible small horizontal inhomogeneity effects were considered as uncertainties in this comparison. SDs of the LSTs obtained using the concurrent data acquired by the system at the above-mentioned zenith and azimuth angles were computed. The uncertainty assigned to the ground LST was root of sum of squares (RSS) of the ground SD within a scan and the uncertainty obtained with Eq. (2) due to the uncertainties estimated for $L^{\downarrow}_{i\ a,hem}$, ε_i and $L_i(\theta,\phi)$. The latter was considered as the uncertainty estimated for the Apogee SI-121 radiometers. Apogee radiometers were calibrated against a National Institute of Standards and Technology (NIST) blackbody during a comparison of TIR radiometers carried out in Miami by the Committee on Earth Observation Satellites (CEOS) (Theocharous et al., 2010). Additionally, the field radiometers were calibrated every year against a Landcal blackbody source P80P, which in turns was compared with an absolute reference during both the CEOS campaign in 2009 and a recent CEOS comparison campaign performed in the framework of the European Space Agency's FRM4STS project in 2016 (Theocharous et al., 2010, 2016), yielding an accuracy better than 0.1 K for temperatures ranging from 273 to 320 K. According to these calibration measurements, the accuracy of the Apogee SI-121 radiometer was established at 0.2 K.

The SDs of the LST data within a scan were typically 0.16 K and 0.09 K for flooded soil at day and night overpass times, respectively. SDs were 0.2 K and 0.10 K for full vegetation cover, and 0.5 K and 0.11 K for bare soil, at daytime and nighttime, respectively. The minimum LST SDs were obtained for the flooded soil at the rice paddy site. Bare soils showed the maximum deviations. In any case, the SD values, which are mostly related with possible surface inhomogeneity effects, were considered in the assessment of the ground LST uncertainties.

4. Validation results

4.1. Evaluation of the VIIRS LST product versus ground data

Cloud-free, concurrent VIIRS and ground LSTs from mid-December 2014 to mid-August 2016 were used to evaluate the accuracy of the VIIRS V1 LST product distributed by NOAA's CLASS. Cloud-free data were selected by filtering the matchups using the VIIRS QFs and the cloud-screening procedure described in Section 3.2.1.

Table 1
Angular emissivities (8–13 μm) for flooded soil (water) and bare soil covers.

Site cover	0°	28°	38°	58°
Flooded soil (water)	0.986 ± 0.004	0.986 ± 0.004	0.983 ± 0.004	0.955 ± 0.005
Wet bare soil[a,c]	0.973 ± 0.006	0.973 ± 0.006	0.969 ± 0.006	0.956 ± 0.006
Dry bare soil[b,c]	0.968 ± 0.008	0.966 ± 0.009	0.965 ± 0.009	0.960 ± 0.009

[a] Soil Moisture (SM) of ~0.40 m^3 m^{-3}.
[b] SM = 0.03 m^3 m^{-3}.
[c] Soil textural and mineralogical characteristics described in Table I of García-Santos et al. (2014) (sample D).

The data acquired with the system within five minutes of the VIIRS overpass times were used to obtain the concurrent ground-truth LSTs, like in Liu et al. (2015). The 4 pixels of the VIIRS LST products nearest to the station location were averaged with a weighting function given by $1/d_i^2$; d_i being the distance from the pixel center to the station coordinates (Shepard, 1968; Coll et al., 2012).

The data acquired by the system at zenith angles lower than 40° were first used as ground-truth data to evaluate the VIIRS LST product at VIIRS zenith angles lower than 40°, since the regression coefficients used in the product algorithm were trained for this range of VIIRS zenith angles (Yu et al., 2005; VIIRS LST ATBD, 2013; Guillevic et al., 2014). Table 2 shows statistical parameters to quantify the differences between VIIRS and ground LST data for zenith angles lower than 40°. It includes: median, robust standard deviation (i.e., RSD = 1.483·median($|\{(LST_{VIIRS} - LST_{ground})_j - \text{median}(\{LST_{VIIRS} - LST_{ground}\}_j)|$) (Niclòs et al., 2011)), robust root-mean-square difference (R-RMSD), i.e., the square root of the quadratic sum of the median and RSD, and number of events. R-RMSD is an estimate of the product total LST uncertainty. Medians represent systematic uncertainties and RSDs show random uncertainties. Both parameters minimize the impact of outliers and they are considered statistically more reliable for validation purposes than mean and standard deviation (Schneider et al., 2012). Table 2 shows the evaluation results for daytime and nighttime overpasses separately. Results are shown for all covers together and for each cover separately.

Fig. 3 shows VIIRS V1 LST product data against ground LSTs for VIIRS zenith angles ≤40° and for (a) daytime and (b) nighttime overpasses, respectively. Data acquired over the different seasonal land covers at the rice paddy site are shown in colors: flooded soil in blue, full vegetation cover in green and bare soil in red. The vertical error bars associated to the VIIRS data in Fig. 3 show the variability (SD) of the 4 pixels nearest to the station location. At daytime, we obtained average VIIRS LST error bars of 0.6 ± 0.3 K for flooded soil and full vegetation cover, and 0.9 ± 0.5 K for bare soil. Values of 0.4 ± 0.3 K were obtained for nighttime data for all the surface covers. Ground LST uncertainties, shown as horizontal bars in Fig. 3, were obtained as detailed in Section 3.2.3. Typical ground LST error bars of 0.5 ± 0.2 K were obtained for flooded soil and full vegetation cover and of 1.0 ± 0.3 K for bare soil at daytime; while values of 0.4 ± 0.2 K were obtained for all the surface covers at nighttime.

Both Table 2 and Fig. 3 show that the VIIRS LST product at zenith angles ≤40° yields a good accuracy, with average systematic uncertainties (medians) of 0.4 K and 0.12 K and R-RMSDs of 1.2 K and 1.1 K at daytime and nighttime, respectively, for all the covers together. These values are within the abovementioned threshold requirements for the VIIRS LST product (bias of 1.4 K and SD of 2.5 K), and even within the goal accuracy (bias of 0.8 K and SD of 1.5 K), and they are also better than results obtained previously at other sites (summarized in Section 2). Liu et al. (2015) showed root-mean-square differences (RMSDs) always larger than 2 K for different cropland sites. RMSDs ≥2 K were also obtained in Guillevic et al. (2014) for the VIIRS beta LST product at different cropland and grassland sites. In fact, the use of SURFRAD data as ground-truth data in the previous references can be considered not accurate enough for satellite LST product validation (Guillevic et al., 2014). SURFRAD station locations are not usually in thermally homogeneous areas at the spatial resolution of the VIIRS observations, and were not specifically designed for satellite LST product validation.

Table 2 shows slightly higher RSDs for daytime than for nighttime matchups in the case of bare soil and full vegetation covers, although they are quite similar likely due to the site thermal homogeneity. This fact was also observed by Guillevic et al. (2014) when using data collected at Lake Tahoe. However, higher SDs were obtained for daytime than for nighttime at other experimental sites due to thermal heterogeneities (Yu et al., 2005; Guillevic et al., 2014; Liu et al., 2015). We obtained different systematic uncertainties (i.e., medians) between daytime and nighttime overpasses for all the different seasonal land covers in the rice paddy site. Namely, the differences between daytime and nighttime medians were 1.4 K, −0.6 K, and 0.5 K for flooded soil, full vegetation cover and bare soil, respectively. Systematic differences between daytime and nighttime overpasses were also obtained by Li et al. (2014) for barren surfaces, and by Guillevic et al. (2014) and Liu et al. (2015) for most of the studied sites. Liu et al. (2015) showed differences between daytime and nighttime biases from −3.5 K to 1.9 K at the different sites studied. However, Guillevic et al. (2014) showed differences for the VIIRS beta LST product from −1.9 K to 3.5 K depending on site. These systematic differences between daytime and nighttime overpasses can be due to the different coefficients assigned to the 17 IGBP surface types at daytime and nighttime overpasses, and the different values obtained by Guillevic et al. (2014) and Liu et al. (2015) can be a consequence of the different set of coefficients used in the algorithm, since they showed validation results for different versions of the VIIRS LST product.

Table 3 shows statistical data of the differences between the VIIRS and ground LSTs for zenith angles >40°. The reference ground LSTs were obtained in this case using the system data acquired at zenith angles >40° for a better comparison.

Fig. 4 shows VIIRS LST product data against ground LSTs for those angles and for (a) daytime and (b) nighttime overpasses, respectively. Mostly, R-RMSDs are larger for VIIRS zenith angles >40° than for ≤40°, mainly due to larger RSDs. In this case, the differences between daytime and nighttime medians are quite similar to those for angles ≤40°; 1.4 K, −0.8 K, and 0.1 K for flooded soil, full vegetation cover and bare soil, respectively.

Unlike previous results for arid or semi-arid sites, like those at the Gobabeb station (Guillevic et al., 2014; Liu et al., 2015), we did not observe significant negative systematic LST differences for the bare soil at the rice paddy site. The previously observed

Table 2
Differences between the VIIRS-retrieved and the ground LSTs for zenith angles <40°. The table includes: median, robust standard deviation (RSD), robust root-mean-square differences (R-RMSD, i.e., the square root of the quadratic sum of the median and RSD), and number of cloud-free, concurrent events (N).

VIIRS zenith angle <40°		Median (K)	RSD (K)	R-RMSD (K)	N
All surface covers	Day	0.4	1.1	1.1	123
	Night	−0.03	1.1	1.1	112
Flooded soil (water)	Day	1.0	0.8	1.3	36
	Night	−0.4	0.8	0.9	36
Full vegetation cover	Day	0.3	1.0	1.0	42
	Night	1.0	0.8	1.2	39
Bare soil	Day	−0.03	1.1	1.1	45
	Night	−0.6	0.7	0.9	37

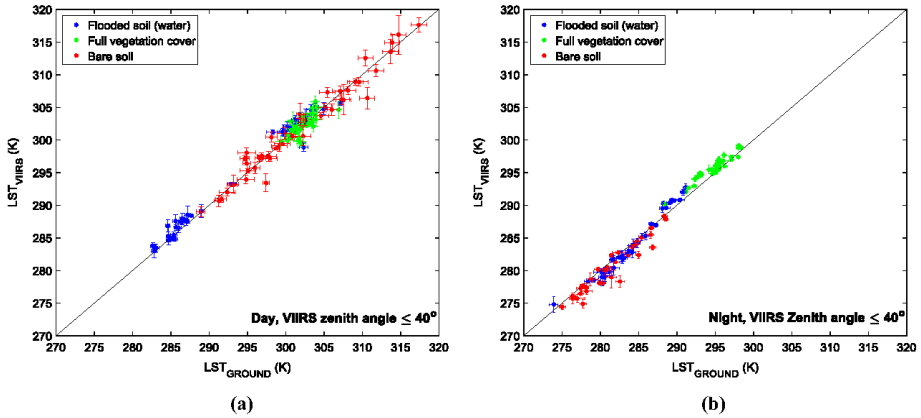

Fig. 3. Scatterplots of VIIRS LSTs against ground LSTs for daytime and nighttime and VIIRS zenith angles <40°. Data acquired for the different seasonal land covers at the rice paddy site are shown in different colors. (For interpretation of the references to colour in this figure legend, the reader is referred to the web version of this article.)

Table 3
Differences between the VIIRS-retrieved and the ground LSTs for zenith angles >40°.

VIIRS zenith angle >40°		Median (K)	RSD (K)	R-RMSD (K)	N
All surface covers	Day	−0.5	1.6	1.7	110
	Night	−0.8	1.0	1.2	102
Flooded soil (water)	Day	0.7	1.0	1.2	28
	Night	−0.7	0.9	1.2	32
Full vegetation cover	Day	−1.2	1.2	1.7	50
	Night	−0.5	1.2	1.3	30
Bare soil	Day	−0.8	1.6	1.8	32
	Night	−0.9	0.8	1.2	40

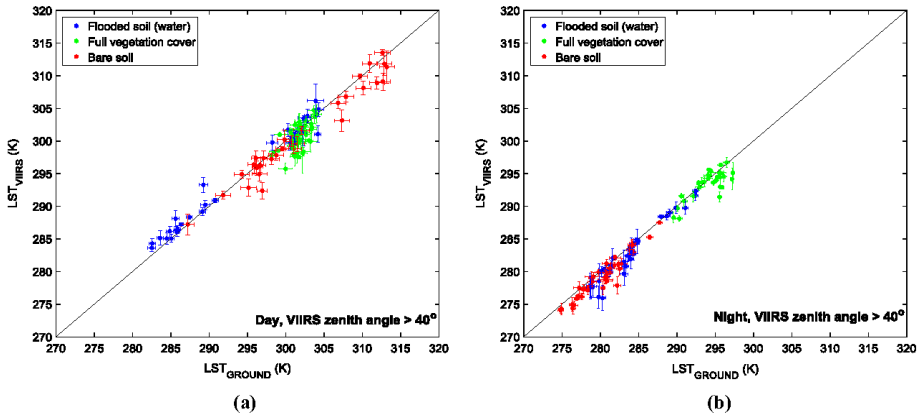

Fig. 4. Scatterplots of VIIRS LSTs against ground LSTs for daytime and nighttime and VIIRS zenith angles >40°. Data acquired for the different seasonal land covers at the rice paddy site are shown in different colors. (For interpretation of the references to colour in this figure legend, the reader is referred to the web version of this article.)

systematic underestimations up to 5 K at these sites for the VIIRS beta LST product (Justice et al., 2013; Li et al., 2014) was explained as a consequence of an overestimation of the emissivity values used to obtain the regression coefficients for barren surfaces in the algorithm (Guillevic et al., 2014). This emissivity overestimation did not happen in the case of the VIIRS V1 LST product (Liu et al., 2015; emissivities of 0.965 and 0.97 for VIIRS M15 and M16, respectively), and thus it cannot explain the negative bias of −1.6 K still observed by Liu et al. (2015) for the Gobabeb bare soil site. However, large brightness temperature differences

between M15 and M16 bands, mainly observed over arid areas at daytime, have an important impact due to the non-linear term in the LST algorithm, since these differences are usually far beyond the simulation database range (i.e., differences from −1 K to 3 K) (Liu et al., 2015). In our validation dataset, brightness temperature differences from −0.1 K to 4 K were found for bare soil at daytime, with an average of 1.4 ± 0.9 K, i.e., quite similar to the algorithm simulation database range. Therefore, like in Guillevic et al. (2014), the validation at the rice paddy was not able to quantify the degradation of the VIIRS algorithm performance under high atmospheric water contents.

Additionally, as we acquired nadir measurements along transects in the rice paddy area with hand-held CE-312 radiometers, we used these data as reference for a complementary evaluation of the VIIRS V1 LST product. Similarly to the SI-212 radiometer, the CE-312 radiometers were calibrated against traceable standard references in the CEOS radiometer comparisons (Theocharous et al., 2010, 2016) and regularly against the calibrated P80P blackbody, showing an uncertainty of 0.1 K for the temperature range of the ground measurements. A set of 21 concurrent ground and VIIRS cloud-free data were obtained. All of them were acquired at daytime along 2016. Table 4 shows a statistical summary of the differences between the VIIRS-retrieved and the transect LST data. Results are shown all together, without surface type distinction due to the reduced number of data, and then split into VIIRS zenith angles ≤40° and >40°. Fig. 5 shows VIIRS LST product data against ground LSTs acquired along transects with the CE-312 radiometers in the rice paddy area.

Although the results in Table 4 correspond to a limited number of data, they can be compared with the analog cases when the ground LSTs measured by the automated system were used (all covers together, daytime data in Tables 2 and 3 for viewing angles smaller and larger than 40°, respectively). There was a good agreement between both datasets in terms of systematic LST differences, with biases of +0.4 K and −0.4 K for viewing angles lower and larger than 40°, respectively, while they were +0.4 K in Table 2 and −0.5 K in Table 3. However, the magnitude of those systematic differences was relatively small, well within the uncertainty limits of the ground-measured LSTs. With regard to the SD, values in Table 4 were 0.3 K larger than those in Tables 2 and 3, and so was the RMSD. The larger dispersions found when using LSTs acquired along transects can be due in part to the fact that the CE-312 measurements were performed close to nadir regardless of the VIIRS viewing angle, so there may be angular LST differences between the ground and satellite measurements, such differences depending on the surface type. In any case, the VIIRS LST results are still within the threshold accuracy requirements and even close to the goal accuracy, mainly for VIIRS zenith angles ≤40°.

4.2. Surface type and emissivity assignment evaluation

Since the coefficients in the split-window algorithm of the VIIRS LST product are different for each surface type, an evaluation of such surface type dependence is particularly needed (Liu et al., 2015). According to Liu et al. (2015), the overall accuracy of the land cover typing is around 70% and thus 30% of pixels might be misclassified. The VIIRS LST product identifies the pixels at the rice

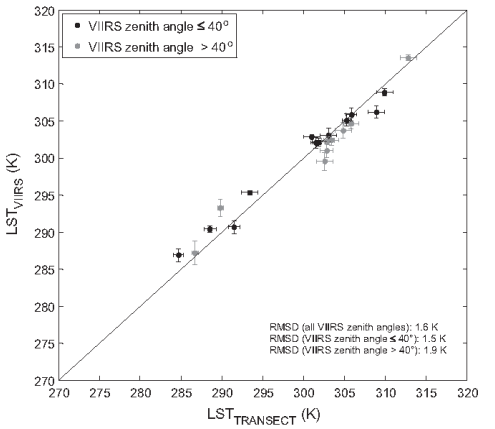

Fig. 5. Scatterplots of VIIRS LSTs against ground LSTs acquired along transects in the rice paddy area. Matchups at VIIRS zenith angles <40° and >40° are shown in black and grey, respectively.

paddy site mostly as croplands (IGBP surface type 12) and cropland/natural vegetation (IGBP 14), and mixed forest (IGBP 5) in some cases, with no significant differences along the year. However, the surface cover and thus the associated emissivity are highly variable at the site along the year, as detailed in Section 3. Emissivity is one of the most relevant uncertainty sources of LST retrieval (Hook et al., 2007), and surface type misclassification, or variation along the year, involves using inaccurate emissivities for the VIIRS M15 and M16 bands or incorrect algorithm coefficients. The impact on LST results depends on how similar or distinct the emission properties are among the misclassified and actual surface types.

Liu et al. (2015) evaluates the uncertainty due to possible land cover/emissivity misclassification, with an overall LST uncertainty of 0.7 K (0.8 K for nighttime and 0.6 K for daytime). A global surface type distribution over land obtained from statistics was used for the theoretical analysis. Liu et al. (2015) showed the estimate LST uncertainty for every IGBP land cover (except for water bodies), and for day and night, separately. This theoretical analysis showed that nighttime uncertainty due to misclassification is higher than that for daytime due to the algorithm coefficients and nighttime atmospheric conditions. However, the misclassification impact at daytime was shown to be more significant than that at nighttime when using actual data, with overall LST errors of 1.5 K and 0.8 K at day and night, respectively.

We analyzed the effect of changing the surface type and thus the algorithm coefficients, which indirectly implies changing the surface emissivities, assigned to every seasonal land cover at the rice paddy site. Eq. (1) was used for the analysis, in which the complete set of VIIRS V1 LST regression coefficients was tested. The coefficients for the IGBP surface types 17 (inland water), 11 (permanent wetlands), and 16 (barren/sparsely vegetated) were

Table 4
Differences between the VIIRS-retrieved LSTs and the ground LSTs acquired along transects at the rice paddy throughout 2016 (daytime data).

All surface covers	Bias (K)	SD (K)	RMSD (K)	N
All VIIRS angles	0.01	1.6	1.6	21
VIIRS zenith angle <40°	0.4	1.4	1.5	12
VIIRS zenith angle >40°	−0.4	1.9	1.9	9

considered, in principle, more suitable for the flooded soil, full vegetation cover, and bare soil conditions, respectively, at the rice paddy. Table 5 shows the validation results when using these VIIRS V1 LST coefficients for the three different covers for the daytime and nighttime matchups at VIIRS zenith angles ≤40°, and Table 6 shows the same results for VIIRS zenith angles >40°. Although this change in the surface type assignment was expected to improve the validation results, the improvement was just limited to daytime results for flooded soil and nighttime results for full vegetation cover (when using the matchups for VIIRS angles ≤40°).

Using the coefficients for all the 17 surface types considered in the algorithm, R-RMSDs from 0.7 K (IGBP 17; inland water) to 3.3 K (IGBP 16; Barren/sparsely vegetated) were obtained for the flooded soil matchups at daytime, while R-RMSDs from 1.0 K (IGBP 13; Urban and built-up) to 2.1 K (IGBP 15; Snow and ice) were obtained at nighttime. Therefore, the dependence of the results on the considered IGBP surface type, and the corresponding coefficient sets, is larger for daytime than nighttime in this case. Although the coefficients for the IGBP 17 surface type (inland water) provides the minimum R-RMSD for daytime, at nighttime the minimum R-RMSD is obtained for the IGBP 13 type (Urban and built-up, 1.00 K), with similar results for types 4 (deciduous broadleaf forest, 1.01 K), 10 (grassland, 1.07 K), and 12 (Croplands, 1.06 K), but not for type 17 (1.65 K). This fact can be a consequence of the reduced variation in the emissivities considered for the different surface types in the regression process. The SDs of the emissivity values associated to the 17 different IGBP surface types are 0.005 and 0.003 for M15 and M16 bands, respectively. The emissivity SDs are smaller using all the IGBP surface types except type 16 (barren/sparsely vegetated), with values of 0.002 and 0.001 for M15 and M16 bands, respectively. Even the IGBP 13 type (urban and built-up) has similar assigned emissivity values (0.980 and 0.987 for M15 and M16, respectively; Dr. Liu personal communication) to the vegetated types, like those identified by the VIIRS product for the pixels at the rice paddy site, i.e., IGBP 12 (croplands), 14 (cropland/natural vegetation), and 5 (mixed forest), with emissivity pairs of about 0.983 and 0.986 for M15 and M16, respectively. Even though the emissivities considered for type 17 (inland water; 0.986/0.984 for M15/M16) are lower than those assumed for water surfaces, e.g. 0.991 and 0.985, respectively (Niclòs et al., 2005b), the emissivity underestimation in the VIIRS LST product due to the surface type misclassification for the flooded soil matchups could explain the LST product overestimation observed at daytime and the improvement of the results when surface type is changed to IGBP type 17.

For the full vegetation cover period, R-RMSDs from 1.0 K (IGBP 4; deciduous broadleaf forest) to 2.9 K (IGBP 16; Barren/sparsely vegetated) were obtained for the matchups at daytime, while R-RMSDs from 0.7 K (IGBP 17; Inland waters) to 3.0 K (IGBP 16; Barren/sparsely vegetated) were obtained at nighttime. The coefficients for the IGBP 11 surface type (permanent wetlands) provide quite good results at nighttime, with R-RMSD of 0.9 K, but not the minimum. At daytime, the minimum R-RMSD is for the IGBP 4 type (deciduous broadleaf forest, 1.00 K), with similar results for types 2 (evergreen broadleaf forest, 1.04 K), 3 (deciduous needleleaf forest, 1.05 K), and 12 (croplands, 1.05 K), but not for type 11 (1.48 K). The IGBP type 10 also provides similar results at daytime (grassland, 1.13 K), but at nighttime the R-RMSD is 1.53 K. The worst results were obtained when using the coefficients corresponding to the IGBP 16 type (barren/sparsely vegetated), which makes sense according to the emissivity setting for this type (0.965 and 0.973 for VIIRS M15 and M16 bands; Liu et al., 2015); the minimum emissivities considered for all the surface types.

However, for the barren soil matchup sets, the coefficients for the IGBP 16 type provided again the worst results at daytime, which was not expected due to the quite good agreement between the IGBP type and the rice paddy surface conditions (Fig. 1) and between the emissivity setting for this IGBP type and the emissivity measurements for bare soils at the site (Table 1, and Fig. 6 in Niclòs et al. (2015)). R-RMSDs from 1.0 K (IGBP 11; permanent wetlands) to 2.3 K (IGBP 16; barren/sparsely vegetated) were obtained for the matchups at daytime, while R-RMSDs from 0.8 K (IGBP 13; urban and built-up) to 2.0 K (IGBP 15; snow and ice) were obtained at nighttime. The coefficients for the IGBP 16 surface type (barren/sparsely vegetated) give a R-RMSD of 1.5 K at nighttime, while the minimum R-RMSD is for the IGBP type 13 (urban and built-up, 0.80 K), with similar results for types 10 (grassland, 0.81 K) and 12 (croplands, 0.82 K). This similarity can be again a consequence of the reduced variation in the emissivities considered for the different surface types in the regression process. The dependence of the results on the considered IGBP surface type, and the corresponding coefficient sets, is in fact relatively small

Table 5
Differences between the VIIRS and ground LSTs for zenith angles <40°. In this case, the VIIRS LSTs where assessed using Eq. (1) and the VIIRS V1 LST regression coefficients for the IGBP surface type 17 (inland water), 11 (permanent wetlands), and 16 (barren/sparsely vegetated) for flooded soils, full vegetation cover, and bare soil, respectively, at the rice paddy.

VIIRS zenith angle <40°		Median (K)	RSD (K)	R-RMSD (K)	N
Flooded soil (water)	Day	0.2	0.7	0.7	36
	Night	−1.2	1.1	1.7	36
Full vegetation cover	Day	1.0	1.1	1.5	42
	Night	0.6	0.7	0.9	39
Bare soil	Day	2.0	1.0	2.3	45
	Night	1.2	0.9	1.5	37

Table 6
The same as Table 5 but for VIIRS zenith angles >40°.

VIIRS zenith angle >40°		Median (K)	RSD (K)	R-RMSD (K)	N
Flooded soil (water)	Day	−0.2	1.3	1.3	28
	Night	−0.9	1.1	1.4	32
Full vegetation cover	Day	0.1	1.4	1.4	50
	Night	−0.9	1.1	1.4	30
Bare soil	Day	1.9	1.4	2.4	32
	Night	1.3	0.9	1.6	40

in this case (around 1 K). Since the assignment of IGBP surface type 16 (barren/sparsely vegetated) deteriorates significantly the results for the barren surfaces in the rice paddy site, we additionally tested the sets of coefficients used to generate the VIIRS beta LST product for the IGBP 16 surface type (Guillevic et al., 2014). In this case, R-RMSD of 1.4 K and 1.0 K were obtained for daytime and nighttime, respectively, instead of 2.3 K and 1.5 K obtained, respectively, when using the coefficient of the VIIRS V1 LST product. Therefore, the sets of coefficients for the IGBP type 16 (Barren/sparsely vegetated) in the current V1 version of the VIIRS LST product should be thoroughly examined and validated.

5. Conclusions

This paper evaluates the performance and accuracy of the VIIRS V1 LST product, and thus the surface-type dependent algorithm, using ground data acquired by an autonomous and multiangular system set up in a permanent station at a rice paddy site with seasonal surface type variation. The VIIRS V1 LST product was analyzed for VIIRS zenith angles less or equal than 40° and larger than 40° separately, using ground data acquired by the system at similar zenith angles to avoid possible differences between the satellite and system views due to angular dependences of the LSTs (both emissivity dependences and different proportions of the elements within the footprint; the last being hardly probable due to the surface homogeneity in the rice paddy for the three different seasonal surface types; Fig. 1). The system multiangular capability permits more confident validation results. On one hand the VIIRS and ground LSTs were acquired at similar viewing angle and they are more comparable than in other validation studies with radiometers looking down at nadir, since such observation difference could imply significant satellite and ground LST differences for sites with partial vegetation (Liu et al., 2015). Currently no operational LST algorithms correct for viewing angle, i.e., normalizing to nadir, and systematic errors can appear when comparing off-nadir satellite data to in situ nadir-viewing measurements (Guillevic et al., 2014). On the other hand, the multiangular system permits to constrain the validation matchups to be confidently cloud-free since it provides an accurate method for cloud screening.

A good accuracy is observed for the VIIRS V1 LST product at zenith angles $\leq 40°$, with average systematic uncertainties (medians) of 0.4 K and 0.12 K and R-RMSDs of 1.2 K and 1.1 K at daytime and nighttime, respectively, for all the covers together. These values are within the threshold requirements for the VIIRS LST product (bias of 1.4 K and SD of 2.5 K), and even within the goal accuracy (bias of 0.8 K and SD of 1.5 K), and are also better than results obtained previously at other sites for the beta version of the product (Guillevic et al., 2014) and VIIRS data reprocessed using the calibrated algorithm coefficients implemented from April 2014 (Liu et al., 2015).

Since the surface land cover misclassifications observed for the pixels at the rice paddy site (with surface type assignment rather invariant along the year) could turn in assuming inaccurate emissivity values for the split-window bands, we analyzed in detail this matter, and tested the algorithm results when more appropriate surface types are considered for each of the seasonal land surfaces at the rice paddy. However, although this change was expected to improve the validation results, the improvement was just limited for some matchup sets (i.e., flooded soil at daytime and full vegetation cover at nighttime). This can be a consequence of the reduced range of variability of the emissivities considered for the different land cover types in the algorithm coefficient regression process, with SDs of the emissivity values associated to the 17 different IGBP surface types of 0.005 and 0.003 for M15 and M16 bands, respectively, or 0.002 and 0.001 excluding type 16 (barren/sparsely vegetated). The impact on LST validation depends on the difference or similarity among the emission properties of misclassified and actual surface types. Additionally, the surface type assignment deteriorates significantly the results for the barren surfaces in the rice paddy site, and better results were obtained when testing the sets of coefficients used in the VIIRS beta LST product for the IGBP 16 surface type (Guillevic et al., 2014). Although the VIIRS V1 LST product performs well and validation results are within those expected, both the emissivity values and the regression coefficients should be thoroughly revised for the different IGBP surface types, mainly those used for the IGBP 16 surface type (barren/sparsely vegetated). On the view of the difficulties observed due to the surface type coefficient dependent algorithm used to generate the VIIRS LST product, one possible solution would be to introduce explicitly surface emissivity dependent terms in the split-window algorithm, or use retrieved dynamic surface emissivities like those from temperature and emissivity separation methods (Islam et al., 2017).

Acknowledgments

We wish to thank Dr. Liu (University of Maryland) for the assistance with the VIIRS V1 LST algorithm. This work was funded by the Spanish Ministry of Economy and Competitiveness and the European Regional Development Fund (FEDER) (project CGL2015-64268-R (MINECO/FEDER, UE) and Dr. Raquel Niclòs' "Ramón y Cajal" RYC-2010-06213 research contract).

References

Anderson, M.C., Allen, R.G., Morse, A., Kustas, W.P., 2012. Use of Landsat thermal imagery in monitoring evapotranspiration and managing water resources. Rem. Sens. Environ. 122, 50–65. https://doi.org/10.1016/j.rse.2011.08.025.

Augustine, J.A., Hodges, G.B., Cornwall, C.R., Michalsky, J.J., Medina, C.I., 2005. An update on SURFRAD—the GCOS surface radiation budget network for the continental United States. J. Atmos. Ocean. Technol. 22, 1460–1472.

Baldridge, A.M., Hook, S.J., Grove, C.I., Rivera, G., 2009. The ASTER spectral library version 2.0. Rem. Sens. Environ. 113, 711–715.

Berk, A., Anderson, G.P., Acharya, P.K., Bernstein, L.S., Muratov, L., Lee, J., Fox, M., Adler-Golden, S.M., Chetwynd, J.H., Hoke, M.L., Lockwood, R.B., Gardner, J.A., Cooley, T.W., Borel, C.C., Lewis, P.E., Shettle, E.P., 2006. MODTRAN5: 2006 Update. Proc. SPIE 6233 (62331F), 2006.

Coll, C., Caselles, V., Galve, J.M., Valor, E., Niclòs, R., Sánchez, J.M., Rivas, R., 2005. Ground measurements for the validation of land surface temperatures derived from AATSR and MODIS data. Rem. Sens. Environ. 97, 288–300.

Coll, C., Caselles, V., Valor, E., Niclós, R., Sánchez, J.M., Galve, J.M., Mira, M., 2007. Temperature and emissivity separation from ASTER data for low spectral contrast surfaces. Rem. Sens. Environ. 110 (2), 162–175.

Coll, C., Wan, Z., Galve, J.M., 2009. Temperature-based and radiance-based validations of the V5 MODIS land surface temperature product. J. Geophys. Res. 114, D20102. https://doi.org/10.1029/2009JD012038.

Coll, C., Caselles, V., Valor, E., Niclòs, R., 2012. Comparison between different sources of atmospheric profiles for land surface temperature retrieval from single channel thermal infrared data. Rem. Sens. Environ. 117, 199–210.

Duan, S.B., Li, Z.L., Cheng, J., Leng, P., 2017. Cross-satellite comparison of operational land surface temperature products derived from MODIS and ASTER data over bare soil surfaces. ISPRS J. Photogramm. Rem. Sens. 126, 1–10.

García-Santos, V., Valor, E., Caselles, V., Coll, C., Burgos, M.A., 2014. Effect of soil moisture on the angular variation of thermal infrared emissivity of inorganic soils. IEEE Geosci. Rem. Sens. Lett. 11, 1091–1095.

Ghent, D., Kaduk, J., Remedios, J., Ardö, J., Balzter, H., 2010. Assimilation of land surface temperature into the land surface model JULES with an ensemble Kalman filter. J. Geophys. Res.: Atmos. 115 (D19), 112. https://doi.org/10.1029/2010JD014392.

Gillespie, A.R., Matsunaga, T., Rokugawa, S., Hook, S.J., 1998. Temperature and emissivity separation from Advanced Spaceborne Thermal Emission and Reflection Radiometer (ASTER) images. IEEE Trans. Geosci. Rem. Sens. 36, 1113–1125.

Göttsche, F.M., Olesen, F.S., Bork-Unkelbach, A., 2013. Validation of land surface temperature derived from MSG/SEVIRI with in situ measurements at Gobabeb, Namibia. Int. J. Rem. Sens. 34 (9–10), 3069–3083.

Guillevic, P.C., Privette, J.L., Coudert, B., Palecki, M.A., Demarty, J., Ottlé, C., et al., 2012. Land Surface Temperature product validation using NOAA's surface climate observation networks – scaling methodology for the Visible Infrared

Imager Radiometer Suite (VIIRS). Rem. Sens. Environ. 124, 282–298. https://doi.org/10.1016/j.rse.2012.05.004.
Guillevic, P.C., Bork-Unkelbach, A., Göttsche, F.M., Hulley, G.C., Gastellu-Etchegorry, J.-P., Olesen, F.S., et al., 2013. Directional viewing effects on satellite Land Surface Temperature products over sparse vegetation canopies—a multisensor analysis. IEEE Geosci. Rem. Sens. Lett. 99, 1–5.
Guillevic, P.C., Biard, C.J., Hulley, G.C., Privette, J.L., Hook, S.J., Olioso, A., Göttsche, F. M., Radocinski, R., Román, M.O., Yu, Y., Csiszar, I., 2014. Validation of land surface temperature products derived from the Visible Infrared Imaging Radiometer Suite (VIIRS) using ground-based and heritage satellite measurements. Rem. Sens. Environ. 154, 19–37.
Hook, S.J., Prata, A.J., Alley, R.E., Abtahi, A., Richards, R.C., Schladow, S.G., et al., 2003. Retrieval of lake bulk and skin temperatures using Along-Track Scanning Radiometer (ATSR-2) data: a case study using Lake Tahoe, California. J. Atmos. Ocean. Technol. 20 (4), 534–548.
Hook, S.J., Vaughan, R.G., Tonooka, H., Schladow, S.G., 2007. Absolute radiometric in-flight validation of mid infrared and thermal infrared data from ASTER and MODIS on the Terra spacecraft using the Lake Tahoe, CA/NV, USA, automated validation site. IEEE Trans. Geosci. Rem. Sens. 45, 1798–1807.
Hulley, G.C., Hughes, C.G., Hook, S.J., 2012. Quantifying uncertainties in land surface temperature and emissivity retrievals from ASTER and MODIS thermal infrared data. J. Geophys. Res. [Atmos.] 117, D23113. https://doi.org/10.1029/2012JD018506.
Islam, I., Hulley, G.C., Malakar, N.K., Radocinski, R.G., Guillevic, P.C., Hook, S.J., 2017. A physics-based algorithm for the simultaneous retrieval of land surface temperature and emissivity from VIIRS thermal infrared data. IEEE Trans. Geosci. Rem. Sens. 55 (1), 563–576. https://doi.org/10.1029/2012JD018506.
Joint Polar Satellite System (JPSS) Program (2014). Level 1 Requirements, SUPPLEMENT – Final. Version 2.10. <http://www.jpss.noaa.gov/assets/pdfs/technical documents/level 1 requirements supplement.pdf>.
Justice, C.O., Román, M.O., Csiszar, I., Vermote, E.F., Wolfe, R., Hook, S.J., et al., 2013. Land and cryosphere products from Suomi NPP VIIRS: overview and status. J. Geophys. Res. [Atmos.] 118, 9753–9765.
Kondratyev, K.Y., 1969. Radiation in the Atmosphere. Academic Press, New York and USA.
Legrand, M., Pietras, C., Brogniez, G., Haeffelin, M., Abuhassan, N.K., Sicard, M., 2000. A high-accuracy multiwavelength radiometer for in situ measurements in the thermal infrared. Part I: Characterization of the instrument. J. Atmos. Ocean Techn. 17, 1203–1214.
Li, H., Sun, D., Yu, Y., Wang, H., Liu, Y., Liu, Q., et al., 2014. Evaluation of the VIIRS and MODIS LST products in an arid area of Northwest China. Rem. Sens. Environ. 142, 111–121. https://doi.org/10.1016/j.rse.2013.11.014.
Liu, Y., Yu, Y., Peng, Y., Göttsche, F.M., Trigo, I.F., 2015. Quality assessment of S-NPP VIIRS land surface temperature product. Rem. Sens. 7, 12215–12241. https://doi.org/10.3390/rs70912215.
Mira, M., Schmugge, T.J., Valor, E., Caselles, V., Coll, C., 2009. Comparison of thermal infrared emissivities retrieved with the two-lid box and the TES methods with laboratory spectra. IEEE Trans. Geosci. Rem. Sens. 47, 1012–1021.
Niclòs, R., Caselles, V., Coll, C., Valor, E., Sánchez, J.M., 2005a. In situ surface temperature retrieval in a boreal forest under variable cloudiness conditions. Int. J. Rem. Sens. 26 (18), 3985–4000.
Niclòs, R., Valor, E., Caselles, V., Coll, C., Sánchez, J.M., 2005b. In situ angular measurements of thermal infrared sea surface emissivity—validation of models. Rem. Sens. Environ. 94, 83–93.
Niclòs, R., Caselles, V., Valor, E., Coll, C., Sánchez, J.M., 2009. A simple equation for determining the sea surface emissivity in the 3–15 μm region. Int. J. Rem. Sens. 30, 1603–1619.
Niclòs, R., Galve, J.M., Valiente, J.A., Estrela, M.J., Coll, C., 2011. Accuracy assessment of land surface temperature retrievals from MSG2-SEVIRI data. Rem. Sens. Environ. 115, 2126–2140.
Niclòs, R., Doña, C., Bisquert, M., Valor, E., 2014. Thermal-infrared spectral and angular characterization of crude oil and seawater emissivities for oil slick identification. IEEE Trans. Geosci. Rem. Sens. 52, 5387–5395.
Niclòs, R., Valiente, J.A., Barberà, M.J., Coll, C., 2015. An autonomous system to take angular thermal-infrared measurements for validating satellite products. Rem. Sens. 7, 15269–15294 http://www.mdpi.com/2072-4292/7/11/15269.
Rubio, E., Caselles, V., Badenas, C., 1997. Emissivity measurements of several soils and vegetation types in the 8–14 mm waveband: analysis of two field methods. Rem. Sens. Environ. 59, 490–521.
Rubio, E., Caselles, V., Coll, C., Valor, E., Sospedra, F., 2003. Thermal-infrared emissivities of natural surfaces: improvements on the experimental set-up and new measurements. Int. J. Rem. Sens. 24 (24), 5379–5390.
Sánchez, J.M., López-Urrea, R., Doña, C., Caselles, V., González-Piqueras, J., Niclòs, R., 2015. Modeling evapotranspiration in a spring wheat from thermal radiometry: crop coefficients and E/T partitioning. Irrig. Sci. 33 (6), 399–410.
Schneider, P., Hook, S.J., 2010. Space observations of inland water bodies show rapid surface warming since 1985. Geophys. Res. Lett. 37, L22405. https://doi.org/10.1029/2010GL045059.
Schneider, P., Ghent, D., Corlett, G., Prata, F., Remedios, J., 2012. AATSR validation: LST validation protocol. Internal publication, UL-NILU-ESA-LST-LVP Issue 1 Revision 0, 39 p. Available on line at <http://lst.nilu.no/Portals/73/Docs/Reports/UL-NILU-ESA-LST-LVP-Issue1-Rev0-1604212.pdf>.
Shepard, D., 1968. A two-dimensional interpolation function for irregularly-spaced data. Proc. ACM National Conference, Princeton, USA. ACM, New York, pp. 517–524.
Tang, B.-H., Shao, K., Li, Z.-L., Wu, H., Nerry, F., Zhou, G., 2015. Estimation and validation of land surface temperatures from Chinese second-generation polar-orbit FY-3A VIRR data. Rem. Sens. 7, 3250–3273. https://doi.org/10.3390/rs70303250.
Theocharous, E., Usadi, E., Fox, N.P., 2010. CEOS comparison of IR brightness temperature measurements in support of satellite validation. Part I: Laboratory and ocean surface temperature comparison of radiation thermometers. NPL REPORT OP3, National Physical Laboratory, Teddington, UK.
Theocharous, E., Barker, I., Snook and Fox, N.P., 2016. 2016 comparison of IR brightness temperature measurements in support of satellite validation. Part 1: Blackbody Laboratory comparison. NPL REPORT ENV12, National Physical Laboratory, Teddington, UK.
VIIRS LST ATBD, 2013. Joint Polar Satellite System (JPSS) VIIRS Land Surface Temperature Algorithm Theoretical Basis Document (ATBD). <https://www.star.nesdis.noaa.gov/jpss/documents/ATBD/D0001-M01-S01-022 JPSS ATBD VIIRS-LST A.pdf>.
Wan, Z., Li, Z.-L., 2008. Radiance-based validation of the V5 MODIS land-surface temperature product. Int. J. Rem. Sens. 29 (17–18), 5373–5395.
Weng, Q., 2009. Thermal infrared remote sensing for urban climate and environmental studies: methods, applications, and trends. ISPRS J. Photogramm. Rem. Sens. 64 (4), 335–344.
Yu, Y., Privette, J.L., Pinheiro, A., 2005. Analysis of the NPOESS VIIRS land surface temperature algorithm using MODIS data. IEEE Trans. Geosci. Rem. Sens. 43 (10), 2340–2350.

Anexo H

Laboratory calibration and field measurement of land surface temperature and emissivity using thermal infrared multiband radiometers

El siguiente trabajo fue publicado en International Journal of Applied Earth Observation and Geoinformation en febrero del 2019. Esta revista tiene un factor de impacto de 4,65 y ocupa la posición 8 de 30 revistas en la categoría Remote Sensing según Journal Citation Reports en la edición de 2019.

Int J Appl Earth Obs Geoinformation 78 (2019) 227–239

Contents lists available at ScienceDirect

Int J Appl Earth Obs Geoinformation

journal homepage: www.elsevier.com/locate/jag

Laboratory calibration and field measurement of land surface temperature and emissivity using thermal infrared multiband radiometers

César Coll[a,*], Raquel Niclòs[a], Jesús Puchades[a], Vicente García-Santos[b], Joan Miquel Galve[c], Lluís Pérez-Planells[a], Enric Valor[a], Evangelos Theocharous[d]

[a] Department of Earth Physics and Thermodynamics, Faculty of Physics, University of Valencia. C/Dr. Moliner, 50. 46100, Burjassot (Valencia), Spain
[b] EOLAB SPAIN S.L., Parc Científic de la Universitat de València, C/Catedrático Agustín Escardino, 9. 46980, Paterna (Valencia), Spain
[c] Applied Physics Department, Regional Development Institute, University of Castilla-La Mancha, Campus Universitario s/n, 02071, Albacete, Spain
[d] National Physical Laboratory, Hampton Road, Teddington, Middlesex, TW11 0LW, United Kingdom

ARTICLE INFO

Keywords:
Land surface temperature
Ground measurements
Emissivity
Radiometer calibration

ABSTRACT

Accurate ground measurements of land surface temperature (LST) are necessary for validating satellite LST products. In order to provide reliable data, ground radiometers must be calibrated with reference to an international standard, and radiometric temperatures must be corrected for land surface emissivity. As opposed to water, land surface emissivity is not usually known for many ground covers, so an emissivity value has to be assumed, assigned from spectral emissivity libraries or measured for each land cover and spectral band considered. The aim of this study is to show the laboratory calibration and the methodology for simultaneous field measurements of LST and emissivity employed in the comparison experiment held in the project Fiducial Reference Measurements for validation of Surface Temperature from Satellites (FRM4STS) funded by the European Space Agency. We used multiband CE-312 radiometers (five narrow bands plus one broad band in the 8–13 μm window) to simultaneously retrieve LST and band emissivities by means of the temperature-emissivity separation (TES) method for different ground covers (clover, tarmac, soil, gravel and sand). The TES method requires near-simultaneous measurements of ground-leaving radiances and sky downwelling radiances; the latter being measured in the field using a gold reflectance panel. For each surface cover, TES provided band emissivities in the CE-312 bands and LST from continuous radiance measurements performed over time. As a result of the experiment, we present the laboratory calibration of the CE-312 radiometers carried out against a traceable, reference blackbody, and the LST series and band emissivity values for the ground covers considered, together with a detailed LST uncertainty analysis including the uncertainties associated to the calibration of ground radiometers, the emissivity estimation by means of the TES method, and the sky radiance measurements, among others. According to these results, the total LST uncertainty was estimated as 0.4-0.6 K for the ground covers measured during the experiment.

1. Introduction

In recent years, a number of land surface temperature (LST) datasets derived from thermal infrared (TIR) satellite measurements have been provided to the user for a variety of applications in many environmental sciences (Li et al., 2013). It is therefore essential to carry out an independent validation of the satellite-derived LSTs and a reliable estimation of the LST uncertainty with reference to traceable, international standards. Recently, international initiatives have arisen with the aim of defining the best practices for ground measurements and validation of satellite LST products at global scale (Guillevic et al., 2017; Martin and Göttsche, 2016). Direct comparison of satellite LST products with ground measurements performed with TIR radiometers in thermally homogenous test sites is generally considered as the reference validation method (Guillevic et al., 2017). With this aim, several research groups have established validation sites in different environments and surface types where in situ LSTs are measured with TIR radiometers (Hook et al., 2007; Göttsche et al., 2016; Tang et al., 2015; Niclòs et al., 2018). Apart of the representativeness of in situ measurements with regard to satellite data due to the dissimilarity in the spatial scale (from typically less than 1 m^2 to 1 km^2 or more), two other problems must be addressed in order to provide accurate ground LST

* Corresponding author.
E-mail addresses: cesar.coll@uv.es (C. Coll), raquel.niclos@uv.es (R. Niclòs), jesus.puchades@uv.es (J. Puchades), vicente.garcia-santos@uv.es (V. García-Santos), joanmiquel.galve@uclm.es (J.M. Galve), Lluis.Perez@uv.es (L. Pérez-Planells), enric.valor@uv.es (E. Valor), theo.theocharous@npl.co.uk (E. Theocharous).

https://doi.org/10.1016/j.jag.2019.02.002
Received 10 July 2018; Received in revised form 6 February 2019; Accepted 11 February 2019

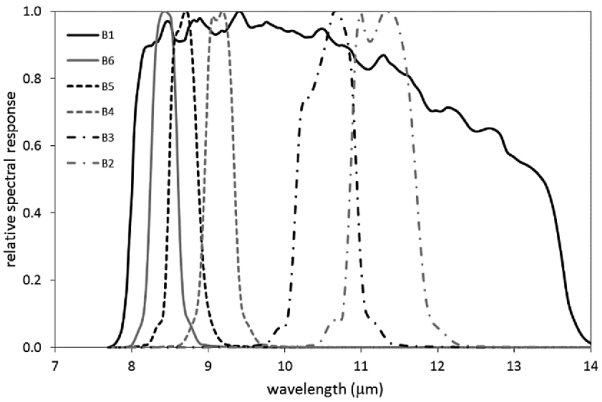

Fig. 1. Relative spectral response of the six CE-312 bands as a function of wavelength.

measurements: (i) the calibration of the field radiometers with reference to SI (*Système International*) standards, and (ii) the measurement of the land surface emissivity.

In 2009, the Committee on Earth Observation Satellites (CEOS) organised a comparison of TIR radiometric instrumentation (radiometers and blackbodies) used to support calibration and validation of satellite-borne sensors with emphasis on sea surface temperature (Theocharous et al., 2010a, b). Stage 1 of this comparison included laboratory measurements at the National Physical Laboratory (NPL), which provided the reference transfer radiometer AMBER (Theocharous et al., 1998) to calibrate the participant's blackbodies, and the NPL ammonia heat-pipe reference blackbody (Chu and Machin, 1999) to calibrate the participant's radiometers. In Stage 2 of the 2009 CEOS comparison, similar experiments were conducted at the Rosenstiel School of Marine and Atmospheric Science (RSMAS), University of Miami, with the National Institute of Standards and Technology (NIST) providing traceability to SI units (Theocharous and Fox, 2010b). As a follow up, analogous comparisons were held up at NPL in 2016, namely the Fiducial Reference Measurements for validation of Surface Temperature from Satellites (FRM4STS, http://www.frm4sts.org), funded by the European Space Agency (ESA), which also focused on land and ice surface temperature measurement. The Thermal Remote Sensing Group of the University of Valencia (TRSG-UV) participated in both the 2009 and 2016 experiments using TIR multiband radiometers CIMEL CE-312 (Sicard et al., 1999; Legrand et al., 2000), which have several bands in the 8–13 μm range, and the Landcal P80P blackbody source (www.landinst.nl/wordpress/calibration/p80p).

The objective of the present paper is to show the methodology followed by TRSG-UV for the laboratory calibration of radiometers and blackbodies, and the simultaneous measurement of LST and emissivity in field conditions, including a detailed uncertainty analysis. Data from the AMBER radiometer and the NPL blackbody measured in the FRM4STS laboratory comparison (Theocharous et al., 2017a; Barker-Snook et al., 2017) were used in this paper. We also show and discuss the field LST and emissivity measurements over five different land covers considered in the FRM4STS field LST comparison (Theocharous et al., 2017b). As opposed to water, land surface emissivity is usually unknown for many ground covers, so it has to be either assumed, assigned from spectral emissivity libraries or, ideally, measured for each land cover and spectral band considered.

One possibility is the use of the box method for field emissivity measurement in either the two-lid or one-lid version (Rubio et al., 2003); however it is time-consuming and has to be implemented independently of the LST measurements in a separate experiment. Another possibility is the application of the Temperature-Emissivity Separation (TES) method (Gillespie et al., 1998) to multiband CE-312 radiometer measurements for simultaneously retrieving LST and emissivity in the radiometer bands. The method is based on an empirical relationship between the apparent band emissivity contrast and the minimum band emissivity, which breaks down the well-known under determination problem in TIR measurements. The TES method, originally proposed for the Advanced Spaceborne Thermal Emission and Reflection Radiometer (ASTER) on board the Terra satellite, can also be applied to field multiband measurements (Mira et al., 2009) and was selected by our group for the FRM4STS field LST comparison.

The paper follows with the description of the field radiometer and the results of the laboratory calibration, including the FRM4STS experiment and the characterisation of the radiometer uncertainty. Section 3 describes the TES method and its application with the field radiometer in the FRM4STS LST comparison. In Section 4, the LST and emissivity results are shown and discussed and the total LST uncertainty is estimated. Finally, Section 5 presents the main conclusions of the study.

2. Instrument description and laboratory calibration

2.1. CIMEL CE-312 TIR multiband radiometer

The CIMEL-Electronique CE-312 radiometer (Sicard et al., 1999; Legrand et al., 2000) has a field of view of 10° and six spectral bands within 8 and 13 μm spectral range (Fig. 1): one wide band B1 (8.0–13.3 μm) and five narrow bands B2 (10.9–11.7 μm), B3 (10.2–11.0 μm), B4 (9.0–9.3 μm), B5 (8.5–8.9 μm) and B6 (8.3–8.6 μm) similar to those of the space borne ASTER sensor. The broad band is composed of a Germanium window with zinc sulphide filters and the narrow bands are interference filters. Measurements can be taken for a single selected band or for all bands consecutively (B1 to B6).

The detector is a thermopile at ambient temperature. The instrument has a built-in radiance reference made of a concealable gold-coated mirror occupying the same field of view as the target measurements which enables comparison between the target radiance and the reference radiation from inside the detector cavity. The temperature of the detector is measured with a calibrated platinum resistance thermometer (PRT), thus allowing compensation for the cavity radiation. The relevant outputs of the radiometer are the detector temperature and the difference in digital counts between the signals from the target and the detector cavity.

In order to measure the radiance coming from a target in a given

band, two consecutive radiance measurements are performed. First, with the concealable gold mirror closed, the detector measures the radiance at the detector's cavity (L_i(cav); unknown) plus the radiance coming from the detector itself which is reflected off the gold mirror, so we can write for band i

$$L_i(\text{closed}) = L_i(\text{cav}) + B_i(T_d) \quad (1)$$

where B_i is the Planck's radiance function integrated for band i, and T_d is the detector temperature measured with the PRT. Then, the gold mirror is open so the detector measures the target's radiance (L_i) plus the detector's cavity radiance, that is

$$L_i(\text{open}) = L_i + L_i(\text{cav}) \quad (2)$$

The unknown value of L_i(cav) can be thus eliminated by subtracting the open and closed radiance measurements so that the radiance coming for the target can be expressed as

$$L_i = B_i(T_d) + \Delta L_i \quad (3)$$

where ΔL_i is the difference between the open and closed radiance measurements. The radiometer radiance outputs are given in terms of digital numbers (DN_i) in the range 0–60000, and ΔL_i is obtained from the difference ΔDN_i between the digital numbers for the open and closed measurements as

$$\Delta L_i = \Delta DN_i / S_i \quad (4)$$

where S_i are the band sensitivity coefficients provided by the manufacturer based on laboratory calibration measurements in 2008. This calibration procedure will be hereafter referred to as standard calibration (sc). According to the manufacturer, the linear calibration (Eq. (4)) holds for target temperatures ranging between -40 and 50 °C, with the detector being at laboratory temperature.

On the other hand, the Planck's radiance function for band i of the CE-312 radiometer can be accurately expressed as

$$B_i(T) = \frac{a_i}{\exp\left(\frac{b_i}{T^{n_i}}\right) - d_i} \quad (5)$$

where coefficients a_i, b_i, n_i and d_i were provided by the manufacturer. When L_i is obtained from the radiometer outputs (T_d, ΔDN_i) following the above procedure, the equivalent radiometric temperature for band i (T_i) can be calculated from L_i by inversion of Planck's radiance function (that is, taking $B_i(T_i) = L_i$ and inverting Eq. (5)).

2.2. Laboratory calibration

Due to the decrease of the radiometer detector's sensitivity with time, the standard calibration must be corrected for the calibration drift using laboratory measurements against a reference blackbody source for a range of temperatures of interest. The calibration drift particularly has an effect on the calculation of ΔL_i (Eq. (4)), which in turns is a function on the temperature or radiance difference between the target and the detector. Since the relationship between ΔL_i and ΔDN_i is linear, we can assume a linear recalibration equation as

$$L_i(\text{cal}) = L_i(\text{sc}) + \alpha_i[L_i(\text{sc}) - B_i(T_d)] + \beta_i \quad (6)$$

where L_i(cal) is the re-calibrated radiance (that is, the radiance corresponding to the reference blackbody temperature), L_i(sc) is the radiance measured with CE-312 using the standard calibration, and α_i and β_i are band-dependent coefficients obtained from linear regression over a set of calibration radiance measurements. Alternatively, Eq. (6) can be written in terms of temperature if the difference between the target and detector temperature is not excessive (as shown below in this section and Section 2.3):

$$T_i(\text{cal}) = T_i(\text{sc}) + A_i[T_i(\text{sc}) - T_d] + B_i \quad (7)$$

where $T_i(\text{cal}) = T_{BB}$ is the reference blackbody temperature, T_i(sc) is the brightness temperature with standard calibration, and A_i and B_i are band-dependent coefficients obtained from linear regression over a set of calibration temperatures. Note that coefficients β_i and B_i in Eqs. (6) and (7), respectively, should be close to zero since there is no independent term in Eq. (4).

Two CE-312 radiometer units (hereafter referred to as CE1 and CE2) were calibrated in the laboratory in May 2016 (before the FRM4STS comparison at NPL in July 2016), for which we used a Landcal P80 P blackbody source (www.landinst.nl/wordpress/calibration/p80p). The blackbody cavity is made of aluminum with black, high temperature refractory coating and has dimensions of 50 mm (diameter) × 155 mm (length), with a 120° cone at the closed end. The nominal temperature range is from -10 to 80 °C, and the emissivity of the cavity is > 0.995 according to the manufacturer. The instrument is equipped with two thermometers: one internal PRT connected to digital display with resolution of 0.01 K and one external PRT with uncertainty of 0.1 K traceable to National Standards (calibration certificate). Previously to the calibration measurements, we checked that both PRTs yielded the same temperatures (within their uncertainty limits) for all the temperature range.

Since the cavity emissivity is not exactly equal to one, the blackbody temperatures measured by the PRTs must be corrected for emissivity effects (including the reflection of ambient radiation) in order to be compared with radiometric temperature measurements. Thus, the radiometric temperature of the blackbody, T_{BB}, is given by

$$B_i(T_{BB}) = \varepsilon B_i(T'_{BB}) + (1-\varepsilon)L_i(\text{amb}) \quad (8)$$

where ε is the cavity emissivity, T'_{BB} is the PRT blackbody temperature, and L_i(amb) is the ambient radiance, which can be approximated as $L_i(\text{amb}) = B_i(T_a)$ with T_a being the ambient (laboratory) temperature when a radiometer operating at ambient temperature (as CE-312) is placed in front of the blackbody cavity to take measurements. The assumption that the detector and the ambient temperature are close is reasonable when the radiometer is kept in the laboratory at least one hour before the measurements start. In such conditions, differences between detector and ambient temperatures never exceed ± 2 K during the experiment. Since ε is high (> 0.995), the differences between T_{BB} and T'_{BB} are small, so Eq. (8) can be approximated with sufficient accuracy regardless of the radiometer band as

$$T_{BB} = T'_{BB} - (1-\varepsilon)(T'_{BB}-T_a) \approx T'_{BB} - 0.005(T'_{BB}-T_a) \quad (9)$$

where in practice we take the lower emissivity bound (0.995) thus yielding the upper limit (in absolute value) for the emissivity correction. Note that, in this case, the difference T_{BB}-T'_{BB} can reach -0.1 K (+ 0.1 K) for T'_{BB}-T_a = + 20 K (-20 K).

The P80 P blackbody was calibrated in the CEOS 2009 comparison against the NPL AMBER radiometer, showing agreement within ± 0.15 K in the 20–30 °C temperature range (Theocharous and Fox, 2010b). The emissivity correction of Eq. (9) was not applied at that time. In the FRM4STS 2016 experiment, the emissivity correction was applied and, for temperatures from 0 to 50 °C, the P80 P blackbody minus AMBER temperatures ranged from -0.04 to 0.08 K, with a mean bias of 0.02 K, standard deviation of 0.04 K and root mean squared difference (rmsd) of 0.05 K (Theocharous et al., 2017a). The AMBER radiometer is characterized with an uncertainty of 53 mK (Theocharous et al., 2017a), so the agreement is good within the combined uncertainty limits. If the emissivity correction was not applied, the mean bias, standard deviation and rmsd would be 0.07, 0.05 and 0.09 K respectively. Temperatures below 0 °C are problematic because ice formation in the blackbody cavity and they were not considered in this experiment. The good calibration results in both the CEOS 2009 comparison and the FRM4STS 2016 experiment show the long-term stability and the accuracy of the P80 P blackbody.

For the laboratory calibration of the CE-312 radiometers, the P80 P

blackbody source was set at six fixed temperatures (0 to 50 °C) in two different runs with instrument re-aligning. Enough time (about 1 h) was allowed for the blackbody to reach equilibrium at each temperature. The blackbody temperature was corrected for emissivity (Eq. (9)) taking T_a as the laboratory temperature. Radiometers were aligned with the black body cavity, and placed at a distance so that the field of view was smaller than the cavity diameter. Taking into account the radiometer nominal field of view (10°) and the length of the cavity (155 mm), we estimated that placing the radiometer at 20 mm from the cavity entrance yields a diameter of 30 mm on the cavity closed end, which is considerably smaller than the cavity diameter (50 mm). The standard calibration was applied to the radiometer readouts to calculate the equivalent brightness temperature. For each temperature and band, we made 15 radiance measurements for which the average value and standard deviation were calculated. For a given band, the difference between the average values for the same temperature in the two runs (with re-alignment) gives an estimate of the reproducibility of measurements, whereas the standard deviation of 15 measurements for a given temperature (without re-alignment) gives the repeatability. The detector temperature ranged between 24 and 28 °C during the experiment. Fig. 2 shows the calibration results for the six bands of the CE2 unit (similar results were obtained for CE1) together with the linear regression according to Eq. (7). Table 1 gives the calibration coefficients A_i and B_i of Eq. (7), the coefficient of determination and the standard error of the regression for each band and radiometer. These results show that the linear calibration equation is accurate for all bands in the temperature range considered and it is necessary to apply it to the standard calibration due to the detector's sensitivity drift, especially when the target temperature is not close to the detector temperature. Moreover, B_i values are close to zero in all cases as anticipated.

Table 1
Calibration coefficients A_i and B_i of Eq. (7) derived from the laboratory measurements in Valencia, May 2016, using the P80 P blackbody. The coefficient of determination (r^2) and the standard regression error (σ) are also given. (a) CE1. (b) CE2.

(a) CE1 band	A_i	B_i (K)	r^2	σ (K)
1	0.01613	−0.01	0.964	0.06
2	0.00981	−0.06	0.931	0.05
3	0.00496	−0.08	0.810	0.04
4	0.00875	−0.13	0.930	0.04
5	0.01512	−0.08	0.971	0.05
6	0.00747	−0.16	0.898	0.05
(b) CE2 band	A_i	B_i (K)	r^2	σ (K)
1	0.01674	0.02	0.986	0.04
2	0.00955	0.00	0.968	0.03
3	0.00645	−0.03	0.927	0.03
4	0.01157	−0.07	0.934	0.06
5	0.01511	−0.01	0.988	0.03
6	0.01115	−0.07	0.947	0.05

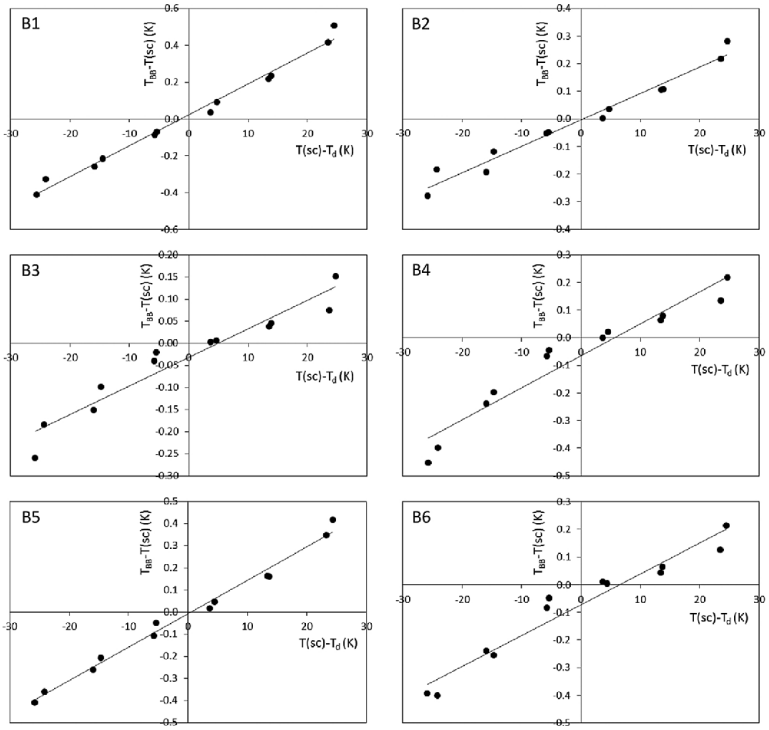

Fig. 2. Laboratory calibration measurements performed in May 2016 for the six bands of CE2 using the P80 P blackbody. The straight lines show the linear regression according to Eq. (7). For each band, differences between the blackbody temperatures, T_{BB}, and radiometric temperatures with standard calibration, T(sc), are plotted against differences between the latter and the detector temperatures, T_d.

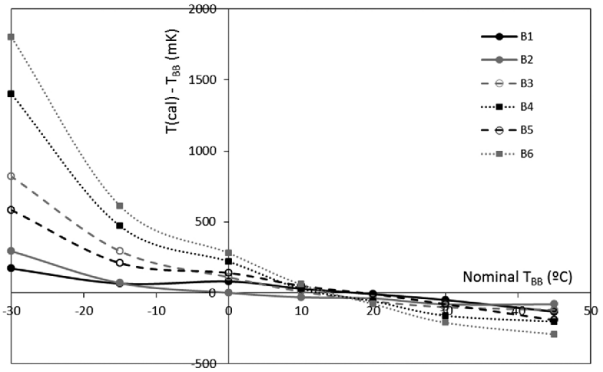

Fig. 3. Differences between the CE-312 (CE1) temperature measurements calibrated with Eq. (7) for the six bands and the NPL blackbody temperature against the nominal NPL blackbody temperature.

2.3. FRM4STS calibration

The two CE-312 radiometers were calibrated against the NPL ammonia heat-pipe reference blackbody in the FRM4STS experiment in June 2016, so the previous laboratory calibration can be compared with a reference standard. The NPL blackbody is characterized with an uncertainty of 0.04 K (Barker-Snook et al., 2017) and it was set at nominal temperatures of -30, -15, 0, 10, 20, 30 and 45 °C (the exact values were unknown at the time of measurements). Note that the temperature range covered temperatures well below 0 °C, unlike the P80 P blackbody that cannot operate at such low temperatures due to ice formation in the cavity. For each blackbody temperature, we performed 12 consecutive measurements for each band of each CE-312 radiometer, for which the average and standard deviation (repeatability) was calculated and compared with the blackbody temperatures. The detector temperature of both radiometers ranged between 21 and 24 °C during the experiment.

Fig. 3 shows the results of the FRM4STS comparison for the six bands of the CE1 instrument (similar results were obtained for CE2). It is apparent that there were important differences for bands 3–6 at the lower temperature values, which were out of the calibration range in the previous experiment with the P80 P blackbody. For such bands, we can also observe that the difference between the CE-312 and the blackbody temperatures does not hold a linear relationship with temperature in the full temperature range considered, as opposite to the linear standard calibration (Eq. (4)) and the laboratory re-calibration (Eq. (7)). However, the agreement between the measured and blackbody temperatures is good and approximately linear in the 0–45 °C range, with linear correlation coefficients ranging between 0.938 (B3) and 0.998 (B1 and B5) for CE1, and between 0.931 (B4) and 0.998 (B2 and B5) for CE2.

In Table 2, we show the basic statistics of the differences $T_i(cal)$-T_{BB} for the six bands of the two radiometers in the 0–45 °C interval, which is the most useful for LST measurements. According to these results, the rmsd was between 0.06 and 0.10 K for bands B1-B3 and between 0.13 and 0.23 K for bands B4-B6 of both instruments. The best (worst) accuracy was obtained for band B2 (B6). If the laboratory re-calibration was not applied (standard calibration only), the rmsd would yield 0.2 K for bands B2 and B3, and 0.3-0.4 K for bands B1 and B4-B6.

In Fig. 3 we can observe that the differences between measured and blackbody temperatures are close to zero around 20 °C (close laboratory temperature), where differences change sign. Besides, the largest differences (in absolute value) between measured and blackbody temperatures occur for the largest differences (in absolute value) between measured and detector temperatures. This suggests that the above FRM4STS calibration data can be used to derive new coefficients A_i and B_i for the re-calibration of the CE-312 radiometers according to Eq. (7). In order to keep the linearity of the re-calibration, and because there were no data enough below 0 °C we only considered the 0–45 °C temperature range to obtain the calibration coefficients from linear regression. This is shown in Fig. 4 where, as examples, we plot the differences between the blackbody temperatures and the measured temperatures with standard calibration against the differences between that temperature and the detector's temperature for band 1 (the most accurate) and band 6 (the less accurate) of CE1 considering the full temperature range of the experiment (-30 to 45 °C). Fig. 4 also shows the linear regression for the 0–45 °C range only, which were used to derive the new coefficients A_i and B_i.

Table 3 shows the calibration coefficients to be applied to the standard calibration derived for the six bands of the two radiometers, together with the coefficient of determination and the standard regression error. Results show high correlation and small uncertainty in the linear calibration for all bands in the considered temperature range. Note that the calibration coefficients were derived in laboratory conditions with quite stable ambient (and detector) temperatures (21–24 °C). However, the calibration of the CE-312 radiometers is based on the radiance difference between the target and the detector (Eq. (4)) and then, in principle, it depends only on the difference between T_d and the target temperature and not on T_d itself, provided that the sensitivity of the detectors is independent of temperature. This assumption could

Table 2
Basic statistics of the differences between the CE-312 measurements calibrated with Eq. (7) for the six bands and the NPL reference blackbody temperatures in the 0–45 °C range from the FRM4STS laboratory comparison. (a) CE1. (b) CE2.

(a) Radiometer CE1	B1	B2	B3	B4	B5	B6
minimum difference (K)	−0.13	−0.08	−0.12	−0.20	−0.19	−0.29
maximum difference (K)	0.08	0.00	0.11	0.22	0.14	0.28
bias (K)	−0.02	−0.05	−0.03	−0.03	−0.02	−0.05
standard deviation (K)	0.08	0.03	0.09	0.17	0.13	0.23
rmsd (K)	0.08	0.06	0.10	0.17	0.13	0.23

(b) Radiometer CE2	B1	B2	B3	B4	B5	B6
minimum difference (K)	−0.15	−0.10	−0.13	−0.17	−0.22	−0.22
maximum difference (K)	0.08	0.04	0.14	0.26	0.19	0.35
bias (K)	−0.02	−0.03	−0.01	−0.01	−0.01	0.01
standard deviation (K)	0.09	0.05	0.10	0.17	0.16	0.22
rmsd (K)	0.09	0.06	0.10	0.17	0.16	0.22

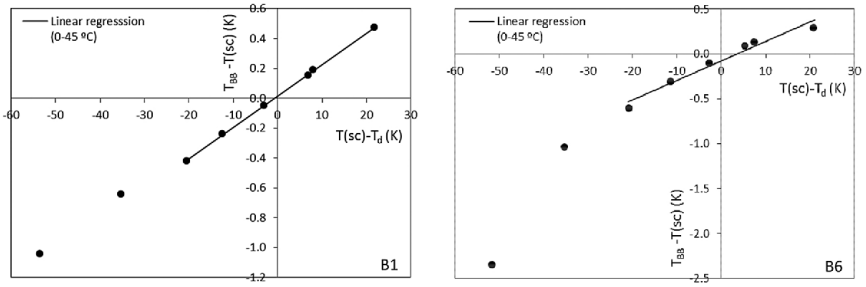

Fig. 4. FRM4STS calibration measurements performed at NPL, June 2016 for bands 1 (left) and 6 (right) of CE1 using the NPL reference blackbody. T_{BB} is the blackbody temperature, T(sc) is the radiometric temperature with standard calibration, and T_d is the detector temperature. The straight lines show the linear regression for the 0–45 °C interval according to Eq. (7).

Table 3
Calibration coefficients A_i and B_i of Eq. (7) derived from the FRM4STS measurements at NPL, June 2016 using the NPL reference blackbody for the 0–45 °C interval. The coefficient of determination (r^2) and the standard regression error (σ) are also given. (a) CE1. (b) CE2.

(a) CE1 band	A_i	B_i (K)	r^2	σ (K)
1	0.02103	0.02	0.9997	0.01
2	0.01195	−0.01	0.9955	0.01
3	0.01043	−0.03	0.9515	0.04
4	0.01854	−0.07	0.9634	0.06
5	0.02288	−0.04	0.9978	0.02
6	0.02177	−0.08	0.9645	0.07
(b) CE2 band	A_i	B_i (K)	r^2	σ (K)
1	0.02200	0.04	0.9995	0.01
2	0.01275	0.03	0.9994	0.01
3	0.01253	0.00	0.9759	0.03
4	0.02129	−0.04	0.9649	0.07
5	0.02455	0.02	0.9990	0.01
6	0.02411	−0.05	0.9596	0.08

only be checked by performing calibration experiments for different values of T_d covering a wide range of ambient temperatures in field conditions, for what a climatic chamber with controlled and variable ambient temperature would be required. Unfortunately, this was not possible in the FRM4STS laboratory comparison. With this caveat in mind, we assumed that the re-calibration coefficients of Table 3 can be applicable regardless the detector's temperature if the difference between the detector and target temperatures is within ± 25 °C as in Fig. 4. Out of this range (e.g., sub-zero temperatures corresponding to measurement of atmospheric radiances), there could be large discrepancies for most of the CE-312 bands.

2.4. Uncertainty budget

As a summary of this section, we present a detailed uncertainty analysis of the temperature measurements of the CE-312 radiometers, which was carried out following the guidelines of the Joint Committee for Guides in Metrology (JCGM, 2008). According to it, we distinguished two types of uncertainty contribution: Type A, referring to the evaluation of a component of measurement uncertainty by a statistical analysis of measured quantity values obtained under defined measurement conditions (e.g., random), and Type B, that is an evaluation of a component of measurement uncertainty determined from non-statistical calculations, including uncertainties taken from calibration certificates or derived from the characterisation of the performance of the instruments being used (e.g., systematic). Results shown here correspond to the laboratory calibration experiment performed in May 2016 prior to the FRM4STS experiment.

For Type A, we considered the repeatability and reproducibility derived from multiple measurements as mentioned in Section 2.2. For Type B, several error sources were considered:

- The uncertainty of the primary calibration, which was taken as the total uncertainty of the P80 P blackbody (0.05 K) according to the FRM4STS blackbody calibration results (Theocharous et al., 2017b).
- The linearity of radiometer, which was taken as 0.06 K as the typical value for all bands in the temperature range 0–40 °C (Legrand et al., 2000).
- Correction of calibration drift: It was corrected for by means of linear re-calibration equations derived from P80 P blackbody measurements for each band and radiometer (Section 2.2). The uncertainty for this correction is the root sum square (RSS) of the typical estimation uncertainty of the linear regression (0.05 K for CE1 and 0.04 K for CE2) and the uncertainties resulting from the propagation of input temperature errors (standard deviations for 15 measurements at a fixed temperature) in the linear correcting equation. The resulting uncertainty in the correction of calibration drift is 0.07 K for CE1 and 0.05 K for CE2.
- Ambient temperature fluctuations: This effect is compensated by the CE312 radiometers by measuring the detector cavity temperature by means of a calibrated PRT as explained in Section 2.1. The uncertainty in this process is the uncertainty of the internal PRT, which is 0.04 K according to Legrand et al. (2000).
- Finally, the effect of atmospheric absorption and emission was estimated as negligible (< 0.01 K) due to very short path length and radiometers working in the atmospheric window.

Table 4 summarizes the different uncertainty estimates for both

Table 4
Uncertainty analysis of the two CE-312 radiometers considering the different error sources (see text). RSS is the root sum square, and the total RSS represents the standard uncertainty of the radiometer, with coverage factor k = 1.

Uncertainty Contribution	Radiometer CE1		Radiometer CE2	
	Type A (K)	Type B (K)	Type A (K)	Type B (K)
Repeatability of measurement	0.05		0.03	
Reproducibility of measurement	0.08		0.06	
Primary calibration		0.05		0.05
Linearity of radiometer		0.06		0.06
Correction of calibration drift		0.07		0.05
Ambient temperature fluctuations		0.04		0.04
RSS	0.09	0.11	0.07	0.10
Total RSS	**0.15**		**0.12**	

radiometers, as well as the RSS for Types A and B, and the total RSS considered as the standard uncertainty of the radiometers (that is, with coverage factor k = 1). The uncertainty estimations shown here are compatible with most of the differences between the measured and the NPL blackbody temperatures shown in section 2.3 for the FRM4STS comparison in the 0–45 °C range. These results show the accuracy and precision of the CE-312 radiometers, which is suitable for ground measurements for validating satellite LSTs.

3. Simultaneous measurement of LST and emissivity in field conditions

In order to measure LST in field conditions, an estimate of the surface emissivity is necessary. This is not always an easy task, since land surface emissivity can be rather variable depending on the cover type, the spectral band used, the soil moisture, and the observation angle, among others. The best option is usually to measure emissivity at the same field conditions as LST. To this end we propose the use of the Temperature-Emissivity Separation (TES) method (Gillespie et al., 1998) to simultaneously retrieve LST and emissivity using the five narrow bands (B2-B6) of the CE-312 radiometer.

3.1. The TES method

The TES method starts from the calibrated radiance measured at surface level in band i of the ground radiometer, which can be written as

$$L_i^{surf} = \varepsilon_i B_i(T) + (1-\varepsilon_i)L_i^{sky} \quad (10)$$

where T is the LST, ε_i is the surface emissivity in band i and L_i^{sky} is the sky downwelling radiance in band i, which needs to be measured in the field near-simultaneously to the target radiance. If Eq. (10) is applied to the N spectral bands of a radiometer, we have N + 1 unknowns (one LST and N band emissivities ε_i), so the problem is underdetermined. In the TES method, the under-determination is solved with an empirical relationship between the apparent spectral contrast in emissivity, or maximum-minimum emissivity difference (MMD) and the minimum spectral emissivity (Gillespie et al., 1998). The application of the TES method involves the following steps:

1. Normalized emissivity method (NEM): We assume an emissivity value $\varepsilon_{NEM} = 0.98$ in Eq. (10) for all bands and calculate T_{NEMi} for each band; that is

$$B_i(T_{NEMi}) = \frac{L_i^{surf} - (1-\varepsilon_{NEM})L_i^{sky}}{\varepsilon_{NEM}} \quad (11)$$

2. Select the maximum value of T_{NEMi} ($T_{max} = \max(T_{NEMi})$, i = 1,.., N) and use T_{max} to obtain an estimate of the N NEM emissivities according to

$$\varepsilon_{NEMi} = \frac{L_i^{surf} - L_i^{sky}}{B_i(T_{max}) - L_i^{sky}} \quad (12)$$

3. Calculate the β_i spectrum from the NEM emissivities as

$$\beta_i = \frac{\varepsilon_{NEMi}}{\bar{\varepsilon}} \quad (13)$$

where $\bar{\varepsilon}$ is the average NEM emissivity for the five bands. From the β_i spectrum, the MMD is defined as the difference between the maximum and minimum β_i values (MMD = max(β_i)-min(β_i)).

4. Calculate the minimum band emissivity (ε_{min}) from the MMD using the empirical relationship

$$\varepsilon_{min} = 0.9951 - 0.7264 \times MMD^{0.7873} \quad (14)$$

which was derived by Hulley and Hook (2009) from laboratory emissivity spectra taken from the ASTER spectral library (ASL, Baldridge et al., 2009). They selected 49 soil spectra from ASL in terms of taxonomy (14 aridisols, 9 alfisols, 10 entisols, 7 inceptisols and 9 mollisols) plus nine additional dune sand samples, which were linearly combined with the conifer vegetation emissivity spectrum (with reflectance reduced by a factor of two to account for canopy scattering effects) by varying the fractional vegetation cover from 0 to 100% in steps of 5% (Hulley and Hook, 2009). The resulting spectra were convolved to the spectral response functions of the ASTER bands and then the ε_{min}-MMD relationship was obtained by regression. The numerical coefficients of Eq. (14) differ from the coefficients of the original ε_{min}-MMD relationship derived by Gillespie et al. (1998) and, according to Hulley and Hook (2009), they improve the estimations for vegetated surfaces characterized by low values of MMD and high values of ε_{min}.

Although Eq. (14) was obtained originally for the ASTER bands, it can be applied to the similar CE-312 narrow bands as well (Mira et al., 2009). We checked this assumption using the same emissivity spectra from ASL (except for the nine sand dune spectra which were not available) and the linear mixture of soil and vegetation spectra mentioned above to calculate the emissivities in the CE-312 and ASTER bands. We found that the CE-312 emissivities were very close to the ASTER emissivities in the equivalent bands, with rmsd of 0.0003 for CE-312 band B2 (equivalent to ASTER band 14), 0.0010 for B3 (band 13), 0.0020 for B4 (band 12), 0.0010 for B5 (band 11) and 0.0083 for B6 (band 10). Differences were larger for band B6 because its center (8.45 μm) is slightly shifted with respect to ASTER band 10 (center at 8.29 μm). Fig. 5 shows the ε_{min}-MMD relationship for both CE-312 and ASTER using the calculated emissivities, together with the Hulley and Hook (2009) regression curve (Eq. (14)). We can see that there is a good agreement between the CE-312 and ASTER for the whole range of the data, with rmsd of 0.004 for both MMD and ε_{min}. Equation (14) also agrees well with ε_{min} values for both CE-312 and ASTER (rmsd of 0.005 for CE-312 and 0.007 for ASTER for the full data range), although the agreement is better for MMD values lower than 0.15. For larger MMD values, Eq. (14) slightly overestimates ε_{min} by about 0.01 for both CE-312 and ASTER. This is because Eq. (14) was optimized for a wider range of samples, with higher (lower) MMD (ε_{min}) values corresponding to the sand dune spectra used by Hulley and Hook (2009) but not considered in the present study. Therefore, we consider that the ASTER ε_{min}-MMD empirical relationship can be also applied to CE-312 data, as it provides an accurate estimation of ε_{min} (rmsd of 0.005) within the typical estimation error of the ε_{min}-MMD relationship (about 0.01 according to Gillespie et al., 1998).

5. The final emissivity values are obtained by scaling the β_i spectrum with ε_{min} according to

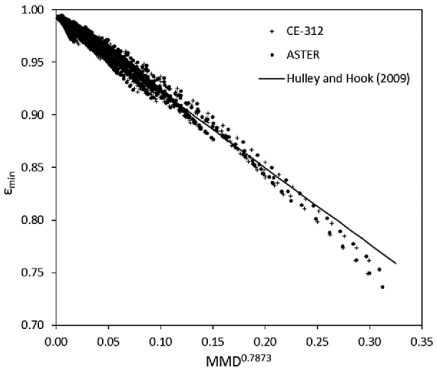

Fig. 5. Empirical relationship between ε_{min} and MMD for CE-312 (crosses) and ASTER (dots) using the emissivities calculated form ASL spectra with linear combinations of conifer vegetation and 49 soil samples. The continuous line shows the ε_{min}-MMD curve from Hulley and Hook (2009).

$$\varepsilon_i = \varepsilon_{min}[\beta_i/\min(\beta_i)] \quad (15)$$

and they are used to re-calculate the surface temperature for each band as in Eq. (11). Ideally, such temperatures should be band-independent; however, they may differ slightly (< 0.1 K) in practice. Finally, the LST is taken as the maximum band temperature.

3.2. Application in field conditions

In the FRM4STS LST comparison, the CE2 radiometer was used for continuous multiband measurement of the radiance from the surface (L_i^{surf}) because its accuracy was slightly better than CE1. We planned to use CE1 for continuous measurements of sky downwelling radiance (L_i^{sky}) using a diffuse reflectance gold panel (García-Santos et al., 2012) simultaneously to the surface measurements of CE2. However, CE1 showed electronical and power problems during the campaign and did not provide useful data for most of the time. Therefore, sky radiance measurements were performed with CE2 by placing the diffuse reflectance gold panel in the field of view of the radiometer at regular, short intervals during the measurement of surface radiances. The measured sky radiances were then linearly interpolated to the time of the surface radiance measurements. During the FRM4STS field comparison, environmental conditions were not ideal for LST measurements, with partial and rather variable cloud cover. Therefore L_i^{sky} varied considerably and the interpolation procedure was subject to significant error. Besides, the CE-312 measurements were calibrated in the 0–50 °C range (Section 2.2, Table 1), so L_i^{sky} measurements that correspond to low temperatures may be affected by severe errors depending on the band (Section 2.3). Fortunately, the impact of L_i^{sky} uncertainties on LST is small compared to other error sources, as discussed in Section 4.3.

The multiband CE-312 measurements are not really simultaneous but successive, from B1 to B6 with a gap of 6 s between two consecutive bands and a total of 39 s for a six-band measurement series including filter rearrangement. This means that there is a time gap of 24 s between measurements in bands B2 and B6 in a series and a gap of 39 s for a given band between two consecutive series. In the TES method, it is required that LST is the same for all bands what may be a problem if surface temperature changes significantly during the multiband measurement. This was the case in FRM4STS where variable cloud cover caused rapid changes in temperature, so the sample was not isothermal during the 24-s multiband measurement. In order to mitigate this problem, we applied a correction method based on linear temporal interpolation between consecutive multiband series. To do that, we selected the measurement time of band B3 as the reference time for each series so B3 measurements remain unchanged and the measurements for all other bands are reduced to that time by means of linear interpolation between the two closest measurements, one from the same measurement series and the other from either the preceding (bands B1 and B2) or the next series (bands B4-B6). While this procedure may not be required in ideal field conditions were surface temperatures may remain constant during the multiband measurement, the particular conditions during the FRM4STS experiment made the correction necessary.

4. Results and discussion

The field LST measurements were performed at the NPL campus in July 2016 (Theocharous et al., 2017b). Five different samples were considered (see Fig. 6): clover, tarmac, soil (dark, with high content of organic matter), gravel and sand (yellowish, typical construction sand). The last three samples were placed in open containers with dimensions of 1.5 m × 1.1 m and the surface was tilled flat and uniform. The CE2 radiometer was placed at a height of 2.5 m from the sample and looking at 25° from nadir, thus covering a quasi-elliptic area with semi axes of 23 and 27 cm over the surface. Measurements were taken off-nadir to prevent reflections from the base of the radiometer mount but keeping the viewing angle as small as possible to avoid directional effects on LST and make sure that the field of view of the radiometers fitted within the target.

For each sample, continuous multiband measurements were performed during different time intervals, ranging from 40 min for clover to more than 2 h for gravel. That sample was measured in two different days (July 6 and 7). As mentioned before, the CE2 measurements were calibrated with coefficients of Table 1, the temporal interpolation was applied to the band brightness temperatures and the TES method was used. We present here the results obtained in terms of LST and band emissivities, including a detailed uncertainty analysis.

4.1. LST and emissivity

In the TES method, LST is obtained for the band where surface emissivity is maximum, which was B2 (10.9–11.7 μm) for the five samples considered. Fig. 7 shows the LST values obtained as a function of time for each sample. We can observe rapid changes in LST for some cases, which are indicative of variable cloud cover. In the cases of sand, soil and gravel there were variations of about 10 K in few minutes, with soil, gravel and tarmac LSTs reaching about 50 °C around noon. The dynamic range of LST was about 10 K for sand and gravel, while it reached 20 K for soil. LSTs were more constant for clover and tarmac, with variations of about 5 K during the measurement period in both cases. It should be also noted that the difference between the sample and detector's temperature reached 20–25 °C for soil, tarmac and gravel thus being close to the upper limit of the calibration range but still within it (e.g., Fig. 2). A good calibration of the instrument is important for such cases, otherwise biases up to -0.5 K could be obtained. In the case of sand, the difference between sample and detector's temperature reached 15 °C only because measurements were made early in the morning. For clover, both temperatures were quite similar, with differences ranging from -4 to 1 °C.

For each LST retrieval, TES provides an estimation of the B2-B6 band emissivities. However, emissivity must be constant for a given sample during the measurement time, so we calculated the mean value and the standard deviation of the TES derived emissivities for each band during the measurement period corresponding to each sample. The mean values were taken as the band emissivities and the uncertainty in the retrieved emissivity was calculated as the RSS of the standard deviation of band emissivity, the standard estimation error of the empirical ε_{min}-MMD relationship (Eq. (14)), which is 0.010 (Gillespie et al., 1998), and the rmsd of the ASTER ε_{min}-MMD empirical relationship (Eq. (14)) with regard to CE-312 (0.005; Section 3.1). We also checked the influence of the initial ε_{NEM} assumption (taken as 0.98 in the present study) on the TES method. To do this, we varied ε_{NEM} by ± 0.01 and compared the resulting TES emissivities and LSTs with those obtained with original ε_{NEM} value. Results showed that the impact of ε_{NEM} was very small for all targets considered. The highest (lowest) impact was found for clover (sand), with variations of 9×10^{-5} (1.3×10^{-5}) in maximum emissivity (band B2), 0.003 (0.003) in minimum emissivity (band B6) and rmsd of 0.07 K (0.001 K) in LST. Such variations can be considered as negligible when compared to the other uncertainty sources considered above.

Fig. 8 shows the emissivity spectra obtained for the five samples, and Table 5 gives the emissivity for band B2 corresponding to the maximum emissivity value and for band B6 usually corresponding to the minimum emissivity.

The CE-312 wideband B1 (8.0–13.3 μm) is not used in the TES method, however the radiances measured in such band can be used to retrieve emissivity in band B1 according to

$$\varepsilon_1 = \frac{L_1^{surf} - L_1^{sky}}{B_1(T) - L_1^{sky}} \quad (16)$$

Fig. 6. Pictures of the five samples considered in the FRM4STS field LST measurements.

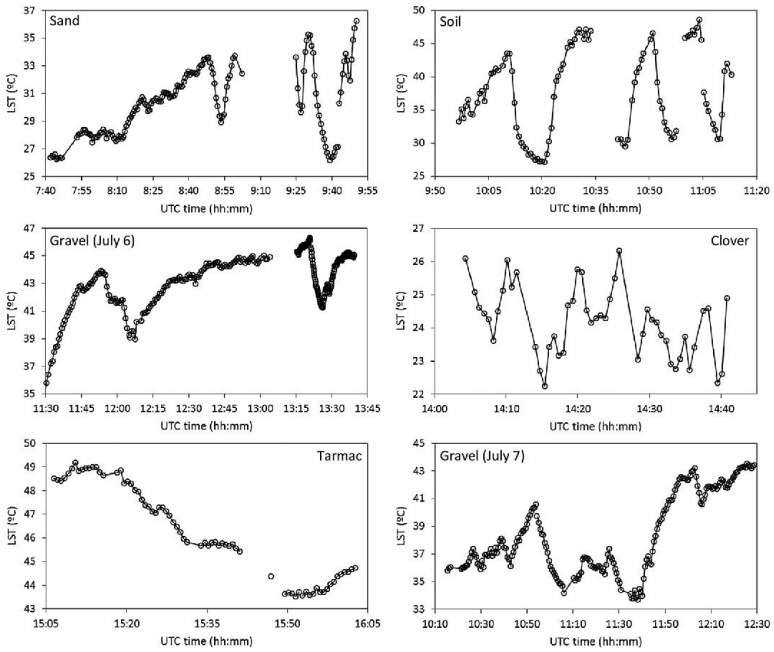

Fig. 7. LST values as a function of time for the samples measured during the FRM4STS field experiment. Gaps in the LST series correspond to power and/or electronic problems with the radiometer.

where T is the LST retrieved from TES. Table 5 also gives the emissivity in band B1 for the five samples.

4.2. Discussion

Results show that emissivity in long wavelength bands B2 and B3 was high and with small variability among the different covers considered ranging roughly from 0.95 to 0.98, which is an optimal case for radiometric LST measurements. Differently, short wavelength bands B4-B6 showed much larger variability and lower values for sand (≈0.80) and gravel (≈0.85) which show the characteristic features due to quartz absorption at 8–9 μm (*reststrahlen* bands; Rowan and Mars, 2002). This also translates into low emissivity values for broad band B1 in such cases. Besides, we can note that gravel emissivity estimates for two different days were in very good agreement within the uncertainty limits. For clover and soil with high content in organic matter, we

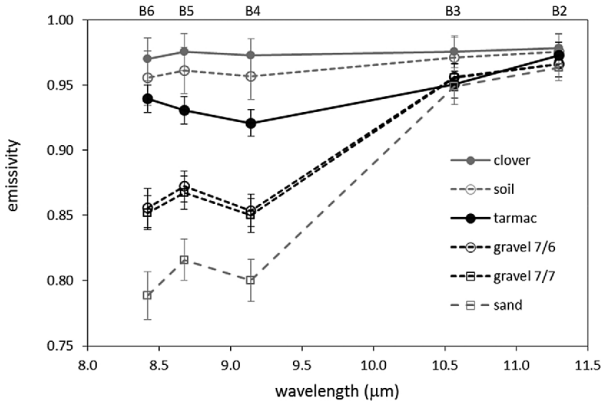

Fig. 8. Emissivity of the samples measured in FRM4STS as a function of the centre wavelength of the narrow bands of CE-312. Results for the gravel sample measured in two different days are presented.

obtained flat, near grey body spectra with relatively high values as expected (Salisbury and D'Aria, 1992).

Unfortunately, independent emissivity measurements were not performed for the samples considered in the FRM4STS field LST comparison, so we cannot validate the TES derived emissivities and estimate their uncertainty with regard to an absolute reference. To this end, emissivity spectra obtained from field Fourier Transform Infrared (FTIR) spectrometer data taken in the same conditions as the LST measurements would be required. In the present FRM4STS comparison, participants were encouraged to make their own best estimate of the target emissivities for their radiometer under the conditions which prevailed during the LST measurements, but such measurements cannot be compared with the TES emissivity estimates because the different spectral bands of the radiometers.

As pointed out above, emissivities in band B2 (B6) were the highest (lowest) for each cover and also showed the lowest (highest) variability along the multiple TES measurements performed for a given target and thus the lowest (highest) uncertainty as shown in Table 5. This implies that B2 (B6) is the most (less) appropriate band for LST retrieval. We can show this calculating the LST for a given band from the at-surface and sky radiances according to

$$B_i(T) = \frac{L_i^{surf} - (1 - \varepsilon_i)L_i^{sky}}{\varepsilon_i} \quad (17)$$

where ε_i is the average band emissivity in band i. For a given target, such LSTs would differ from the LSTs derived from TES due to the variability of TES-retrieved emissivities during the measurement period. We compared the TES LSTs with those derived from Eq. (17) in bands B2, B6 and B1 using the average emissivities of Table 5. Fig. 9 shows the LST differences between TES and Eq. (17) (ΔT_i) for two targets (sand and gravel on July, 6), and Table 6 gives the rmsd with respect to TES LSTs for the three bands and all targets considered in the study. We can see that, as expected, B2 yielded the smallest rmsd compared to the other bands for all targets, with values of 0.01-0.02 K except for the soil and clover targets, which were the most affected by variable atmospheric conditions prevailing during the campaign and thus yielded more variable TES emissivity estimations. In any case, B2 showed very good stability during the measurement periods, B6 being less stable in time with respect to TES LSTs owing to more variable emissivity values obtained from TES. B1 showed intermediate results between B2 and B6.

Finally, we show the effect of the temporal interpolation method described in Section 3.2 taking as an example the sand emissivity results for band B6 (8.3–8.6 μm). Fig. 10 shows the emissivity values obtained for each multiband series during the sand measurement period, with comparison to the case when temporal interpolation was not applied. We can see that the dispersion in emissivity is larger for the latter case, especially at times around 8:55 and from 9:25, when LST showed rapid variations due to variable cloud cover (see Fig. 7 for sand). When applying the temporal interpolation method, the retrieved emissivity values were more uniform for the whole measurement period, yielding a mean value of 0.787 with standard deviation of 0.008 (0.788 and 0.014 respectively without temporal interpolation).

We can also observe in Fig. 10 an increase of emissivity with time (or LST) of the sand sample in the first part of the measurement period. We do not believe that the emissivity variation is due to the LST variation since the retrieved emissivities remained constant for gravel and tarmac while LST varied considerably during their measurement periods (see Fig. 7). The observed increase of sand emissivity could be due to an increase of the real sky downwelling radiance which was not detected by our L_i^{sky} measurements due to rapid changes in cloud cover and insufficient sampling of L_i^{sky} during the measurement period. In

Table 5
Emissivity values and uncertainties for the five FRM4STS samples in narrow bands B2 and B6 and in wideband B1.

Target	B2 (10.9-11.7 μm)		B6 (8.3-8.6 μm)		B1 (8.0-13.3 μm)	
	Emissivity	Uncertainty	Emissivity	Uncertainty	Emissivity	Uncertainty
Clover	0.978	0.012	0.970	0.017	0.973	0.014
Soil	0.976	0.014	0.955	0.021	0.970	0.015
Tarmac	0.973	0.011	0.939	0.012	0.951	0.010
Gravel	0.966	0.011	0.854	0.015	0.925	0.010
Sand	0.963	0.011	0.789	0.019	0.900	0.011

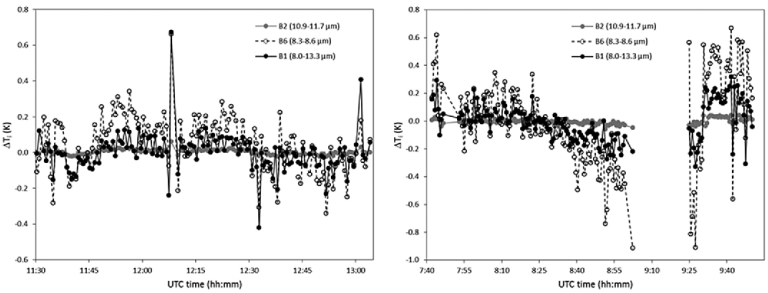

Fig. 9. LST difference between TES and Eq. (17) (ΔT_i) for bands B2, B6 and B1 as a function of time for gravel, July, 6 (left) and sand (right).

Table 6
Root mean squared differences (K) between LSTs derived from TES and Eq. (17) (ΔT_i) for bands B2, B6 and B1 and the targets considered in the study.

Target	B2 (10.9-11.7 μm)	B6 (8.3-8.6 μm)	B1 (8.0-13.3 μm)
clover	0.19	0.34	0.28
soil	0.36	0.66	0.44
tarmac	0.02	0.14	0.07
gravel (July, 6)	0.01	0.16	0.11
gravel (July, 7)	0.02	0.30	0.11
sand	0.02	0.32	0.14

fact we used mostly constant values of L_i^{sky} for the sand sample while there was variability in cloud cover during the measurements. As pointed out before, atmospheric conditions were not ideal during most of the campaign so it is difficult to assess the reason for the emissivity increase shown in Fig. 10. One option would be to repeat the experiment in ideal atmospheric conditions (i. e., with completely clear skies) but with variable LST to check if the emissivity remains constant with time. However, it is out of our possibilities in the present study and it is considered as a future work.

4.3. LST uncertainty analysis

An uncertainty analysis considering all the error sources affecting the LST retrieval was conducted following the same guidelines as in Section 2.4. Part of the LST uncertainty comes from the radiometer itself, therefore the error sources from Table 4 were taken into account again. In addition, the following error sources were considered.

- Target emissivity and sky downwelling radiance: We used the emissivity uncertainty values for B2 (the band where LST is obtained) given in Table 5. As mentioned before, the sky radiance was rather variable during the experiment, showing sky brightness temperatures in B2 ranging from -7 to -27 °C, which is roughly equivalent to a variation of ± 15% in sky downwelling radiance. This uncertainty bound also includes radiometer calibration errors at low temperatures, and the effect of self-emission of the gold panel used for the measurement of L_i^{sky}, which is lower than 5% according to Garcia-Santos et al. (2013). The impact of both emissivity and sky radiance uncertainties on LST was assessed through Eq. (10).

- Angle of view from nadir: An uncertainty of 2.5° in zenith angle was considered for the analysis, which results in emissivity uncertainty of 0.0003 at observation angle of 25° from nadir (García-Santos et al., 2012).

- Atmospheric absorption and emission: Atmospheric transmittances and upwelling radiances in the path length between the sample and the radiometer (height of 2.5 m and observation angle of 25° from nadir) were simulated with the MODTRAN 5 radiative model (Berk et al., 2006) using standard summer atmospheric conditions.

Results for each error source are shown in Table 7 for the soil sample, which yielded the largest total LST uncertainty (0.64 K). Clearly, the total LST error was practically determined by the uncertainty in the target emissivity and sky radiance that was the largest error source (0.63 K for soil). The magnitude of this effect depends on the sample, the minimum value being 0.46 K for clover (total LST uncertainty of 0.47 K) due to lower emissivity uncertainty and LST values in this case. Moreover, the impact of emissivity uncertainty is much larger than that of the sky radiance due to the high emissivity values in band B2 for all samples considered. Taking into account the uncertainty in the sky radiance alone (taken as 15% here), the resulting LST

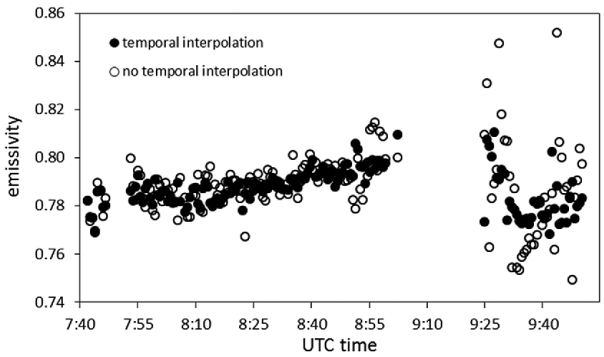

Fig. 10. Comparison of emissivity values retrieved in narrow band B6 for the sand sample when the temporal interpolation was applied and when it was not applied.

Table 7
Uncertainty analysis of LST measured by the CE2 radiometer for the soil sample considering the different error sources (see text). RSS is the root sum square, and the total RSS represents the standard uncertainty of LST, with coverage factor k = 1.

Uncertainty Contribution	Type A (K)	Type B (K)
Repeatability of measurement	0.03	
Reproducibility of measurement	0.06	
Primary calibration		0.05
Linearity of radiometer		0.06
Correction of calibration drift		0.05
Ambient temperature fluctuations		0.04
Target emissivity and sky radiance		0.63
Angle of view from nadir		0.02
Atmospheric absorption and emission		0.02
RSS	0.07	0.56
Total RSS	**0.64**	

uncertainty was only between 0.1 and 0.2 K depending on the sample, whereas the impact of emissivity error alone ranged between 0.4 and 0.6 K.

5. Conclusions

The validation of satellite LST products requires accurate and precise ground measurements performed in thermally homogeneous land covers. In this paper we addressed the two main error sources in ground LST measurements, which are radiometer calibration and uncertainty in target emissivity. Ground radiometers must be calibrated with reference to traceable SI standards in the temperature range of interest. The CEOS 2009 and ESA's FRM4STS 2016 experiments provided the framework for such calibration experiments against NPL reference radiometers and blackbodies, as well as an opportunity for harmonising methods and protocols for international groups involved in ground LST measurements. On the other hand, emissivity is not usually known in advance for land surface targets; therefore it should be measured in the field for the spectral band used by the radiometer for each cover type considered. A detailed uncertainty analysis including all error sources in the LST measurement should be provided together with the ground LST.

The detector of the CE-312 radiometer operates at ambient temperature, but the effect of the radiance from the detector's cavity on the target radiance is corrected by measuring the detector's temperature with a PRT and taking two radiance measurements, one with the radiometer aperture closed with a gold-coated mirror and the other with the aperture open to the target. However, due to the decrease of the detector's sensitivity with time, it is necessary to re-calibrate the CE-312 measurements; otherwise there could be errors up to ± 0.5 K for target versus detector temperature differences of ± 20 K. Linear re-calibration equations (e.g., Eq. 7) were used to this end, with coefficients obtained from laboratory measurements against the P80 P blackbody source in the temperature range 0–50 °C. The P80 P blackbody was in turn calibrated against the NPL reference AMBER radiometer in the 2009 and 2016 comparisons, showing long-term stability and good accuracy (0.05 K) in the aforementioned range when the correction for non-unity in blackbody emissivity (Eq. 9) was applied. Using the re-calibration equations derived with the P80 P blackbody shortly before the FRM4STS 2016 comparison, the two CE-312 radiometers showed rmsd ranging between 0.1 and 0.2 K (depending on the band) with respect to the NPL reference blackbody in the 0–45 °C range, which is the most useful for LST measurements. If only the standard calibration was applied, rmsd values would be between 0.2 and 0.4 K. It is therefore recommended to perform calibration experiments yearly to correct for calibration drifts. Outside of the above mentioned temperature range, the CE-312 radiometers could show larger biases (in excess of 1 K for certain bands at -30 °C) and non-linearity effects, especially for sub-zero temperatures corresponding to sky radiance measurements. Fortunately, the impact of sky radiance errors on the retrieved LST is rather small for samples with high emissivity.

Thanks to the multiband capability of the CE-312 radiometers, the TES method can be applied to ground measurements to simultaneously retrieve LST and band emissivities in the field. This was done in the FRM4STS LST comparison for five different samples. Although conditions were not ideal for field LST measurements due to changing cloud cover, the derived emissivity values were reasonable according to the nature of the covers considered (Salisbury and D'Aria, 1992; Rowan and Mars, 2002). However, it was not possible to validate the TES emissivities against independent emissivity measurements for the FRM4STS samples in the same conditions. Results showed that long wavelength TIR bands (i.e., 10–12 μm) yielded the highest emissivity values with small variation among samples, thus being the most suitable for LST retrieval. The uncertainty of retrieved emissivities in band B2 (10.9–11.7) ranged from 0.011 to 0.014 for the five samples, being larger for bands B4-B6 located in the 8.3–9.3 μm range (up to 0.02 in band B6, 8.3–8.6 μm) were emissivity varied considerably among samples (roughly from 0.80 for sand to 0.97 for clover). A detailed LST uncertainty analysis was performed, showing that emissivity was the largest source of error and total LST uncertainties ranging between 0.5 K (clover) and 0.6 K (soil). This stresses the need for accurate emissivity estimations for the different ground covers used for field LST measurements.

Acknowledgments

Financial support was obtained from research projects CGL2015-64268-R and CGL2013-46862-C2-1-P (Ministerio de Economía y Competitividad), the "Juan de la Cierva" (FJCI-2015-24876) Research Contract of Dr. Galve and the "Torres Quevedo" program through the Spanish Government under Contract PTQ-16-08578 of Dr. García-Santos. We thank the anonymous reviewers, who helped to improve the manuscript.

References

Baldridge, A.M., Hook, S.J., Grove, C.I., Rivera, G., 2009. The ASTER spectral library version 2.0. Remote Sens. Environ. 113, 711–715.
Barker-Snook, I., Theocharous, E., Fox, N.P., 2017. 2016 Comparison of IR Brightness Temperature Measurements in Support of Satellite Validation. Part 2: Laboratory Comparison of Radiation Thermometers. NPL REPORT ENV 14. National Physical Laboratory, Teddington, UK.
Berk, A., Anderson, G.P., Acharya, P.K., Bernstein, L.S., Muratov, L., Lee, J., Fox, M., Adler-Golden, S.M., Chetwynd, J.H., Hoke, M.L., Lockwood, R.B., Gardner, J.A., Cooley, T.W., Borel, C.C., Lewis, P.E., Shettle, E.P., 2006. MODTRAN5: 2006 update. Proceedings of SPIE, vol. 6233.
Chu, B., Machin, G., 1999. A low-temperature blackbody reference source to -40 °C. Meas. Sci. Technol. 10, 1–6.
García-Santos, V., Valor, E., Caselles, V., Mira, M., Galve, J.M., Coll, C., 2013. Evaluation of different methods to retrieve the hemispherical downwelling irradiance in the thermal infrared region for field measurements. Ieee Trans. Geosci. Remote. Sens. 51 (4), 2155–2165 Apr 2013.
García-Santos, V., Valor, E., Caselles, V., Burgos, M.Á., Coll, C., 2012. On the angular variation of thermal infrared emissivity of inorganic soils. J. Geophys. Res. 117, D19116. https://doi.org/10.1029/2012JD017931. 2012.
Gillespie, A.R., Matsunaga, T., Rokugawa, S., Hook, S.J., 1998. Temperature and emissivity separation from advanced spaceborne thermal emission and reflection radiometer (ASTER) images. Ieee Trans. Geosci. Remote. Sens. 36, 1113–1125.
Göttsche, F.-M., Olesen, F.S., Trigo, I.F., Bork-Unkelbach, A., Martin, M.A., 2016. Long term validation of land surface temperature retrieved from MSG/SEVIRI with continuous in-situ measurements in Africa. Remote Sens. (Basel) 8 (5), 1–27 n° 410.
Guillevic, P., Göttsche, F., Nickeson, J., Hulley, G., Ghent, D., Yu, Y., Trigo, I., Hook, S., Sobrino, J.A., Remedios, J., Román, Mi, Camacho, F., 2017. Land Surface Temperature Product Validation Best Practice Protocol, Version 1.0 - October, 2017. Committee on Earth Observation Satellites Working Group on Calibration and Validation, Land Product Validation Subgroup.
Hook, S.J., Vaughan, R.G., Tonooka, H., Schladow, S.G., 2007. Absolute radiometric in-flight validation of mid infrared and thermal infrared data from ASTER and MODIS on the Terra spacecraft using the Lake Tahoe, CA/NV, USA, automated validation site. IEEE Trans. Geosci. Remote Sens. 45, 1798–1807.
Hulley, G., Hook, S., 2009. The North American ASTER land surface emissivity database (NAALSED) version 2.0. Remote Sens. Environ. 113, 1967–1975.

JCGM, 2008. Evaluation of measurement data – guide to the expression of uncertainty in measurement, Joint Committee for Guides in Metrology. Report JCGM 100 2008.

Legrand, M., Pietras, C., Brogniez, G., Haeffelin, M., Abuhassan, N.K., Sicard, M., 2000. A high-accuracy multiwavelength radiometer for in situ measurements in the thermal infrared. Part I: characterization of the instrument. J. Atmos. Ocean Techn. 17, 1203–1214.

Li, Z.-L., Tang, B.-H., Wu, H., Ren, H., Yan, G., Wan, Z., Trigo, I.F., Sobrino, J.A., 2013. Satellite-derived land surface temperature: current status and perspectives. Remote Sens. Environ. 131, 14–37.

Martin, M., Göttsche, F., 2016. Satellite LST Validation Report. Available online at. DUE Globtemperature Project. http://www.globtemperature.info/index.php/public-documentation/deliverables-1/117-validation-report-del12.

Mira, M., Schmugge, T.J., Valor, E., Caselles, V., Coll, C., 2009. Comparison of thermal emissivities retrieved with the two-lid box and TES methods with laboratory spectra. Ieee Trans. Geosci. Remote. Sens. 47 (4), 1012–1021.

Niclòs, R., Pérez-Planells, L., Coll, C., Valiente, J.A., Valor, E., 2018. Evaluation of the S-NPP VIIRS land surface temperature product using ground data acquired by an autonomous system at a rice paddy. Isprs J. Photogramm. Remote. Sens. 135, 1–12 2018.

Rowan, L.C., Mars, J.C., 2002. Lithologic mapping in the Mountain Pass, California area using advanced spaceborne thermal emission and reflection radiometer (ASTER) data. Remote Sens. Environ. 84 (3), 350–366.

Rubio, E., Caselles, V., Coll, C., Valor, E., Sospedra, F., 2003. Thermal-infrared emissivities of natural surfaces: improvements on the experimental set-up and new measurements. Int. J. Remote Sens. 24 (24), 5379–5390.

Salisbury, J.W., D'Aria, D.M., 1992. Emissivity of terrestrial materials in the 8-14 μm atmospheric window. Remote Sens. Environ. 42, 83–106.

Sicard, M., Spyak, P.R., Brogniez, G., Legrand, M., Abuhassan, N.K., Pietras, C., Buis, J.P., 1999. Thermal infrared field radiometer for vicarious cross-calibration: characterization and comparisons with other field instruments. Opt. Eng. 38 (2), 345–356.

Tang, B.-H., Shao, K., Li, Z.-L., Wu, H., Nerry, F., Zhou, G., 2015. Estimation and validation of land surface temperatures from Chinese second-generation polar orbitFY-3A VIRR data. Rem. Sens. 7, 3250–3273. https://doi.org/10.3390/rs70303250.

Theocharous, E., Fox, N.P., 2010. CEOS Comparison of IR Brightness Temperature Measurements in Support of Satellite Validation. Part II: Laboratory Comparison of the Brightness Temperature of Blackbodies. NPL REPORT OP4. National Physical Laboratory, Teddington, UK.

Theocharous, E., Fox, N.P., Sapritsky, V.I., Mekhontsev, S.N., Morozova, S.P., 1998. Absolute measurements of black-body emitted radiance. Metrologia 35, 549–554.

Theocharous, E., Usadi, E., Fox, N.P., 2010. CEOS Comparison of IR Brightness Temperature Measurements in Support of Satellite Validation. Part I: Laboratory and Ocean Surface Temperature Comparison of Radiation Thermometers. NPL REPORT OP3. National Physical Laboratory, Teddington, UK.

Theocharous, E., Barker Snook, I., Fox, N.P., 2017a. 2016 Comparison of IR Brightness Temperature Measurements in Support of Satellite Validation. Part 1: Blackbody Laboratory Comparison. NPL REPORT ENV 12. National Physical Laboratory, Teddington, UK.

Theocharous, E., Barker Snook, I., Fox, N.P., 2017b. 2016 Comparison of IR Brightness Temperature Measurements in Support of Satellite Validation. Part 4: Land Surface Temperature Comparison of Radiation Thermometers. NPL REPORT ENV 13. National Physical Laboratory, Teddington, UK.

Anexo I

Evaluation of Six Directional Canopy Emissivity Models in the Thermal Infrared Using Emissivity Measurements

El siguiente trabajo fue publicado en Remote Sensing en diciembre del 2019. Esta revista tiene un factor de impacto de 4,51 y ocupa la posición 9 de 30 revistas en la categoría Remote Sensing según Journal Citation Reports en la edición de 2019.

remote sensing

MDPI

Article

Evaluation of Six Directional Canopy Emissivity Models in the Thermal Infrared Using Emissivity Measurements

Lluís Pérez-Planells *, Enric Valor, Raquel Niclòs, César Coll, Jesús Puchades and Manuel Campos-Taberner

Department of Earth Physics and Thermodynamics, Faculty of Physics, University of Valencia, E-46100 Burjassot, Spain; enric.valor@uv.es (E.V.); Raquel.Niclos@uv.es (R.N.); cesar.coll@uv.es (C.C.); jesus.puchades@uv.es (J.P.); manuel.campos@uv.es (M.C.-T.)

* Correspondence: lluis.perez@uv.es

Received: 18 November 2019; Accepted: 12 December 2019; Published: 14 December 2019

check for updates

Abstract: Land surface temperature (LST) is a fundamental physical quantity in a range of different studies, for example in climatological analyses and surface–atmosphere heat flux assessments, especially in heterogeneous and complex surfaces such as vegetated canopies. To obtain accurate LST values, it is important to measure accurately the land surface emissivity (LSE) in the thermal infrared spectrum. In the past decades, different directional emissivity canopy models have been proposed. This paper evaluates six radiative transfer models (FR97, Mod3, Rmod3, 4SAIL, REN15, and CE-P models) through a comparison with in situ emissivity measurements performed using the temperature-emissivity separation (TES) method. The evaluation is done using a single set of rose plants over two different soils with very different spectral behavior. First, using an organic soil, the measurements were done for seven different observation angles, from 0° to 60° in steps of 10°, and for six different values of leaf area index (LAI). Taking into account all LAIs, the bias (and root mean square error, RMSE) obtained were 0.003 (±0.006), −0.004 (±0.005), −0.009 (±0.011), 0.005 (±0.007), 0.004 (±0.007), and 0.005 (±0.007) for FR97, Mod3, Rmod3, 4SAIL, REN 15, and CE-P models, respectively. Second, using an inorganic soil, the measurements were done for six different LAIs but for two different observation angles: 0° and 55°. The bias (and RMSE) obtained were 0.012 (±0.014), 0.004 (±0.007), −0.020 (±0.035), 0.016 (±0.017), 0.013 (±0.015), 0.013 (±0.015) and for FR97, Mod3, Rmod3, 4SAIL, REN15, and CE-P models, respectively. Overall, the Mod3 model appears as the best model in comparison to the TES emissivity reference measurements.

Keywords: angular dependence; canopy; emissivity; land surface temperature; thermal infrared

1. Introduction

Land surface temperature (LST) is a fundamental physical quantity in a range of diverse studies on physical phenomena, such as climatological analyses, surface-atmosphere heat energy interactions (e.g., evapotranspiration), to mention some examples [1,2]. Atmospheric and surface emissivity corrections are the main factors that affect an accurate retrieval of LST for data acquired from satellite sensors in the thermal infrared spectrum (TIR). Then, a precise characterization of the land surface emissivity (LSE) is important for the LST retrieval [3]. Moreover, the emissivity spectrum is a characteristic feature of each surface, so it could be used to differentiate between different soil classes [4,5], vegetated species [6,7], and other surfaces, such as inland waters or manmade materials.

The emissivity of homogeneous surfaces such as bare soils and rocks is relatively well-known. A number of previous works have analyzed the dependence of soil emissivity on viewing angle [8–10]

and soil moisture [11–13] from an empirical perspective. Different theoretical models based on the Mie theory have been proposed to predict the emissivity of these kind of surfaces considering the refraction index, the size particle distribution, etc., [14,15] that have been recently compared with laboratory data [16,17].

However, for heterogeneous surfaces the emissivity modeling is a more challenging point because of its structural complexity. This difficulty is found over canopy areas. For canopy areas, the emissivity modeling is affected by the interaction of the surface-leaving radiance and the plant elements, and between the different layers of the plant. For that, it is necessary to consider the multiple reflections that take place inside the canopy when the emissivity is being modeled. Different models that estimate the directional canopy emissivity can be found in the literature of the last decades [18]. Mainly, these models can be classified in three types: bidirectional reflectance distribution function models, BRDF [19], geometrical models, GM [20,21], and radiative transfer models, RTM [22–25]. BRDF models make use of a linear combination of defined kernels in order to obtain the directional-hemispherical reflectance, which is later used to obtain the directional emissivity by applying the Kirchhoff's law. GMs are based on the assessment of the proportions of the different parts of the canopy actually seen at the instrument viewpoint. To apply the GMs, it is required the prior knowledge of the dimension of the canopy elements viewed by the sensor. With that, the emissivity is estimated taking into account the contribution of each one of the elements to the total measured radiance. Lastly, RTMs obtain the directional emissivity from the simulation of the radiative interaction with the different components of the canopy at the different layers. It is used the directional gap frequency, which is based on the leave density function, in order to estimate the radiance at the top of the canopy cover and, then, the emissivity. These models differ from the GMs in the fact that the canopy is not considered as an opaque medium.

In this work, the different RTMs proposed by François et al. in [22] (FR97 model), François in [23] (Mod3 model), Shi in [26] (Rmod3 model), Ren et al. in [27] (REN15 model), and Cao et al. in [28] (CE-P model) are analyzed. Also, the 4SAIL (scattering by arbitrarily inclined leaves) [25] is used in this study, since it is extensively used as a reference for other simpler algorithms. Different authors compared simulated emissivity values obtained with these models in order to analyze the emissivity spectrum for various leaf area index (LAI) values over a canopy. For example, Sobrino et al. [29] determined that for the FR97 model, the emissivity increases with the observation angle for LAI values lower or equal to 1.0 m^2/m^2. However, for LAI values higher than 1.0 m^2/m^2, the emissivity decreases when the observation angle increases. Ren et al. [27] compared the differences between FR97 and Mod3 models with simulated values obtained with the 4SAIL model, which is used as a reference. It is concluded that, since the Mod3 model does not take into account the multiple interactions between the different layers of vegetation, the emissivity values obtained with this method are lower than those obtained with the FR97 model, but both underestimate the values given by the 4SAIL model. Moreover, Ren et al. [27] proposed new values for the cavity effect term of the FR97 model to make their values closer with those given by 4SAIL, especially for high observation zenith angles. Finally, Cao et al. [28] compared simulated measurements of the CE-P with 4SAIL simulations, obtaining absolute differences lower than 0.002 between both models.

To our knowledge, there are no previous works that have analyzed the variation of canopy emissivity with observation angle using in situ measurements with real canopies. However, some studies have analyzed the emissivity of canopies based on in situ nadir measurements. For example, Neinavaz et al. [30] found a relationship between the emissivity and LAI of different canopies for nadir hyperspectral measurements; this relationship allowed obtaining the LAI of a plant from a combination of emissivity measurements in different spectral bands provided that LAI was not very high. Also, in Neinavaz et al. [31], at-nadir canopy emissivity spectra of different species were analyzed, resulting that in the spectral range between 8 ĵim and 10 ĵim the discrimination among species is more accurate. Moreover, it was found that emissivity values increase with increasing LAI, but from LAI values of 4 m^2/m^2 the emissivity takes a nearly constant value for higher LAI values.

Thus, the objective of this paper is twofold. First, to use a set of in situ emissivity measurements acquired on a canopy at different viewing observation conditions and for LAI values in the range 0.5 m^2/m^2 to 3.3 m^2/m^2, for studying the emissivity change with viewing angle and vegetation amount. Second, to compare and evaluate the four RTM-type algorithms described above using these in situ data, in order to investigate their predictive power in the assessment of canopy emissivity. All emissivity measurements were acquired using the temperature-emissivity separation (TES) algorithm [32] adapted to multiband ground radiometers CIMEL Electronique CE312-2 [33].

2. Experimental Setup and Data Processing

The experiment took place at the Facultat de Física of the Universitat de València, Spain (13°30′25″ N, 0°25′13″ W), using a goniometer placed on the roof of the building. It was carried out in two different periods, first on the months of October and November, 2017, and second on four consecutive days, from 29 May to 1 June 2019. For both periods the measurements were made on cloudless days. The same plant species (a set of rose plants) were used in the two periods, but different soil backgrounds were selected for each case: organic soil in the first period and inorganic soil (sand) in the second one. A six-band Cimel Electronique CE312-2 radiometer [34] was used to make the measurements over the sample of the study. In the first period, seven different observation angles, varying from 0° to 60° in steps of 10°, were considered. In order to reduce the LAI values of the sample, the plant leaves were cut off when the set of measurements at different observation angles was done. The measurements were repeated for six different values of LAI ranging from 2.8 m^2/m^2 to 0.5 m^2/m^2, which were measured with Android app Pocket-LAI [35]. For the second period, a similar procedure was carried out. This time, we considered observation angles of nadir and 55°, with LAI measured values ranging from 3.3 m^2/m^2 to 0.6 m^2/m^2. During the second experiment, the number of observation angles was reduced because of two reasons: First, in García-Santos et al. [10] it was found that the decrease of emissivity on sand sample was observed for observation angles higher than 40°. Second, no significant variation with angle was observed in the emissivity measurements during the first period. Then, the measurements were repeated with just two observation angles because no significant differences with angle were expected for lower observation angles.

In order to assure enough measurements for adequate statistics, the number of radiance measurements was of 15 for each band, observation angle, and LAI value. Therefore, a total of 630 measurements of the sample for each band for the first period and 180 measurements for each band for the second period were used in this study. The height of the radiometer was adjusted for each observation angle in order to assure a constant field of view of 0.048 m^2. Also, a second six-band Cimel CE312-2 radiometer was used to measure the hemispherical downwelling radiance, simultaneously to each measurement, making use of a Labsphere golden panel with high reflectivity in the TIR [36]. The experimental setup is shown in Figure 1.

2.1. Cimel ElectroniqueCE312-2

Sample radiances and downwelling hemispheric radiances were measured using two Cimel Electronique CE312-2 radiometers. This field instrument focuses its six spectral bands in the TIR spectrum, covering from 8 to 13 μm. Its first band is a wide band covering all the wavelength range (band 1: 8–13.3 μm), whereas the other five bands are distributed along this spectral range: 10.9–11.7 μm (band 2), 10.2–11.0 μm (band 3), 9.0–9.3 μm (band 4), 8.5–8.9 μm (band 5), and 8.3–8.6 μm (band 6). These five narrow bands are coincident with the ASTER sensor TIR bands. The CE312-2 radiometer has an accuracy of 0.2 K according to the manufacturer and a field of view of 10°. Moreover, both radiometers were calibrated against the National Physical Laboratory (NPL) ammonia heat-pipe reference blackbody during the Fiducial Reference Measurements for validation of surface temperature from satellites (FRM4STS) experiment in June 2016. It was obtained a root mean square error (RMSE) between 0.06 and 0.10 K for bands 1 to 3 and a RMSE between 0.13 and 0.23 K for bands 4 to 6 [33,37].

Figure 1. Experimental setup established for the radiometric measurements.

In order to retrieve emissivity values from sample radiance measurements, it is required to measure the hemispheric downwelling radiance. For that reason, it was measured over an Infragold Reflectance Target (IRT-94-100) made by Labsphere [36]. This target is a high diffuse reflectivity gold panel, with reflectivity values close to 0.92 for the six spectral bands of the CE312-2 radiometer [38].

2.2. TES Algorithm

The TES method [31] was first devised and extensively applied to ASTER sensor [39–41], but because of the similarities between the ASTER and the CE312-2 spectral bands, it can also be applied to the latter using the same empirical equations for both instruments [33,42]. The TES algorithm starts with the normalized emissivity method (NEM) [43] using the at-surface and the downwelling radiance measurements taken by the five ASTER TIR channels. NEM calculates five different temperatures assuming a common initial emissivity guess value, typically 0.990. The highest temperature value is assumed as a first-guess land surface temperature, which is known as T_{NEM}. With the obtained T_{NEM}, the so-called NEM emissivity ($\varepsilon_{NEM,i}$) is retrieved for each spectral band using the corresponding at-surface and downwelling radiances. Dividing each $\varepsilon_{NEM,i}$ by the mean value of the NEM emissivities, the temperature-independent β_i index is calculated. Next, an empirical relation relating the minimum emissivity ε_{min} with the maximum-minimum emissivity difference (MMD) is used to obtain ε_{min}. For that, the MMD is obtained from the difference of the maximum and minimum value of β_i index. To avoid possible systematic errors in the TES results, the empirical MMD-ε_{min} relationship proposed by Hulley and Hook [44] was used, which was obtained using different samples of vegetation (with different covers), rocks, soils, water, and snow, since using a relationship not appropriate for vegetation samples could provide significant errors. Additionally, the CE312-2 radiometer has a relatively low noise equivalent difference of temperature (NEΔT). This fact minimizes the possibility of obtaining MMDs higher than usual, which could result also in systematic errors. Lastly, using both ε_{min} and β_i, the emissivity values are obtained for the five CE312-2 spectral bands.

2.3. Pocket-LAI

Leaf area index (LAI) is a good descriptor of vegetation density. It is defined as half of the total green leaf area per unit projected horizontal ground surface area [45], in units of m^2/m^2. Two methods

are known for LAI estimation. Direct methods make use of destructive procedures on the plant for the measurement of LAI; indirect methods take advantage of optical and radiance analyses to retrieve the LAI [35]. For the latter methods, the instruments which make use of these techniques, are based on the analyzing of the gap fraction by means of radiance measurements at different angles (e.g., LICOR-2000 instrument) or by means of optical properties provided by hemispherical lenses (e.g., hemispherical photography cameras).

Pocket-LAI is a smartphone code that calculates LAI of the canopy using the mobile camera. It is based on the approximation of the projection function to 0.5 for a viewing angle of 57.5°, which is used in the estimation of the gap fraction. Then, from the inversion of the gap fraction equation, the LAI value is obtained [46,47]. Therefore, by making a picture at 57.5° from ground to the leaves (looking upwards), using the mobile accelerometer sensor to assure the viewing angle, Pocket-LAI Android App makes possible to estimate the LAI of the plant.

This inexpensive technique for LAI measurements is analyzed in different studies over a diverse variety of vegetated areas, comparing the results with those obtained with other instruments like AccuPAR ceptometer, LICOR-2000 or digital hemispherical photography (DHP). Overall, Pocket-LAI app values show a good agreement with the other instruments. Francone et al. [48] compared Pocket-LAI app values with an AccuPAR ceptometer over maize and grassland fields, obtaining differences lower than 0.5 m^2/m^2. Orlando et al. [49] evaluated Pocket-LAI over vineyard, using as a reference a DHP and direct methods. The accuracy obtained in these cases was ± 0.57 m^2/m^2 when the reference was DHP measurements, and ± 0.16 m^2/m^2 when the reference was a direct method. Similarly, Campos-Taberner et al. [47] evaluated the Pocket-LAI values over rice fields using a DHP and a LICOR-2000, obtaining RMSE values of ± 0.67 m^2/m^2 using the DHP, and of ± 0.35 m^2/m^2 using the LICOR-2000. Nevertheless, a disagreement between Pocket-LAI and DHP measurements was found over conifers by Orlando et al. [50], where a correlation coefficient of 0.15 was obtained in the comparison of both instruments. Consequently, it is determined the good performance of the Pocket-LAI app for the LAI retrieval over broadleaved plants, as it is the case of the rose plant leaves used in this study, but not over needle-shaped leaves. Then, although no comparison with other instruments is done in this study for LAI measurements, it is considered that the data obtained from the pocket-LAI measurements is reliable within the uncertainties stated in the above mentioned studies.

2.4. Sample

During this study, we used two sets of twenty-seven rose plants set on an organic soil. The soil of the set used during the second period was covered with sand, which was separated from the organic soil by a piece of fabric, to avoid mixing the samples. They were located in a container with dimensions of 113 cm × 84 cm × 9 cm. During the first period, the plants were watered twice per week. However, in order to assure a constant value in soil emissivity during the study, the soil of the sample was re-covered using dry soil before each set of measurements. At the second period, because of the short time, the plants where watered before covering the organic soil with sand.

The plant and soils samples were selected for different reasons. First, when all the plants are planted together, they form a continuous canopy. The random distribution of rose plants leaves allows cutting off the leaves while controlling the plant structure as convenience to maintain a close uniform distribution during the measurements. Moreover, the rose plant stem is strong but fine enough to have a minimal influence in the canopy emissivity. Two different soils were chosen because of their different features on the spectral and angular emissivity variation. The organic bare soil has a low spectral and angular emissivity variation. The angular emissivity variation between nadir and 60° was measured, obtaining an emissivity decreasing of 0.01 for the 10–12 μm range and of 0.02 for the 8–9.5 μm range. However, the sand has a high spectral and angular emissivity variation, especially for the 8–9.5 μm range, which was measured by García-Santos et al. [10]. The emissivity decreasing observed for the sand was of 0.03 for the 10–12 μm range and of 0.06 for the 8–9.5 μm range.

The nadir emissivity of green leaves, dry organic bare soil (OBS), and sand (inorganic bare soil, IBS) for the five narrow bands of the CE312-2 radiometer, which are shown in Figure 2, are required to apply the canopy emissivity models in order to obtain the canopy emissivity. For that, a sample of cut off leaves and a sample of OBS and IBS were used to characterize its emissivity at nadir using twenty radiance measurements to apply the TES algorithm as described in Section 2.2. The standard deviation of the twenty measurements was taken as the emissivity uncertainty for each sample and spectral band.

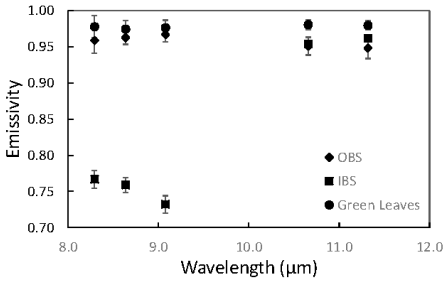

Figure 2. Band emissivity of green leaves, organic bare soil (OBS) and inorganic bare soil (IBS) measured in situ with the temperature-emissivity separation (TES) algorithm.

Figure 2 shows that the emissivity spectrum is nearly flat for green leaves, with an average value of 0.978 and a difference of 0.006 between the maximum and the minimum values. In contrast, we found lower emissivities for bare soils. For OBS, a difference of 0.018 was obtained between the maximum value and the minimum, with a maximum value of 0.967. In the case of IBS, the difference was up to 0.23, with a maximum value of 0.962. The expected emissivity differences between both soil samples emissivities at 8–9.5 μm spectral range, which are between 0.19 and 0.24, are also observed in Figure 2. Mean uncertainty for green leaves and OBS is ±0.010, and it is ±0.008 for IBS.

3. Models

3.1. FR97 Model

François et al. [22] proposed a physical model to obtain canopy emissivity, which is based on the RTM proposed by Prévot in [51]. The FR97 model aims at the retrieval of canopy components temperature. For that purpose, the directional canopy emissivity is included as a parametric equation. According to François et al. [22], the emissivity must react to the modification of the vegetation distribution within the canopy; consequently, the parametric equation is related with LAI and leaf inclination distribution function (LIDF), the emissivity of soil and leaves and the viewing zenith angle (VZA). Therefore, with these considerations, the directional canopy emissivity (ε_c) is given as:

$$\varepsilon_c(\theta) = 1 - k_s(1 - \varepsilon_s) - k_l(1 - \varepsilon_l) \quad (1)$$

where k_s and k_l are soil and leaf coefficients, and ε_s and ε_l are the soil and leaf emissivity, respectively, and θ is the VZA. The coefficients k_s and k_l are dependent on LAI, directional gap frequency ($b(\theta)$), and the shielding hemispherical factor (σ_f). These coefficients are defined as $k_s = b(\theta)(1 - \sigma_f)$ and $k_l = \alpha\left(1 - b(\theta)\left(1 - \sigma_f\right)\right)$, where α is the cavity effect coefficient. François et al. [22] defined the α coefficient as a parameter dependent on the limit emissivity (ε_{lim}), obtained for high LAI values, and the leaf emissivity:

$$\alpha = \frac{1 - \varepsilon_{lim}}{1 - \varepsilon_l} \quad (2)$$

Moreover, François et al. [22] analyzed that α is not dependent on LAI, but it should be dependent on the VZA and the LIDF. In the expression given in [22], α is estimated from the limit emissivity, which is the emissivity to which it tends when the LAI value increases. In the case of a spherical LIDF, the α coefficient is calculated and tabulated in [23] for each VZA.

Also, for a spherical LIDF, considering a random dispersion, $b(\theta)$ is given as $b(\theta) = e^{-0.5LAI/\cos(\theta)}$, while for these same conditions, according to François in [23], the shielding hemispherical factor could be approximated as $\sigma_f = 1 - e^{-0.825LAI}$.

Applying these expressions to Equation (1), the directional canopy emissivity defined by the FR97 model is finally given as:

$$\varepsilon_c(\theta) = 1 - b(\theta)\left(1-\sigma_f\right)(1-\varepsilon_s) - \alpha\left[1 - b(\theta)\left(1-\sigma_f\right)\right](1-\varepsilon_l) \quad (3)$$

3.2. Mod3 Model

The Mod3 was proposed by François in [23]. It gives a parametric expression for the directional canopy emissivity, which 9is based on the canopy RTM proposed by Prévot in [51], as the FR97 model. It consists in a variation of the Mod2 model, which is described by Chehbouni et al. in [52]. This modification of the Mod2 model was justified by François in [23] arguing an incorrect consideration of the radiative interactions between the soil and the leaves, which was reflected in the expression that defines the directional canopy emissivity. For that reason, the shielding hemispherical factor was added in Mod3 model, which was not present in the previous model [23].

Therefore, the directional canopy emissivity is given by the Mod3 model according to the following expression:

$$\varepsilon_c(\theta) = 1 - [1 - b(\theta)](1-\varepsilon_l) - \frac{b(\theta)\left(1-\sigma_f\right)(1-\varepsilon_s)}{1-(1-\varepsilon_s)\sigma_f(1-\varepsilon_l)} \quad (4)$$

Then, the main difference between the FR97 model and the Mod3 model is the lack of a cavity effect term in the latter. In this model, it is not included the multiple scattering inside the vegetation, and it is just considered between the soil and vegetation components.

3.3. Rmod3 Model

In semiarid areas, it is quite common to find mixed pixel of bare soil and vegetation. The vegetation cover fraction (P_v) was introduced by Shi [26] with the intention of improving the Mod3 model for that areas with mixed pixels. Then, the Rmod3 model uses the P_v as an input in order to modify the Mod3 model.

The directional canopy reflectance obtained in the Mod3 model is weighted by the P_v in this model. Also, an additional term relating the bare soil emissivity and the fraction of the viewing of the sensor corresponding to bare soil, without vegetation above it. The parametric expression corresponding to the Rmod3 model is defined as:

$$\varepsilon_c(\theta) = 1 - P_v\left\{[1 - b(\theta)](1-\varepsilon_l) + \frac{b(\theta)\left(1-\sigma_f\right)(1-\varepsilon_s)}{1-(1-\varepsilon_s)\sigma_f(1-\varepsilon_l)}\right\} - (1-P_v)(1-\varepsilon_s) \quad (5)$$

3.4. SAIL Model

SAIL is a four stream RTM proposed by Verhoef et al. [53]. It expresses the scattering and extinction coefficients of the canopy in the visible and near infrared (VNIR) spectral regions by means of the LIDF, the leaf optical properties, and the observation geometry. It distinguishes between two direct fluxes, which are the incident solar flux and radiance in the viewing direction, and two diffuse fluxes, corresponding to the upward and downward hemispherical fluxes. Four lineal differential equations, which can be analytically solved, describe the interaction among the four fluxes and form the basis of this model [25].

The 4SAIL is an extended version of the SAIL RTM to the TIR described by Verhoef et al. in [25]. It is programmed and free delivered in Fortran language (available at http://teledetection.ipgp.jussieu.fr/prosail/). In this version, canopy emissivity can be obtained using the leaf and soil emissivity, the LAI and the VZA as inputs. Finally, the hemispherical-directional reflectivity of the canopy is given as an output, which is easily converted to canopy emissivity by applying the Kirchfoff's law.

3.5. REN15 Model

Ren et al. [27] observed that the α coefficient tabulated in [23] for the FR97 model was overestimated, yielding to differences between FR97 and 4SAIL model specially for large VZAs because of the cavity effect term. REN15 model updates the FR97 model by updating the cavity effect term. For that, the limit emissivity is estimated using the 4SAIL model. Then, α is calculated using Equation (2). Finally, canopy emissivity is estimated using the FR97 model Equation (3) with the α coefficient obtained by REN15.

For this study, α was obtained for the different VZAs and CE312-2 bands applying the REN15 model with the measured component emissivity values (see Section 2.4). As the limit emissivity depends only on the leaf emissivity, the same α values were used for both samples, with organic and inorganic soil.

3.6. CE-P Model

The new directional canopy emissivity model (CE-P model) based on spectral invariants was proposed by Cao et al. [28]. This model makes use of the recollision probability parameter (p) instead of the cavity effect parameter used in other models such as FR97 or REN15. The p parameter gives the probability that a photon interacts with a component after an interaction with another one. The p parameter is commonly used in the VNIR spectral range and it is extended to the TIR spectrum in the CE-P model. This parameter is given by $1 - e_u - e_d$, where e_u (e_d) is the upward (downward) escape probability [28]. As the previous models, the CE-P model is given as an analytical expression considering a homogeneous vegetation and an spherical LIDF. Then, the CE-P model emissivity is defined by Equation (6):

$$\varepsilon(\theta) = \frac{i_0\varepsilon_l}{1-p(1-\varepsilon_l)} + \frac{(1-i_0)(1-\varepsilon_s)i_0'\frac{\varepsilon_p}{1-p(1-\varepsilon_l)}}{1-r_{c2}^*(1-\varepsilon_s)i_0'} + \frac{i_0 r_{c1}^*(1-\varepsilon_s)i_0'\frac{\varepsilon_p}{1-p(1-\varepsilon_l)}}{1-r_{c2}^*(1-\varepsilon_s)i_0'} + \frac{(1-i_0)\varepsilon_s}{1-r_{c2}^*(1-\varepsilon_s)i_0'} + \frac{i_0 r_{c1}^*\varepsilon_s}{1-r_{c2}^*(1-\varepsilon_s)i_0'} \quad (6)$$

where i_0 is the directional intercept probability ($i_0 = 1 - b(\theta)$), i_0' is the hemispherical intercept probability $\left(i_0' = 1 - M\right)$, r_{c1}^* and r_{c2}^* are the forward and backward diffuse reflectance of the canopy, which are given by $(1 - \varepsilon_l)e_d/(1 - 1 - \varepsilon_l)p)$ and $(1 - \varepsilon_1)e_u/(1 - (1 - \varepsilon_l)p)$, respectively.

Different simplifications of this model are proposed in [28,54]; however, the authors recommend not to use the simplification for leaves (soil) emissivity lower than 0.94 (0.90). Then, since the sand emissivity is lower than this soil value, the complete model is used in this study with no simplifications.

4. Results

4.1. Leaf Area Index and Vegetation Cover Fraction Measurements

The LAI values required to apply the different models were obtained using Pocket-LAI App. For each LAI, obtained by cutting leaves of the rose plants used as sample, 36 pictures were taken in order to obtain the statistical values. Therefore, the value given for each LAI corresponds to the mean of these 36 pictures. These LAI values are shown in Table 1. Also, the uncertainty for each value is given. This uncertainty is calculated by the standard deviation of the 36 measurements.

Table 1. Leaf area index (LAI) and vegetation cover fraction (P_v) measured values required at the different models of the study to the sample with organic soil (OS) and inorganic soil (IS).

LAI (m^2/m^2)—OS	P_v—OS	LAI (m^2/m^2)—IS	P_v—IS
2.8 ± 0.4	0.95 ± 0.03	3.3 ± 0.5	0.98 ± 0.03
2.4 ± 0.4	0.90 ± 0.03	2.8 ± 0.3	0.96 ± 0.04
2.0 ± 0.3	0.83 ± 0.06	2.4 ± 0.3	0.91 ± 0.05
1.5 ± 0.2	0.77 ± 0.05	1.8 ± 0.3	0.81 ± 0.05
0.9 ± 0.2	0.57 ± 0.06	1.1 ± 0.2	0.62 ± 0.03
0.52 ± 0.12	0.41 ± 0.04	0.64 ± 0.07	0.44 ± 0.03

In order to calculate the P_v needed for Rmod3 model, six pictures were taken of the rose plants, covering the study sample uniformly, for each LAI. Then, the pixels corresponding to vegetation were distinguished by means of the selection of green pixels using image editing software. Finally, the P_v of each picture was obtained by dividing the quantity of green pixels by the total number of pixels. The results of the mean P_v value of the six pictures for each LAI, and its uncertainty obtained as the standard deviation, are also shown in Table 1.

4.2. Canopy Emissivity Variation with LAI at Nadir

The emissivities measured in situ with TES algorithm at nadir are compared in Figure 3 with those emissivities given by the six RTM for the different LAI quantities in the case of the organic soil. Figure 3 is composed of five graphs, each one corresponding to a spectral narrow band of the CE312-2 radiometer.

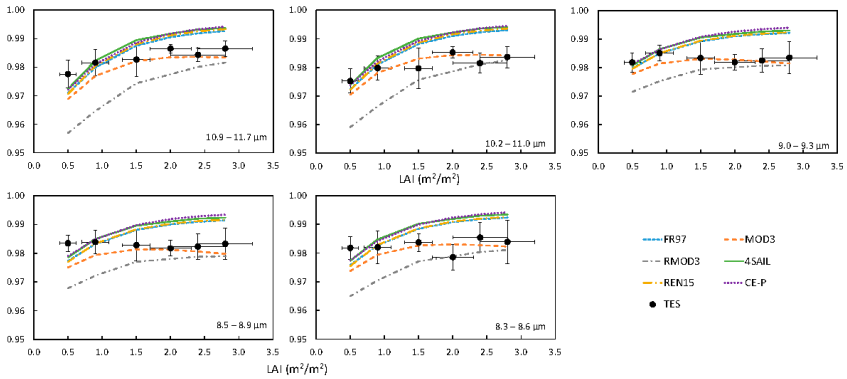

Figure 3. TES in situ nadir emissivity and emissivity values given by FR97, Mod3, Rmod3, REN15, CE-P, and 4SAIL models for nadir observation for different LAIs over the organic soil.

From Figure 3, it is observed that TES emissivity values range from 0.975 to 0.987. The lower values were found for LAI of 0.5 m^2/m^2 and in 10.2–11.0 µm, whereas the higher value was obtained for LAI of 2.8 m^2/m^2 in 10.9–11.7 µm. Also, the uncertainties observed for emissivity range from ±0.002 to ±0.008, whereas LAI uncertainties are those of Table 1.

Figure 4 shows the at nadir emissivity obtained from TES measurements and the emissivity estimated from the RTM for the case of the inorganic soil. In Figure 4, TES emissivity values range from 0.887 obtained for 9.0–9.3 µm to 0.984 obtained for 10.9–11.7 µm. The uncertainties found for each emissivity value range from ±0.002 to ±0.009, while LAI uncertainties are those in Table 1. The spectral

ci

range of 10–12 µm shows less variation with LAI (around 0.02) because of the soil emissivity is closer to the vegetation emissivity. However, the low emissivity of sand for 8–9.5 µm range causes a high variation in the emissivity with LAI. This variation has a higher slope for LAI < 2 m^2/m^2, where the difference of LAI has a major effect on emissivity. For LAI > 2 m^2/m^2, the emissivity trends to plateau, taking values close to the ε_{lim}.

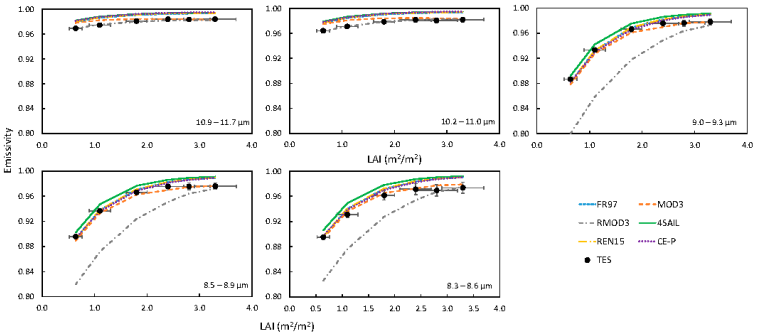

Figure 4. TES in situ nadir emissivity and emissivity values given by FR97, Mod3, Rmod3, REN15, CE-P, and 4SAIL models for nadir observation for different LAIs over the inorganic soil.

Because of the spectral variation of sand emissivity, the higher differences between the models and the TES emissivity were found for 8–9.5 µm range in Figure 4. While for 10–12 µm of the inorganic soil measurements, we found similar results to those obtained for the organic soil, because of the similar soil emissivity. In the latter case, FR97, 4SAIL, REN15, and CE-P gave similar results, with differences lower than 0.002 between them. However, these differences are up to 0.01 for the lower LAIs when the difference between soil and leaf emissivity increase (8–9.5 µm range), but they are reduced when the LAI increase. Mod3 model gives similar values to FR97 model for low LAIs, with a difference around 0.002, but they differ with LAI, giving differences up to 0.013, with similar differences for both soils. In the case of Rmod3 model, differences with the Mod3 model decrease with LAI, varying from 0.012 to 0.001 in the case of the organic soil and 10–12 µm range of the inorganic soil. But these differences range from 0.078 to 0.004 in the case of 8–9.5 µm with the inorganic soil, when the soil and leaf emissivity differs more.

The six models were compared with at-nadir TES emissivity. The statistical results are summarized in Tables 2 and 3 for the different LAI values. For the organic soil, differences between models with TES emissivity were lower. It is observed in Table 2 that, for LAI < 1.5 m^2/m^2, FR97, 4SAIL, REN15, and CE-P are the models with lower RMSE. However, for LAIs ≥ 1.5 m^2/m^2, Mod3 model shows the lowest RMSE. Also, the RMSE for Rmod3 model decreases with LAI, because of the soil term is reduced and the values are closer to the Mod3 model. In the overall analyses, where all LAIs and spectral bands are included, Mod3 model has the lowest bias and RMSE, but the values are close to the other models, with differences in RMSE lower than 0.005. Nevertheless, for the case of inorganic soil (Table 3) the Mod3 model gives the lowest RMSE for all LAIs, although for the lowest LAI (LAI = 0.64 m^2/m^2) the results are the same as those obtained with FR97 and REN15 models. 4SAIL RMSE values are slightly higher than those given by the FR97, REN15, and CE-P models. Moreover, despite of 10–12 µm on Figure 4 shows that Rmod3 is the closest model to the TES measurements, the emissivity of the Rmod3 model decrease considerably for 8–9.5 µm range, yielding to values far to those given by TES emissivity. This decreasing in the Rmod3 canopy emissivity is caused by the difference between the soil and leaf emissivity. In the overall analyses, as occurs with the organic soil, it is the Mod3 model which shows the lower bias and RMSE in comparison with TES emissivity. But in this case, the differences of the

Mod3 RMSE with the RMSE obtained for other models are higher, from 0.005 in the case of FR97 model to 0.036 in the case of Rmod3.

Table 2. Statistical values from the at-nadir comparison of the canopy emissivity models and TES algorithm for the different LAI measurements and for all bands with the organic soil.

LAI	FR97		MOD3		RMOD3		4SAIL		REN15		CE-P	
	bias	RMSE	bias	RMSE	bias	RMSE	bias	RMSE	bias	RMSE	bias	RMSE
0.5	−0.005	0.005	−0.007	0.007	−0.016	0.016	−0.003	0.004	−0.005	0.005	−0.003	0.004
0.9	−0.0001	0.0012	−0.003	0.004	−0.013	0.013	0.0019	0.002	0.0001	0.0011	0.0013	0.0017
1.5	0.006	0.006	0.000	0.002	−0.006	0.006	0.008	0.008	0.006	0.006	0.007	0.007
2	0.008	0.008	0.000	0.003	−0.004	0.006	0.009	0.009	0.008	0.009	0.009	0.010
2.4	0.008	0.009	−0.001	0.002	−0.003	0.004	0.010	0.010	0.009	0.009	0.010	0.010
2.8	0.008	0.008	−0.0019	0.003	−0.003	0.004	0.009	0.009	0.009	0.009	0.010	0.010
Overall	0.004	0.007	−0.002	0.004	−0.007	0.009	0.006	0.008	0.004	0.007	0.006	0.008

Table 3. Statistical values from the at-nadir comparison of the canopy emissivity models and TES algorithm for the different LAI measurements and for all bands with the inorganic soil.

LAI	FR97		MOD3		RMOD3		4SAIL		REN15		CE-P	
	bias	RMSE	bias	RMSE	bias	RMSE	bias	RMSE	bias	RMSE	bias	RMSE
0.64	0.003	0.009	0.001	0.009	−0.047	0.063	0.010	0.011	0.003	0.009	0.004	0.010
1.1	0.007	0.010	0.003	0.008	−0.039	0.053	0.013	0.014	0.007	0.010	0.006	0.010
1.8	0.008	0.009	0.001	0.005	−0.025	0.034	0.012	0.012	0.008	0.009	0.007	0.009
2.4	0.009	0.009	−0.001	0.004	−0.014	0.019	0.012	0.012	0.009	0.010	0.009	0.009
2.8	0.012	0.013	0.002	0.004	−0.005	0.008	0.014	0.015	0.013	0.013	0.012	0.013
3.3	0.012	0.013	0.001	0.003	−0.002	0.003	0.014	0.014	0.013	0.013	0.013	0.013
Overall	0.009	0.010	0.001	0.005	−0.022	0.036	0.013	0.013	0.010	0.011	0.009	0.011

4.3. Canopy Emissivity Variation with Viewing Angle for Different LAI Values

4.3.1. Organic Soil

The six directional canopy emissivity models were also compared with the TES emissivity measured for the seven different VZAs in the case of the organic soil, from 0° to 60° in steps of 10° and for the six LAI values given in Table 1 for this soil. In Figures 5–9, these comparisons are shown, each figure corresponding to one spectral narrow band of the CE312-2 radiometer. They show the emissivity given by the six models, as well as the emissivity measured by the CE312-2 radiometer with the TES algorithm.

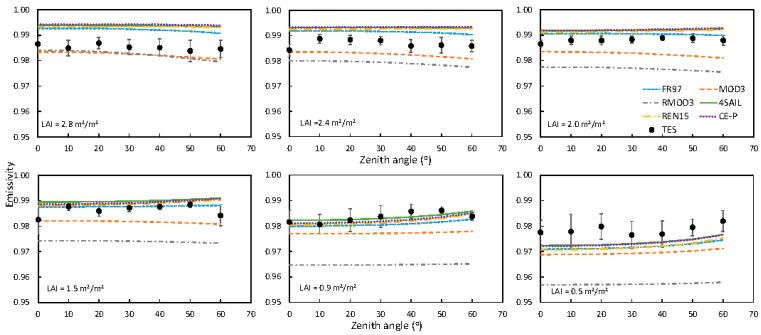

Figure 5. TES emissivity measurements and FR97, Mod3, Rmod3, 4SAIL, REN15, and CE-P models emissivity values at different zenith angles and LAI values for the CE312-2 radiometer 10.9–11.7 spectral band using an organic soil.

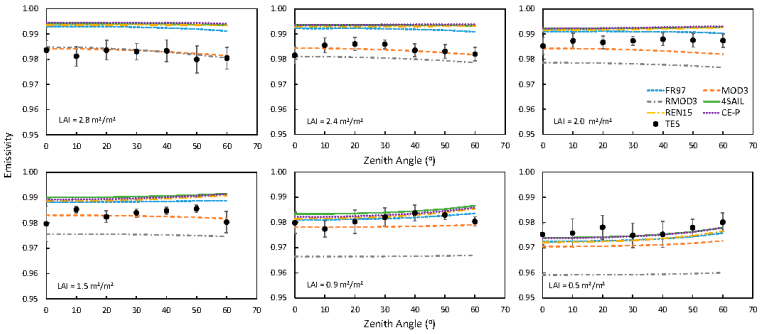

Figure 6. TES emissivity measurements and FR97, Mod3, Rmod3, 4SAIL, REN15, and CE-P models emissivity values at different zenith angles and LAI values for the CE312-2 radiometer 10.2–11.0 µm spectral band using an organic bare soil.

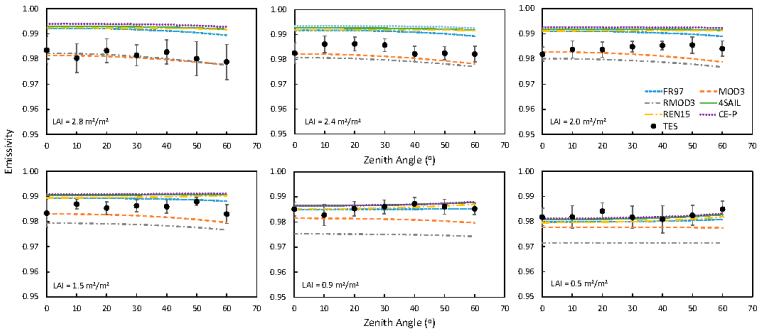

Figure 7. TES emissivity measurements and FR97, Mod3, Rmod3, 4SAIL, REN15, and CE-P models emissivity values at different zenith angles and LAI values for the CE312-2 radiometer 9.0–9.3 µm spectral band using an organic soil.

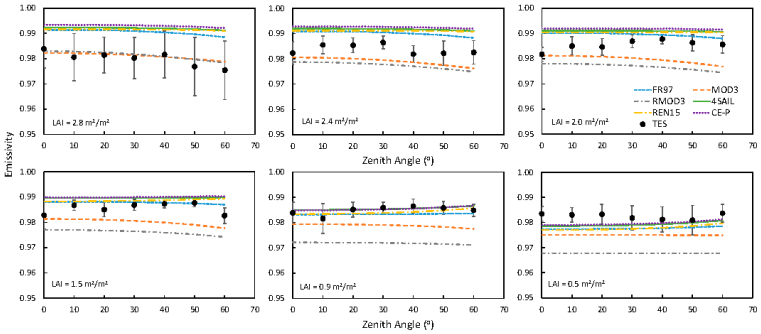

Figure 8. TES emissivity measurements, and FR97, Mod3, Rmod3, 4SAIL, REN15, and CE-P models emissivity values at different zenith angles and LAI values for the CE312-2 radiometer 8.5–8.9 µm spectral band using and organic soil.

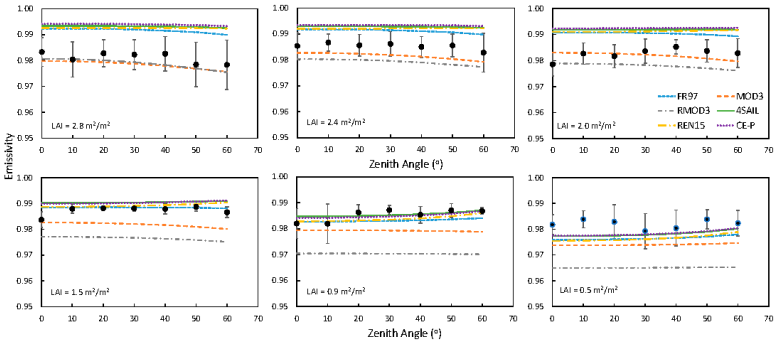

Figure 9. TES emissivity measurements and FR97, Mod3, Rmod3, 4SAIL, REN15, and CE-P models emissivity at different zenith angles and LAI values for the CE312-2 radiometer 8.3–8.6 μm spectral band using an organic soil.

Figures 5–9 show the emissivity values obtained with TES algorithm for the 5 CE312-2 spectral bands over the rose plants and the organic soil. The obtained values ranged from 0.975 to 0.989 depending on LAI, VZA, and spectral range. The mean uncertainty, obtained as the standard deviation of the measurements, was between ±0.003 (Figures 5 and 6) and ±0.005 (Figure 9).

From Figures 5–9, very little variation is observed with the VZAs in the range from 0° to 60°. Also, a slight fluctuation on the TES emissivities can be observed in some figures but it is within the measurement uncertainty. As for nadir observation, 4SAIL and FR97 show a slight difference lower than 0.002, while REN15 model is closer to FR97 model for low VZAs and it takes closer values to 4SAIL model when the angle increases, as it was expected [27]. It can be observed how the differences between models are inverted when the LAI is reduced, Mod3 model is close to the FR97 model for lower LAIs (LAI < 2 m^2/m^2), but it is closer for Rmod3 model when LAIs are higher (LAI > 2 m^2/m^2), because the increment of P_v, makes their expressions more similar.

The relation of the models with TES emissivity seems to vary with LAI. An overestimation is observed in the FR97, 4SAIL, REN15, and CE-P models for LAIs ≥ 2.0 m^2/m^2. However, they fit quite well for LAI < 2 m^2/m^2. In the case of Mod3 model, it slightly underestimates the TES measurements in most cases, but no high differences are observed. Rmod3 model is the model which differs from the TES measurements. Only for high LAIs, when the values are close to those given by the Mod3 model, its values are close to the TES emissivities. Table 4 summarizes the bias and RMSE of the comparison of models emissivity with TES emissivity. As it is observed from Figures 5–9, the differences between TES emissivity and FR97, 4SAIL, and REN15 models increase with LAI. Contrarily, for Mod3 and Rmod3 model, the differences decrease with LAI.

Table 4. Statistical analyses of the comparison between the canopy emissivity models and TES method at different viewing zenith angles (VZAs) for the different LAI measurements and for all bands and observation angles using the organic soil in the sample.

LAI	FR97		MOD3		RMOD3		4SAIL		REN15		CE-P	
	bias	RMSE	bias	RMSE	bias	RMSE	bias	RMSE	bias	RMSE	bias	RMSE
2.8	0.010	0.010	−0.001	0.002	−0.001	0.002	0.011	0.011	0.011	0.011	0.012	0.012
2.4	0.006	0.007	−0.003	0.004	−0.006	0.006	0.008	0.008	0.007	0.008	0.009	0.009
2	0.005	0.005	−0.004	0.005	−0.008	0.008	0.006	0.007	0.006	0.006	0.007	0.007
1.5	0.003	0.004	−0.004	0.005	−0.010	0.010	0.005	0.005	0.004	0.004	0.005	0.005
0.9	−0.001	0.002	−0.005	0.006	−0.014	0.015	0.001	0.002	0.000	0.002	0.0007	0.002
0.5	−0.005	0.005	−0.007	0.007	−0.016	0.017	−0.003	0.004	−0.004	0.005	−0.003	0.003
Overall	0.003	0.006	−0.004	0.005	−0.009	0.011	0.005	0.007	0.004	0.007	0.005	0.007

4.3.2. Inorganic Soil

For the inorganic soil, the VZAs measured were 0° and 55° for the LAIs defined in Table 1 for this soil. Figures 10–14 show the emissivities obtained for the five CE312-2 narrow bands from the six directional emissivity canopy models and the TES emissivity measurement for both angles. The obtained values ranged from 0.887 to 0.988 depending on LAI, VZA and spectral range. The mean uncertainty, obtained as the standard deviation of the measurements, was between ±0.003 (Figure 10) and ±0.009 (Figure 14).

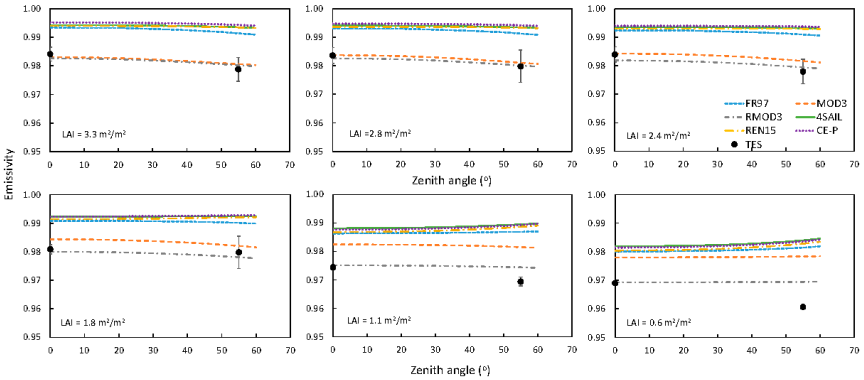

Figure 10. TES emissivity measurements and FR97, Mod3, Rmod3, 4SAIL, REN15, and CE-P models emissivity values at different zenith angles and LAI values for the CE312-2 radiometer 10.9–11.7 µm spectral band using an inorganic soil.

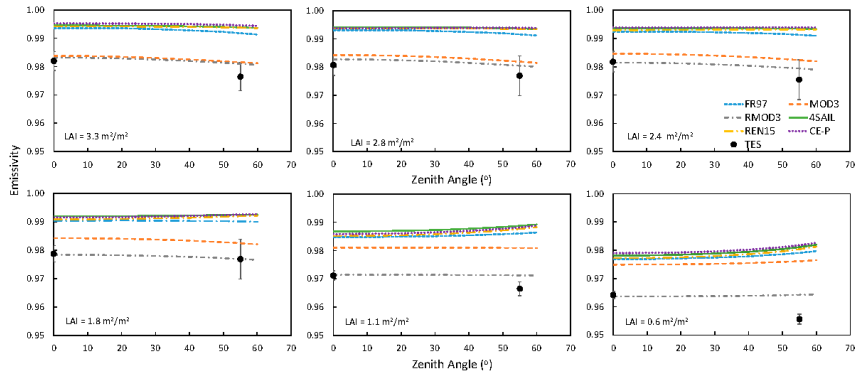

Figure 11. TES emissivity measurements and FR97, Mod3, Rmod3, 4SAIL, REN15, and CE-P models emissivity values at different zenith angles and LAI values for the CE312-2 radiometer 10.2–11.0 µm spectral band using an inorganic bare soil.

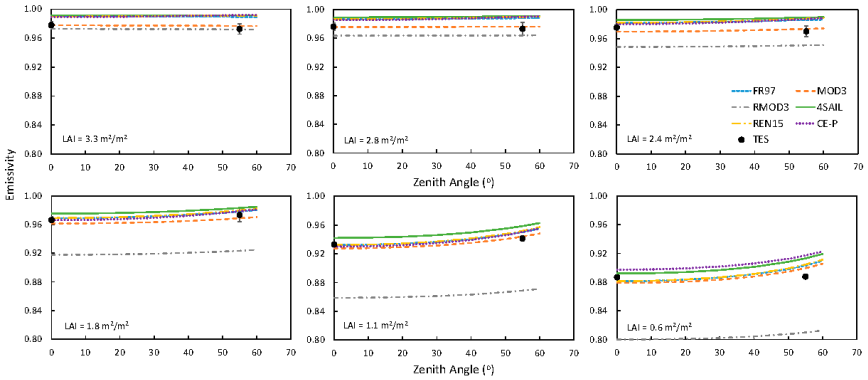

Figure 12. TES emissivity measurements and FR97, Mod3, Rmod3, 4SAIL, REN15, and CE-P models emissivity values at different zenith angles and LAI values for the CE312-2 radiometer 9.0–9.3 µm spectral band using an inorganic soil.

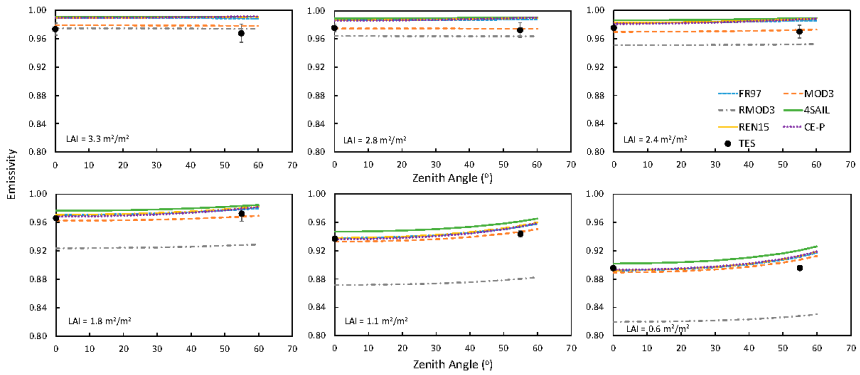

Figure 13. TES emissivity measurements, and FR97, Mod3, Rmod3, 4SAIL, REN15, and CE-P models emissivity values at different zenith angles and LAI values for the CE312-2 radiometer 8.5–8.9 µm spectral band using an inorganic soil.

From Figures 10 and 11, because of the emissivity values are close to the organic soil, the models behavior is similar to that of the observed with this soil. However, differences are found in Figures 12–14, where the soil emissivity is significantly lower. The differences between FR97 and 4SAIL models increase when the LAI is reduced, giving differences up to 0.01. REN15 and CE-P models remains between both, but they are always close to FR97 model for all angles. Also, the differences between Mod3 and RMod3 model increase with LAI, showing similar values for high LAIs, but the Rmod3 model decrease considerably with LAI, yielding to differences with Mod3 model up to 0.08 for the lowest LAI measured.

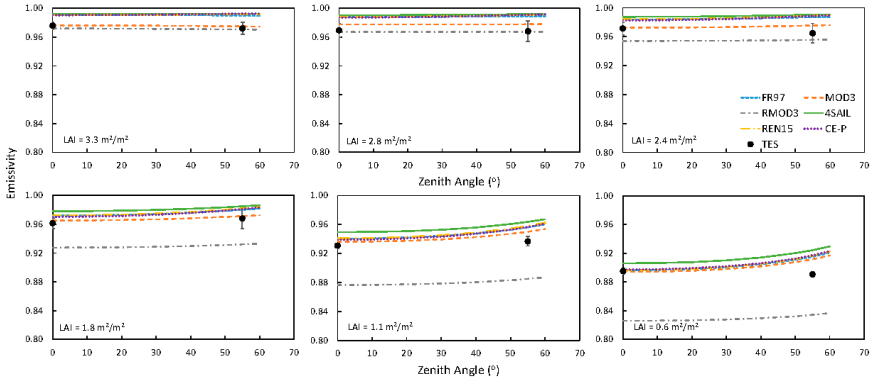

Figure 14. TES emissivity measurements, and FR97, Mod3, Rmod3, 4SAIL, REN15, and CE-P models emissivity values at different zenith angles and LAI values for the CE312-2 radiometer 8.3–8.6 µm spectral band using an inorganic soil.

In the comparison with TES emissivity, FR97, 4SAIL, REN15, and CE-P models overestimate the emissivity for most cases. Opposite to the observations in the comparison of the organic soil, Rmod3 model is the model that fits better to the TES emissivity for 10–12 µm range. However, this model is largely the model that differs more with TES emissivity for 8–9.5 µm range and LAI < 2.0 m^2/m^2, as it is shown in Figures 12–14. It is Mod3 model which shows the best agreement with TES emissivity in Figures 12–14, but it also gives close values for 8.3–8.9 µm and LAI > 1.5 m^2/m^2. Table 5 shows the bias and RMSE of the comparison of the models emissivity with TES emissivity. Taking into account all data, Mod3 model shows the best agreement with TES emissivity, with an overall RMSE of 0.007. Rmod3 model, although it shows the lowest RMSE and a null bias for LAI = 3.3 m^2/m^2, it has largely the highest global RMSE. FR97, 4SAIL, REN15, and CE-P models obtain similar RMSE for all LAIs and total data also, obtaining a similar RMSE to Mod3 model just for the lowest LAI.

Table 5. Statistical analyses of the comparison between the canopy emissivity models and TES method at different VZAs for the different LAI measurements and for all bands and observation angles using the inorganic soil in the sample.

LAI	FR97		MOD3		RMOD3		4SAIL		REN15		CE-P	
	bias	RMSE	bias	RMSE	bias	bias	bias	RMSE	bias	RMSE	bias	RMSE
3.3	0.015	0.015	0.002	0.004	0.000	0.016	0.016	0.017	0.016	0.016	0.016	0.017
2.8	0.014	0.014	0.003	0.005	−0.004	0.015	0.016	0.017	0.015	0.015	0.015	0.016
2.4	0.013	0.014	0.002	0.005	−0.011	0.014	0.016	0.016	0.014	0.015	0.014	0.015
1.8	0.009	0.009	0.001	0.004	−0.026	0.010	0.013	0.013	0.010	0.011	0.009	0.010
1.1	0.011	0.013	0.006	0.009	−0.037	0.012	0.017	0.018	0.012	0.014	0.011	0.014
0.64	0.012	0.016	0.009	0.014	−0.042	0.012	0.018	0.021	0.012	0.017	0.013	0.017
Overall	0.012	0.014	0.004	0.007	−0.020	0.013	0.016	0.017	0.013	0.015	0.013	0.015

5. Discussion

Six RTM to retrieve the canopy emissivity were evaluated using in situ TES emissivity over a set of rose plants and two different soils, an organic and inorganic soil. During the time the experiment was carried out, for LAIs higher than 2.0 m^2/m^2, the canopy was seen as an almost continuous layer of leaves. However, for LAI lower than 2.0 m^2/m^2, the quantity of ground which was seen by the sensor increased considerably when LAI decreased (See Table 1). Therefore, for lower LAIs, it was expected to obtain higher uncertainty values, mainly because of the arbitrariness of the position of leaves causes the structure of the plant be more unpredictable, and as a consequence, it could be viewed slightly

different by the sensor for each VZA. However, all the uncertainties calculated from the measurements resulted in quite similar values.

From the at nadir comparison of the emissivity models, an increase of emissivity from low to high LAI values was observed, obtaining a value close to the limit emissivity for the highest LAI. Although the limit emissivity reached with each soil is the same, since there is no effect of soil emissivity on the limit emissivity retrieval [22,27], closer values to the limit emissivity were obtained for the organic soil for LAI values lower than for the inorganic soil. Then, the soil emissivity has no impact on the canopy limit emissivity, but it does on the value of emissivity for high LAIs analyzed in this study.

When the soil emissivity is high, close to the leaf emissivity, as for the cases of the organic soil at all wavelengths and the inorganic soil at 10–12 μm, all models show differences which could be reasonable taking into account the emissivity error, since the difference values given by the different models are quite close. Despite of that, it is observed that Mod3 model provides slightly better overall results, but they cannot be conclusive, since differences are within the TES uncertainties and also depend on the LAI analyzed. But when differences between soil and leaf emissivity increase, as for 8–9.5 μm range of the inorganic soil, Mod3 is the model that best fits with TES emissivity for the data analyzed in this study. In these cases, the other models show significant discrepancies with TES emissivity. If it is just taken into account the 8–9.5 μm range of the measurements with the inorganic soil, the bias of FR97, 4SAIL, REN15, and CE-P models are 0.011, 0.017, 0.012, and 0.011, respectively, which are similar to those obtained in Table 5. Mod3 model obtains a bias of 0.002 in this case. This model differs from the FR97 model in the consideration of the multiple reflections between the leaves of the canopy. Since Mod3 model takes into account the interaction between the soil and leaves in a more adequate way, then the canopy emissivity obtained is lower than the one obtained with FR97 model; this effect is stressed in the cases where the LAI, and the quantity of leaves, is higher. It is in these cases, when the LAI is higher, in which Mod3 model shows better results than FR97 model, for both organic and inorganic soils. Rmod3 model obtained accurate results when its values were close to those given by Mod3 model, that is, when LAI is high and the contribution of soil emissivity is weak, but also for 10–12 μm range with the inorganic soil. In these cases, the same occurred for REN15, CE-P, and 4SAIL models because of a systematic difference was observed between these models and FR97 model. This is because REN15 model modifies the cavity effect of the FR97 model by using the limit emissivity values obtained from the 4SAIL model. In the case of CE-P model, despite it is based on spectral invariants as the recollision and escape probabilities instead of the cavity effect coefficient, the values obtained are quite close to those obtained by the FR97 and REN15 models. However, when the LAI decreases, and consequently the P_v does, the soil emissivity gains weight and, if the soil emissivity is much lower than leaf emissivity, a strong decrease in the canopy emissivity is expected. This is why the Rmod3 model considerably decreases when LAI decreases, especially for 8–9.5 μm range measurements over the inorganic soil. In the case of the organic soil, this decrease is not so significant because of the similar values of the soil and leaf emissivity at all wavelengths.

Regarding the angular emissivity variation, a clear trend was not observed in any of the analyzed cases. The organic soil shows a decrease of emissivity with VZA (from 0 to 60°) between 0.01 and 0.02, and the inorganic soil between 0.03 and 0.06 [10]. However, models predict an increase in emissivity when LAI is reduced and more soil is seen, because of the cavity effect. TES emissivity measurements do not reflect clearly the increase or decrease with VZA. In the case of the organic soil, for LAI < 2 m^2/m^2 and depending on the spectral range, the emissivity increases with angle with respect to the nadir between 0.001 and 0.005, which are values within the uncertainty. For the highest LAI (LAI = 2.8 m^2/m^2), the emissivity decreases with respect to nadir between 0.003 and 0.008, depending on the spectral range. But for high LAIs, this decreasing should be attributed to the cavity effect. For the inorganic soil, it is expected some decrease with angle; however, it is only observed for all LAIs in 10–12 μm, which are the bands with low decrease when bare soil is analyzed. These differences on the emissivity observed for the different VZAs range from 0.002 to 0.008 depending on the LAI, being higher when more soil is observed. For 8–9.5 μm range and LAI > 2 m^2/m^2, the decrease observed is

around 0.005, and also for 10.9–11.7 μm and LAI of 0.6 m^2/m^2. But for LAIs between 1 and 2 m^2/m^2, the emissivity increases around 0.007 with angle. Therefore, taking into account the uncertainty of the TES emissivity measurements, no significant variation of emissivity with VZAs between 0° and 60° is observed for canopy emissivity in this study.

6. Summary and Conclusions

An accurate retrieval of LST requires a precise knowledge of surface emissivity. Over vegetated areas, it is necessary to consider the multiple reflections between ground and vegetation when the canopy emissivity is calculated. Several methods to obtain the canopy emissivity are found in the literature. In this work, six RTM-based directional canopy emissivity models are evaluated with in situ TES emissivity measurements acquired with a CE312-2 radiometer. The selected models are FR97 [22], Mod3 [23], Rmod3 [26], REN15 model [27], CE-P [28], and 4SAIL model [25].

The sample used during the study was a set of rose plants with organic soil as background in the first period and with inorganic soil (sand) in a second period. Several measurements were done over the sample using a CE312-2 radiometer with five bands within 8 μm and 13 μm. We took 15 radiance measurements for each one of the seven (two) VZAs and for six LAI levels for the first (second) period. Also, the component (leaves and soil) emissivities were measured with the TES algorithm. From these emissivities, a flat spectrum was seen for the leaves, close to 0.98. For the bare soils, the obtained values were between 0.949 and 0.967 for the organic soil, and between 0.732 and 0.962 for the inorganic soil. These values were used as the input of the models for each spectral band.

We compared the model-derived and measured emissivities at nadir. For organic soil, results showed that the measured TES emissivities were similar for different LAI values. However, for inorganic soil, where the difference between soil and leaf emissivity was higher, the increase in emissivity predicted by the models is clearly reproduced by the TES measurements. The Mod3 model agreed with the TES measurements better than the other models, according to the RMSE obtained from the statistical analysis with both organic and inorganic soil, especially for bands where the difference on soil–leaf emissivity is high.

The evaluation carried out at different VZAs obtained a quite constant emissivity for both models and TES emissivity, with small variation with the VZA for both organic and inorganic soil. Thus, from this study, no variation with angle is expected for canopy emissivity in similar conditions. From the comparison among models with the TES method, for the organic soil, where the difference of soil–leaf emissivity is little, Mod3 obtained a slightly lower overall RMSE compared with FR97, REN15, CE-P, and 4SAIL, but the differences between them were within the measurement uncertainties. In addition, the model which adjusted best with the reference measurements depended on the LAI range, being the Mod3 model which provided best results for LAI > 2.0 m^2/m^2 and the FR97 model when LAI < 2.0 m^2/m^2. However, when the difference soil–leaf emissivity is high, as for 8–9.5 μm range of the inorganic soil, the Mod3 model gave the best results compared with TES emissivity measurements, while the FR97, REN15, CE-P, and 4SAIL models overestimated considerably the TES measurements and Rmod3 largely underestimated the TES emissivity, especially for low LAI values.

Author Contributions: Conceptualization, E.V., R.N. and L.P.; formal analysis, L.P.-P.; investigation, L.P.-P.; resources, J.P.; software, M.C.-T.; supervision, E.V., R.N. and C.C.; writing—original draft, L.P.-P.; writing—review and editing, E.V., R.N. and C.C.

Funding: This work was funded by the Spanish Ministry of Economy and Competitiveness and the European Regional Development Fund (FEDER) (project CGL2015-64268-R (MINECO/FEDER, UE)), the Spanish Ministry of Economy and Competitiveness under the project CGL2013-46862-C2-1-P, and by the grant supported by the regional program of training of technicians for R&D&i—Youth Guarantee GJIDI-2018-A-142.

Acknowledgments: We thank Biao Cao for providing the CE-P model codes. We are also grateful to the three reviewers for their comments and suggestions, which improved this manuscript.

Conflicts of Interest: The authors declare no conflict of interest.

References

1. Anderson, M.C.; Kustas, W.P.; Norman, J.M.; Hain, C.R.; Mecikalski, J.R.; Schultz, L.; González-Dugo, M.P.; Cammalleri, C.; D'Urso, G.; Pimstein, A. Mapping daily evapotranspiration at field to continental scales using geostationary and polar orbiting satellite imagery. *Hydrol. Earth Syst. Sci.* **2011**, *15*, 223–239. [CrossRef]
2. Sánchez, J.M.; López-Urrea, R.; Rubio, E.; González-Piqueras, J.; Caselles, V. Assessing crop coefficients of sunflower and canola using two-source energy balance and thermal radiometry. *Agric. Water Manag.* **2014**, *137*, 23–29. [CrossRef]
3. Li, Z.; Tang, B.; Wu, H.; Ren, H.; Yan, G.; Wan, Z.; Trigo, I.F.; Sobrino, J.A. Satellite-derived land Surface temperature: Current status and perspectives. *Remote Sens. Environ.* **2013**, *131*, 14–37. [CrossRef]
4. Salisbury, J.W.; D'Aria, M. Emissivity of terrestrial materials in the 8–14 μm atmospheric window. *Remote Sens. Environ.* **1992**, *42*, 83–106. [CrossRef]
5. Baldridge, A.M.; Hook, S.J.; Grove, C.I.; Rivera, G. The ASTER spectral library version 2.0. *Remote Sens. Environ.* **2009**, *113*, 711–715. [CrossRef]
6. Ullah, S.; Schlerf, M.; Skidmore, A.K.; Hecker, C. Identifying plant species using mid-wave infrared (2.5–6 μm) and thermal infrared (8–14 μm) emissivity spectra. *Remote Sens. Environ.* **2012**, *118*, 95–102. [CrossRef]
7. Rock, G.; Gerhards, M.; Schlerf, M.; Hecker, C.; Udelhoven, T. Plant species discrimination using emissive thermal infrared imaging spectroscopy. *Int. J. Appl. Earth Obs. Geoinf.* **2016**, *53*, 16–26. [CrossRef]
8. Labed, J.; Stoll, M.P. Angular variation of land surface spectral emissivity in the thermal infrared: Laboratory investigations on bare soils. *Int. J. Remote Sens.* **1992**, *12*, 2299–2310. [CrossRef]
9. Cuenca, J.; Sobrino, J.A. Experimental measurements for studying angular and spectral variation of thermal infrared emissivity. *Appl. Opt.* **2004**, *43*, 4598–4602. [CrossRef]
10. García-Santos, V.; Valor, E.; Caselles, V.; Burgos, M.A.; Coll, C. On the angular variation of thermal infrared emissivity of inorganic soils. *J. Geophys. Res.* **2012**, *117*, D19116. [CrossRef]
11. Salisbury, J.W.; D'Aria, M. Infrared (8–14 mm) remote sensing of soil particle size. *Remote Sens. Environ.* **1992**, *42*, 157–165. [CrossRef]
12. Mira, M.; Valor, E.; Caselles, V.; Rubio, E.; Coll, C.; Galve, J.M.; Niclos, R.; Sánchez, J.M.; Boluda, R. Soil moisture effect on thermal infrared (8–13-mm) emissivity. *IEEE Trans. Geosci. Remote Sens.* **2010**, *48*, 2251–2260. [CrossRef]
13. García-Santos, V.; Valor, E.; Caselles, V.; Coll, C.; Burgos, M.A. Effect of Soil Moisture on the Angular Variation of Thermal Infrared Emissivity of Inorganic Soils. *IEEE Geosci. Remote Sens. Lett.* **2014**, *11*, 1091–1095. [CrossRef]
14. Warren, S.G.; Wiscombe, W.J. A model for the spectral albedo of snow. II: Snow containing atmospheric aerosols. *J. Atmos. Sci.* **1980**, *37*, 2734–2745. [CrossRef]
15. Hapke, B. *Theory of Reflectance and Emittance Spectroscopy*; Cambridge Univ. Press: NewYork, NY, USA, 2012; p. 455.
16. García-Santos, V.; Valor, E.; Caselles, V.; Doña, C. Validation and comparison of two models based on the Mie theory to predict 8–14 μm emissivity spectra of mineral surfaces. *J. Geophys. Res. Solid Earth* **2016**, *121*, 1739–1757. [CrossRef]
17. García-Santos, V.; Valor, E.; Di Biagio, C.; Caselles, V. Predictive Power of the Emissivity Angular Variation of Soils in the Thermal Infrared (8–14 μm) Region by Two Mie-Based Emissivity Theoretical Models. *IEEE Geosci. Remote Sens. Lett.* **2018**, *15*, 1115–1119. [CrossRef]
18. Cao, B.; Liu, Q.; Du, Y.; Roujean, J.L.; Gastellu-Etchegorry, J.P.; Trigo, I.F.; Zhan, W.; Yu, Y.; Cheng, J.; Jacob, F.; et al. A review of earth surface thermal radiation directionality observing and modeling: Historical development, current status and perspectives. *Remote Sens. Environ.* **2019**, *232*, 111304. [CrossRef]
19. Snyder, W.C.; Wan, Z. BRDF models to predict spectral reflectance and emissivity in the thermal infrared. *IEEE Trans. Geosci. Remote Sens.* **1998**, *36*, 214–225. [CrossRef]
20. Sobrino, J.A.; Caselles, V. Thermal infrared radiance model for interpreting the directional radiometric temperature of a vegetative surface. *Remote Sens. Environ.* **1990**, *33*, 193–199. [CrossRef]
21. Valor, E.; Caselles, V. Validation of the vegetation cover method for land surface emissivity estimation. In *Recent Research Developments in Thermal Remote Sensing*; Research Signpost: Kerala, India, 2005.

22. François, C.; Ottlé, C.; Prévot, L. Analytical parameterization of canopy directional emissivity and directional radiance in the thermal infrared. Application on the retrieval of soil and foliage temperatures using two directional measurements. *Int. J. Remote Sens.* **1997**, *18*, 2587–2621. [CrossRef]
23. François, C. The potential of directional radiometric temperatures for monitoring soil and leaf temperature and soil moisture status. *Remote Sens. Environ.* **2002**, *80*, 122–133. [CrossRef]
24. Guillevic, P.; Gastellu-Etchegorry, J.P.; Demarty, J.; Prévot, L. Thermal infrared radiative transfer within three-dimensional vegetation covers. *J. Geophys. Res.* **2003**, *108*, 4248. [CrossRef]
25. Verhoef, W.; Jia, L.; Xiao, Q.; Su, Z. Unified Optical-Thermal Four-Stream Radiative Transfer Theory for Homogeneous Vegetation Canopies. *IEEE Trans. Geosci. Remote Sens.* **2007**, *45*, 1808–1822. [CrossRef]
26. Shi, Y. Thermal infrared inverse model for component temperatures of mixed pixels. *Int. J. Remote Sens.* **2011**, *32*, 2297–2309. [CrossRef]
27. Ren, H.; Liu, R.; Yan, G.; Li, Z.L.; Qin, Q.; Liu, Q.; Nerry, F. Performance evaluation of four directional emissivity analytical models with thermal SAIL model and airborne images. *Opt. Express* **2015**, *23*, A346–A360. [CrossRef] [PubMed]
28. Cao, B.; Guo, M.; Fan, W.; Xu, X.; Peng, J.; Ren, H.; Du, Y.; Li, H.; Bian, Z.; Hu, T.; et al. A new directional canopy emissivity model based on spectral invariants. *IEEE Trans. Geosci. Remote Sens.* **2018**, *56*, 6911–6926. [CrossRef]
29. Sobrino, J.A.; Jiménez-Muñoz, J.C.; Verhoef, W. Canopy directional emissivity: Comparison between models. *Remote Sens. Environ.* **2005**, *99*, 304–314. [CrossRef]
30. Neinavaz, E.; Skidmore, A.K.; Darvishzadeh, R.; Groen, T.A. Retrieval of leaf area index in different plant species using thermal hyperspectral data. *ISPRS J. Photogramm. Remote Sens.* **2016**, *119*, 390–401. [CrossRef]
31. Neinavaz, E.; Darvishzadeh, R.; Skidmore, A.K.; Groen, T.A. Measuring the response of canopy emissivity spectra to leaf area index variation using thermal hyperspectral data. *Int. J. Appl. Earth Obs. Geoinf.* **2016**, *53*, 40–47. [CrossRef]
32. Gillespie, A.; Rokugawa, S.; Matsunaga, T.; Cothern, J.S.; Hook, S.; Kahle, A.B. A Temperature and Emissivity Separation Algorithm for Advanced Spaceborne Thermal Emission and Reflection Radiometer (ASTER) Images. *IEEE Trans. Geosci. Remote Sens.* **1998**, *36*, 1113–1126. [CrossRef]
33. Coll, C.; Niclòs, R.; Puchades, J.; García-Santos, V.; Galve, J.M.; Pérez-Planells, L.; Valor, E.; Thecharous, E. Laboratory calibration and field measurement of land surface temperature and emissivity using thermal infrared multiband radiometers. *Int. J. Appl. Earth Obs. Geoinf.* **2019**, *78*, 227–239. [CrossRef]
34. Legrand, M.; Pietras, C.; Brogniez, G.; Haeffelin, M.; Abuhassan, N.K.; Sicard, M. A high-accuracy multiwavelength radiometer for in situ measurements in the thermal infrared. Part I: Characterization of the instrument. *J. Atmos. Ocean. Technol.* **2000**, *17*, 1203–1214. [CrossRef]
35. Confalonieri, R.; Foi, M.; Casa, R.; Aquaro, S.; Tona, E.; Peterle, M.; Boldini, A.; Carli, G.D.; Ferrari, A.; Finotto, G. Development of an app for estimating leaf area index using a smartphone. Trueness and precision determination and comparison with other indirect methods. *Comput. Electron. Agric.* **2013**, *96*, 67–74. [CrossRef]
36. Korb, A.R.; Dybwad, P.; Wadsworth, W.; Salisbury, J.W. Portable Fourier transform infrared spectroradiometer for field measurements of radiance and emissivity. *Appl. Opt.* **1996**, *35*, 1679–1692. [CrossRef] [PubMed]
37. Theocharous, E.; Fox, N.P.; Barker-Snook, I.; Niclòs, R.; García-Santos, V.; Minnett, P.; Göttsche, F.M.; Poutier, L.; Morgan, N.; Nightingale, T.; et al. The 2016 CEOS infrared radiometer comparison: Part 2: Laboratory comparison of radiation thermometers. *J. Atmos. Ocean. Technol.* **2019**, *36*, 1079–1092. [CrossRef]
38. García-Santos, V.; Valor, E.; Caselles, V.; Mira, M.; Galve, J.M.; Coll, C. Evaluation of different methods to retrieve the hemispherical downwelling irradiance in the thermal infrared region for field measurements. *IEEE Trans. Geosci. Remote Sens.* **2013**, *51*, 2155–2165. [CrossRef]
39. Coll, C.; Caselles, V.; Valor, E.; Niclòs, R.; Sánchez, J.M.; Galve, J.M.; Mira, M. Temperature and emissivity separation from ASTER data for low spectral contrast surfaces. *Remote Sens. Environ.* **2007**, *110*, 162–175. [CrossRef]
40. Gillespie, A.R.; Abbott, E.A.; Gilson, L.; Hulley, G.; Jiménez-Muñoz, J.C.; Sobrino, J.A. Residual errors in ASTER temperature and emissivity standard products AST08 and AST05. *Remote Sens. Environ.* **2011**, *115*, 3681–3694. [CrossRef]

41. Pérez-Planells, L.; Valor, E.; Coll, C.; Niclòs, R. Comparison and Evaluation of the TES and ANEM Algorithms for Land Surface Temperature and Emissivity Separation over the Area of Valencia, Spain. *Remote Sens.* **2017**, *9*, 1251. [CrossRef]
42. Mira, M.; Schmugge, T.J.; Valor, E.; Caselles, V.; Coll, C. Comparison of thermal emissivities retrieved with the two-lid box and TES methods with laboratory spectra. *IEEE Trans. Geosci. Remote Sens.* **2009**, *47*, 1012–1021. [CrossRef]
43. Gillespie, A. *Lithologic Mapping of Silicate Rocks Using TIMS*; TIMS Data User'sWorkshop Jet Propulsion Laboratory: Pasadena, CA, USA, 1986; pp. 29–44.
44. Hulley, G.; Hook, S.J. The North American ASTER Land Surface Emissivity Database (NAALSED) Version 2.0. *Remote Sens. Environ.* **2009**, *113*, 1967–1975. [CrossRef]
45. Chen, J.M.; Black, T.A. Defining leaf area index for non-flat leaves. *Plant Cell Environ.* **1992**, *15*, 421–429. [CrossRef]
46. Baret, F.; De Solan, B.; Lopez-Lozano, R.; Ma, K.; Weiss, M. GAI estimates of row crops from downward looking digital photos taken perpendicular to rows at 57.5 zenith angle: Theoretical considerations based on 3D architecture models and application to wheat crops. *Agric. For. Meteorol.* **2010**, *150*, 1393–1401. [CrossRef]
47. Campos-Taberner, M.; García-Haro, F.J.; Confalonieri, R.; Martínez, B.; Moreno, Á.; Sánchez-Ruiz, S.; Gilabert, M.A.; Camacho, F.; Boschetti, M.; Busetto, L. Multitemporal Monitoring of Plant Area Index in the Valencia Rice District with PocketLAI. *Remote Sens.* **2016**, *8*, 202. [CrossRef]
48. Francone, C.; Pagani, V.; Foi, M.; Cappelli, G.; Confalonieri, R. Comparison of leaf area index estimates by ceptometer and PocketLAI smart app in canopies with different structures. *Field Crop. Res.* **2014**, *155*, 38–41. [CrossRef]
49. Orlando, F.; Movedi, E.; Coduto, D.; Parisi, S.; Brancadoro, L.; Pagani, V.; Guarneri, T.; Confalonieri, R. Estimating Leaf Area Index (LAI) in Vineyards Using the PocketLAI Smart-App. *Sensors* **2016**, *16*, 2004. [CrossRef] [PubMed]
50. Orlando, F.; Movedi, E.; Paleari, L.; Gilardelli, C.; Foi, M.; Dell'Oro, M.; Confalonieri, R.; Hermy, M. Estimating leaf area index in tree species using the PocketLAI smart app. *Appl. Veg. Sci.* **2015**, *18*, 716–723. [CrossRef]
51. Prévot, L. Modélisation des Échanges radiatifs au Sein des Couverts Végétaux. Application à la Télédétection. Validation sur un Couvert de Maïs. Ph.D. Thesis, University of Paris VI, Paris, France, 1985.
52. Chehbouni, A.; Nouvellon, Y.; Kerr, Y.H.; Moran, M.S.; Watts, C.; Prévot, L.; Watts, C.; Goodrich, D.C.; Rambal, S. Directional effect on radiative surface temperature measurements over a semi-arid grassland site. *Remote Sens. Environ.* **2001**, *76*, 360–372. [CrossRef]
53. Verhoef, W. Light scattering by leaf layers with application to canopy reflectance modeling: The SAIL model. *Remote Sens. Environ.* **1984**, *16*, 125–141. [CrossRef]
54. Guo, M.; Cao, B.; Fan, W.; Ren, H.; Cui, Y.; Du, Y.; Liu, Q. Scattering effect contributions to the directional canopy emissivity and brightness temperature based on CE-P and CBT-P models. *IEEE Geosci. Remote Sens. Lett.* **2019**, *16*, 957–961. [CrossRef]

Anexo J

Validation of the Sentinel-3 SLSTR operational land surface temperature product and emissivity-dependent split-window algorithms over a rice paddy site

El siguiente trabajo ha sido enviado para su revisión por pares a la revista Remote Sensing of Environment. Esta revista tiene un factor de impacto de 9,01 y ocupa la posición 2 de 30 revistas en la categoría de Remote Sensing según Journal Citation Reports en la edición de 2019.

Elsevier Editorial System(tm) for Remote Sensing of Environment

Manuscript Draft

Manuscript Number: RSE-D-20-01426

Title: Validation of the Sentinel-3 SLSTR operational land surface temperature product and emissivity-dependent split-window algorithms over a rice paddy site

Article Type: Research Paper

Keywords: SLSTR; LST; emissivity; validation; ground data; Split-Window algorithm.

Corresponding Author: Mr. Lluís Pérez-Planells,

Corresponding Author's Institution: University of Valencia

First Author: Lluís Pérez-Planells

Order of Authors: Lluís Pérez-Planells; Raquel Niclòs; Jesús Puchades; César Coll; Frank-M Göttsche; Jose A. Valiente; Enric Valor; Joan M. Galve

Abstract: Land Surface temperature (LST) is an Essential Climate Variable (ECV) for the monitoring of the Earth climate system. To ensure its accurate retrieval from satellite data, it is important to validate LST products and ensure that they are within the required accuracy and precision thresholds (< 1 K). This paper aims to validate the Sentinel-3A SLSTR operational LST product as well as several emissivity-dependent split-window algorithms with in-situ data at a rice paddy site. Furthermore, a new emissivity-dependent split-window algorithm with viewing angle dependence is proposed. The LST retrieval algorithms were validated over three different land covers: flooded soil, bare soil and full vegetation cover. Ground measurements were performed with a wide band thermal infrared radiometer of a permanent station at a rice paddy site. The site has been shown to be thermally homogeneous and, therefore, the permanent station is well suited for LST validation. For the Sentinel-3A SLSTR operational LST product, an overall systematic uncertainty (median) of 1.3 K and a precision (robust standard deviation) of 1.3 K were obtained for the three surface types. A preliminary evaluation of the Sentinel-3B SLSTR operational LST product was also performed: systematic uncertainty was 1.7 K and precision 0.9 K, i.e. we obtained a slightly higher systematic uncertainty but a slightly better precision compared with Sentinel-3A. Three well-established emissivity-dependent split-window algorithms were also validated: overall systematic uncertainties of -0.8 K, -0.7 K and 0.3 K and precisions of 0.9 K, 1.1 K and 1.2 K were obtained for Sobrino16, Zhang19 and Zheng19 algorithms, respectively. The coefficients of the new split-window algorithm proposed here were estimated using the Cloudless Land Atmosphere Radiosounding (CLAR) database: for the same in-situ data, systematic uncertainty was -0.4 K and precision 1.1 K. The results showed that the emissivity-dependent split-window algorithms provide more accurate and precise LSTs than the operational SLSTR product for the three land covers found at the rice paddy site.

Highlights (for review)

Research highlights

- The operational SLSTR LST product was validated over a rice paddy site.
- A median of 1.3 (1.7) K and RSD of 1.3 (0.9) K were obtained for Sentinel-3A(B).
- Three published alternative split-window algorithms were validated.
- A new alternative emissivity-dependent split-window algorithm was proposed.
- Alternative algorithms obtained better validation results than SLSTR LST product.

Anexo K

Evaluation of Landsat-8 TIRS data recalibrations and land surface temperature split-window algorithms over a homogeneous crop area with different phenological land covers

El siguiente trabajo se encuentra en revisión en la revista Journal of Photogrammetry and Remote Sensing. Esta revista tiene un factor de impacto de 7,32 y ocupa la posición 3 de 30 revistas en la categoría de Teledetección según Journal Citation Reports en la edición de 2019.

TITLE: Evaluation of Landsat-8 TIRS data recalibrations and land surface temperature split-window algorithms over a homogeneous crop area with different phenological land covers

AUTHORS: Raquel Niclòs[a], Jesús Puchades[a], César Coll[a], María J. Barberà[a], Lluís Pérez-Planells[a], José A. Valiente[b], Juan M. Sánchez[c]

[a] Department of Earth Physics and Thermodynamics, Faculty of Physics, University of Valencia, 50, Dr. Moliner, E-46100 Burjassot, Spain. E-mail: raquel.niclos@uv.es, jesus.puchades@uv.es, cesar.coll@uv.es, m.jesus.barbera@uv.es, lluis.perez@uv.es

[b] Instituto Universitario Centro de Estudios Ambientales del Mediterráneo–CEAM-UMH, 14 Charles Darwin, E-46980 Paterna, Spain. E-mail: valiente_jospar@gva.es

[c] Regional Development Institute, University of Castilla-La Mancha, Campus Universitario s/n, E-02071 Albacete, Spain. E-mail: JuanManuel.Sanchez@uclm.es

CORRESPONDING AUTHOR INFORMATION:

Raquel Niclòs,

Department of Earth Physics and Thermodynamics, Faculty of Physics, University of Valencia, 50, Dr. Moliner, E-46100 Burjassot, Spain.

E-Mail: raquel.niclos@uv.es

Tel.: +34-963-543-308; Fax: +34-963-543-385

ABSTRACT

The Landsat-8 TIRS dataset has been modified several times, since its launch in 2013, to introduce instrument calibration updates, mainly to solve the effect of out-of-field stray light on the detectors. In this paper, the performances of the different reprocessings of TIRS data were evaluated. Measurements taken by TIR radiometers along transects in a rice paddy area (with different phenological covers) between 2014 and 2019 were used as reference. The results showed that the original TIRS data provided biases lower than the constant values that were subtracted from the original data in the 2014 reprocessing. Thus, data after this reprocessing showed underestimations at the site, with biases between satellite brightness temperatures and those estimated from ground data of -1.4 K and -1.6 K for bands 10 and 11, respectively. However, when using data after the 2017 reprocessing (i.e., that applied to remove out-of-field radiation and to generate the current available dataset in Collection 1), the results showed negligible biases and root-mean-square differences less than 1.5 K. We also evaluated the calibration update announced in December 2019 for TIRS data in the next Landsat Collection 2. This new calibration mainly modified the biases in our results, improving slightly the results for band 10 and introducing a calibration response difference between both bands, not observed in the current data.

Taking into account the improvements in the TIRS data calibration after the 2017 reprocessing, we also evaluated single-channel (SC) corrections and split-window (SW) algorithms to retrieve land surface temperature (LST) from TIRS data. The SC correction showed negligible biases for both bands, and the lowest root-mean-square differences (<1.6 K) when using band 10 data. Five SW algorithms with different sets of coefficients, with a total of seventeen different SW versions, were evaluated. Seven of them showed negligible or small biases and LST root-mean-square differences lower than or equal to 1 K when applied to TIRS data after the 2017 reprocessing and compared with ground LSTs measured at the site. On the view of the results, three of them are mainly recommended for users of the current data; one of them being the proposed to generate a SW product in the Landsat Collection 3. Finally, the SC results improved slightly for band 10 after applying the 2019 calibration

update to our dataset. Bias differences around 1.4 K were shown in the results of the SW algorithms after the update.

KEYWORDS: Landsat-8 TIRS, calibration, LST algorithms, validation, in-situ measurements, thermal-infrared.